Ab-initio Wannier Functions, Coulomb Matrix Elements, Hartree (-Fock) and LSDA Calculations for the 3d Transition Metals Fe, Co, Ni and Cu

Ilan Schnell

University of Bremen, Germany

2002

Ab-initio Wannier Functions, Coulomb Matrix Elements, Hartree (-Fock) and LSDA Calculations for the 3d Transition Metals Fe, Co, Ni and Cu

Vom Fachbereich für Physik und Elektrotechnik
der Universität Bremen

zur Erlangung des akademischen Grades
DOKTOR DER NATURWISSENSCHAFTEN (Dr. rer. nat.)
genehmigte Dissertation

von

Dipl.-Phys. Ilan Schnell
aus Lilienthal

1. Gutachter: Prof. Dr. G. Czycholl
2. Gutachter: Prof. Dr. F. Jahnke

Tag des Promotionskolloquiums: 15. 10. 2002

Preface

This Ph.D. thesis has been carried out in the period from 1999 till 2002. The work is organized as follows. After an introduction, concerning the goals and key ideas of this work, we review the density functional theory. This is followed by a look at how the electronic structure calculations are performed, in particular the LMTO method and the tetrahedron method. Next, a chapter is devoted to the calculation of maximally localized Wannier functions using a method proposed by Marzari and Vanderbilt. We then focus on the second quantized Hamiltonian, its matrix elements in Wannier representation and their evaluation within the atomic sphere approximation. By then, we will have all the pieces to perform many-particle calculations using this second quantized Hamiltonian with its matrix elements from first-principle, which will be dealt with in chapter 6. Finally, we present results for the $3d$ transition metals iron, cobalt, nickel and copper.

Acknowledgments

I am most grateful to my supervisor Gerd Czycholl, who has encouraged my Ph.D. studies all the years and has supported my work on many different levels.

I am also very thankful for all what Robert C. Albers has done for me. My collaboration with Bob began in 1998 when I started working on my Diploma thesis. Thanks to my supervisor Gerd Czycholl and Bob, I had the great opportunity to visit Bob at the Los Alamos National Laboratory in New Mexico for two months in 1998 to learn about computational methods in electronic structure theory. Many visits followed after that.

I would also like to thank the people in our department at the university for interesting discussions, in particular, I would like to thank Veljko Zlatic for suggesting the application of the FFT algorithm in the Coulomb matrix element calculations.

Part of this work, the LMTO method, has been based on existing codes written by Niels E. Christensen whom I had the pleasure to meet in Århus. For his helpfulness, I would like to thank him.

Section 4.3.3 was inspired by David Vanderbilt whom I was fortunate to meet in Indianapolis at the 2002 APS March Meeting.

Also, I would like to thank everybody else who supported me over the last years: My parents for encouragement, my brother Arvin for helping me getting started with the concept of object-oriented programming in C++ and my girlfriend Mary for her spiritual support. And anyone else I should have forgotten to mention. Thank you all very much!

For financial support I would like to thank: The University of Bremen, the Graduiertenkolleg “Komplexe Dynamische Systeme”, the US Government Department of Energy, the Deutsche Forschungsgesellschaft, the WE-Heraeus-Stiftung.

Bremen, August 2002

Ilan Schnell

Contents

Chapter 1

Introduction

An interesting branch of solid state physics is dealing with bulk properties of materials. Experimentally, a number of these properties, e.g. (mass) density, binding energy (or ionization energy), bulk modulus, are easily accessible. During the past few decades, powerful numerical methods have been developed for the ab-initio (first-principles) calculation of electronic ground state properties of crystalline solids. These are solids with a periodic crystal structure to which a large number of materials, in particular metals, on a microscopic scale, condense.

In most of these methods, density functional theory (DFT) [1] has been used to treat the electron-electron Coulomb repulsion. Within DFT, the so-called local density approximation (LDA) [2], or the local spin density approximation (LSDA) for magnetic systems, is commonly used for the exchange-correlation potential. For a wide range of materials, many ground state properties, such as crystal structure, lattice constant, crystal anharmonicity [3], are in good agreement with experiment. Despite its success, DFT has its limitations. The band gap of semiconductors is not properly reproduced, for instance. Furthermore, for systems such as high-temperature superconductors, heavy fermion materials, transition metal oxides and $3d$ itinerant magnets, i.e. for systems in which the Fermi level falls into a region of narrow energy bands, the LDA is usually not sufficient for an accurate description. Even for pure nickel, differences between LSDA and the experiment exist. There are at least two inconsistencies with the photoemission [4] spectra of ferromagnetic nickel [5]: (i) The measured width of the (occupied) part of the $3d$-band is about 30% narrower than the calculated one. (ii) The LSDA density of states does not show the so-called “Ni 6 eV satellite”, i.e. a peak about 6 eV below the Fermi level. Nevertheless, LSDA predicts the spin magnetic moment of Ni very accurately. It is generally accepted that the problem for these materials are the strong electronic correlations that are responsible for their electronic properties.

Usually, one approaches the description of strongly correlated systems differently. Instead of DFT, a model Hamiltonian, such as the Hubbard model [6] and its multi-band generalizations, is the starting point for considerations. The model Hamiltonian approach is more general and powerful since there exist systematic theoretical methods to investigate the many-body problem. But in these models, the Coulomb interaction matrix elements and also the one-particle hopping matrix elements (that determine the un-perturbed band structure) are usually treated as free, adjustable parameters. That is, they are not known from “first

principles" for the given material. The uncertainty in the choice of the model parameters and the technical complexity of the correlation problem itself prevent the model approach from being a reliable and flexible tool for studying real materials. Nevertheless, Coulomb correlations can be studied within reliable many-body approximations that go beyond the Hartree-Fock approximation.

Both the ab-initio LDA and the many-body model-Hamiltonian methods based on Hubbard-like models have their merits, but until rather recently, they have been almost separate and complementary approaches. In view of the power of each, a combination of these methods is desirable, and, in fact, during the last few years there have been some attempts in this direction (see Refs. [7-18]). All of these recent developments add local screened Coulomb (Hubbard) correlations U between localized orbitals to the un-correlated (one-particle) part of the Hamiltonian obtained from an ab-initio LDA band structure calculation. They differ in how the correlation part is handled, however. In the earliest attempts, the LDA+U method [7] uses essentially a static mean-field-like (or Hubbard-I-like) approximation for the correlation. The simplest approximation beyond Hartree-Fock, i.e. second order perturbation theory (SOPT) in U, was used [8, 9, 12, 16, 18] to study the electronic properties of $3d$-systems (like Fe and Ni) and heavy fermion systems (like UPt_3). The LDA++ approach [11, 13, 14] has a similar strategy, but uses other many-body approximations to treat the correlation problem, namely either the fluctuation exchange approximation (FLEX) [19] or the dynamical mean field theory (DMFT) [20]. Some of the other many-body treatments [10, 15, 17] also use DMFT, which is based on the limit of large-dimension ($d \to \infty$) approximation for correlated lattice electrons (see Ref. [21]). Within DMFT, the self-energy becomes local, i.e. independent of momentum $\mathbf{k}$, which allows a mapping of the lattice problem onto an effective impurity model. The LDA+DMFT treatments [13-17] mentioned above differ in the many-body method. They make use of the effective impurity problem, namely quantum Monte Carlo (QMC) [17], the non-crossing approximation (NCA) [15] or iterated perturbation theory (IPT) [10].

However, all these approaches, including the LDA+U, have in common that they still introduce a Hubbard-U as an additional parameter, and hence are not real first-principles treatments. Although they use an LDA ab-initio method to obtain a realistic band structure, i.e. single-particle properties, Coulomb matrix elements for any particular material are not known, and the Hubbard-U remains an adjustable parameter.

One can obtain estimates on the magnitude of U either from experiment (high-energy spectroscopy) or from the constrained LDA method (Refs. [7,22-27]). Within the latter method, one adds the constraint that the electron occupation number for the correlated bands is fixed to a given number through a Lagrange parameter.[1] One can then use LDA to calculate the ground state energy for different occupations of the correlated states, and the difference between the energy for double and single occupation is an estimate for the Hubbard-U. This method has the advantage that effects of screening are already somehow included. On the other hand, there are usually several bands and many interaction matrix elements (on-site, intra-band, inter-band, direct, exchange, inter-site, etc.) that have different magnitudes, and the constrained LDA can only give some average value for these various Coulomb matrix elements and not the individual ab-initio parameters, i.e. the Coulomb matrix elements.

[1] Apart from the constraint that the (effective) one-particle wave functions are normalized.

We pursue a different approach [28], namely, the direct ab-initio calculation of single-particle (hopping, tight-binding) and two-particle (Coulomb) interaction matrix elements for first-principles Wannier functions [29, 30]. These (orthogonal) Wannier functions serve as a minimal (localized) basis for a many-body multi-band Hamiltonian. By minimal we mean that the basis contains only the $4s$, $4p$ and $3d$ orbitals (customized to the problem at hand). We then treat the many-body Hamiltonian in the Hartree-Fock approximation. This is the main idea, which we will now describe in more detail.

The (one-particle) Hamiltonian from which we construct the Wannier functions can be regarded as an auxiliary Hamiltonian, since its purpose is merely to construct an orthogonal basis for the description of the physical Hamiltonian in second quantization. In order to construct these Wannier functions, we start from a standard electronic band structure calculation, namely we use the linearized muffin-tin orbital (LMTO) method [31, 32] within the atomic sphere approximation (ASA). Apart from the eigenvalues, i.e. the one-particle energy bands, the band structure calculation yields the energy eigenstates, i.e. the Bloch functions, for this auxiliary Hamiltonian. When chosen properly, these $4s$, $4p$ and $3d$ Bloch states form an adequate basis of the one-particle Hilbert space. The Wannier functions are closely related to the Bloch functions via a unitary transformation, and, thus, span the same one-particle space as the Bloch functions. However, Wannier functions are not unique, since the phases of the Bloch functions are undetermined.

The non-uniqueness (gauge freedom) of Wannier functions can be used to construct "maximally localized Wannier functions" which are just Wannier functions with a special gauge that makes them optimally localized according to some criterion. To determine this special gauge, we use a method proposed by Marzari and Vanderbilt [33]. A proper localization of the Wannier functions is important, because only then do the standard assumptions of the model treatments hold.

Next, in order to describe the physical Hamiltonian in second quantization, we have developed methods to evaluate the required hopping and Coulomb matrix elements. The evaluation of hopping matrix elements is not very complicated, and takes advantage of two features of our Wannier functions, i.e. the spherical expansion within each muffin-tin and the (with respect to energy) linearized nature of the wave functions. These are features of the LMTO-ASA Bloch functions which are passed on to the Wannier functions. Once the hopping matrix is determined, we can (as a check) re-evaluate the band structure and compare it with the original energy bands, i.e. the LMTO energy eigenvalues.

We propose two different methods to calculate Coulomb matrix elements from Wannier functions. The first method, which we call "spherical expansion method", uses the LMTO-ASA properties of the wave functions and can be used to evaluate the Coulomb integrals efficiently, similarly to what was done in Ref. [34]. The second method, which we call "FFT method", uses the fast Fourier transformation (FFT). It does not rely on the property of the wave functions being linear and is therefore more general. Both methods are completely independent of each other. Thus, having achieved good agreement of their results, we have reliable Coulomb matrix elements which are (for Wannier states with mainly $3d$-character) on the magnitude of 20 to 25 eV for direct on-site Coulomb matrix elements for Fe, Co, Ni and Cu. Nearest-neighbor off-site matrix elements are found to be about 6 eV and on-site exchange matrix elements are about 1 eV. These Hubbard-U's are extremely large compared

to the U's commonly used in model Hamiltonians, and we will discuss reasons for this discrepancy.

Having determined the first-principles matrix elements, we turn to the treatment of the many-body Hamiltonian in the Hartree-Fock approximation. First, however, it is instructive to consider the Hartree approximation which can also easily be performed within DFT (omitting the exchange-correlation). To do this, we need to evaluate the hopping matrix elements of the (one-particle) Hamiltonian which contains no Coulomb repulsion among the valence electrons, since we want to treat these interactions on the second quantized level. It turns out that the choice of our auxiliary Hamiltonian, which determines the minimal basis set consisting of maximally localized Wannier functions, is crucial. The result of the actual Hartree-Fock calculation is an effective hopping matrix from which the band structure can be determined.

To illustrate the methods and steps involved, we perform actual calculations for a well understood system, copper, although this material is not a strongly correlated system, it has almost completely filled (narrow) $3d$-bands. We give results for the ferromagnetic $3d$ transition metals iron, cobalt and nickel (as well as for copper), since these are relatively simple systems with only one atom per unit cell.

We close this work with a discussion of our results, in particular, we will discuss the large magnitude of our Hubbard-U's. Also, we discuss how to extend and further apply the current approach.

Chapter 2

Density Functional Theory

Since the mid 1970's, the density functional theory (DFT) has become a very powerful tool for ab-initio calculations in chemistry and solid state physics. Today, the DFT is a standard method in many fields, and Walter Kohn received the Nobel prize for chemistry in 1998 for his work in this area. Within the framework of DFT, the so-called local density approximation (LDA) is very commonly used. However, despite its success, the LDA is based on assumptions that are not easy to justify, and it is well known that in some cases the LDA gives wrong results. We will first take a look at the DFT in general before turning to the LDA.

A system of many interacting (non-relativistic) fermions is described by the Hamiltonian[1]

$$H = T + V + W = \sum_{i=1}^{N_e} \frac{\mathbf{p}_i^2}{2m} + \sum_{i=1}^{N_e} v_{\text{ext}}(\mathbf{r}_i) + \sum_{i>j} \frac{e^2}{|\mathbf{r}_i - \mathbf{r}_j|} \quad , \tag{2.1}$$

where N_e is the number of electrons and v_{ext} is an external potential caused by the nuclei in the molecule or solid. We are interested in the ground state of (2.1). Instead of determining the complicated many-particle ground state Ψ, we consider the electronic density of the ground state:

$$n(\mathbf{r}) = \int d^3\mathbf{r}_1 \ldots \int d^3\mathbf{r}_{N_e} \Psi^*(\mathbf{r}_1, \ldots, \mathbf{r}_{N_e}) \sum_{i=1}^{N_e} \delta(\mathbf{r} - \mathbf{r}_i) \Psi(\mathbf{r}_1, \ldots, \mathbf{r}_{N_e}) \tag{2.2}$$

Equations (2.1) and (2.2) define the following maps:[2]

$$C: \quad v_{\text{ext}} \to \Psi \qquad\qquad D: \quad \Psi \to n \tag{2.3}$$

The first map C is surjective by construction: Ψ contains no element which is not associated with some element of v_{ext}. The second map D of the ground state wave functions on the ground state density n is trivially surjective. Hohenberg and Kohn have shown that the

[1] The non-interacting part of the Hamiltonian is $H_0 = T + V$ and the interacting part is H_W or just W. We prefer to use the letter W (*German:* Wechselwirkung) instead of I (interaction).

[2] For the sake of simplicity, we restrict ourselves to the case of non-degenerate ground states.

maps C and D are also injective (one to one) and thus fully invertible.[3]. This means that the external potential v_{ext} and the ground state Ψ are uniquely determined by the ground state density n. Hence the energy functional

$$E[n] = \langle \Psi | H | \Psi \rangle = F[n] + \int d^3\mathbf{r}\, v_{\text{ext}}(\mathbf{r}) n(\mathbf{r}) \ , \quad F[n] = \langle \Psi | T + W | \Psi \rangle \tag{2.4}$$

is a unique functional of the density n. Furthermore, F is universal in the sense that it does not depend on the external potential. It may be separated:

$$F[n] = \frac{1}{2} \int d^3\mathbf{r} \int d^3\mathbf{r}' \, \frac{e^2 n(\mathbf{r}) n(\mathbf{r}')}{|\mathbf{r} - \mathbf{r}'|} + G[n] \tag{2.5}$$

Hohenberg and Kohn have shown that $E[n]$ assumes its minimal value, the ground state energy, for the correct ground state density. If the functional $G[n]$ were known, it would be relatively simple to use the variational principle to determine the ground state energy and density for any given external potential. Unfortunately, the functional $G[n]$ (and thus $E[n]$) is not known, and the full complexity of the many-electron problem is associated with its determination.

2.1 Local Density Approximation

The theorems in the preceeding section apply equally to the case of non-interacting electrons. Consider an auxiliary system with no Coulomb interaction described by the Hamiltonian:

$$H_S = T + V_S \tag{2.6}$$

The ground state Ψ_S of this single-particle problem is simply a Slater determinant obtained by populating the lowest one-electron orbitals ψ_i defined by the Schrödinger equation:

$$\left(-\nabla^2 + v_S(\mathbf{r})\right) \psi_i(\mathbf{r}) = \varepsilon_i \psi_i(\mathbf{r}) \tag{2.7}$$

Here and throughout, we use atomic Rydberg units, see Appendix A, in which $\hbar/2m = 1$. According to the theorem of Hohenberg and Kohn, there exists a unique energy functional

$$E_S[n] = T_S[n] + \int d^3\mathbf{r}\, v_S(\mathbf{r}) n(\mathbf{r}) \ , \tag{2.8}$$

for which $\delta E_S[n] = 0$ yields the exact ground state density of H_S. The central assumption in establishing the Kohn-Sham equations is that for every interacting system there exists a local single-particle potential $v_S(\mathbf{r})$ such that the exact ground state density n of the interacting system equals the ground state density of the auxiliary problem:

$$n(\mathbf{r}) = n_S(\mathbf{r}) = \sum_{i=1}^{N_e} |\psi_i(\mathbf{r})|^2 \tag{2.9}$$

[3]This is known as the theorem of Hohenberg and Kohn. For a proof see for example Ref. [35]

We are looking for the potential for which (2.9) is the density of the interacting system. To this end, we write:

$$G[n] = T_S[n] + E_{\rm xc}[n] \ , \tag{2.10}$$

where $T_S[n]$ is the kinetic energy functional of the non-interacting electrons:

$$T_S[n] \equiv \langle \Psi_S | T | \Psi_S \rangle = \sum_{i=1}^{N_e} \int d^3\mathbf{r} \psi_i^*(\mathbf{r}) \left(-\nabla^2\right) \psi_i(\mathbf{r}) \tag{2.11}$$

We have isolated two terms in $F[n]$, the Hartree term in (2.5) and the kinetic energy (2.11), which play a decisive role in the single-particle picture, and which are presumably also the dominant terms in the interacting system. What remains is $E_{\rm xc}[n]$, which describes the difference between the true kinetic energy and that of the non-interacting system, plus the difference between the true interaction energy and that of the Hartree contribution. Since these corrections are due to exchange and correlation, it is called the exchange-correlation (XC) energy functional.

Now, we introduce the local density approximation (LDA) itself, which assumes corrections due to exchange and correlation to be *local*:

$$E_{\rm xc}[n] = \int d^3\mathbf{r} \ n(\mathbf{r}) \varepsilon_{\rm xc}(n(\mathbf{r})) \tag{2.12}$$

This approximation is exact in the limit of slowly varying densities, and $\varepsilon_{\rm xc}(n)$ is obtained from a homogeneous electron gas with density n. Various estimates for $\varepsilon_{\rm xc}(n)$ have been proposed. In this work, we will use the estimate by Barth and Hedin [36], see Eq. (C.19) in the appendix C.3.

Using the LDA and collecting the above assumptions, our energy functional can be written as:

$$E[n] = \langle \Psi_S | T | \Psi_S \rangle + \int d^3\mathbf{r} \left[\frac{1}{2} \int d^3\mathbf{r}' \ \frac{e^2 n(\mathbf{r}')}{|\mathbf{r} - \mathbf{r}'|} + v_{\rm ext}(\mathbf{r}) + \varepsilon_{\rm xc}(n(\mathbf{r})) \right] n(\mathbf{r}) \tag{2.13}$$

A minimization with respect to the density n (under the constraint that the one-particle wave functions are normalized) leads to the well-known Kohn-Sham equations:

$$\left(-\nabla^2 + \int d^3\mathbf{r}' \ \frac{e^2 n(\mathbf{r}')}{|\mathbf{r} - \mathbf{r}'|} + v_{\rm ext}(\mathbf{r}) + v_{\rm xc}(n(\mathbf{r})) \right) \psi_i(\mathbf{r}) = \varepsilon_i \psi_i(\mathbf{r}) \tag{2.14}$$

By comparison with (2.7), we see that the non-interacting electron moves in the effective potential:

$$v_S(\mathbf{r}) = \int d^3\mathbf{r}' \ \frac{e^2 n(\mathbf{r}')}{|\mathbf{r} - \mathbf{r}'|} + v_{\rm ext}(\mathbf{r}) + v_{\rm xc}(n(\mathbf{r})) \tag{2.15}$$

The first term is the “Hartree term”, caused by the classical electron-electron repulsion, the second term is the external potential which is caused by the nuclei (plus external fields). The third term is called “exchange-correlation potential”, this term is given by

$$v_{\rm xc}(n(\mathbf{r})) = \frac{\delta E_{\rm xc}[n]}{\delta n(\mathbf{r})} \ . \tag{2.16}$$

2.2 Self Consistency

The Kohn-Sham equations (2.14) have to be solved self-consistently, since they depend on the density $n(\mathbf{r})$ which itself depends on the effective one-electron wave functions $\psi_i(\mathbf{r})$ via equation (2.9). The self-consistency cycle is straightforward and fairly simple, we review its steps merely for later reference.

1. Initial guess for the density $n(\mathbf{r})$.
2. Calculate the effective potential $v_S(\mathbf{r})$ using (2.15).
3. Solve the effective Schrödinger equation (2.7).
4. Recalculate a density $\widetilde{n}(\mathbf{r})$ using (2.9).
5. Compare $\widetilde{n}(\mathbf{r})$ with $n(\mathbf{r})$. If a criterion for convergence is satisfied, then exit the cycle.
6. Set $n(\mathbf{r})$ to $\alpha\widetilde{n}(\mathbf{r}) + (1-\alpha)n(\mathbf{r})$ and go back to step 2.

A few remarks should be made about some of these steps:

i.) The initial density in step 1 can be obtained from solving a one-electron Schrödinger equation for the external potential.

ii.) For the crystal, step 3 requires the solution of the band problem (see chapter 3).

iii.) The number of electrons in our system enters (2.9) in step 4, because only the lowest one-particle states are populated.

iv.) Since exact self consistency will never be achieved numerically, we have to exit the cycle when reasonable convergence is achieved. We found that a good criterion for convergence is $\int d^3\mathbf{r}\, |n(\mathbf{r}) - \widetilde{n}(\mathbf{r})| \; < \; \varepsilon$ where ε is a small parameter.

v.) Step 6 is known as the Broyden mixing scheme.

vi.) Whenever a (pure) Hartree calculation is done, we perform exactly these steps just leaving out the exchange-correlation term in the relevant equations.

vii.) The cycle is easily extended to the spin polarized case, see section 2.5.

2.3 Total Energy

The LDA total energy functional is given by (2.13) and it assumes its minimal value for the self-consistent density achieved by going through the self-consistency cycle:

$$E[n] = \langle\Psi|T|\Psi\rangle + \int d^3\mathbf{r} \left[\frac{1}{2}\int d^3\mathbf{r}' \, \frac{e^2 n(\mathbf{r}')}{|\mathbf{r}-\mathbf{r}'|} + v_{\text{ext}}(\mathbf{r}) + \varepsilon_{\text{xc}}(n(\mathbf{r}))\right] n(\mathbf{r}) \quad (2.17)$$

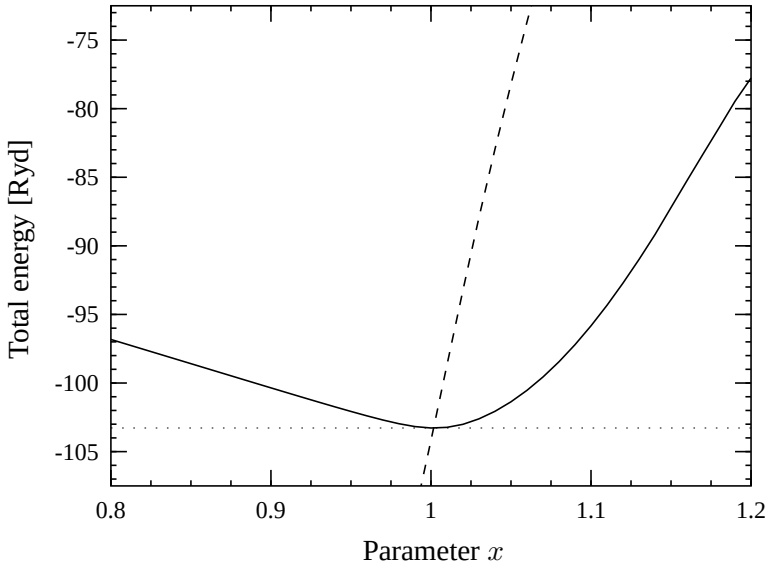

Figure 2.1: Total energy of the valence electrons per atom for FCC copper (solid line) calculated as a function of x. The dashed line shows the badly calculated total energy. Here, v_0 is taken to be the potential for no interaction among the valence electrons (3.48).

Where the kinetic energy (2.11) term can be written (from (2.7) and (2.9)) as:

$$\langle \Psi | T | \Psi \rangle = \sum_{i=1}^{N_e} \varepsilon_i - \int d^3\mathbf{r}\; v_S(\mathbf{r}) n(\mathbf{r}) \tag{2.18}$$

The total energy should be calculated using these two equations, i.e. as the sum of one-particle energies for the non-interacting system: The sum of the kinetic energies plus the sum of the potential energies corrected for double counting. One should not try to use (2.15) to combine terms in (2.18) with terms in (2.17). The reason for this is a little subtile and therefore we now wish to illustrate the situation in the following example.

2.3.1 Illustration

Let us suppose we have found the exact self-consistent density and thus the self-consistent effective LDA potential (2.15) which we call v_{LDA}. Further, we have a potential $v_0 \neq v_{\mathrm{LDA}}$ which is not a solution of the Kohn-Sham equations. Using these two potentials, we introduce a potential which depends on a variable x

$$v(x) = (1-x)\, v_0 + x\, v_{\mathrm{LDA}} \quad , \tag{2.19}$$

so that $v(1) = v_{\mathrm{LDA}}$. First, we note that the evaluation of the total energy from $v(x)$ requires the *re*-evaluation of the Hartree term and the exchange-correlation energy in (2.17). Using $v(x)$ potential in (2.7), we obtain the one-particle energies ε_i and one-particle wave

functions ψ_i; from (2.9) the density n; and from n, we evaluate the Hartree potential and exchange-correlation energy. We now have all the pieces to evaluate the total energy E as a function of x, and since v_0 is not a solution of the Kohn-Sham equations, $E(x)$ assumes its minimal value at $x = 1$. Calculating the total energy correctly leads to the solid curve in Fig. 2.1.

On the other hand, when we use (2.15) to combine terms in (2.18) with terms in (2.17), we use (for instance) the re-evaluated Hartree term to evaluate the kinetic energy term. But this is not consistent with the one-particle energies ε_i obtained from $v(x)$, since for $x \neq 1$ the potential $v(x)$ is no longer a solution of the Kohn-Sham equations, these re-evaluated potentials are different from the ones included in (2.18). It is thus important to evaluate the kinetic energy using the energy eigenvalues belonging to $[+\nabla^2 - v(x)]$, and the last term in (2.17) should be evaluated using only the density (2.9).

The badly calculated total energy is also shown (as a function of x) in Fig. 2.1. Obviously, something is wrong since there is no minimal value assumed at $x = 1$. However, at $x = 1$ this badly calculated energy is correct, but, as indicated earlier, exact self consistency is never obtained numerically, thus $x \neq 1$. And since the badly calculated energy curve has such a large slope, even an x very close to 1 will lead to a wrong result. As we shall see, quite often the total energy is needed to high accuracy.

2.3.2 Universal Features of the Binding Energy

The universal features of the binding energy offer a way to compare our ab-initio total energy calculations with experimental data. This is an important task to be done since all theory is based on experiment. Theoretical calculations have to be compared with experimental data for several reasons:

i.) Most importantly, to see whether the basic laws of physics are valid. Here the law of physics is quantum mechanics, a very well understood theory, which is not doubted any more.

ii.) The assumptions made in the DFT can be proven to be reasonable or unreasonable for the systems under consideration.

iii.) Numerical errors and accuracy in the calculations have to be checked.

Since this section is a test for our calculations, and not the main interest of this work, we will keep the theory short. For detailed information concerning the theory and experimental data, the reader is advised to read the excellent paper [3].

Ab-initio calculations for many different materials (including crystalline solids) have shown that the binding energy as a function of the lattice parameter has the same form, once the binding energy and the separation have been scaled:

$$E(S) = \Delta E \; E^*(a^*) \qquad \text{where} \quad a^* = \frac{S - S_E}{\ell} \tag{2.20}$$

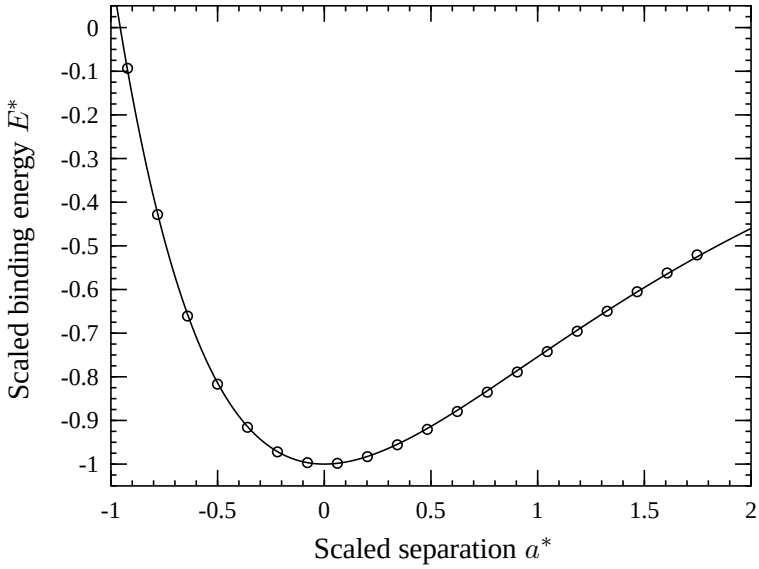

Figure 2.2: Scaled binding energy for FCC copper (circles). The line is the universal function (2.22).

Here, $E(S)$ is the binding energy per atom, S is the Wigner-Seitz radius[4], and ΔE is the equilibrium binding energy. The parameter a^* is a scaled length determined by the equilibrium Wigner-Seitz radius S_E and the length scale ℓ. Because the function $E(S)$ will always have a minimum at S_E, we chose:

$$E^*(0) = -1 \qquad E^{*\prime}(0) = 0 \qquad E^{*\prime\prime}(0) = 1 \tag{2.21}$$

A universal function $E^*(a^*)$ which obeys (2.21) and is in good agreement with the calculated curves is (see Ref. [3]):

$$E^*(a^*) = (-1 - a^* - 0.05a^{*3})e^{-a^*} \tag{2.22}$$

Now, the bulk modulus B, the ratio between the change in pressure P and the resulting relative change in volume Ω, is related to the length scale ℓ by[5]

$$B \equiv -\Omega \left.\frac{\partial P}{\partial \Omega}\right|_{\Omega_E} = \frac{\Delta E}{12\pi S_E \ell^2} \ , \tag{2.23}$$

as can be seen by taking two derivatives of (2.20) and using (2.21).

Our own total energy calculations are scaled onto the curve (2.22) by adjusting the three parameters S_E, ΔE and ℓ. This is done in Fig. 2.2 for FCC copper. As can be seen, our binding curve reveals the universal feature (2.22) perfectly.[6] Here, the three parameters

[4]See appendix A.

[5]Note that: $P(\Omega) = -\partial E/\partial \Omega$

[6]The mismatch can hardly be seen, however, note that this does not at all mean that our adjusted parameters agree with experiment.

Material	Structure	S_E [Å]	ℓ [Å]	ΔE [eV]
Copper	FCC	1.41	0.272	3.50
Cu		1.40	0.258	4.14
Aluminum	FCC	1.58	0.336	3.34
Al		1.53	0.320	3.70
Silver	FCC	1.60	0.269	2.96
Ag		1.61	0.240	2.75
Lithium	BCC	1.72	0.553	1.65
Li		1.66	0.512	1.74
Iron	BCC	1.41	0.274	4.29
Fe		1.37	0.274	7.78
Cobalt	HEX	1.39	0.262	4.39
Co	FCC	1.36	0.262	6.75
Nickel	FCC	1.38	0.270	4.44
Ni		1.37	0.263	5.62

Table 2.1: Calculated and experimental values for the equilibrium Wigner-Seitz radius S_E, the length scale ℓ, and the cohesive energy ΔE. For each material, the first line shows experimental values (Ref. [3]) and the second line shows our own result using the LMTO method for treating the valence electrons up to d-orbitals (see chapter 3). We have treated Cobalt in the FCC crystal structure.

were found to be: $S_E = 2.65a_0$, $\ell = 0.487a_0$ and $\Delta E = 0.304$ Ryd. We are thus in a position to calculate the lattice constant, the cohesive energy and the bulk modulus B from first-principles and compare these results with experimental data. A comparison is shown in Table 2.1 for different metals. Note that ℓ can be evaluated from experimental date using the bulk modulus B and (2.23).

In this connection it should be mentioned that these calculations require a very accurate evaluation of the (relative) total energy since, e.g. for copper, the total energy of the valence electrons (per atom) for equilibrium (LDA) volume is -103.286115 Ryd but for a 1% volume increase the energy is -103.286070 Ryd. This is an extremely small energy difference of just 45$\cdot 10^{-6}$ Ryd, or a relative change of about $4 \cdot 10^{-7}$. Hence, we have to be precise to at least seven or eight digits.

Factors that contribute to the mismatch in Table 2.1 include:

i.) The local density approximation.

ii.) Use of the atomic sphere approximation (ASA), see section 3.2.

iii.) Use of the frozen core approximation, see chapter 3.

iv.) We neglect the so-called Ewald correction [37] to the ASA which arises from Coulomb interactions between the potential from the nuclei contained in the external potential.

v.) For Fe, Co and Ni, we have neglected spin-polarization.

It is remarkable that, despite these factors, the equilibrium volume (or S_E) and the scaled length ℓ, which together provide a measure of the anharmonicity $\eta \equiv S_E/\ell$ of a crystal, are predicted very well. However, the cohesive energy is predicted poorly, since the accuracy required exceeds the absolute accuracy of the total energy LDA calculation, see Fig. 7.23.

2.4 Constrained LDA

The purpose of this section is to estimate the Hubbard U, defined as the Coulomb energy cost to place two (in our case d) electrons at the same site. This is

$$U_{dd} = E(N_d + 1) + E(N_d - 1) - 2E(N_d) \; . \tag{2.24}$$

Here, $E(N_d)$ is the ground state energy with N_d d-electrons. If we consider this energy as a continuous function of N_d, where we constrain the value of N_d to be away from its minimized (ground state) value, then the Hubbard U is given by:

$$U_{dd} = \frac{\delta^2 E(N_d)}{\delta N_d^2} \tag{2.25}$$

In order to evaluate $E(N_d)$, we have applied the "constrained" LDA, proposed in Ref. [22]. In the "un-constrained" LDA described above, we have minimized the energy functional (2.13) under the constraint that the one-particle wavefunctions are normalized. Explicitly:

$$\delta_{\psi_i} \left\{ E[n] - \sum_{j=1}^{N_e} \varepsilon_j \left(\int d^3r |\psi_j(\mathbf{r})|^2 - 1 \right) \right\} = 0 \tag{2.26}$$

The result of this minimization are the Kohn-Sham equations (2.14). Constrained LDA is a generalization of LDA where an *additional* constraint is taken into account by an additional Lagrange parameter in (2.26). We are interested in a variation of the d-charge in transition metals. Hence, the additional constraint is given by:

$$v_d \left(\int d^3r n_d(\mathbf{r}) - N_d \right) \tag{2.27}$$

Here, $n_d(\mathbf{r})$ is the d-charge density which should be constrained to a total d-charge of N_d electrons per unit cell. Inserting (2.27) into (2.26) and minimizing with respect to the density n, we obtain Kohn-Sham equations with a modified potential:

$$v_S(\mathbf{r}) = \int d^3\mathbf{r}' \frac{e^2 n(\mathbf{r}')}{|\mathbf{r} - \mathbf{r}'|} + v_{\text{ext}}(\mathbf{r}) + v_{\text{xc}}(n(\mathbf{r})) + \begin{cases} v_d & \ell = 2 \\ 0 & \text{otherwise} \end{cases} \tag{2.28}$$

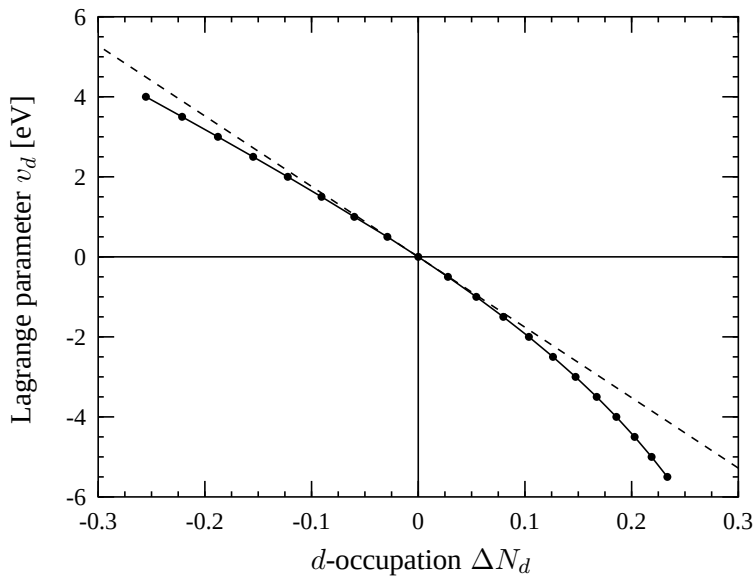

Figure 2.3: Lagrange parameter v_d vs. relative d-occupation ΔN_d for copper (solid line) and $v_d = -\eta N_d$, where $\eta = 17.6$ eV (dashed line).

The extra constant potential v_d only acts on the d-component of the wave functions and accordingly controls the number of d-electrons. Within the LMTO method, this is accomplished by adding a constant potential, v_d, when solving the radial Schrödinger equation for $\ell = 2$. Physically, we can regard the potential v_d as the "force" necessary to constrain the system to the desired configuration. Instead of evaluating $E(N_d)$ directly, we may as well evaluate the energy difference to ground state energy $E^0 = E(N_d^0)$, by making use of the Hellmann-Feynman (see Eq. (2) Ref. [22]) theorem:

$$\frac{dE(N_d)}{dN_d} = -v_d(N_d) \quad \text{or} \quad \Delta E(N_d) \equiv E(N_d) - E^0 = -\int_{N_d^0}^{N_d} dN_d' v_d(N_d') \tag{2.29}$$

Here, N_d^0 is the number of d-electrons for the ground state. Hence the knowledge of $v_d(N_d')$ is sufficient to evaluate $E(N_d)$ and thus our estimate for the Hubbard-U (2.25). From (2.29), we see that for the ground state the force $v_d(N_d^0)$ vanishes, since $E(N_d)$ assumes a minimum for the ground state. Moreover, for small charge deviations around N_d^0, the force $v_d(N_d)$ will be proportional to the deviation ΔN_d:

$$v_d(N_d) = -\eta \Delta N_d \qquad \text{where} \qquad \Delta N_d = N_d - N_d^0 \tag{2.30}$$

The negative sign was only introduced for convenience, since inserting (2.30) into (2.29) yields:

$$\Delta E(N_d) = \tfrac{1}{2}\eta \Delta N_d^2 \qquad \text{and from (2.25) we have:} \qquad U_{dd} = \eta \tag{2.31}$$

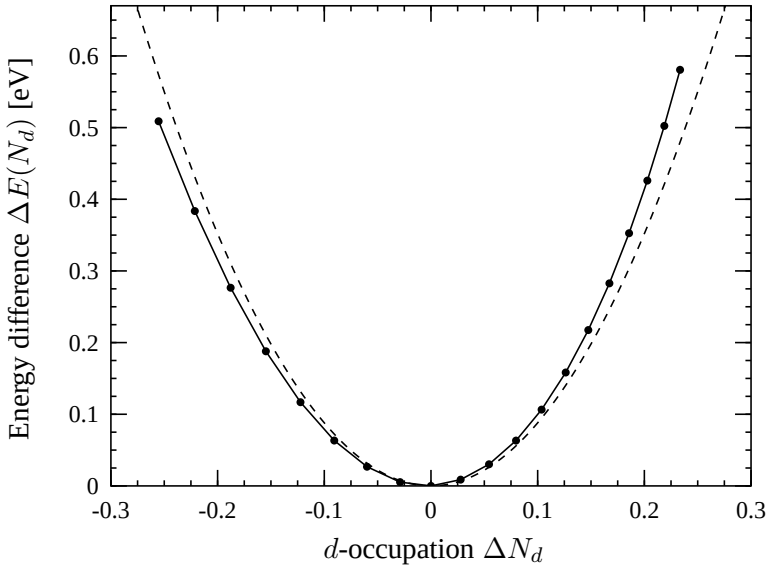

Figure 2.4: The energy difference $\Delta E(N_d)$: From Eq. (2.32) (solid line) and $\Delta E = \frac{1}{2}\eta\Delta N_d^2$, where $\eta = 17.6$ eV (dashed line).

2.4.1 Results for some Solids

In our calculations, we have only used a one-atom unit cell. If a larger unit cell is chosen, one could do a variety of additional constraints (e.g. changing the d-occupation separately on two different atoms). Such calculations could attempt to sort out more details of effective Hamiltonians. However, such calculations would take our work in a different direction from what we are interested in. Also, given the intuitive nature of the constrained method and the difficulties in fitting such a large parameter space, it is not clear how useful the resulting parameters would be or their uniqueness.

Further, the LMTO method was used up to f-orbitals (see chapter 3). However, using only d-orbitals yields almost the same results (within 1%) since the additional freedom for electrons to occupy f-states is hardly used because only a few f-like states, for the materials under consideration, are below the Fermi level. Nevertheless, there lies no harm in including them.

The method is illustrated for copper in Fig. 2.3. For the ground state, we obtain $N_d^0 = 9.50$ (per atom) and as expected (2.30), i.e. the linear dependence is only valid in a narrow range around N_d^0. Therefore, we perform calculations at $v_d = 0$ eV and $v_d \pm 0.05$ eV and fit the linear coefficient $-\eta$ in (2.30) using linear regression[7]. We find $\eta = 17.6$ eV, as indicated by the dashed line. Results for several other metals are shown in Table 2.2.

We may also take a look at the total LDA energy

$$E(N_d) = \min\left[E[n] + v_d\left(\int d^3r n_d(\mathbf{r}) - N_d\right)\right] \quad , \tag{2.32}$$

[7]Looking only at such a narrow range, where the dependence is almost linear, it is not surprising that we find linear correlation coefficients $r < -0.999$.

Material	Structure	S [a_0]	U_{dd} [eV]	N_d^0
Iron	BCC	2.662	11.7	6.53
Cobalt	FCC	2.621	12.2	7.53
Nickel	FCC	2.602	12.5	8.55
Copper	FCC	2.669	17.6	9.50
Silver	FCC	3.005	18.8	9.57

Table 2.2: Hubbard-U estimates from constrained LDA. The Wigner-Seitz radius S is the experimental value [31] for which the calculation was performed.

instead of just looking at the energy difference. Fig. 2.4 shows this energy dependence as well as the quadratic dependence (2.31) using $\eta = 17.6$ eV (dashed line). It should be stressed that the energies in Fig. 2.4 are relative energies, and $E^0 \approx -1.4$ keV. Hence, high precision of the total energy is needed which is avoided when making use of the Hellmann-Feynman theorem. Therefore, we have not used (2.32), i.e. fit the curve to a parabola, to compile the Table 2.2 [but used (2.30)].

2.4.2 Different Approach for Atomic Lithium

From a quite simple straightforward calculation, we find one-particle energies and Coulomb interaction energies for atomic Li. Our interaction energies differ from those one finds from the constrained LDA method. Because this method becomes more complicated for solids, we restrict ourselves to the very simple case of atomic Li with only three electrons. The idea is the following. The three electrons can occupy the four lowest one-particle states, i.e. $1s^{\uparrow}$, $1s^{\downarrow}$, $2s^{\uparrow}$ and $2s^{\downarrow}$. For simplicity, we always consider as many electrons in the spin-up as in the spin-down states. We will call the total number of electrons in the $1s$ states n_0 and call this state 0; and call the total number of electrons in the $2s$ states n_1 and call this state 1. Then the total (electronic) energy of the atom can be expressed as:

$$E_{\text{tot}} = n_0\varepsilon_0 + n_1\varepsilon_1 + \frac{n_0^2}{4}U_{00} + \frac{n_1^2}{4}U_{11} + n_0 n_1 U_{01} \tag{2.33}$$

Here, ε_i is the one-particle energy of state i and U_{ij} is the Coulomb energy added to the system for n_i electrons in states i and n_j electrons in states j. The factor $1/4$ in front of U_{ii} arises because the state $\uparrow$ and $\downarrow$-state are filled with $n_i/2$ electrons. The main idea is to fix n_0 and set $n_1 = 3 - n_0$, and calculate the total energy with LDA for various n_0. In this way, we obtain a set of equations that allows us to determine the U_{ij}'s. We may use Janak's formula $\partial E/\partial n_i = \varepsilon_i^{\text{LDA}}$ [38], which is valid in density functional theory, to express our one-particle energies in terms of LDA one-particle energies (which are known). This reduces the number of unknown quantities from five to three. From Janak's formula and (2.33), we have:

$$\varepsilon_i^{\text{LDA}} = \varepsilon_i + \frac{n_i}{2}U_{ii} + n_{1-i}U_{01} \tag{2.34}$$

Inserting (2.34) into (2.33) yields:

$$E_{\rm tot} - n_0\varepsilon_0^{\rm LDA} - n_1\varepsilon_1^{\rm LDA} = -\frac{n_0^2}{4}U_{00} - \frac{n_1^2}{4}U_{11} - n_0 n_1 U_{01} \tag{2.35}$$

The LHS of this equation is completely determined from the output of an LDA calculation. Hence, if we perform three LDA calculations with different n_0 (and $n_1 = 3 - n_0$), the equations (2.35) form a linear set of equations for U_{00}, U_{11} and U_{01}. We find

$$U_{00} = 68.6 \text{ eV} \ , \quad U_{11} = 17.5 \text{ eV} \ , \quad U_{01} = 10.8 \text{ eV} \ , \tag{2.36}$$

and for the one-particle energies we have

$$\varepsilon_0 = -130.9 \text{ eV} \ , \quad \varepsilon_1 = -33.8 \text{ eV} \ . \tag{2.37}$$

These energies may be compared with corresponding values of Coulomb matrix elements obtained from hydrogen-atom-like wave functions for $Z = 3$, see (C.13) in the appendix C.2). We should mention that one may replace the $n^2/4$ terms in Eq. (2.33) by $n(n-1)/2$ (which may seem reasonable too). Also, one can use fixed values for ε_0 and ε_1 in (2.33) which can be obtained from the hydrogen-atom-like energy eigenfunction (for $Z = 3$), i.e. (C.14). For all these different treatments, the estimates of the U's are of the same order of magnitude.

On the other hand, we can do a constrained LDA calculation. Here, U is defined as the Coulomb energy cost to place two, for instance two $2s$-electrons, at the same site. This is

$$U^{\rm CLDA} = E(n_1+1) + E(n_1-1) - 2E(n_1) \ . \tag{2.38}$$

$E(n_1)$ is the ground-state energy with n_1 $2s$-electrons. If we consider this energy as a continuous function of n_1, where we constrain the value of n_1 to be away from its minimized value, then U_{11} is given by

$$U^{\rm CLDA} = \frac{\delta^2 E(n_1)}{\delta n_1^2} = \frac{1}{2}U_{00} + \frac{1}{2}U_{11} - 2U_{01} = 21.45 \text{ eV} \ . \tag{2.39}$$

Where we used $n_0 = 3 - n_1$ and (2.33). Obviously, $U^{\rm CLDA} \neq U_{11}$ and moreover from constrained LDA, we would find exactly the same estimate for U_{00}. This example casts serious doubts upon the constrained LDA method. Nevertheless, the constrained LDA is intuitive and contains some type of screening within a one-electron LDA approach since for each LDA calculation (with fixed v_d), the electrons are free to rearrange themselves. It is not clear which actual approximations this involves, however. Furthermore, there are several d-bands in transition metals and many interaction matrix elements (on-site, density-density, intra-band, inter-band, exchange, inter-site, etc.) that have different magnitudes, and the constrained LDA can only give some average value for these various Coulomb matrix elements and not the individual ab-initio Coulomb matrix elements. For these reasons, we will not pursue the constrained LDA any further.

2.5 Spin-polarized Scheme

The DFT can be extended to a spin density formalism. We shall take a look at the spin-polarized LDA which is known as the local spin density approximation (LSDA). Now, the spin-up density $n^{\uparrow}(\mathbf{r})$ and the spin-down density $n^{\downarrow}(\mathbf{r})$ become the independent variables. In terms of these basic variables, the electron density $n(\mathbf{r})$ and the magnetization density $m(\mathbf{r})$ are:

$$n(\mathbf{r}) = n^{\uparrow}(\mathbf{r}) + n^{\downarrow}(\mathbf{r}) \quad \text{and} \quad m(\mathbf{r}) = n^{\uparrow}(\mathbf{r}) - n^{\downarrow}(\mathbf{r}) \tag{2.40}$$

Hence, allowing spin polarization, we minimize (2.13) which we rewrite as:

$$\begin{aligned} E[n^{\uparrow}, n^{\downarrow}] &= \langle \Psi_S^{\uparrow} | T | \Psi_S^{\uparrow} \rangle + \langle \Psi_S^{\downarrow} | T | \Psi_S^{\downarrow} \rangle + \\ &+ \int d^3\mathbf{r} \left[\frac{1}{2} \int d^3\mathbf{r}' \, \frac{e^2 n(\mathbf{r}')}{|\mathbf{r} - \mathbf{r}'|} + v_{\text{ext}}(\mathbf{r}) + \varepsilon_{\text{xc}}(n^{\uparrow}(\mathbf{r}), n^{\downarrow}(\mathbf{r})) \right] n(\mathbf{r}) \end{aligned} \tag{2.41}$$

In analogy to the Kohn-Sham equations (2.14), we now find that for each spin direction the electrons move in an effective one-particle potential

$$v_S^{\sigma}(\mathbf{r}) = \int d^3\mathbf{r}' \frac{e^2 n(\mathbf{r}')}{|\mathbf{r} - \mathbf{r}'|} + v_{\text{ext}}^{\sigma}(\mathbf{r}) + v_{\text{xc}}^{\sigma}(n^{\uparrow}(\mathbf{r}), n^{\downarrow}(\mathbf{r})) \quad , \tag{2.42}$$

where estimates for

$$v_{\text{xc}}^{\sigma}(n^{\uparrow}(\mathbf{r}), n^{\downarrow}(\mathbf{r})) = \frac{\delta E_{\text{xc}}[n^{\uparrow}, n^{\downarrow}]}{\delta n^{\sigma}(\mathbf{r})} \tag{2.43}$$

and $\varepsilon_{\text{xc}}(n^{\uparrow}(\mathbf{r}), n^{\downarrow}(\mathbf{r}))$ are again given by Barth and Hedin [36], see Eqs. (C.17) and (C.18). For each spin direction, we have to solve an effective Schrödinger equation:

$$\left(-\nabla^2 + v_S^{\sigma}(\mathbf{r})\right) \psi_i^{\sigma}(\mathbf{r}) = \varepsilon_i^{\sigma} \psi_i^{\sigma}(\mathbf{r}) \tag{2.44}$$

Note carefully that v_{xc}^{σ}, i.e. $v_{\text{xc}}^{\uparrow}$ *and* $v_{\text{xc}}^{\downarrow}$, are different functions (unless the spin-up and spin-down densities are equal). We only consider the absence of an external magnetic field, where v_{ext}^{σ} is spin-independent, thus v_{xc}^{σ} is the only spin-dependent term in (2.42). Hence, in the pure Hartree case (where $v_{\text{xc}}^{\sigma} = 0$), we have $v_S^{\uparrow}(\mathbf{r}) = v_S^{\downarrow}(\mathbf{r})$, and the spin-up and spin-down electrons move in the same effective potential.

For the spin-polarized case, the self-consistency cycle in section 2.2 basically remains the same. Apart, from obviously having to use two spin densities $n^{\uparrow}$ and $n^{\downarrow}$, changes include:

i.) Use of (2.42) in step 2.

ii.) Performing two energy band calculations in step 3.

iii.) Recalculation of the spin-up and spin-down densities in step 4.[8]

iv.) At some point, we have to break the spin symmetry since obviously for $n^{\uparrow} = n^{\downarrow}$ from (2.43), we have $v_{\text{xc}}^{\uparrow}(\mathbf{r}) = v_{\text{xc}}^{\downarrow}(\mathbf{r})$.

[8] This involves the determination of the Fermi level using (3.40).

The spin magnetic moment per atom may be defined as the total magnetization M (i.e. the integral of magnetization density $m(\mathbf{r})$ over the unit cell) times the Bohr magneton μ_B. It turns out that M is the difference in the spin-up and spin-down number of states at the Fermi level[9]

$$M \equiv \int d^3r\, m(\mathbf{r}) = n^{\uparrow}(E_F) - n^{\downarrow}(E_F) \ . \tag{2.45}$$

We can use either of these expressions (in Eq. (2.45)) to evaluate the magnetic moment but prefer to use the latter. Since v_{xc}^{σ} (as noted above) is the only spin-dependent term in (2.42), the magnetic moment is completely determined by the exchange-correlation functional. No additional adjustable parameters have to be introduced to fit the magnetic moment to experiment.

[9] This follows from (3.38) and (3.31), see section 3.4.2.

Chapter 3

Electronic Structure Calculation

At several points in the preceeding chapter, it was mentioned that an effective Schrödinger equation has to be solved. Since we are mainly concerned with metals, which have a periodic crystal structure, this means that the so-called band problem has to be solved. This is not an easy task. Many different methods have evolved over time. One of these methods is the LMTO[1] method [31, 32, 39] which we use within the atomic sphere approximation (ASA). We are aware of the fact that this method is not as precise as state-of-the-art methods, but believe that it serves our purposes very well. State-of-the-art methods include the FP-LMTO[2] [40] and FP-LAPW[3] [41] method. These methods have proven to be very successful for calculating solids at extreme conditions, e.g. high compression, and materials with highly complex (open) structures. In comparison to the LMTO-ASA method, the full potential approach has a few (serious) drawbacks:

- State-of-the-art full potential methods, e.g. the "WIEN code" [42], come in big software packages and are more difficult to handle than the rather small LMTO-ASA code.
- Loss of conceptual simplicity: The wave functions take a quite simple expansion in the LMTO-ASA method. The ℓ-decomposition is only done inside the muffin-tin (MT) in FP methods.
- Computationally expensive and thus considerable more time consuming.

For these reasons, we have decided to use the LMTO-ASA method. After a review of the band problem itself, we will introduce the atomic sphere approximation. Hereafter, we describe the LMTO method as far as needed for our purposes, mainly the evaluation of Bloch eigenenergies and Bloch eigenfunctions. We then turn to Brillouin zone integration, using the tetrahedron method [43] which is useful for evaluating various physical quantities. In the last section we apply the calculations to copper for several reasons: (i) Copper will be a test case throughout this work. (ii) To illustrate the calculations. (iii) For later reference.

[1] Linearized muffin-tin orbitals
[2] Full potential linearized muffin-tin orbitals
[3] Full potential linearized augmented plane waves

We should note that we use the "frozen core approximation" where the total charge density is decomposed into the spin independent core charge density $n_c(\mathbf{r})$ and the spin dependent valence charge densities $n_v^{\uparrow}(\mathbf{r})$ and $n_v^{\downarrow}(\mathbf{r})$. The core charge density $n_c(\mathbf{r})$ is assumed constant, i.e. it is obtained from an atomic calculation and remains "frozen" during iteration towards self-consistency.

3.1 Band Problem

Merely for later reference, we review the band problem. For more details see for instance Refs. [30, 31, 44, 45, 46].

Since the external potential is given by the nuclei, which are arranged in a periodic structure, our effective potential v_S, which enters the Schrödinger equation, is periodic too. This symmetry can be expressed using the translation operator $T_{\mathbf{R}}$, i.e.:

$$T_{\mathbf{R}} v_S(\mathbf{r}) \equiv v_S(\mathbf{r}+\mathbf{R}) = v_S(\mathbf{r}) \qquad \mathbf{R} = n_1\mathbf{a}_1 + n_2\mathbf{a}_2 + n_3\mathbf{a}_3 \tag{3.1}$$

Where n_i are integers and the set of translation vectors $\mathbf{a}_i$ are given for the FCC structure by (A.2) and for BCC by (A.5). Hence, $T_{\mathbf{R}}$ commutes with the Hamiltonian:

$$[H, T_{\mathbf{R}}] = 0 \qquad H = -\nabla^2 + v_S(\mathbf{r}) \tag{3.2}$$

Thus, there exists a basis of the one-particle Hilbert space of states that are eigenstates of H and *simultaneously* eigenstates of $T_{\mathbf{R}}$:

$$H|\psi_{n\mathbf{k}}\rangle = E_n(\mathbf{k})|\psi_{n\mathbf{k}}\rangle \qquad T_{\mathbf{R}}|\psi_{n\mathbf{k}}\rangle = e^{i\mathbf{k}\mathbf{R}}|\psi_{n\mathbf{k}}\rangle \tag{3.3}$$

These states $|\psi_{n\mathbf{k}}\rangle$ are called Bloch eigenstates. The statement of Bloch's theorem is that they can be written as:

$$\langle\mathbf{r}|\psi_{n\mathbf{k}}\rangle \equiv \psi_{n\mathbf{k}}(\mathbf{r}) = e^{i\mathbf{k}\mathbf{r}} u_{n\mathbf{k}}(\mathbf{r}) \qquad \text{where } u_{n\mathbf{k}}(\mathbf{r}) = u_{n\mathbf{k}}(\mathbf{r}+\mathbf{R}) \tag{3.4}$$

That is, the function $u_{n\mathbf{k}}(\mathbf{r})$ is periodic again. Notice that $\psi_{n\mathbf{k}}(\mathbf{r})$ is only an eigenfunction for any real $\mathbf{k}$, since from (3.4) $\psi_{n\mathbf{k}}(\mathbf{r})$ would become infinitely large as $\mathbf{r} \to \infty$ for complex $\mathbf{k}$. The vector $\mathbf{k}$ is not uniquely determined by (3.3) since we can always add a vector $\mathbf{G}$ which obeys:

$$e^{i\mathbf{G}\mathbf{R}} = 1 \qquad \forall\, \mathbf{R} \tag{3.5}$$

Equation (3.5) defines the reciprocal lattice whose vectors $\mathbf{G}$ can easily be calculated from the set of translation vectors $\mathbf{a}_i$. It follows that the band structure $E_n(\mathbf{k})$ is periodic in $\mathbf{k}$-space, i.e. $E_n(\mathbf{k}) = E_n(\mathbf{k}+\mathbf{G})$. Further, we always chose the band index such that $E_n(\mathbf{k}) \leq E_{n+1}(\mathbf{k})$ and we start counting the bands at $n = 0$. The band problem is defined by solving (3.3), more specific: For a given periodic potential, one has to find the Bloch eigenenergies and eigenfunctions. The LMTO method does just that.

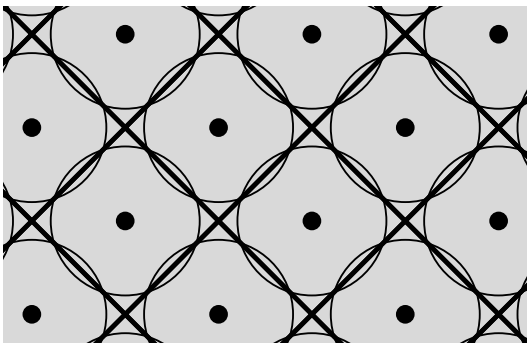

Figure 3.1: Overlapping spheres in the ASA

3.2 Atomic Sphere Approximation

In the atomic sphere approximation (ASA), the Wigner-Seitz cell is approximated by a sphere with equal volume Ω. The radius of the sphere is called Wigner-Seitz radius S. From this definition, we (trivially) find:

$$\frac{4\pi}{3}S^3 = \Omega = \mathbf{a}_1 \cdot (\mathbf{a}_2 \times \mathbf{a}_3) \tag{3.6}$$

This implies that the muffin-tin spheres are overlapping with an overlap volume equal to the volume of the interstitial region, see Fig. 3.1. Relations between the Wigner-Seitz radius S, the lattice constant a and the cell volume Ω are given for FCC and BCC in the appendix (A.3,A.6). The wave functions are expanded in terms of spherical harmonics within each sphere, which involves a cut-off, usually $\ell = 2$ (d) or $\ell = 3$ (f). In particular, potentials themselves (and hence densities) are approximated spherical symmetric, i.e. cut-off $\ell = 0$.

It is known that the ASA is more accurate for close-packed (FCC, HCP) or nearly close-packed (BCC) structures than for open crystal structures. In an open structure, e.g. the diamond crystal structure, the overlap and interstitial regions are larger and since the ASA neglects this region, it becomes less reliable. There are however ways to avoid this limitation of the ASA. One possibility is to insert so-called empty spheres, i.e. atoms with zero nuclear charge that fill out the interstitial regions. One can also employ "correction terms" that improve the ASA for open structures somewhat. However, this is not a major concern when dealing with the FCC or BCC structure.

3.3 The LMTO Method

We shall now discuss the LMTO method within the ASA[4] and for one atom per unit cell. The LMTO method can be viewed as linearized form of the KKR-ASA (Korringa, Kohn,

[4]In this work, the term MTO (muffin-tin orbital) should be understood in the sense of ASA muffin-tin orbitals, hence LMTO should be understood as LMTO-ASA.

Rostoker) method. In the KKR-ASA method, the basis set is energy dependent, whereas in the LMTO method the basis set is independent of the energy. For practical band structure calculations, the KKR-ASA method is much more time consuming, but it gives a vivid picture of the formation of energy bands. Thus, it is instructive to review the KKR-ASA method. Moreover, in the KKR-ASA equations, the "potential function" and the "structure constants" are introduced, from which "canonical bands" can be obtained easily. These are important concepts which hold the key for successfully linearizing the KKR-ASA equation, as Ole K. Andersen did [32]. Hence, we briefly describe the KKR-ASA equations, which serve as an introduction to its linear correspondence, the LMTO equations.

A complete reference for the LMTO method is the book [31]. Additional numerical details as well as a concise review are given in Ref. [47].

Let us re-state the (single-particle) band problem. We wish to find solutions of

$$H\psi_{n\mathbf{k}}(\mathbf{r}) = \left[-\nabla^2 + v(\mathbf{r})\right]\psi_{n\mathbf{k}}(\mathbf{r}) = E_n(\mathbf{k})\psi_{n\mathbf{k}}(\mathbf{r}) \tag{3.7}$$

where the Bloch eigenfunctions $\psi_{n\mathbf{k}}(\mathbf{r})$ obey

$$\psi_{n\mathbf{k}}(\mathbf{r}+\mathbf{R}) = e^{i\mathbf{k}\mathbf{R}}\psi_{n\mathbf{k}}(\mathbf{r}) \quad . \tag{3.8}$$

The band structure $E_n(\mathbf{k})$ is formally defined by these equations, however, this definition is physically not very illuminating.

3.3.1 KKR-ASA Equations

The starting point is the energy-dependent orbital[5]

$$\chi_L(E,\mathbf{r}) = i^\ell Y_L(\hat{\mathbf{r}}) \cdot \begin{cases} \psi_\ell(E,r) + p_\ell(E)(\frac{r}{S})^\ell & r < S \\ (\frac{S}{r})^{\ell+1} & r > S \end{cases} \quad , \tag{3.9}$$

where $\psi_\ell(E,r)$ is a solution of the radial Schrödinger equation

$$\left[-\frac{d^2}{dr^2} + \frac{\ell(\ell+1)}{r^2} + v(r) - E\right] r\,\psi_\ell(E,r) = 0 \tag{3.10}$$

inside the atomic sphere of radius S. The muffin-tin orbital $\chi_L(E,\mathbf{r})$ is continuous and has continuous derivatives everywhere. The so-called "potential function" $p_\ell(E)$ is obtained from the boundary conditions, i.e. continuity and differentiability at $r = S$:

$$p_\ell(E) \equiv \frac{D_\ell(E) + \ell + 1}{D_\ell(E) - \ell} \tag{3.11}$$

where $D_\ell(E)$ is the "logarithmic derivative" defined as:

$$D_\ell(E) \equiv S \cdot \frac{\partial \ln \psi_\ell(E,r)}{\partial r}\Big|_{r=S} = \frac{S}{\psi_\ell(E,S)}\,\frac{\partial \psi_\ell(E,r)}{\partial r}\Big|_{r=S} \tag{3.12}$$

[5] Here, as commonly used: $L = \{\ell, m\}$ (see appendix A)

The tail of the orbital $(S/r)^{\ell+1}$ is a solution of (3.10) for $T = E - v(r) = 0$, i.e. zero kinetic energy. Hence, the tail is a solution of the Laplace equation $\nabla^2\chi(\mathbf{r}) = 0$. As a consequence, the tail of an orbital centered at $\mathbf{R} \neq \mathbf{0}$ can be expanded at $\mathbf{R} = \mathbf{0}$ in terms of $i^\ell Y_L(\hat{\mathbf{r}})(r/S)^\ell$. Thus, the so-called "Bloch sum", i.e. $\sum_{\mathbf{R}} e^{i\mathbf{k}\mathbf{R}}$, of all tails from orbitals centered at $\mathbf{R} \neq \mathbf{0}$ can be expanded at $\mathbf{R} = \mathbf{0}$ giving:

$$\sum_{\mathbf{R}\neq 0} e^{i\mathbf{k}\mathbf{R}} \left(\frac{S}{|\mathbf{r}-\mathbf{R}|}\right)^{\ell+1} i^\ell Y_L(\mathbf{r}-\mathbf{R}) = \sum_{L'} \frac{-1}{2(2\ell'+1)} \left(\frac{r}{S}\right)^{\ell'} i^{\ell'} Y_{L'}(\mathbf{r}) \mathcal{S}^{\mathbf{k}}_{L',L} \quad (3.13)$$

This equation defines the "structure constants" $\mathcal{S}^{\mathbf{k}}_{L',L}$ which play an important role as we shall shortly see.

We are now in a position to realize that a linear combination of Bloch sums of muffin-tin orbitals $\chi_L(E,\mathbf{r})$

$$\sum_L a_L^{n\mathbf{k}} \sum_{\mathbf{R}} e^{i\mathbf{k}\mathbf{R}} \chi_L(E, \mathbf{r}-\mathbf{R}) \quad (3.14)$$

can be a solution of (3.7), i.e. the desired solution of the band problem.[6] First of all, (3.14) is constructed in a way that it will always obey Bloch's theorem (3.8). Secondly, inside any atomic sphere, the first term in (3.9), namely $i^\ell Y_L(\hat{\mathbf{r}})\psi_\ell(E,r)$, is already a solution of (3.10). Hence,[7]

$$\psi_{n\mathbf{k}}(\mathbf{r}) = \sum_L a_L^{n\mathbf{k}} \sum_{\mathbf{R}} e^{i\mathbf{k}\mathbf{R}} i^\ell Y_L(\hat{\mathbf{r}})\psi_\ell(E,r) \quad (3.15)$$

is a solution of the band problem, provided that the tails from all other spheres cancel the second term in (3.9), namely $i^\ell Y_L(\hat{\mathbf{r}})p_\ell(E)(r/S)^\ell$. This condition is called "tail cancellation". Using (3.13), we realize that this cancellation occurs when

$$\sum_L \left\{P_\ell(E)\delta_{L'L} - \mathcal{S}^{\mathbf{k}}_{L'L}\right\} a_L^{n\mathbf{k}} = 0 \quad \text{where} \quad P_\ell(E) = 2(2\ell+1)p_\ell(E) \ . \quad (3.16)$$

These are the well-known KKR-ASA equations. This linear set of homogeneous equations has a non-trivial solution for those energies $E = E_n(\mathbf{k})$ for which the determinant vanishes:

$$\det\left[P_\ell(E)\delta_{L'L} - \mathcal{S}^{\mathbf{k}}_{L'L}\right] = 0 \quad (3.17)$$

While the potential function $P_\ell(E)$ *only* depends on the potential $v(r)$ inside the atomic sphere, the structure constants $\mathcal{S}^{\mathbf{k}}_{L',L}$ *only* depend on the crystal structure. Hence, the KKR-ASA equations establish the connection between the potential and the structural part of the band problem. In this sense, they provide the connection between the energy E and wave vector $\mathbf{k}$, i.e. the energy band structure.

While equation (3.16) gives a picture of the formation of energy bands, which will become more vivid in the following section, (3.16) is difficult to handle for numerical calculations. The reason for this is that the energy E must be found individually by tracing the roots

[6] Provided that we are able to determine the correct expansion coefficients $a_L^{n\mathbf{k}}$.

[7] Note that $\psi_{n\mathbf{k}}(\mathbf{r})$ is another function than $\psi_\ell(E,r)$.

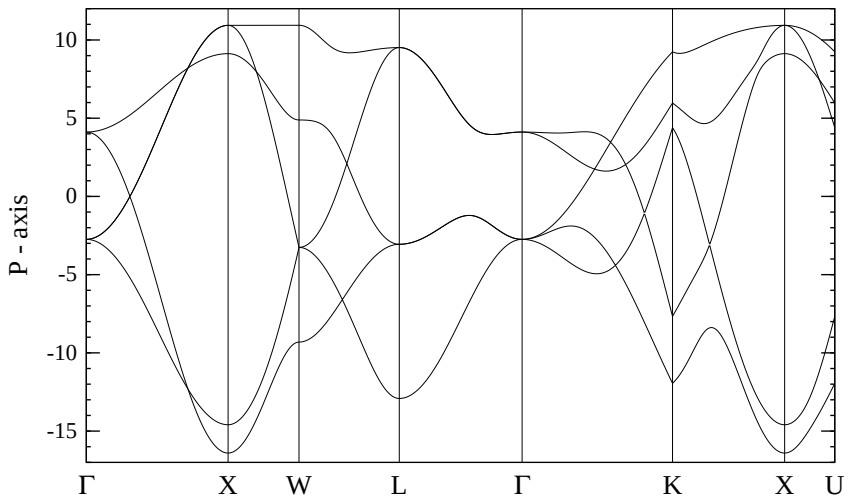

Figure 3.2: The (unhybridized) canonical d-bands for the FCC structure.

of (3.17). Note that (3.16) is not an eigenvalue problem for E, not even for the potential function, since $P_\ell(E)$ depends on the angular quantum number ℓ. The reason for that again is that our starting point was an energy-dependent basis set (3.9). In the LMTO method, an energy-independent basis set will be established. Hence, (3.16) will become an eigenvalue problem for E which is favorable from the computational standpoint.

3.3.2 Canonical Band Theory

Canonical band theory exploits the fact that the KKR-ASA equations may be solved without specifying the potential functions P_ℓ, considering them (rather than the energy E) as the independent variables. We will briefly consider non-hybridized canonical band theory where structure constants with $\ell \neq \ell'$ are neglected.

Equation (3.13) defines the structure constants $\mathcal{S}^{\mathbf{k}}_{L',L}$ which depend solely on the crystal structure, not even on the lattice constant. In Ref. [47], we describe in detail how they can be obtained numerically.

Using the ASA, the potential $v(\mathbf{r})$ is spherical inside the muffin-tin. As a consequence, the potential function $P_\ell(E)$ does not depend on the magnetic quantum number m, and the KKR-ASA equations may be brought into a form in which the sub-blocks $\mathcal{S}^{\mathbf{k}}_{\ell m',\ell m}$ become diagonal for a given ℓ. This is achieved by unitary transformations of the sub-blocks which leave the KKR-ASA equations invariant.

Thus, in the non-hybridized theory the structure matrix becomes completely diagonal and the determinant (3.17) becomes the product of the diagonal elements $(P_\ell(E) - \mathcal{S}^{\mathbf{k}}_{\ell i})$, accordingly the KKR-ASA equations have solutions whenever

$$P_\ell(E) = \mathcal{S}^{\mathbf{k}}_{\ell i} \ . \tag{3.18}$$

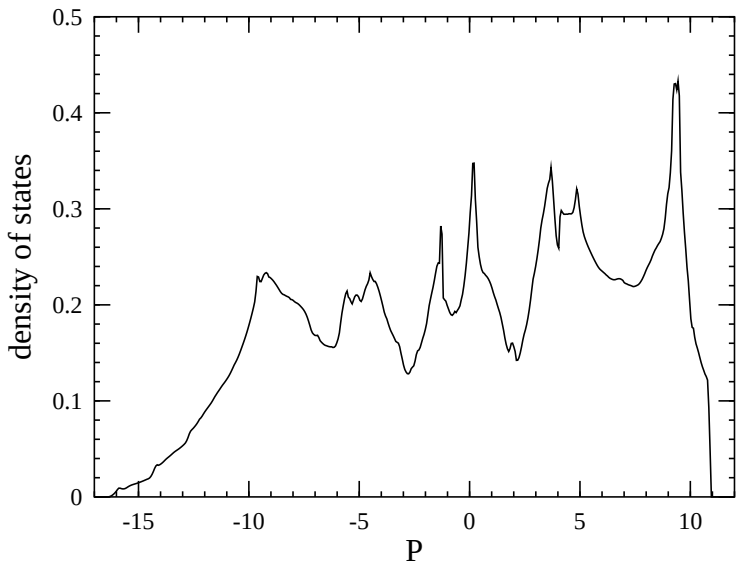

Figure 3.3: Canonical d-DOS for the FCC crystal structure.

The $2\ell + 1$ diagonal elements $\mathcal{S}_{\ell i}^{\mathbf{k}}$ of the ℓth sub-block are called the "canonical ℓ-bands".

Having solved the non-hybridized canonical band problem, we show (as an example) the canonical d-bands for the FCC crystal structure (Fig. 3.2) and the canonical d-density of states as a function of P_d (Fig. 3.3). The density of states was evaluated from the canonical bands using the tetrahedron method which will be described in section 3.4.2. At this point, we already realize that the density of states has an amazingly rich structure, considering that the *only* quantity entering the evaluation of the graph in Fig. 3.3 is the crystal structure.[8]

Canonical bands have a number of important characteristics which are independent of the crystal structure:

i.) The sum of the ℓ-bands (for $\ell > 0$) vanishes at each $\mathbf{k}$-point, i.e. $\sum_i \mathcal{S}_{\ell i}^{\mathbf{k}} = 0$.

ii.) Accordingly, the average over the Brillouin zone vanishes as well, i.e.

$$\sum_i \int_{\text{BZ}} d^3\mathbf{k}\, \mathcal{S}_{\ell i}^{\mathbf{k}} = 0 \qquad \forall\ \ell\ . \tag{3.19}$$

iii.) The Wigner-Seitz rule predicts that an ℓ-band is formed in the range:

$$-2\,\frac{2\ell+1}{\ell}\,(\ell+1)\ <\ P_\ell\ <\ 2\,(2\ell+1) \tag{3.20}$$

Fig. 3.3, suggests that the band is centered at $P = 0$. The center of a band is conveniently chosen to be the energy, here the P-value P_{C}, for which the first order moment[9] about P_{C}

[8] And, of course, the ℓ-character.

[9] See appendix Eq. (B.8).

vanishes. From (3.37) and (3.19) it follows that

$$\int dP\ N(P)\ P = \sum_i \int_{\mathrm{BZ}} d^3\mathbf{k} \int dP\ \delta(P - \mathcal{S}_{\ell i}^{\mathbf{k}})\ P = \sum_i \int_{\mathrm{BZ}} d^3\mathbf{k}\ \mathcal{S}_{\ell i}^{\mathbf{k}} = 0\ . \quad (3.21)$$

That is, the first order moment about the origin vanishes. Hence, $P_{\mathrm{C}} = 0$, i.e. *all* canonical ℓ-bands[10], are centered at the origin of the P-axis. Moreover, the Wigner-Seitz rule predicts a range from -15 to 10 for the FCC d-band which is a good estimate, as can be seen from Fig. 3.3.

3.3.3 The Linear Method

If we could replace the energy-dependent terms in (3.9) by energy-independent functions, we would arrive at a generalized eigenvalue problem, instead of (3.16), which is desirable from the computational point of view. As radial basis functions, for each ℓ, we use[11]

$$\phi_{\nu\ell}(r) \equiv \phi_\ell(E_{\nu\ell}, r) \quad \text{where} \quad \phi_\ell(E,r) = \frac{\psi_\ell(E,r)}{\sqrt{\langle \psi_\ell^2(E,r)\rangle}}\ , \quad (3.22)$$

and its energy derivate

$$\dot{\phi}_{\nu\ell}(r) \equiv \frac{\partial \phi_\ell(E,r)}{\partial E}\Big|_{E_{\nu\ell}}\ . \quad (3.23)$$

Since $\langle \phi_\ell^2(E,r)\rangle \equiv \int_0^S dr\, r^2 \phi_\ell^2(E,r) \equiv 1$, it follows that $\phi_{\nu\ell}(r)$ and $\dot{\phi}_{\nu\ell}(r)$ are orthogonal, and it may be shown that they are both orthogonal to the core states. The radial logarithmic derivates (3.12)

$$D_{\nu\ell} \equiv \frac{S\phi'_{\nu\ell}(S)}{\phi_{\nu\ell}(S)} \quad \text{and} \quad D_{\dot{\nu}\ell} \equiv \frac{S\dot{\phi}'_{\nu\ell}(S)}{\dot{\phi}_{\nu\ell}(S)} \qquad \text{where } {}' \equiv \frac{\partial}{\partial r} \quad (3.24)$$

are always different, as shown in [32]. Hence, a function with arbitrary logarithmic derivate is a linear combination of (3.22) and (3.23). We choose this linear combination to be:

$$\Phi_\ell(D,r) = \phi_{\nu\ell}(r) + \omega_\ell(D)\dot{\phi}_{\nu\ell}(r) \quad (3.25)$$

The function $\omega_\ell(D)$ is constructed such that $\Phi_\ell(D,r)$ has a logarithmic derivate which equals D. It can be shown that (3.25) may be used to replace the energy dependent terms in (3.9). The boundary condition at $r = S$ determines $D = -\ell - 1$ which, as we shall see later when we consider the example copper, turns out to be the center of the ℓ-band. To summarize, we write the energy-independent orbital as:

$$\chi_L(E,\mathbf{r}) = i^\ell Y_L(\hat{\mathbf{r}}) \cdot \begin{cases} \Phi_\ell(-\ell-1,r) & r < S \\ (\frac{S}{r})^{\ell+1} & r > S \end{cases} \quad (3.26)$$

[10] Not just the one shown in Fig. 3.3.

[11] Again, $\psi_\ell(E,r)$ is a solution of (3.10) for $r < S$. And $E_{\nu\ell}$ is a *fixed* energy for every ℓ.

In analogy to the derivation of the KKR-ASA equations, i.e. expanding the tails around the origin as a Bloch sum, we can now obtain the LMTO-ASA equations from (3.26), these are:

$$\sum_L \left\{ H^{\mathbf{k}}_{L'L} - E_n(\mathbf{k}) O^{\mathbf{k}}_{L'L} \right\} a^{n\mathbf{k}}_L = 0 \tag{3.27}$$

We have thoroughly discussed these equations in [47]. In particular, all numerical details are given there. However, one should make some remarks about the LMTO equations:

i.) The Hamilton matrix $H^{\mathbf{k}}_{L'L}$ and the overlap matrix $O^{\mathbf{k}}_{L'L}$, which are explicitly given in [47], are obtained from the structure matrix $\mathcal{S}^{\mathbf{k}}_{L'L}$ and the so-called four "potential parameters" (and $E_{\nu\ell}$) for each ℓ. These are found when solving (3.10) for a given $E_{\nu\ell}$, and arise from a parameterization of the potential function around $E_{\nu\ell}$.

ii.) Eqs. (3.27) have the form on a generalized eigenvalue problem, which can be reduced to an ordinary eigenvalue problem.

iii.) The Bloch wave functions are given in terms of the radial basis functions (3.22) and (3.23) inside the atomic sphere as

$$\psi_{n\mathbf{k}}(\mathbf{r}) = \sum_L \left\{ \phi_{\nu\ell}(r) A^{n\mathbf{k}}_L + \dot{\phi}_{\nu\ell}(r) B^{n\mathbf{k}}_L \right\} Y_L(\hat{\mathbf{r}}) \ , \qquad r < S \tag{3.28}$$

which we normalize to unity. Note that $\phi_{\nu l}(r)$ and $\dot{\phi}_{\nu l}(r)$ are real functions. Numerically, our radial functions ($\phi_{\nu l}(r)$, $v(r)$, $n(r)$ etc.) are represented on a mesh $r_n = r_0 e^{n\delta_x}$. This has two advantages: (i) Near the nucleus, the mesh is fine and capable of coping with rapid oscillations. (ii) Since $r = e^x$, we can write $dr = r dx$. We chose $\delta_x \approx 0.04$, and approximately 220 mesh points inside the atomic sphere.

iv.) The choice of the $E_{\nu\ell}$'s is crucial for the LMTO method to work. This "linearization energy" has to be chosen inside the respective band.[12] Hence, it is helpful to first solve the corresponding atomic problem, i.e. solve (3.10), and use the atomic energy eigenvalue (for the desired n and ℓ) as an initial guess for $E_{\nu\ell}$. The resulting bands can then be inspected and one can choose a better set of $E_{\nu\ell}$'s. It is numerically quite inexpensive to iterate this procedure a few times.

v.) From (3.28), we can obtain a simple expression for the ℓ-character $C^{n\mathbf{k}}_\ell$ for each given band n and $\mathbf{k}$-point:

$$C^{n\mathbf{k}}_\ell \equiv \sum_{m=-\ell}^{\ell} \left| \langle \ell m | \psi_{n\mathbf{k}} \rangle \right|^2 = \sum_m \left\{ |A^{n\mathbf{k}}_{\ell m}|^2 + \langle \dot{\phi}^2_{\nu\ell} \rangle |B^{n\mathbf{k}}_{\ell m}|^2 \right\} \tag{3.29}$$

It follows that the ℓ-characters add up to unity, i.e. $\sum_\ell C^{n\mathbf{k}}_\ell = 1$.

[12] If the $E_{\nu\ell}$ is chosen outside the band, so-called "ghost bands" may arise from solving the LMTO equations.

3.3.4 Moment Expansion of Charge Density

For the LDA self-consistency cycle on page 13, the actual wave functions (3.28) are of minor interest since only the electronic charge density $n(\mathbf{r})$ is required to evaluate the effective potential for the next iteration. From (3.28), we may write the spherically averaged (valence) charge density (per spin) as:

$$4\pi\, n(r) \equiv \int_{4\pi} d^2\Omega\, n(\mathbf{r}) = \frac{1}{N}\sum_{Ln\mathbf{k}}^{\text{occ.}} \Big\{ \phi^2_{\nu\ell}(r)|A_L^{n\mathbf{k}}|^2 + \dot{\phi}^2_{\nu\ell}(r)|B_L^{n\mathbf{k}}|^2 + \\ + \phi_{\nu\ell}(r)\dot{\phi}_{\nu\ell}(r)\left[A_L^{n\mathbf{k}*}B_L^{n\mathbf{k}} + B_L^{n\mathbf{k}*}A_L^{n\mathbf{k}}\right]\Big\} \tag{3.30}$$

Here, N is the number of $\mathbf{k}$-points in the Brillouin zone and the sum only includes occupied states, i.e. $E_n(\mathbf{k}) < E_F$. One should not use (3.30) to evaluate the electronic density since there is a more elegant and accurate way of doing this calculation which we want to describe now. Let us re-consider the KKR-ASA equations (3.16) where the wave function $\phi_\ell(E,r)$ is dependent of energy. If, for each ℓ, we knew how many states exist in a small energy range ΔE, then the electronic density would simply be the sum of all the number of states in ΔE times $\phi^2_\ell(E,r)$ for all energies below E_F. Accordingly, in the continuum limit we find:

$$4\pi\, n(r) = \sum_\ell \int^{E_F} dE\, N_\ell(E)\phi^2_\ell(E,r) \tag{3.31}$$

$N_\ell(E)$ is the ℓ-projected density of states, as defined in (3.44). Since our orbitals are not energy dependent in the LMTO, we can not use (3.31). However, $\phi_\ell(E,r)$ can simply be expanded around $E_{\nu\ell}$ in terms of $\phi_{\nu l}(r)$ and $\dot{\phi}_{\nu\ell}(r)$ as a Taylor series in energy:

$$\phi_\ell(E,r) = \phi_{\nu\ell}(r) + \varepsilon\dot{\phi}_{\nu\ell}(r) + \tfrac{1}{2}\varepsilon^2\ddot{\phi}_{\nu\ell}(r) + \ldots \qquad \varepsilon \equiv E - E_{\nu\ell} \tag{3.32}$$

Inserting this Taylor series into (3.31) gives an expression for the electronic charge density which is useful within the LMTO method:

$$4\pi\, n(r) = \sum_\ell \Big\{ \phi^2_{\nu\ell}(r)M_{\ell 0} + 2\phi_{\nu\ell}(r)\dot{\phi}_{\nu\ell}(r)M_{\ell 1} + \left[\dot{\phi}^2_{\nu\ell}(r) + \phi_{\nu\ell}(r)\ddot{\phi}_{\nu\ell}(r)\right] M_{\ell 2} + \ldots \Big\} \tag{3.33}$$

In the above equation, we introduced the qth moments about $E_{\nu\ell}$ given by:

$$M_{\ell q} = \int^{E_F} dE\, N_\ell(E)\cdot(E - E_{\nu\ell})^q \tag{3.34}$$

Note that the first order moment (3.21) has the same form, except that the upper limit of the integral in (3.21) is infinity, while now the limit is the Fermi level. Physically, this difference lies in considering the band, regardless of its occupation, or just the occupied part of the band. In section 3.4.4, we will show how they can be evaluated using the tetrahedron

method. From their definition, we immediately realize that $M_{\ell 0}$ is the number of states with ℓ-character at the Fermi level, i.e. the number of electrons (per spin) with character ℓ

$$M_{\ell 0} = n_\ell(E_F) \qquad \text{and} \qquad \sum_\ell M_{\ell 0} = n(E_F) = N_e \quad , \tag{3.35}$$

where N_e is the number of (valence) electrons per atom and spin. From $\langle \phi_{\nu\ell} | \dot{\phi}_{\nu\ell} \rangle = 0$ and $\langle \dot{\phi}^2_{\nu\ell} \rangle + \langle \phi_{\nu\ell} | \ddot{\phi}_{\nu\ell} \rangle = 0$, which can be derived from (3.22), it follows that only the first term in (3.33) contributes to the net charge in a sphere, i.e.:

$$\int\limits_{\mathrm{MT}} d^3r\, n(\mathbf{r}) = \int\limits_0^S dr\, r^2\, 4\pi n(r) = \int\limits_0^S dr\, r^2 \sum_\ell \phi^2_{\nu\ell}(r) M_{\ell 0} = N_e \tag{3.36}$$

In the last step we used (3.35). Note that (3.33), on the account of the $\phi_{\nu\ell}(r)\ddot{\phi}_{\nu\ell}(r)$ term, is more accurate than (3.30). It may seem surprising that we write the Taylor expansion (3.32) to higher terms than ε, while, on the other hand, we are using a linear method. The reason for this is that the LMTO method is a linear method in the logarithmic derivate D and not ε, which leads to more than linear order accuracy in ε. Hence, we don't have to truncate the moment expansion (3.33) after moments of order $q = 1$. We truncate the expansion after order $q = 2$, since the higher terms become more complicated and less significant.

Also note, that by means of (3.34), we can choose $E_{\nu\ell}$ in a way that the first order moments $M_{\ell 1}$ vanish. In fact, this corresponds to choosing $E_{\nu\ell}$ in the center of the *occupied* part of the ℓ-band which is our choice used in self-consistency calculations.

3.4 Brillouin Zone Integration and Fermi Energy

The density of states (DOS) per spin is defined by

$$N(E) \equiv \frac{\Omega}{(2\pi)^3} \sum_n \int\limits_{\mathrm{BZ}} d^3\mathbf{k}\, \delta(E - E_n(\mathbf{k})) \quad , \tag{3.37}$$

where Ω is the volume of the unit cell. Note that the volume of the Brillouin zone (BZ) Ω_{BZ} is just $(2\pi)^3/\Omega$. The number of states (NOS) $n(E)$ is defined as the integral of the DOS up to the energy E, i.e.[13]

$$n(E) \equiv \int^E dE' N(E') = \frac{\Omega}{(2\pi)^3} \sum_n \int\limits_{\mathrm{BZ}} d^3\mathbf{k}\, \Theta(E - E_n(\mathbf{k})) \quad . \tag{3.38}$$

Here, Θ is the step function (B.9). In addition, we introduce the projected DOS, which is defined by inserting a projection operator P onto certain states into (3.37), i.e.

$$N_{\mathrm{Proj}}(E) \equiv \frac{\Omega}{(2\pi)^3} \sum_n \int\limits_{\mathrm{BZ}} d^3\mathbf{k}\, \langle \psi_{n\mathbf{k}} | P | \psi_{n\mathbf{k}} \rangle \delta(E - E_n(\mathbf{k})) \quad . \tag{3.39}$$

[13] Unfortunately, the letter n is reserved for the NOS $n(E)$, the electronic density $n(\mathbf{r})$ and the band index n. However, in these cases it is either a function of energy, space or no function at all, which tells us its physical meaning.

The projected NOS is defined in complete analogy to the projected DOS, i.e. inserting a projection operator onto certain states into (3.38).

In the case of a metal, where no band gap is present at the Fermi level, the Fermi energy can be defined by the condition that

$$n^{\uparrow}(E_F) + n^{\downarrow}(E_F) = N_e \ . \tag{3.40}$$

Here, N_e is the total number of valence electrons and $n^{\sigma}(E)$ is the valence number of states with spin σ which we evaluate by using the tetrahedron method described below. We evaluate the Fermi energy directly via (3.40) using the bisection method [48]. That is, we find the root of $f(E) = n^{\uparrow}(E) + n^{\downarrow}(E) - N_e$. Since we know that the interval $[E_{\min}, E_{\max}]$[14] contains the root, it is impossible for the bisection method to fail. Moreover, once the energies $E_n^{\sigma}(\mathbf{k})$ for the $\mathbf{k}$-points which construct the tetrahedra, have been evaluated, the summation[15] is quite inexpensive. Hence, we can bisect until the desired accuracy is achieved.

3.4.1 Symmetry

The Hamiltonian is invariant under all operations of the space group[16]. The group of all translations $T_{\mathbf{R}}$ is a sub group of the space group. This symmetry was already explored in section 3.1, leaving us with Bloch's theorem and $E_n(\mathbf{k}) = E_n(\mathbf{k} + \mathbf{G})$. The point group is an *additional* sub group of the space group. For cubic crystal structures, which are the only structures considered in this work, namely, FCC and BCC, the point group consists of 48 rotations[17] α. We denote $\alpha\mathbf{k}$ as the rotation α in the point group applied to the vector $\mathbf{k}$. Now, the irreducible wedge of the Brillouin zone (IBZ) (with volume Ω_{IBZ}) consists of all the irreducible $\mathbf{k}$-points (in a wedge) such that $\alpha\mathbf{k}$ span the full Brillouin zone. Since the point group of cubic crystal structures consists of 48 elements, we find:

$$\Omega_{\mathrm{IBZ}} = \frac{1}{48}\,\Omega_{\mathrm{BZ}} \tag{3.41}$$

The IBZ is *considerable* smaller than the full Brillouin zone and accordingly it is desirable to replace the integrals in (3.37) and (3.38) by integrals over the IBZ. This is possible since for all the 48 rotations α in the point group we have:[18]

$$E_n(\alpha\mathbf{k}) = E_n(\mathbf{k}) \tag{3.42}$$

Now, if we consider a projected DOS (NOS), it is not obvious whether we can reduce the problem to the IBZ since the projected DOS not only requires the Bloch energies at each $\mathbf{k}$-point but also the projected Bloch waves. It is shown in appendix C.1 that this is only possible when the projection operator P commutes with the rotations α in the point group of the crystal.

[14] Where $E_{\min}$ ($E_{\max}$) is the minimal (maximal) energy appearing in the band structure.
[15] I.e. the corresponding summation (3.43) for the NOS.
[16] For more details see e.g. Ref. [30].
[17] Here, rotations are understood to be generalized rotations which include parity operations.
[18] See Eq. (3.6.6) in Ref. [30].

3.4.2 The Tetrahedron Method

In the tetrahedron method, one divides the IBZ[19] into small tetrahedra i and the integral (3.37) is then evaluated as a sum:

$$N(E) = \frac{1}{\Omega_{\text{IBZ}}} \sum_{n,i} N_{n,i}(E) \tag{3.43}$$

Each tetrahedron i has a certain volume V_i and four corner energies for each band. Provided the corner energies are ordered in a way that $E_1 \leq E_2 \leq E_3 \leq E_4$, we can use the table[20] in Ref. [31] (p. 196) to calculate $N_{n,i}(E)$, its contribution to the DOS.

Using the tetrahedron method, we also calculate the NOS as a Brillouin zone integration, i.e. as the last term in (3.38), which is more precise than evaluating the NOS using its definition as an energy integral over the DOS. The corresponding sum looks exactly like (3.43) except that the contributions are now $n_{n,i}(E)$ which are also tabulated in [31].

The IBZ is spanned by a certain number of $\mathbf{k}$-points. Consequently, the IBZ may always be expressed in terms of a certain number of tetrahedra. The IBZ is explicitly given in terms of tetrahedra for the FCC and BCC structures by (A.4) and (A.7). Now, when we divide the IBZ into small tetrahedra, we start from these (initial) tetrahedra and divide them into smaller and smaller tetrahedra until we have a number of tetrahedra[21] that is large enough to evaluate (3.43) to the required accuracy. We should mention that we perform this procedure by always dividing the largest tetrahedron, hence we arrive at tetrahedra that are fairly equal in size.

3.4.3 Projected ℓ-Density of States

This is the most important example of a projected DOS (3.39). Here, we consider a projection operator P_ℓ onto the ℓ-component, i.e. $P_\ell = \sum_m |\ell m\rangle\langle \ell m|$. It follows from (3.29) that the expectation value of the projection operator is simply given by $C_\ell^{n\mathbf{k}}$. Thus:

$$N_\ell(E) = \frac{\Omega}{(2\pi)^3} \sum_n \int_{\text{BZ}} d^3\mathbf{k} \; \underbrace{\langle \psi_{n\mathbf{k}} | P_\ell | \psi_{n\mathbf{k}} \rangle}_{C_\ell^{n\mathbf{k}}} \, \delta(E - E_n(\mathbf{k})) \tag{3.44}$$

In the appendix C.1, we have shown that P_ℓ commutes with the rotations α in the point group of the crystal. Accordingly, we can reduce the problem to the IBZ and write:

$$N_\ell(E) = \frac{1}{\Omega_{\text{IBZ}}} \sum_{n,i} W_\ell^{n,i} \, N_{n,i}(E) \quad , \tag{3.45}$$

[19] In the projected case, when $[P, \alpha] \neq 0$ the full Brillouin zone.

[20] At this point, a small (but important) printing error in the table should be mentioned. The correct function $N(E_1, E_2, E_3, E_4, V_i, E)$ for $E_3 \leq E \leq E_4$ is

$$\frac{3V_i}{D} \frac{(E - E_4)^2}{(E_4 - E_3)D_4} \qquad \text{and } \textit{not} \qquad \frac{3V_i}{D} \frac{(E - E_4)^2}{(E_3 - E_4)D_4} \quad .$$

[21] Usually, on the order of 10^3.

where $W_\ell^{n,i}$ are weight factors found by the average of the four corner weight factors $W_\ell^{n\mathbf{k}} = C_\ell^{n\mathbf{k}}$ for each tetrahedron i. Again, we calculate $n_\ell(E)$, i.e. the projected ℓ-NOS, in complete analogy.

3.4.4 Evaluation of Moments

Another important quantity that can be calculated using the tetrahedron method is the set of moments $M_{\ell q}$ which are defined in (3.34). As can be seen from (3.35), the 0th order moments are nothing but the ℓ-projected NOS at the Fermi energy. From (3.37), (3.38) and the above, it follows that $M_{\ell q}$ can be evaluated as:

$$M_{\ell q} = \frac{1}{\Omega_{\text{IBZ}}} \sum_{n,i} W_{\ell q}^{n,i}\, n_{n,i}(E_F) \quad \text{where} \quad W_{\ell q}^{n\mathbf{k}} = C_\ell^{n\mathbf{k}}\, (E_n(\mathbf{k}) - E_{\nu\ell})^q \tag{3.46}$$

Again, $W_{\ell q}^{n,i}$ is the average of the four $W_{\ell q}^{n\mathbf{k}}$'s at the corners. Evaluating $M_{\ell q}$ via (3.34) directly, i.e. as an integral over energy, should be avoided since the DOS $N_\ell(E)$ has a rich structure, in particular sharp peaks, as can be seen from Fig. 3.3, which will get lost by applying a finite mesh on the energy axis. Hence, we evaluated $M_{\ell q}$ using (3.46), which is not only more precise, but also computationally less time consuming than doing the energy integral.

3.5 Example Copper

We shall now take a closer look at a Hartree calculation for FCC copper at the experimental equilibrium Wigner-Seitz radius of $S = 2.669a_0$ [31]. This metal is commonly used as a test case for various types of calculations and will also be our test case through the following chapters.

The DOS obtained within an LDA calculation for this metal is shown in Fig. 7.17. Since we now perform a Hartree calculation, we don't include the exchange-correlation potential from all electrons, only for the core electrons. One may argue that this is not really a Hartree calculation, which is true, but using the frozen core approximation, we will call this a Hartree calculation anyway, since we are interested in exchange-correlation effects among the valence electrons. Hence, we treat the exchange-correlation among valence and core electrons locally, i.e. using LDA, and exploit exchange-correlation effects among valence electrons using the formalism of second quantization in chapter 6. But now we perform a Hartree calculation on the "first quantization" level.

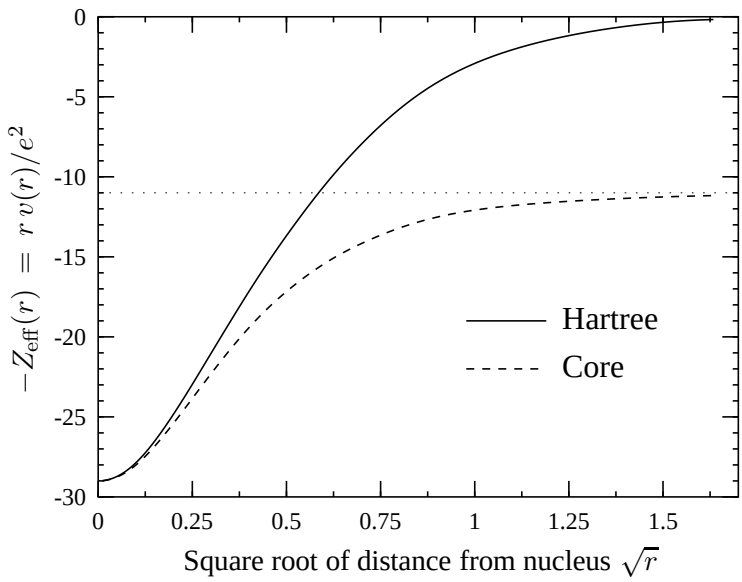

Figure 3.4: Frozen core potential and Hartree potential.

3.5.1 Effective Potential

After clarifying the situation, we can write down the effective potential for which the one-particle wave functions have to be found. This Hartree potential is in essence given by (2.15):[22]

$$v_{\mathrm{H}}(\mathbf{r}) = \int d^3\mathbf{r}' \frac{e^2 n_{\mathrm{tot}}(\mathbf{r}')}{|\mathbf{r}-\mathbf{r}'|} - \frac{e^2 Z}{r} + v_{\mathrm{xc}}(n_c(\mathbf{r})) \tag{3.47}$$

Here, $n_c(\mathbf{r})$ is the core density, n_{tot} the total electronic density and Z the atomic number. This effective potential is found using a self-consistent band calculation and is plotted in Fig. 3.4. In addition, one can consider the potential for the case that no Coulomb interaction is present among the valence electrons present, i.e. not even the classical Hartree interaction. This potential is given by:

$$v_0(\mathbf{r}) = \int d^3\mathbf{r}' \frac{e^2 n_c(\mathbf{r}')}{|\mathbf{r}-\mathbf{r}'|} - \frac{e^2 Z}{r} + v_{\mathrm{xc}}(n_c(\mathbf{r})) \tag{3.48}$$

Once the core density $n_c(\mathbf{r})$, obtained from a self-consistent atomic calculation, is found, *no* self-consistent band calculation is needed to obtain (3.48). This potential is also plotted in Fig. 3.4 and we refer to it as the frozen core potential or just core potential. The difference between $v_{\mathrm{H}}(\mathbf{r})$ and $v_0(\mathbf{r})$ is the Hartree term, caused by the classical Hartree interaction among the valence electrons.

Note carefully that, in Fig. 3.4, not the spherical averaged potentials themselves but rather $-Z_{\text{eff}}(r) \equiv rv(r)/e^2$ are displayed as a function of the square root of the distance from the

[22] We refer to the complete effective potential $v_{\mathrm{H}}(\mathbf{r})$ as the Hartree potential. Usually, only the first term in Eq. (2.15) is called the Hartree potential, which we call Hartree term instead.

nucleus r. Plotting the potentials this way is a lot more illuminating than just plotting $v(r)$. The major part of the radial dependence of the potentials is caused by the nucleus itself:

$$v(r) = \frac{-Ze^2}{r} \quad \rightarrow \quad -Z_{\text{eff}}(r) \equiv \frac{rv(r)}{e^2} = -Z \tag{3.49}$$

Hence, plotting the potential caused only by the nucleus would resolve into a straight line at $Z_{\text{eff}}(r) = Z$, independent of r. Now $Z_{\text{eff}}(r)$ is an effective atomic number dependent of r. A nucleus with atomic number $Z_{\text{eff}}(r)$ causes the same force on an electron at distance r as the potential $v(r)$ would do. Consider:

i.) For the core potential at the Wigner-Seitz radius S, we find $Z_{\text{eff}}(S) \approx 11$, since the nucleus (with 29 protons) is screened by 18 core electrons.

ii.) For the Hartree potential, we find $Z_{\text{eff}}(S) \approx 0$, since the nucleus is shielded by all 29 electrons.

iii.) Very close to the nucleus, we find $Z_{\text{eff}}(r \lesssim 0.002a_0) \approx 29$, since the nucleus is almost unscreened. An electron such close to the nucleus feels its almost unscreened attraction.

3.5.2 Logarithmic derivative

Having established the Hartree potential, we can now move along and look at quantities directly derived from v_{H}. First, let us take a look at the logarithmic derivative function (3.12). Essentially, this function is found by solving the radial Schrödinger equation (3.10) inside the atomic sphere at fixed energies E. Figure 3.5 shows this function in the broader energy range we are interested in. It is well known that the logarithmic derivative is a monotonic decreasing function except at its singularities.

The potential function P_ℓ is related to the logarithmic derivative by (3.11) and (3.16), i.e.

$$P_\ell(E) = 2(2\ell+1)\,\frac{D_\ell(E)+\ell+1}{D_\ell(E)-\ell} \quad . \tag{3.50}$$

In terms of the logarithmic derivative, the Wigner-Seitz rule (3.20) states that ℓ-bands are formed at energies where the logarithmic derivative is negative,[23] i.e. from a zero of $D_\ell(E)$ to the next singularity.

While Fig. 3.5 gives a good overall view of the logarithmic derivative, it is hard to see at a glance the regions where the functions are negative, i.e. where the ℓ-bands are formed. Hence, we have plotted these regions in Fig. 3.6, and they can be associated with principal quantum numbers n.

From (3.21), we know that the center of each ℓ-band is located at the origin $P_\ell = 0$, hence, from (3.50), we see that (in terms of the logarithmic derivative) the center of each ℓ-band corresponds to $D_\ell(E) = -\ell - 1$. We have evaluated the intersections of $D_\ell(E)$ with $-\ell - 1$ and plotted these energies in Fig. 3.6 as well (vertical lines).

[23] Actually, the physical origin of the rule stems from its version $D < 0$, rather then (3.20).

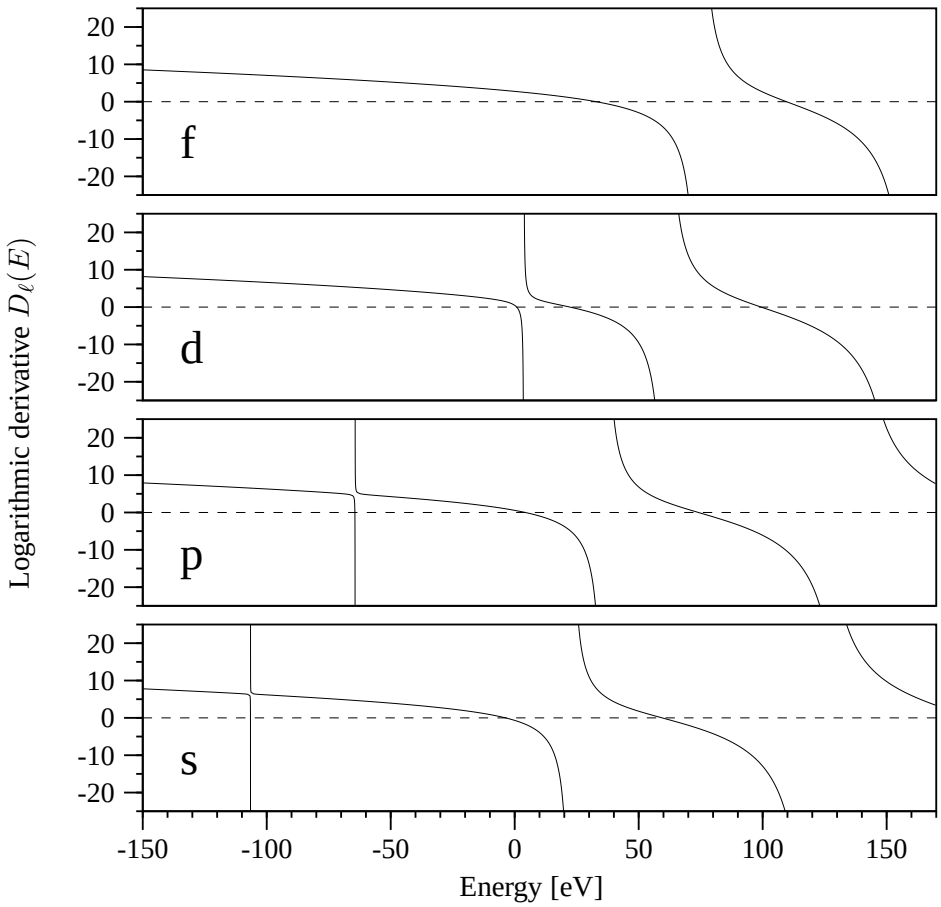

Figure 3.5: Logarithmic derivative (3.12) for the Hartree potential (3.47). *Below* the energy range of the graph, $D_s(E)$ has two singularities at about -9 and -1 keV; $D_p(E)$ has one singularity at about -900 eV; $D_d(E)$ and $D_f(E)$ have none.

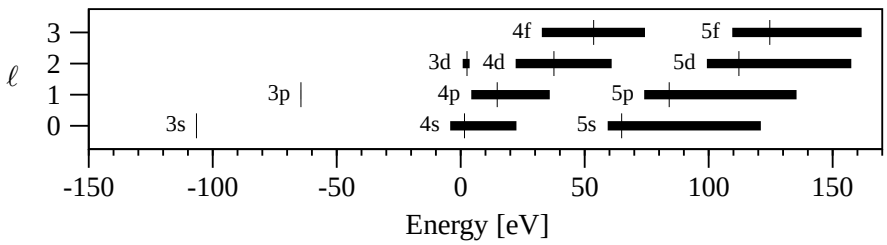

Figure 3.6: Energy regions where the logarithmic derivative (Fig. 3.5) is negative and energies for which $D_\ell(E)$ equals $-\ell-1$. The Wigner-Seitz rule states that the ℓ-bands are formed at those energies, i.e. from a zero of $D_\ell(E)$ to the next singularity. The $3s$ and $3p$-bands are very narrow, i.e. core-like. The $3d$-band turns out to be the most interesting one (in $3d$ transition metals) since it is still quite narrow and close to the Fermi energy.

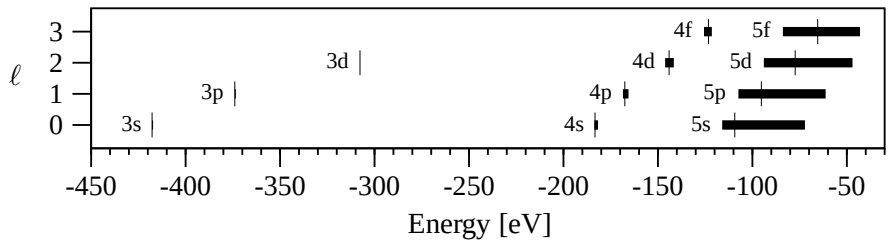

Figure 3.7: Energy regions where the logarithmic derivative is negative, but now for the core potential (3.48).

The $3s$ and $3p$-bands are very narrow and we treat them as frozen core states in self-consistent band structure calculations. By taking a look at Fig. 3.5 again, we realize that for the $3s$ and $3p$-bands, the zero and singularity are very close to each other. It should be mentioned that the lower lying bands are, of course, even much narrower. These are the $1s$, $2s$, and $2p$-bands[24] with one-particle energies about -9 keV, -1 keV and -900 eV respectively.

Looking at the non-hybridized bands in Fig. 3.6 gives an intuitive picture of the bands in terms of their origin from the atomic structure of energy levels. This picture is valid for the core-like levels up to the $3p$-band (level). All higher bands are much broader with increasing width as we move higher in energy.

The $3d$ band can maximally be filled with ten electrons, thus the eleven valence electrons fill the lower part of the $4s$, $4p$ and $3d$ band. Hence, the Fermi energy should be somewhere between 0 and 10 eV (by looking at Fig. 3.6) and the numerical calculation yields $E_F = 5.85$ eV.[25]

For higher energies, more and more bands with different ℓ-character overlap,[26] making it possible for the spherical harmonics expansion for plane waves (see (C.26)) to cope with rapid oscillations.

We will now take a brief look at the situation for the core potential (3.48). It is not surprising that, when the Hartree interaction among the eleven valence electrons is turned off, the bands change drastically as shown in Fig. 3.7.

When the Hartree repulsion among the valence electrons is missing, the electrons can move closer to the nuclei, i.e. they have a higher probability to be in a region of the potential with lower energy. Thus, the one-particle energies are lowered and moreover the bands become narrower since the electrons develop a stronger binding to the nuclei.

These two effects, lowering of energies and narrowing of band width, can be seen very clearly by comparing Fig. 3.6 with Fig. 3.7. In particular, using the core potential, the $3d$-band turns out to be a core-like state, while in the Hartree case, it had a width of 2.8 eV.

[24] One would usually call these “bands” atomic levels.

[25] Eqs. (3.47) and (3.48) fix the position of our (arbitrary) energy scale. However, since only a single MT sphere enters these equations, absolute energy values, e.g. E_F, are of little physical relevance.

[26] Note that we had to truncate the angular character at some point.

3.5.3 Band Structure

In the preceeding section, we used the Wigner-Seitz rule in order to obtain non-hybridized bands. Furthermore, we wanted to give the reader who is not so familiar with $3d$ transition metals an idea about the positions of the various bands and the order of magnitude of their absolute positions.

We will now look at the band structure for the Hartree potential, considering only the (hybridized) $4s$, $4p$ and $3d$-bands. Note that it is actually sufficient to only include these bands in a self-consistent band structure calculation since the higher lying bands are un-occupied, and thus do not contribute to the total charge density.

Fig. 3.8 shows the total and ℓ-projected density of states of the *hybridized* bands obtained from the LMTO and tetrahedron method. The d-projected density of states is largest below the Fermi energy which is located at $E_F = 5.85$ eV. Since this d-like band[27] is narrower than the others and since more electrons can occupy a d-like band, we find the d-DOS largest compared to the others. Note that in Fig. 3.8 the inverse energy scale on the y-axis differs by a factor of 20 for the s and p-DOS. Hence, the total density of states is dominated by the d-DOS.

The ℓ-projected density of states can be compared to the positions of the corresponding *non-hybridized* bands according to the Wigner-Seitz rule. To make this comparison easier, we have plotted a magnification of the corresponding bands from Fig. 3.6 in Fig. 3.9. The Wigner-Seitz rule predicts the positions of the ℓ-bands very well, i.e. the ℓ-projected DOS tends to be largest where the Wigner-Seitz rule predicts the ℓ-bands.

We now take a look at the band structure in terms of their $\mathbf{k}$-dependence. Fig. 3.10 shows the energy eigenvalues plotted along high symmetry lines in the Brillouin zone. The actual $\mathbf{k}$-points belonging to the letters Γ, X, W etc. are given in the appendix A. The d-bands occupy the shadowed region from about 0.7 to 4.2 eV whose width is 3.5 eV. States belonging to these bands are dominated by an angular momentum character of $\ell = 2$, although there is some hybridization with the broad s-band below and the bands above the d-bands.

Note that the bottom of the s-band is very "free-electron-like", i.e. $E(k) \propto k^2$. This can also be seen from Fig. 3.11: The increase of the s-DOS (at the lower band edge) has the form of a square root function[28]

$$N_s(E) \;\propto\; \Big(E - E_0(\mathbf{k}=\mathbf{0})\Big)^{1/2} \;, \qquad \big(\text{ when } \; E > E_0(\mathbf{k}=\mathbf{0})\;\big) \tag{3.51}$$

which is the well-known DOS for free electrons.

Being able to evaluate the eigenenergies $E_n(\mathbf{k})$, we are in a position to determine the Fermi surface defined by

$$E_n(\mathbf{k}) = E_F \;\; . \tag{3.52}$$

[27] Since we are dealing with hybridized bands, we have to call this an "ℓ-like band", sometimes people (including myself) call it an "ℓ-band" anyway for simplicity, although, strictly speaking, there are generally no (pure) ℓ-bands in a hybridized theory.

[28] The band $n = 0$ is the lowest in Fig. 3.10, hence $E_0(\mathbf{k}=\mathbf{0})$ is the lowest energy at the Γ-point.

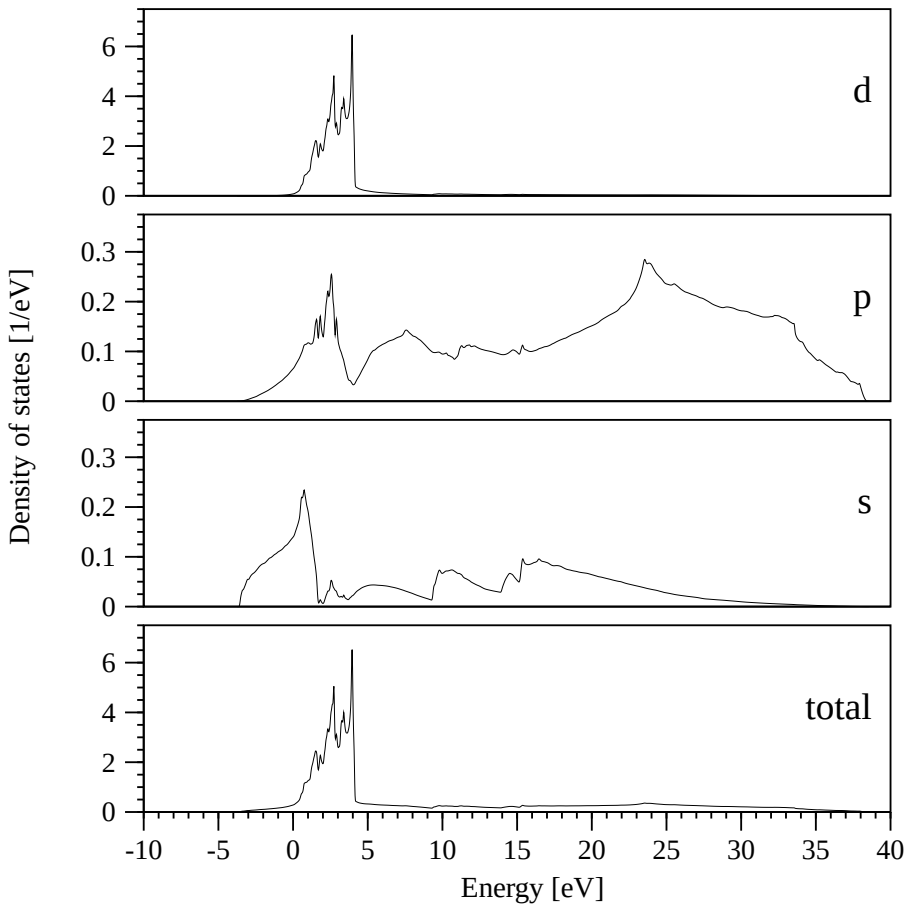

Figure 3.8: Total and projected density of states obtained from the LMTO method for the Hartree potential (3.47). The ℓ-projected DOS of the *hybridized* bands may be to compared to the positions of the corresponding *non-hybridized* bands according to the Wigner-Seitz rule shown in Fig. 3.9. Note that the inverse energy scale on the y-axis differs by a factor of 20 for the s and p-projected DOS.

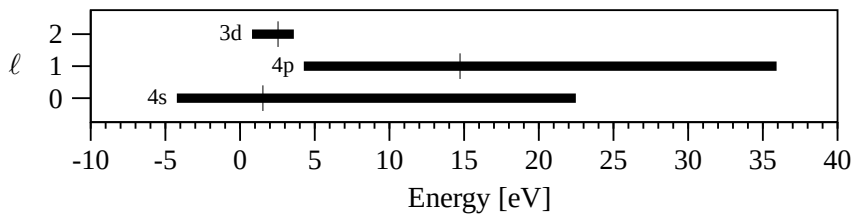

Figure 3.9: Magnification from Fig. 3.6, showing the position of the relevant non-hybridized bands according to the Wigner-Seitz rule.

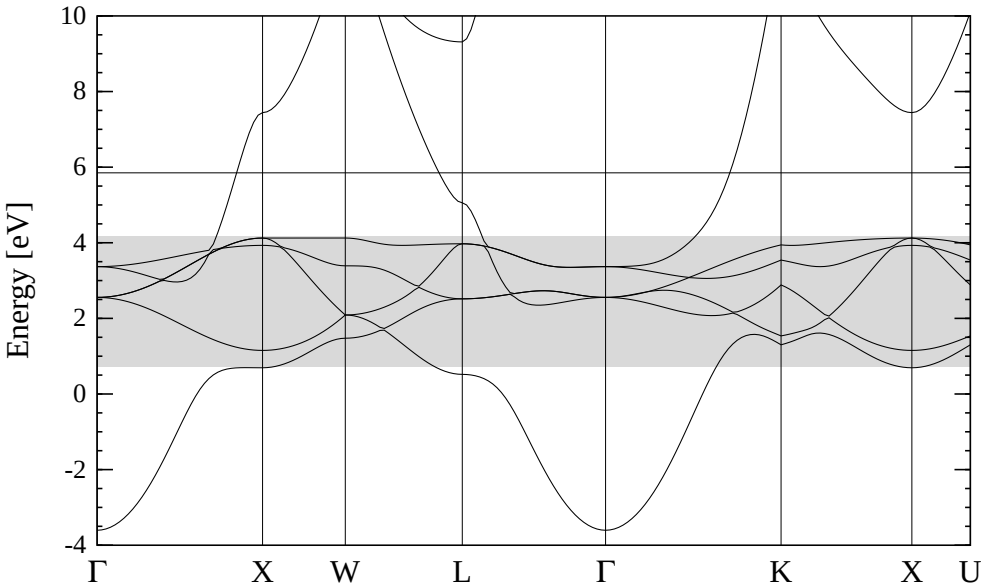

Figure 3.10: Converged Hartree band structure for copper. The Fermi energy is indicated by the line at $E_F = 5.85$ eV. The d-like bands occupy the shadowed region whose width is about 3.5 eV.

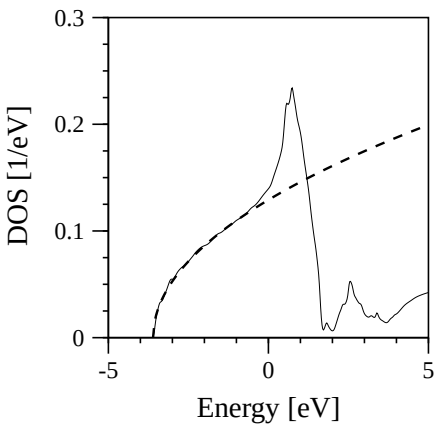

Figure 3.11: Comparison of the free electron DOS (3.51) (dashed) to the lower end of the s-projected density of states from Fig. 3.8.

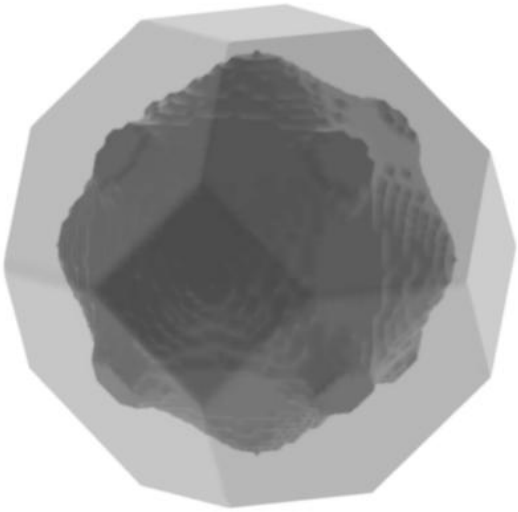

Figure 3.12: Brillouin zone and Fermi surface of copper from an LDA rather than a Hartree calculation. However, the difference between LDA and Hartree is not very significant. Eight necks reach out and connect the Fermi surface in the Brillouin zone to the next Fermi surfaces translated by $\mathbf{G}$. The resulting Fermi surface (over all $\mathbf{k}$-space) is sometimes called "jungle gym".

The Fermi surface is a surface in $\mathbf{k}$-space of constant energy, the Fermi energy. This surface is shown in Fig. 3.12 for the Brillouin zone. The surface divides the Brillouin zone into two regions. For copper, these are regions given by the condition whether the 5th band (starting at 0 from the bottom) is below or above the Fermi level. Inside the surface,[29] the 5th band is below E_F; outside the surface the 5th band is above E_F. Since at the L-point the 5th band is below E_F, eight so-called "necks" reach out around the L-point, and its symmetry related $\mathbf{k}$-points, which connect the Fermi surface in the Brillouin zone to the next Fermi surfaces translated by $\mathbf{G}$ [since $E_n(\mathbf{k}) = E_n(\mathbf{k} + \mathbf{G})$].

[29] Hereby, we mean the region where for instance the Γ and L-point are located.

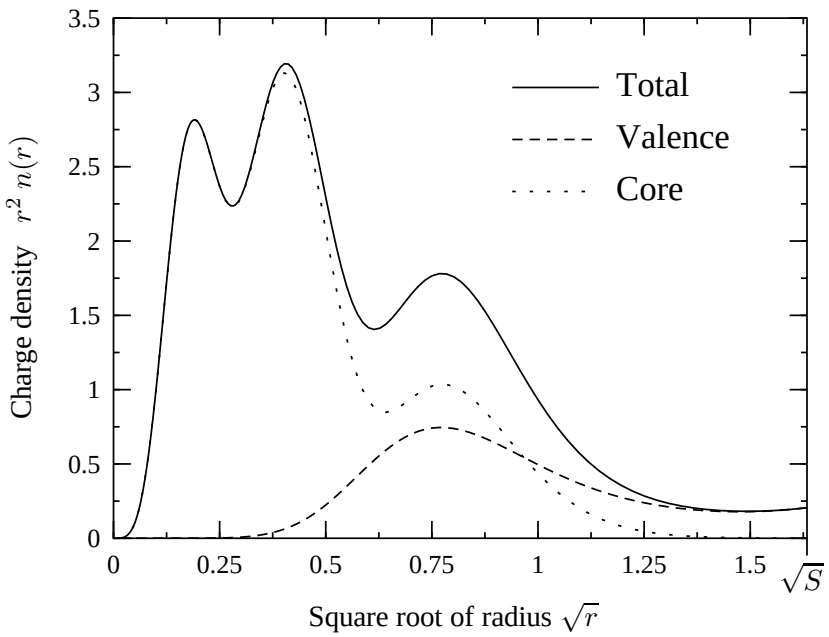

Figure 3.13: Charge densities (total in terms of both spins) for copper. Both the x and y-scale are the same in Ref. [49], to make a comparison easier.

3.5.4 Charge Density

In order to evaluate the Hartree potential (3.47), the knowledge of the total charge density, for some given effective potential, is required since self-consistency has to be achieved. We consider the (self-consistent) charge density now. The total charge density is given by the (frozen) core plus the valence charge density. It is not surprising that, as shown in Fig. 3.13, the total charge density is dominated by the core charge density close to the nucleus, while the valence charge density dominates near the boundary of the Wigner-Seitz sphere S.

The valence charge density may be decomposed into its angular momentum components. By means of (3.33), the spherically averaged ℓ-decomposed valence charge density $n_\ell(r)$ (per spin) is given by

$$4\pi\, n_\ell(r) = \phi^2_{\nu\ell}(r) M_{\ell 0} + 2\phi_{\nu\ell}(r)\dot{\phi}_{\nu\ell}(r) M_{\ell 1} + \left[\dot{\phi}^2_{\nu\ell}(r) + \phi_{\nu\ell}(r)\ddot{\phi}_{\nu\ell}(r)\right] M_{\ell 2} \ , \quad (3.53)$$

such that the total valence charge density is $\sum_\ell n_\ell(r)$. The valence ℓ-charge densities are shown in Fig. 3.14. The valence d-charge is dominating the total valence charge density, since the moment M_{d0} is much larger than M_{s0} and M_{p0}, and not because $\phi_{\nu d}(r)$ is larger than the s and p-radial functions which are normalized per construction, see Eq. (3.22). Also note that only the first term in (3.53) contributes to the net charge.

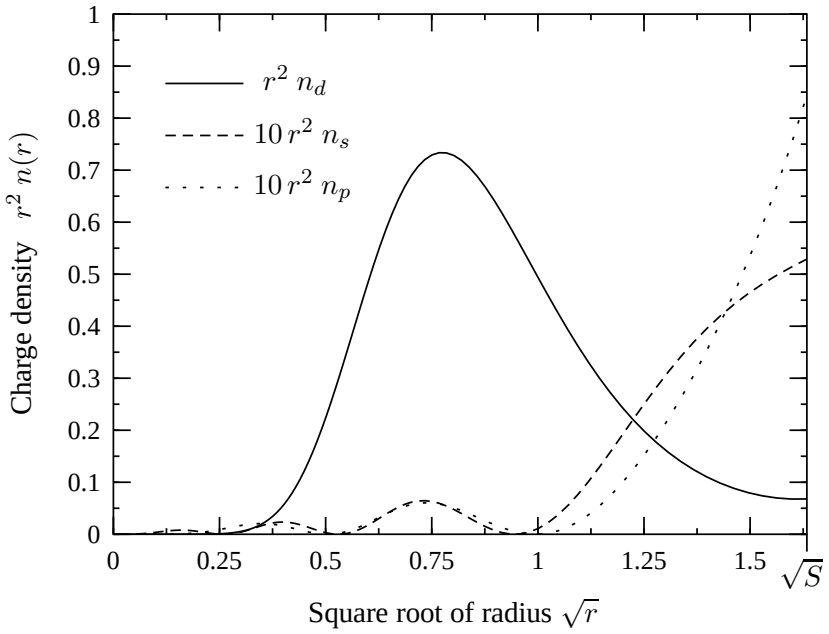

Figure 3.14: Valence charge densities decomposed into their angular momentum components. The s and p-charge densities are multiplied with a factor of 10 (in order to display all l-charge densities in one figure).

Let us take a look at the moments:

$M_{\ell q}$ [Ryd^q]	$q = 0$	$q = 1$	$q = 2$
$l = 0$	3.492973e-01	2.527169e-08	9.068678e-03
$l = 1$	3.584207e-01	2.847762e-08	8.239024e-03
$l = 2$	4.792282e+00	-8.686223e-08	2.780522e-02

We have deliberately left the output from our computer code unchanged to demonstrate the precision of our calculation. These are moments for one spin direction, hence (see (3.35)) the column $q = 0$ adds to 5.5, since there are 11 valence electrons in copper. Next, we see that the $q = 1$ moments are almost zero, which they should, since when we perform self-consistent calculations, the $E_{\nu\ell}$ are chosen in the center of the occupied part of the ℓ-band. For these we find:

$$E_{\nu s} = 0.33 \text{ eV} \quad , \quad E_{\nu p} = 2.34 \text{ eV} \quad , \quad E_{\nu d} = 2.79 \text{ eV} \tag{3.54}$$

One may take a look at these numbers in connection with Figs. 3.10 and 3.8 to see where the center of the ℓ-bands are. Note that e.g. the center of the d-band is not the center of the shadowed region in Fig. 3.10, i.e. 2.45 eV which is too low. From Fig. 3.8, we see that the center of the d-band is actually higher since the d-DOS is skewed to the left, and the center is defined via the first moment. Even from the non-hybridized bands in Fig. 3.9, we see that the center of the d-band is above the middle of the band.

Chapter 4

Wannier Functions

As we will see in chapter 5, the non-interacting part of the Hamiltonian H_0 becomes diagonal (see (5.9)) when the field operator is expanded in terms of Bloch orbitals. The drawback of using Bloch orbitals in this expansion is their non-localized nature, which makes the evaluation of matrix elements a difficult task. The set of Bloch orbitals can be transformed into a set of localized orthonormal Wannier orbitals spanning the same space. We construct these localized Wannier functions by using a method proposed by Marzari and Vanderbilt.

4.1 Preliminaries

The Wannier functions [29] are defined in terms of the Bloch functions $\psi_{n\mathbf{k}}(\mathbf{r})$ as

$$|\mathbf{R}n\rangle = \frac{\Omega}{(2\pi)^3} \int\limits_{\mathrm{BZ}} d^3\mathbf{k}\, e^{-i\mathbf{k}\mathbf{R}} |\psi_{n\mathbf{k}}\rangle \ , \tag{4.1}$$

so that

$$|\psi_{n\mathbf{k}}\rangle = \sum_{\mathbf{R}} e^{i\mathbf{k}\mathbf{R}} |\mathbf{R}n\rangle \ . \tag{4.2}$$

Here, as usual, Ω is the volume of the real-space primitive cell. It is easily shown that the Wannier functions form an orthonormal set, i.e. $\langle \mathbf{R}_1 n | \mathbf{R}_2 m\rangle = \delta_{\mathbf{R}_1,\mathbf{R}_2}\delta_{n,m}$ as well as $\sum_{\mathbf{R}n} |\mathbf{R}n\rangle\langle\mathbf{R}n| = \mathbf{1}$. Since our Bloch functions are represented on a mesh of $\mathbf{k}$-points, we substitute the integral by a sum over these $\mathbf{k}$-points, i.e. $\Omega(2\pi)^{-3}\int d\mathbf{k} \rightarrow 1/N \sum_{\mathbf{k}}$, and write (4.1) as:

$$w_{\mathbf{R}n}(\mathbf{r}) \equiv \langle \mathbf{r}|\mathbf{R}n\rangle = \frac{1}{N}\sum_{\mathbf{k}} e^{-i\mathbf{k}\mathbf{R}} \psi_{n\mathbf{k}}(\mathbf{r}) \tag{4.3}$$

Here, N is the number of $\mathbf{k}$-mesh points in the Brillouin zone or, equivalently, the number of unit cells in the real space supercell that is used to discretize the $\mathbf{k}$-mesh. From (4.3) and (3.4) it is evident, that:

$$w_{\mathbf{0}n}(\mathbf{r}-\mathbf{R}) = \frac{1}{N}\sum_{\mathbf{k}} \psi_{n\mathbf{k}}(\mathbf{r}-\mathbf{R}) = \frac{1}{N}\sum_{\mathbf{k}} e^{-i\mathbf{k}\mathbf{R}} \psi_{n\mathbf{k}}(\mathbf{r}) = w_{\mathbf{R}n}(\mathbf{r}) \tag{4.4}$$

Hence, it is sufficient to consider the Wannier function $w_{\mathbf{0}n} \equiv w_n$ and its periodic images (translated functions).

4.1.1 ASA Wave Functions

From Bloch's theorem (3.4), we see that Bloch functions obey:

$$\psi_{n\mathbf{k}}(\mathbf{r}+\mathbf{R}) = e^{i\mathbf{k}\mathbf{R}}\psi_{n\mathbf{k}}(\mathbf{r}) \tag{4.5}$$

The knowledge of a Bloch function in a single muffin tin sphere is sufficient for the knowledge of the function in the whole crystal. This situation is different when we consider Wannier functions, which can be centered on different sites. Hence, it is useful to introduce a notation that holds for both Bloch and Wannier functions. To do this, we perform an expansion like (3.28) in each muffin tin sphere which we label by its site vector $\mathbf{R}$. The complete wave function (either Bloch or Wannier) is then given by:

$$\Phi_\alpha(\mathbf{r}) = \sum_i \Phi_\alpha(\mathbf{R}_i; \mathbf{r}-\mathbf{R}_i) \tag{4.6}$$

Here, we have used the general notation for the wave function expansion $\Phi_\alpha(\mathbf{R}; \mathbf{r}-\mathbf{R})$ such that:

i.) Φ is any kind of wave function.

ii.) The α stands for quantum numbers (Bloch: $\alpha = \{n\mathbf{k}\}$; Wannier: $\alpha = \{\mathbf{R}n\}$).

iii.) The first argument in the parenthesis indicates the muffin-tin sphere about which we are expanding and is labeled by its site vector.

iv.) The second argument in the parenthesis is the position inside this muffin-tin sphere described by its relative vector. This means that this vector has zero length in the center of the muffin-tin sphere described by the first argument.

v.) Note that for every $\mathbf{R}$: $\quad \Phi_\alpha(\mathbf{R}; \mathbf{r}) = 0 \quad \text{if} \;\; |\mathbf{r}| > S$

In the case where Φ is a Bloch function, we find

$$\psi_{n\mathbf{k}}(\mathbf{R}; \mathbf{r}) = e^{i\mathbf{k}\mathbf{R}}\psi_{n\mathbf{k}}(\mathbf{r}) \; . \tag{4.7}$$

It is easy to see that (4.7) inserted into (4.6) obeys (4.5). We now derive an expression of the form of (4.6) for Wannier functions w_n. From (4.7) and (4.3) we have

$$w_{\mathbf{R}n}(\mathbf{R}'; \mathbf{r}) = \frac{1}{N}\sum_{\mathbf{k}} e^{-i\mathbf{k}\mathbf{R}}\psi_{n\mathbf{k}}(\mathbf{R}'; \mathbf{r}) = \frac{1}{N}\sum_{\mathbf{k}} e^{i\mathbf{k}(\mathbf{R}'-\mathbf{R})}\psi_{n\mathbf{k}}(\mathbf{r}) \; . \tag{4.8}$$

Again, we realize that Wannier functions on different sites have the same form (shape) of their wave functions and differ only by a translation of their origin. For $\mathbf{R} = \mathbf{0}$ equation (4.8) reduces to:

$$w_n(\mathbf{R}; \mathbf{r}) = \frac{1}{N}\sum_{\mathbf{k}} e^{i\mathbf{k}\mathbf{R}}\psi_{n\mathbf{k}}(\mathbf{r}) \tag{4.9}$$

Note that, again, $|\mathbf{r}| < S$. We will later find an expansion like (3.28) in each muffin tin sphere at site $\mathbf{R}$ in order to numerically deal with Wannier functions. Also, we will force the "center" site of the Wannier function w_n, i.e. the site where $w_n(\mathbf{R};\mathbf{r})$ is largest to be the site $\mathbf{R} = \mathbf{0}$.

4.1.2 Isolated and Composite Bands

Isolated bands: A Bloch band is said to be "isolated" if it does not become degenerate with any other band anywhere in the Brillouin zone. In the case of isolated bands, it is natural to define Wannier functions individually for each band. That is, the Wannier function for band n (together with its periodic images) spans the same Hilbert space as does the isolated Bloch band.

Composite bands: Conversely, a group of bands is said to form a "composite group" (or "composite set") if the bands are connected among themselves by degeneracies, but are isolated from all lower or higher bands. In the case of composite bands, however, it is more natural to consider a set of J "generalized Wannier functions" that (together with their periodic images) spans the same Hilbert space as the composite set of J Bloch bands. That is, the "generalized Bloch functions" $\psi_{n\mathbf{k}}$ which are connected with the nth generalized Wannier function will not necessarily be eigenstates of the Hamiltonian at this $\mathbf{k}$, but will be related to them by a $J \times J$ unitary transformation. The terms "Bloch function" and "Wannier function" should be understood in the generalized sense.

4.1.3 Gauge Freedom

As is well known, Wannier functions are not unique. For a single isolated band, the freedom in choice of the Wannier functions corresponds to the freedom in the choice of the phases of the Bloch orbitals as a function of wave vector $\mathbf{k}$. Thus, given one set of Bloch orbitals and associated Wannier functions, another equally good set is obtained from[1]

$$|\psi_{n\mathbf{k}}\rangle \;\rightarrow\; e^{i\phi_n(\mathbf{k})}|\psi_{n\mathbf{k}}\rangle \;, \tag{4.10}$$

where ϕ_n is a real function of $\mathbf{k}$. We call this a gauge transformation of the first kind. In the case of a composite set of bands, this non-uniqueness corresponds to the freedom to mix the bands at each $\mathbf{k}$ vector:

$$|\psi_{n\mathbf{k}}\rangle \;\rightarrow\; \sum_m U^{\mathbf{k}}_{mn}\,|\psi_{m\mathbf{k}}\rangle \tag{4.11}$$

We call this a gauge transformation of the second kind. Here, $U^{\mathbf{k}}_{mn}$ is a unitary matrix. Equation (4.10) can be regarded as a special case of (4.11) that results when the U's are chosen to be diagonal.

The goal will be to pick out, from all the many arbitrary choices of Wannier functions, the particular set that is maximally localized according to some criterion. Nevertheless, the particular set of Wannier functions will, of course, remain arbitrary:

[1] Note that Bloch orbitals are defined via (3.3), thus the phase is arbitrary.

i.) There will always be an arbitrary overall phase of each of the J Wannier functions.

ii.) There is a freedom to permute the J Wannier functions among themselves.

iii.) There is a gauge freedom to translate any one of the J Wannier functions by a lattice vector. That is, to decide which Wannier functions belong to the "home" unit cell labeled by site $\mathbf{0}$.

4.2 Marzari-Vanderbilt Method

We use a method, proposed by Marzari and Vanderbilt [33], for determining a "maximally-localized" set of Wannier functions associated with a set of Bloch bands. The method minimizes a functional that represents the total spread $\sum_n(\langle r^2\rangle_n - \langle \mathbf{r}\rangle_n^2)$ of the Wannier functions in real space, proceeds directly from the Bloch functions as represented on a mesh of $\mathbf{k}$-points, and carries out the minimization in a space of unitary matrices $U^{\mathbf{k}}_{mn}$ describing the rotation among the Bloch bands at each $\mathbf{k}$-point. We will now briefly describe the method and its connection with the LMTO-ASA method. For further details about the method, we recommend the excellent paper [33] and also Ref. [47]. Finally, we will be able to write down Wannier functions in LMTO-ASA fashion, i.e. as a linearized spherical expansion around each muffin tin sphere.

4.2.1 Spread Functional

A measure of the total delocalization or spread of the Wannier functions is given by the so-called spread functional

$$\Omega = \sum_n \langle \big(\mathbf{r} - \langle \mathbf{r}\rangle_n\big)^2\rangle_n = \sum_n \left[\langle \mathbf{r}^2\rangle_n - \langle \mathbf{r}\rangle_n^2\right] \ . \tag{4.12}$$

For any operator A, $\langle A\rangle_n$ denotes the expectation value $\langle \mathbf{0}n|A|\mathbf{0}n\rangle$. Other localization criteria have also been proposed but this functional leads to a particularly elegant formalism, allowing, for example, the decomposition into invariant, diagonal, and off-diagonal contributions:

$$\Omega = \underbrace{\sum_n \left[\langle r^2\rangle_n - \sum_{\mathbf{R}m} \left|\langle \mathbf{R}m|\mathbf{r}|\mathbf{0}n\rangle\right|^2\right]}_{\Omega_{\mathrm{I}}} + \underbrace{\sum_n \sum_{\mathbf{R}m\neq\mathbf{0}n} \left|\langle \mathbf{R}m|\mathbf{r}|\mathbf{0}n\rangle\right|^2}_{\widetilde{\Omega}} \tag{4.13}$$

The first term is "gauge-invariant", i.e. independent of the choice of unitary transformations among the bands. For later reference, it is useful to decompose the second term into band-off-diagonal and band-diagonal pieces:

$$\widetilde{\Omega} = \underbrace{\sum_{m\neq n} \sum_{\mathbf{R}} \left|\langle \mathbf{R}m|\mathbf{r}|\mathbf{0}n\rangle\right|^2}_{\Omega_{\mathrm{OD}}} + \underbrace{\sum_n \sum_{\mathbf{R}\neq\mathbf{0}} \left|\langle \mathbf{R}n|\mathbf{r}|\mathbf{0}n\rangle\right|^2}_{\Omega_{\mathrm{D}}} \tag{4.14}$$

The expressions for Ω are of little use for us since we wish to find the unitary matrices $U^{\mathbf{k}}_{mn}$ on a discretized $\mathbf{k}$-mesh. This mesh is chosen to be simple cubic, and $\mathbf{b}$ are vectors connecting each $\mathbf{k}$-point to its nearest neighbors. We should mention that the construction of such a mesh is not as trivial as it may seem at first sight, since we have to make sure that $\sum_{\mathbf{k}} e^{i\mathbf{kR}} = N\delta_{\mathbf{R},\mathbf{0}}$. This condition imposes that we have to be careful not to double count $\mathbf{k}$-points at the boundary of the Brillouin zone. A description of how this is done can be found in Ref. [47]. We define

$$M^{\mathbf{k},\mathbf{b}}_{mn} = \langle u_{m\mathbf{k}} | u_{n,\mathbf{k}+\mathbf{b}} \rangle \ , \tag{4.15}$$

where $u_{n\mathbf{k}}$ is related to $\psi_{n\mathbf{k}}$ via (3.4), which turn out to be important quantities. Using (4.15), we find expressions for the expectation values of $\mathbf{r}$ and r^2 (see Ref. [33]):

$$\langle \mathbf{r} \rangle_n = -\frac{1}{N} \sum_{\mathbf{k},\mathbf{b}} w_b \mathbf{b} \mathrm{Im} \ \ln M^{\mathbf{k},\mathbf{b}}_{nn} \qquad w_b = \frac{1}{2b^2} \tag{4.16}$$

$$\langle r^2 \rangle_n = \frac{1}{N} \sum_{\mathbf{k},\mathbf{b}} w_b \left\{ [1 - |M^{\mathbf{k},\mathbf{b}}_{nn}|^2] + [\mathrm{Im} \ \ln M^{\mathbf{k},\mathbf{b}}_{nn}]^2 \right\} \tag{4.17}$$

We should note that these expressions are not unique. This non-uniqueness arises from the fact that it is *only* required that these expectation values become exact in the limit of a dense mesh spacing, i.e. $N \to \infty$ and $b \to 0$. Marzari and Vanderbilt have carefully chosen these expressions this way, since they insisted on a desirable property: When a gauge transformation is performed that move the Wannier functions by a lattice site $\mathbf{R}$, one should find

$$\begin{aligned} |u_{n\mathbf{k}}\rangle &\to e^{-i\mathbf{kR}} |u_{n\mathbf{k}}\rangle \\ \langle \mathbf{r} \rangle_n &\to \langle \mathbf{r} \rangle_n + \mathbf{R} \\ \langle r^2 \rangle_n &\to \langle r^2 \rangle_n + 2\langle \mathbf{r} \rangle_n \mathbf{R} + R^2 \ , \end{aligned} \tag{4.18}$$

so that Ω remains unchanged. The expressions (4.16,4.17) obey condition (4.18) while still being exact in the continuum limit. We find expressions for $\Omega = \Omega_{\mathrm{I}} + \Omega_{\mathrm{OD}} + \Omega_{\mathrm{D}}$:

$$\begin{aligned} \Omega_{\mathrm{I}} &= \frac{1}{N} \sum_{\mathbf{k},\mathbf{b}} w_b \left(\mathrm{Tr}\, \mathbf{1} - \sum_{mn} |M^{\mathbf{k},\mathbf{b}}_{nn}|^2 \right) \\ \Omega_{\mathrm{OD}} &= \frac{1}{N} \sum_{\mathbf{k},\mathbf{b}} w_b \sum_{m \neq n} |M^{\mathbf{k},\mathbf{b}}_{mn}|^2 \\ \Omega_{\mathrm{D}} &= \frac{1}{N} \sum_{\mathbf{k},\mathbf{b}} w_b \sum_{n} \left(-\mathrm{Im} \ \ln M^{\mathbf{k},\mathbf{b}}_{nn} - \mathbf{b} \langle \mathbf{r} \rangle_n \right)^2 \end{aligned} \tag{4.19}$$

Note that the trace $\mathrm{Tr}\, \mathbf{1}$ equals the number of bands J. When the steepest-descent cycle (see below) is performed, it is a good idea to keep an eye on Ω_{I} and make sure that it does not change and that $\Omega_{\mathrm{OD}} + \Omega_{\mathrm{D}}$ decreases. However, note that Ω_{D} and Ω_{OD} *individually* do not need to decrease.

4.2.2 Gradient of Spread Functional

We consider the first-order change in Ω arising from an infinitesimal gauge transformation (4.11):

$$U^{\mathbf{k}}_{mn} = \delta_{mn} + dW^{\mathbf{k}}_{mn} \tag{4.20}$$

In order that $U^{\mathbf{k}}$ is unitary, we have to require that dW is anti-hermitian ($dW^{\dagger} = -dW$). Inserting (4.20) into (4.11) yields:

$$|u_{n\mathbf{k}}\rangle \;\; \rightarrow \;\; |u_{n\mathbf{k}}\rangle + \sum_m dW^{\mathbf{k}}_{mn} |u_{m\mathbf{k}}\rangle \tag{4.21}$$

Using the above formalism, Marzari and Vanderbilt have found an expression for the gradient of the spread functional:

$$G^{\mathbf{k}}_{nm} = \frac{d\Omega}{dW^{\mathbf{k}}_{mn}} = \left(\frac{d\Omega}{dW^{\mathbf{k}}}\right)_{nm} \qquad G^{\mathbf{k}} = \frac{d\Omega}{dW^{\mathbf{k}}} \tag{4.22}$$

We will not write down the entire expression but mention that only the matrices $M^{\mathbf{k},\mathbf{b}}_{nm}$ enter this expression. To see this, we realize that (4.21) establishes a relation between dW and dM which becomes obvious when writing (4.21) in connection with its version for $\langle u_{n\mathbf{k}}|$. Hence, dW and $d\Omega$ (and therefore also $G^{\mathbf{k}}$) are entirely given by $M^{\mathbf{k},\mathbf{b}}_{nm}$.

4.2.3 Algorithm

The method now uses a steepest-descent minimization in order to minimize the spread functional. We make small updates of the matrices $U^{\mathbf{k}}$ choosing

$$dW^{\mathbf{k}} = \epsilon\, G^{\mathbf{k}} \;\; . \tag{4.23}$$

It can easily be shown that $d\Omega < 0$, i.e. it is guaranteed that Ω is reduced. In practice, we take a fixed finite step ϵ. The wavefunctions are then updated according to the matrix $\exp[\Delta W^{\mathbf{k}}]$, which is unitary because ΔW is anti-hermitian. It should be noted that the evolution towards the minimum requires only the relatively inexpensive updating of the unitary matrices, and *not* of the wavefunctions. The matrices $M^{\mathbf{k},\mathbf{b}}_{nm}$ only need to be evaluated once during the initialization of the cycle. The Algorithm is:

Initialization: $N = 0$

$$U^{(0)\mathbf{k}}_{mn} = \delta_{mn} \tag{4.24}$$

$$M^{(0)\mathbf{k},\mathbf{b}}_{mn} = \langle u_{m\mathbf{k}} | u_{n,\mathbf{k}+\mathbf{b}} \rangle \tag{4.25}$$

Cycle: $N = 1, 2, 3 \ldots$

$$U^{(N)\mathbf{k}} = U^{(N-1)\mathbf{k}} \; \exp\left[\Delta W^{\mathbf{k}}(M^{(N-1)\mathbf{k},\mathbf{b}})\right] \tag{4.26}$$

$$M^{(N)\mathbf{k},\mathbf{b}} = U^{(N)\mathbf{k}\,\dagger} \, M^{(N-1)\mathbf{k},\mathbf{b}} \, U^{(N)\mathbf{k}+\mathbf{b}} \tag{4.27}$$

This algorithm can almost be considered as a “black box” since the *only* input are the initializing $M^{(0)\mathbf{k},\mathbf{b}}_{mn}$, and once convergence is achieved, the $U^{\mathbf{k}}_{mn}$ are the *only* output.

Applying these $U^{\mathbf{k}}_{mn}$ to the original Bloch orbitals will yield (generalized) Bloch orbitals which, when used in (4.1), will result in maximally localized Wannier functions.

4.2.4 Application

Before minimizing Ω according to this procedure, it is useful to prepare the Bloch orbitals to make the starting Wannier functions somewhat localized. This has two advantages: (i) the minimization procedure converges faster, and (ii) this helps to avoid getting trapped in local minima. Marzari and Vanderbilt suggest several possible preparations. We have found our own method, which seems to work well. This involves a simple gauge transformation for each Bloch band (4.10) which is given by

$$\psi_{n\mathbf{k}}(\mathbf{r}) \;\rightarrow\; \exp\big[-i\,\mathrm{Im}\,\ln\psi_{n\mathbf{k}}(\mathbf{r}_n)\big]\psi_{n\mathbf{k}}(\mathbf{r})\;. \tag{4.28}$$

This gauge transformation has the property that $\mathrm{Im}\ \ln\Psi_{n\mathbf{k}}(\mathbf{r}_n)$ transforms to zero. So at the point $\mathbf{r}_n$, all the Bloch functions will have the same phase (in this case just $1+i0$) and $\langle\mathbf{r}_n|\mathbf{0}n\rangle$ will take a large value. We thus expect the Wannier function to be fairly localized at $\mathbf{r}_n$. To make the method work well, one should choose $\mathbf{r}_n$ where the Wannier functions are expected to be reasonably large. In our calculations, we have chosen this vector to be well away from the expected zeroes of the spherical harmonics and with an absolute value far enough away from the origin to be in a place where the Wannier functions should have a significant magnitude. Also note that we have chosen $\mathbf{r}_n$ individually for each Bloch band n, since we expect the optimally localized Wannier functions to be localized in different regions. We have found that the minimization procedure converges slower when all the $\mathbf{r}_n$ are equal.

In the procedure of Marzari and Vanderbilt, the starting point for the calculation is a set of reference matrices defined by (4.25):

$$M_{mn}^{(0)\mathbf{k},\mathbf{b}} = \langle u_{m\mathbf{k}}|u_{n,\mathbf{k}+\mathbf{b}}\rangle = \langle\psi_{m\mathbf{k}}|e^{-i\mathbf{b}\mathbf{r}}|\psi_{n,\mathbf{k}+\mathbf{b}}\rangle \tag{4.29}$$

We calculate the product of $e^{-i\mathbf{b}\mathbf{r}}$ with the last wave function $|\psi_{n,\mathbf{k}+\mathbf{b}}\rangle$ by using (C.26), (C.25) and solve the remaining integral by using (5.19) inside one atomic sphere. We use a uniform (simple cubic) discrete $\mathbf{k}$-mesh with a spacing of $\Delta k = 0.2\ (2\pi/a)$, i.e. in the case of FCC, we have 500 points in Brillouin zone (for BCC 250). In such a mesh, there are 6 nearest neighbors for the $\mathbf{b}$-vectors needed for the numerical derivatives. We note that the reference matrices obey $M_{mn}^{\mathbf{k},\mathbf{b}} = M_{nm}^{\mathbf{k}+\mathbf{b},-\mathbf{b}\,*}$, hence, e.g. for FCC and a set of 9 composite bands, we need to evaluate $3\cdot 500\cdot 9^2 = 121,500$ complex numbers. For the step size (see Eq. (57) in Ref. [33]), we use $\alpha = 0.4$.

The final result can be written in a form similar to the LMTO wave functions (3.28). Following the notation of section 4.1.1, we find

$$w_n(\mathbf{R};\mathbf{r}) = \sum_L \Big\{\phi_{\nu\ell}(r)A_L^{\mathbf{R}n} + \dot{\phi}_{\nu\ell}(r)B_L^{\mathbf{R}n}\Big\}\,Y_L(\hat{\mathbf{r}})\;, \tag{4.30}$$

where the $A_L^{\mathbf{R}n}$ and $B_L^{\mathbf{R}n}$ originally come from the LMTO wave functions, i.e. $A_L^{n\mathbf{k}}$ and $B_L^{n\mathbf{k}}$, but are then updated from all the relevant phase information (4.28), (4.9) and unitary matrices (4.11).

Because of the normalization of the starting LMTO Bloch wave functions (which are normalized to unity within a single unit cell), each Wannier function is naturally normalized to unity when integrated over all space.

4.3 Properties

Continuing our example from section 3.5, we now explore some properties of maximally localized Wannier functions of copper constructed from an effective Hartree potential. We consider two types of treatment:

Composite treatment: As seen from Fig. 3.10, the valence bands are connected among themselves by degeneracies, hence it is only natural to consider all bands as a composite set of bands, i.e. perform the Marzari-Vanderbilt method for this set of bands. Since we take $4s$, $4p$ and $3d$ orbitals into account, we consider a composite group of 9 bands. Physically, this composite group is not isolated because it is connected to an infinite number of bands in the continuum. These bands have been neglected, since they do not contribute to the electronic charge density. But only *all* these generalized Wannier functions (plus the core orbitals) span the complete one-particle Hilbert space. Thus, we make an approximation at this point. This approximation was not important in section 3.5. We will have to consider this approximation again in chapter (5) when we expand field operators in terms of generalized Wannier functions.

Isolated treatment: We might as well consider the 9 composite Bloch bands individually, i.e. perform the Marzari-Vanderbilt method for each Bloch band, as if all bands are isolated. Here, the order of Bloch bands is (for instance) determined by $E_n(\mathbf{k}) \leq E_{n+1}(\mathbf{k})$ and no unitary gauge transformations of the second kind (4.11) are involved. One may argue that this is not the natural treatment, however, this is only a special case of the composite treatment in which the unitary matrices are chosen to be diagonal. There is nothing wrong in doing this, we just don't allow all the gauge freedom available. The Wannier functions we obtain are as arbitrary as the Wannier functions we obtain using the composite treatment, but, as we have found out, not quite as localized. We are not able to obtain maximally-localized Wannier functions (in their original sense) using the isolated treatment.

In this connection it should be noted that, using the composite treatment, we don't obtain maximally-localized functions (in their original sense) either, since we restrict ourselves to 9 bands (out of an infinite number of bands). This is just another consequence of the approximation we make.

We look at localization properties first, in addition, we wish to present Wannier function projected density of states, i.e. inserting a projection operator onto Wannier states into (3.37). In each of the following (sub) sections, we take a look at the theory in general first, followed by results for the composite and isolated treatment for the bands of copper (constructed from the effective Hartree potential).

4.3.1 Localization of Wannier Functions

Having obtained all expressions in (4.30), i.e. $A_L^{n\mathbf{R}}$, $B_L^{n\mathbf{R}}$ and the radial wave functions which we have already obtained from the LMTO method, we can look at the portions of the

Wannier functions[2] in different muffin-tin spheres centered at $\mathbf{R}$. That is,

$$\langle w_n|w_n\rangle_{\mathbf{R}} \equiv \int\limits_{\mathbf{R}} d^3\mathbf{r}|w_n(\mathbf{r})|^2 = \int\limits_{\mathbf{0}} d^3\mathbf{r}|w_n(\mathbf{R};\mathbf{r})|^2 \quad , \tag{4.31}$$

where the integrals are understood to be taken over the MT sphere at the site indicated. Inserting (4.30) into (4.31) yields

$$\langle w_n|w_n\rangle_{\mathbf{R}} = \sum_{\ell} \underbrace{\sum_{m=-\ell}^{\ell} \left\{ |A_{\ell m}^{\mathbf{R}n}|^2 + \langle \dot{\phi}_{\nu\ell}^2\rangle |B_{\ell m}^{\mathbf{R}n}|^2 \right\}}_{\equiv C_{\ell}^{\mathbf{R}n}} = \sum_{\ell} C_{\ell}^{n\mathbf{R}} \quad . \tag{4.32}$$

Introducing $C_{\ell}^{\mathbf{R}n}$, i.e. the ℓ-portion of the Wannier function n in the MT at site $\mathbf{R}$. The $C_{\ell}^{\mathbf{R}n}$ are the analog of $C_{\ell}^{n\mathbf{k}}$, defined in (3.29).

Composite treatment:

Table 4.1 shows the $C_{\ell}^{\mathbf{R}n}$ and there are some points worth mentioning:

i.) As mentioned earlier, there exists gauge freedom to permute the Wannier functions among themselves. Hence, there is no physical meaning associated with the index n of a Wannier function n, not in terms of energy or any other quantity.

ii.) Wannier functions with high total d-character (third row, last column) are more localized than Wannier functions with smaller d-character. States 0 thru 4, in particular 2 and 3, have the highest d-character and also the highest localization, while 5 thru 8 have more s and p-character and are less localized.

iii.) It is interesting to see that states 5 thru 8, which have small *total* d-character, have a large d-character in their next neighbor spheres (third row, second column).

iv.) One should not be fooled into thinking that the Wannier functions themselves decrease as rapidly as Tab. (4.1) suggests. The $C_{\ell}^{\mathbf{R}n}$'s are averaged densities and contain the square of the wave functions.

v.) All values are given to 4 decimal places, however, these numbers were numerically obtained using double precision.[3] Hence, the rows and columns may not add up exactly to the values shown.

Isolated treatment:

Without showing a big table, we state that this treatment leads to much less localized Wannier functions. For example, $\langle w_n|w_n\rangle_{\mathbf{0}} = \sum_{\ell} C_{\ell}^{\mathbf{0}n}$, i.e. the total portion in the "home" sphere, is only between 6% up to 19%, whereas in the composite treatment above this was never less than 88%. This was expected, since nine gauge transformations of the first kind (4.10) do not allow quite as much freedom as a single unitary gauge transformation. This treatment will become more interesting in the following (sub) section.

[2]The Wannier functions themselves are centered at $\mathbf{0}$, as usual.

[3]We always use double precision which corresponds to about 16 decimal places.

n	ℓ	$C_\ell^{\mathbf{0}n}$	$\sum_{\mathbf{R}}^{\dagger} C_\ell^{\mathbf{R}n}$	$\sum_{\mathbf{R}}^{\ddagger} C_\ell^{\mathbf{R}n}$	$\sum_{\mathbf{R}} C_\ell^{\mathbf{R}n}$
0	s	0.0019	0.0019	0.0001	0.0040
	p	0.1376	0.0037	0.0002	0.1416
	d	0.8330	0.0211	0.0004	0.8544
	$\sum$	0.9725	0.0267	0.0008	1.0000
1	s	0.0007	0.0015	0.0001	0.0024
	p	0.0956	0.0030	0.0002	0.0988
	d	0.8819	0.0166	0.0003	0.8988
	$\sum$	0.9782	0.0212	0.0006	1.0000
2	s	0.0001	0.0008	0.0000	0.0009
	p	0.0240	0.0016	0.0001	0.0257
	d	0.9655	0.0078	0.0001	0.9735
	$\sum$	0.9896	0.0102	0.0003	1.0000
3	s	0.0000	0.0008	0.0000	0.0008
	p	0.0250	0.0015	0.0001	0.0266
	d	0.9647	0.0078	0.0001	0.9726
	$\sum$	0.9897	0.0101	0.0003	1.0000
4	s	0.0018	0.0016	0.0001	0.0035
	p	0.0990	0.0031	0.0002	0.1023
	d	0.8767	0.0172	0.0003	0.8942
	$\sum$	0.9775	0.0219	0.0006	1.0000
5	s	0.2058	0.0073	0.0006	0.2137
	p	0.5473	0.0150	0.0010	0.5633
	d	0.1326	0.0889	0.0015	0.2230
	$\sum$	0.8857	0.1113	0.0031	1.0000
6	s	0.2122	0.0075	0.0006	0.2203
	p	0.5550	0.0153	0.0010	0.5713
	d	0.1164	0.0904	0.0015	0.2084
	$\sum$	0.8837	0.1132	0.0031	1.0000
7	s	0.2381	0.0076	0.0006	0.2463
	p	0.5527	0.0157	0.0010	0.5694
	d	0.0899	0.0928	0.0016	0.1843
	$\sum$	0.8807	0.1161	0.0032	1.0000
8	s	0.2212	0.0075	0.0006	0.2293
	p	0.5582	0.0155	0.0010	0.5746
	d	0.1027	0.0917	0.0016	0.1960
	$\sum$	0.8821	0.1147	0.0032	1.0000

Table 4.1: The $C_\ell^{\mathbf{R}n}$ for our set of maximally localized Wannier functions obtained from the Hartree calculation of copper. The sum $\sum_{\mathbf{R}}^{\dagger}$ includes only next neighbors, $\sum_{\mathbf{R}}^{\ddagger}$ includes second nearest neighbors and up. In the last column, the sum is not restricted, hence, the last column shows the total ℓ-character of the Wannier state n. The last row (for each n) shows the sum of the three values above. Thus, the value in the last row in the $C_\ell^{\mathbf{0}n}$ column is the total portion of the nth Wannier function in its "home" sphere, i.e. $\langle w_n | w_n \rangle_{\mathbf{0}}$.

4.3.2 Wannier Function Projected DOS

We have already discussed the ℓ-projected DOS in section 3.4.3, i.e. P in (3.39) is the projection operator onto the ℓ-component. Now, in complete analogy, we consider the projection operator onto Wannier states:[4]

$$N_{\mathbf{R}j}(E) = \frac{\Omega}{(2\pi)^3} \sum_n \int_{\mathrm{BZ}} d^3\mathbf{k}\, \langle \psi_{n\mathbf{k}} \underbrace{|\mathbf{R}j\rangle\langle\mathbf{R}j|}_{P_{\mathbf{R}j}} \psi_{n\mathbf{k}}\rangle \delta(E - E_n(\mathbf{k})) \tag{4.33}$$

Note that the $\psi_{n\mathbf{k}}$ in this formula have to be the Bloch states before the gauge transformation, since the band structure $E_n(\mathbf{k})$ is related to the untransformed states.

The Wannier states $|\mathbf{R}j\rangle$ span the same Hilbert space as the composite set of Bloch bands. In this (sub) Hilbert space we have completeness, i.e.:

$$\sum_{\mathbf{R}j} P_{\mathbf{R}j} = \sum_{\mathbf{R}j} |\mathbf{R}j\rangle\langle\mathbf{R}j| = \frac{\Omega}{(2\pi)^3} \sum_n \int_{\mathrm{BZ}} d^3\mathbf{k}\, |\psi_{n\mathbf{k}}\rangle\langle\psi_{n\mathbf{k}}| = \mathbf{1} \tag{4.34}$$

However, in (4.33) it is sufficient to only consider the Wannier states $|\mathbf{0}j\rangle$ in our projection and not all the $|\mathbf{R}j\rangle$, since

$$\langle\psi_{n\mathbf{k}}|P_{\mathbf{0}j}|\psi_{n\mathbf{k}}\rangle = \langle\psi_{n\mathbf{k}}|P_{\mathbf{R}j}|\psi_{n\mathbf{k}}\rangle \ , \tag{4.35}$$

which is easy to show from (4.1) and Bloch's theorem. Hence,

$$N_j(E) \equiv N_{\mathbf{0}j}(E) = N_{\mathbf{R}j}(E) \qquad \text{and} \qquad N(E) = \sum_j N_j(E) \ . \tag{4.36}$$

A not too surprising result, considering $|\mathbf{R}j\rangle$ are just periodic images of $|\mathbf{0}j\rangle$.

Again, we can use the tetrahedron method to calculate $N_j(E)$. However, this time the problem can not be reduced to the irreducible wedge of the Brillouin zone since in general P_j does not commute with the rotations α in the point group of the crystal. Thus:

$$N_j(E) = \frac{1}{\Omega_{\mathrm{BZ}}} \sum_{n,i} W_j^{n,i}\, N_{n,i}(E) \qquad \text{where} \quad W_j^{n\mathbf{k}} = \left|\langle\psi_{n\mathbf{k}}|\mathbf{0}j\rangle\right|^2 \tag{4.37}$$

As usual, $W_j^{n,i}$ is the average of the $W_j^{n\mathbf{k}}$ at the corners and the projected NOS is treated in complete analogy. It remains to obtain $W_j^{n\mathbf{k}}$. From (4.11) we have

$$|\mathbf{0}j\rangle = \frac{1}{N} \sum_{\mathbf{k}m} U_{mj}^{\mathbf{k}}\, |\psi_{m\mathbf{k}}\rangle \ , \tag{4.38}$$

such that[5]

$$\langle\psi_{n\mathbf{k}}|\mathbf{0}j\rangle = \frac{1}{N} \sum_{\mathbf{k}'m} U_{mj}^{\mathbf{k}'} \langle\psi_{n\mathbf{k}}|\psi_{m\mathbf{k}'}\rangle = \sum_{\mathbf{k}'m} U_{mj}^{\mathbf{k}'} \delta_{nm}\delta_{\mathbf{k}\mathbf{k}'} = U_{nj}^{\mathbf{k}} \ . \tag{4.39}$$

[4] Here we use the index j for Wannier functions and n is reserved for the band index of Bloch functions and Bloch eigenenergies. We consider the Wannier function projected DOS per spin, except when noted otherwise.

[5] Note that $\langle\psi_{n\mathbf{k}}|\psi_{n\mathbf{k}}\rangle = N$, since we normalize Bloch states to unity inside the atomic sphere.

Hence, we have

$$W_j^{n\mathbf{k}} = |U_{nj}^{\mathbf{k}}|^2 \ , \tag{4.40}$$

and the $U_{nj}^{\mathbf{k}}$ are known from the algorithm in section 4.2.3. Note that the $W_j^{n\mathbf{k}}$ add up to unity for each $n\mathbf{k}$ (as they should), since the matrices $U^{\mathbf{k}}$ are unitary:

$$\sum_j W_j^{n\mathbf{k}} = \sum_j U_{nj}^{\mathbf{k}} U_{nj}^{\mathbf{k}*} = (U^{\mathbf{k}} U^{\mathbf{k}\dagger})_{nn} = (\mathbf{1})_{nn} = 1 \tag{4.41}$$

Also note that, from the completeness of the Bloch functions (4.34), it follows that:

$$\int dE\ N_j(E) = \frac{\Omega}{(2\pi)^3} \sum_n \int_{\mathrm{BZ}} d^3\mathbf{k}\ \langle \mathbf{0}j|\psi_{n\mathbf{k}}\rangle\langle\psi_{n\mathbf{k}}|\mathbf{0}j\rangle = 1 \tag{4.42}$$

In other terms, the $W_j^{n\mathbf{k}}$ add up to unity for each j (expect for the factor N) too:

$$\frac{1}{N}\sum_{n\mathbf{k}} W_j^{n\mathbf{k}} = \frac{1}{N}\sum_{n\mathbf{k}} \langle \mathbf{0}j|\psi_{n\mathbf{k}}\rangle\langle\psi_{n\mathbf{k}}|\mathbf{0}j\rangle = 1 \tag{4.43}$$

Using (4.40), we are in a position to evaluate $N_j(E)$ numerically.

Composite treatment:

As one would expected, the Wannier function projected DOS for $j = 0$ to 4 (with high d-character, see Tab. 4.1) look a lot like the the d-projected DOS $N_d(E)$ in Fig. 3.8. The densities $N_j(E)$ for $j = 5$ to 8 are more spread out in energy, since they have s and p-character. Except for these insights, it is not very illuminating to look at all the $N_j(E)$. Hence, we have not plotted them; we have plotted some Wannier function projected DOS in Ref. [28].

Isolated treatment:

To discuss $N_j(E)$, this treatment is more illuminating. As usual, we choose the band index n of the Bloch bands to obey $E_n(\mathbf{k}) \leq E_{n+1}(\mathbf{k})$. For example, Fig. 4.1 shows the 2nd Bloch band ($n = 2$) which is restricted to a narrow energy range from about 2.2 to 3.8 eV. No unitary gauge transformations (4.11) are involved in the evaluation of the 2nd Wannier function. Hence, the 2nd Wannier function (together with its periodic images) spans the same space as the Bloch functions of the 2nd band. Accordingly, the projected DOS $N_2(E)$ will only be different from zero in the energy range of the 2nd Bloch band and vanish everywhere else. This can be seen very clearly from Fig. 4.2 in which the lowest six $N_j(E)$ are shown.

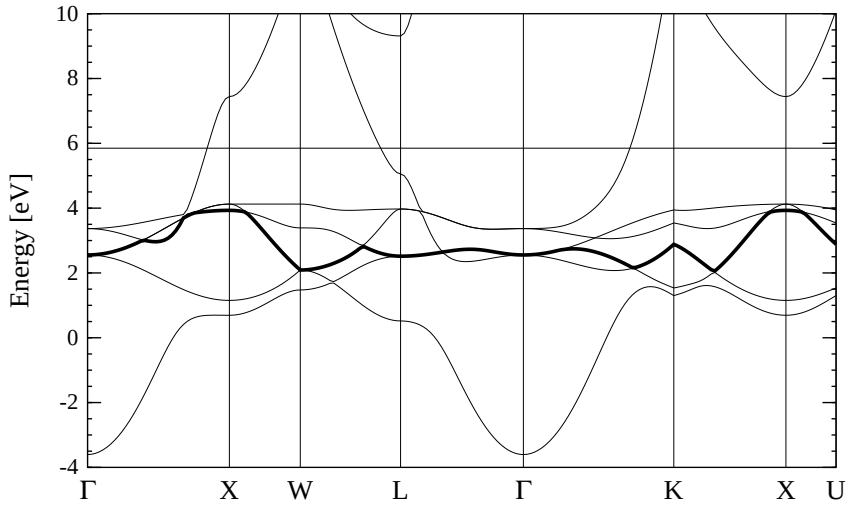

Figure 4.1: The 2nd band from Fig. 3.10 is plotted bold. As usual, the 0th band is the lowest in energy. Note that at some points in $\mathbf{k}$-space this band appears to be the 1st band, e.g. as we move from the L towards the Γ-point. The reason for this are degeneracies with other bands at these $\mathbf{k}$-points. In the corresponding region from L to Γ, we have $E_1(\mathbf{k}) = E_2(\mathbf{k})$. For the Γ-point the degeneracy is $E_1(\mathbf{0}) = E_2(\mathbf{0}) = E_3(\mathbf{0})$.

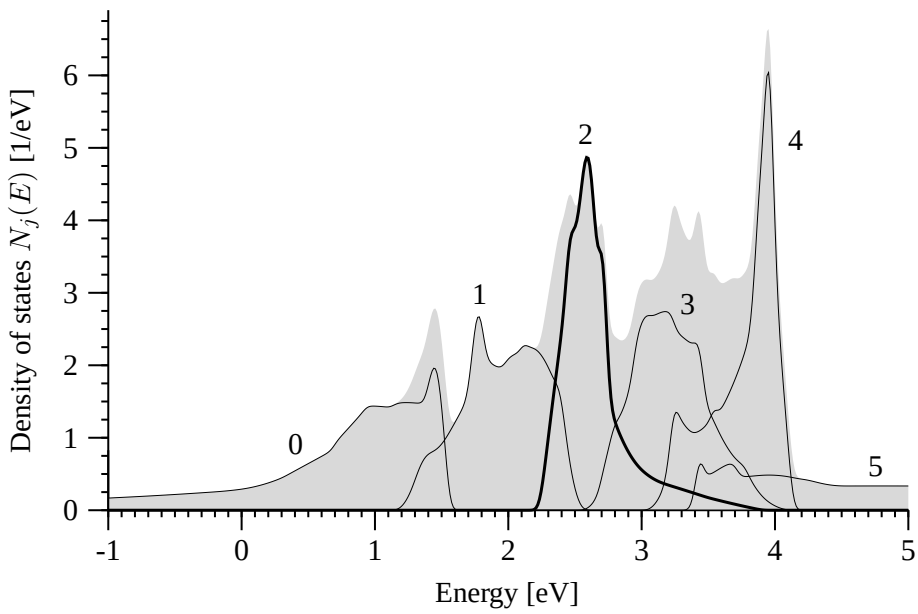

Figure 4.2: Wannier function projected DOS $N_j(E)$ (lines) using the isolated treatment of the copper bands and the total DOS (shadowed). The density $N_2(E)$ is non-vanishing from about 2.2 to 3.8 eV. This corresponds to the region of the 2nd band shown in Fig. 4.1 above. Note: we have plotted the spin-up plus spin-down DOS.

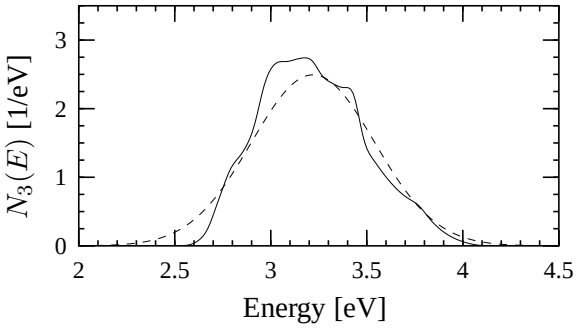

Figure 4.3: Wannier function projected DOS $N_3(E)$ from Fig. 4.2 (solid) and the Gaussian (4.47) with $E_3 = 3.22$ eV and $\sigma_3 = 0.32$ eV, normalized to 2 on account of spin (dashed).

4.3.3 Moments of projected DOS

The qth moment of the jth Wannier function projected DOS (per spin) about energy E_j is given by:

$$M_{jq} = \int dE\ N_j(E) \cdot (E - E_j)^q \tag{4.44}$$

As earlier, see text around Eq. (3.21), we may choose the center of $N_j(E)$ by the condition that the first order moment vanishes, i.e. $M_{j1} \equiv 0$. Using (4.42) and (4.44), we see that:

$$E_j = \int dE\ N_j(E) \cdot E \tag{4.45}$$

Accordingly, we may associate an energy with each Wannier function. If we treat a composite set of bands, we may choose the arbitrary index j such that $E_j \leq E_{j+1}$.

Since (4.45), the moments (4.44) are moments about the center, also known as "central moments" [50]. It is well-known that the second central moment is the variance, thus the square root of M_{j2} is the standard deviation σ_j of the j-projected DOS, i.e.

$$\sigma_j = \sqrt{M_{j2}}\ . \tag{4.46}$$

We may use σ_j as a measure of the width of a Wannier function in terms of energy.

Using the tetrahedron method, we have calculated E_j and the central moments up to second order.[6] We can test our numerics, since from (4.42), we have $M_{j0} = 1$ and per definition $M_{j1} = 0$. Also, just as a check, to see whether the second moments we obtain are reasonable, we pick out a j-projected DOS that comes close to a Gaussian function. It looks like $N_3(E)$ in Fig. 4.2 is the best we have. We now simply compare $N_3(E)$ with the Gaussian

$$\frac{1}{\sigma_3\sqrt{2\pi}}\ \exp\left(-\frac{E - E_3}{2\,\sigma_3^2}\right)\ , \tag{4.47}$$

[6] In analogy to section 3.4.4.

Composite treatment:

j	0	1	2	3	4	5	6	7	8
E_j [eV]	5.86	5.04	3.60	3.61	5.12	15.45	15.66	15.81	15.79
σ_j [eV]	7.64	6.60	3.87	3.91	6.71	11.05	11.02	10.96	10.99
% DOS	9.3	9.6	8.6	8.6	9.2	14.0	13.5	13.7	13.6
$n_j(E_F)$	1.64	1.71	1.87	1.87	1.70	0.59	0.56	0.53	0.54

Isolated treatment:

j	0	1	2	3	4	5	6	7	8
E_j [eV]	0.51	1.95	2.65	3.22	3.76	6.11	16.32	23.50	27.92
σ_j [eV]	1.11	0.33	0.32	0.32	0.28	2.09	5.49	5.15	4.84
% DOS	0.0	0.0	0.0	0.0	0.0	100.0	0.0	0.0	0.0
$n_j(E_F)$	2.00	2.00	2.00	2.00	2.00	1.00	0.00	0.00	0.00

Table 4.2: Shown are (i) The central energy E_j. (ii) The width σ_j. (iii) The portion of the DOS at the Fermi level, i.e. $N_j(E_F)/N(E_F)$ (in percent). (iv) The projected NOS at the Fermi level $n_j(E_F)$, where the values account for both spins, so that $0 \leq n_j(E_F) \leq 2$.

which has the same moments up to second order, where E_3 and σ_3 are obtained from the tetrahedron method. This is done in Fig. 4.3. As can be seen, the curves agree as good as they possibly can, hence the second moment and the center energy we have obtained from the tetrahedron method make good sense.

Remarks concerning Tab. 4.2:

Row 1: For the composite treatment $E_j \nleq E_{j+1}$ in general, however (as noted above), we may choose the arbitrary index j such that $E_j \leq E_{j+1}$; while for the isolated treatment we already have $E_j \leq E_{j+1}$.

Row 2: The widths σ_j are much smaller in the isolated case since we pick out Bloch states which are restricted to a narrow energy range.

Row 3: Note that in the composite case for every j, this portion is non-vanishing. In contrast, in the isolated case, only the 5th Wannier function projected DOS is non-vanishing and all others are zero. This is evident from Fig. 4.2.

Row 4: The projected NOS at E_F in the composite case is largest for the d-like states ($j = 0...4$) since the projected DOS, which looks similar to the d-DOS in Fig. 3.8, is peaked below the Fermi level. In the isolated case $n_j(E_F) = 2$ for $j \leq 4$ and $n_5(E_F) = 1$ since $n(E_F) = 11$ for copper. This is also evident from Fig. 4.2.

Chapter 5

Matrix Elements

Many-body theories of correlated electronic materials are traditionally based upon the formalism of second quantization. Hubbard-like models[1] also assume an underlying basis of localized (Wannier) orbitals. However, these theories often involve a Hubbard-U term as an empirical parameter. First, we take a look at the second-quantized Hamiltonian,[2] mainly to introduce the notation that we will use from here onwards.

A big part of this chapter is devoted to methods we have developed to determine single-particle Hamiltonian and Coulomb interaction matrix elements for localized (generalized) Wannier functions within the framework of LMTO-ASA. In order to make these methods work, it is always assumed that the home sphere is chosen to be the center sphere, in other words, the Wannier function $|\mathbf{R}n\rangle$ is largest inside the sphere around site $\mathbf{R}$.

Obviously, since computing time and memory are not infinite, matrix elements can only be calculated for a limited number of Wannier functions. Hence, we are interested in a "minimal" basis set of maximally localized Wannier functions for our second quantized Hamiltonian. We choose this basis set to only include the orbitals under consideration, i.e. $4s$, $4p$ and $3d$. However, these orbitals arise in any (solid-state) Hamiltonian, e.g. from (3.47) or (3.48) in section 3.5. We will illustrate that the choice of the "basis set Hamiltonian", i.e. the effective one-particle Hamiltonian we use to construct the Wannier functions from, is crucial. On the other hand, one may argue that any basis set is equally good, which is true, but only *as long as* it is a complete set; and a minimal basis is by no means complete,[3] but it is customized to the problem under consideration. Moreover, from a computational standpoint, it is desirable to use as few basis orbitals as possible.

In this connection it is important to notice that the "basis set Hamiltonian", from which the minimal basis set is obtained, may be a *different* (effective) Hamiltonian than the one whose matrix elements we evaluate. Hence, we will talk about different Hamiltonians, and confusion will arise if one is unaware of this distinction.

[1] In particular the Hubbard model [6] itself, the Falicov Kimball model or the Anderson model.
[2] The introduction of second quantization is based upon [44, 51] which we recommend for further details.
[3] See discussion at the beginning of section 4.3.

5.1 Hamiltonian in Second Quantization

Until now, we have only used the formalism of usual quantum mechanics ("first quantization"), i.e. the quantization of classical mechanics. An assumption in establishing the LDA (and the Hartree approximation) was to consider an auxiliary non-interacting system (2.6). The ground state Ψ_S of this single-particle problem is simply a Slater determinant obtained by populating the lowest one-electron orbitals ψ_i, defined by an effective Schrödinger equation. This made things easy, we never actually had to write down the many-particle ground state in terms of the one-electron orbitals ψ_i; all we needed was the ground state density (2.9). However, when dealing with interacting systems, the many-particle ground state can no longer be written as a single Slater determinant, but as a linear combination of all possible N-particle Slater determinants that can be constructed from any complete one-particle basis. The (rather cumbersome) task of constructing Slater determinants can be avoided using a very elegant formalism called "second quantization", which already takes the antisymmetry of the fermion wave functions into account.

The second-quantized Hamiltonian (2.1) for particles in an external potential $v_{\rm ext}$ (independent of spin) is given by:

$$\begin{aligned} H &= H_0 + W = \sum_\sigma \int d^3\mathbf{r}\, \Phi^\dagger_\sigma(\mathbf{r})\Big(-\nabla^2 + v_{\rm ext}(\mathbf{r})\Big)\Phi_\sigma(\mathbf{r}) \;\; + \\ &+ \frac{1}{2}\sum_{\sigma\sigma'} \int d^3\mathbf{r}\, d^3\mathbf{r}'\, \Phi^\dagger_\sigma(\mathbf{r})\Phi^\dagger_{\sigma'}(\mathbf{r}')\, \frac{e^2}{|\mathbf{r}-\mathbf{r}'|}\, \Phi_{\sigma'}(\mathbf{r}')\Phi_\sigma(\mathbf{r}) \end{aligned} \tag{5.1}$$

Here, $\Phi^\dagger_\sigma(\mathbf{r})$ and $\Phi_\sigma(\mathbf{r})$ are field operators that create and annihilate a particle with spin σ at position $\mathbf{r}$. For electrons, these field operators obey:

$$\{\Phi_\sigma(\mathbf{r}), \Phi^\dagger_{\sigma'}(\mathbf{r}')\} = \delta_{\sigma\sigma'}\delta(\mathbf{r}-\mathbf{r}') \;\; , \;\; \{\Phi_\sigma(\mathbf{r}), \Phi_{\sigma'}(\mathbf{r}')\} = \{\Phi^\dagger_\sigma(\mathbf{r}), \Phi^\dagger_{\sigma'}(\mathbf{r}')\} = 0$$

Where $\{A, B\} \equiv AB + BA$.

Remark: Note that the *expectation value* for the energy of a *single* particle moving in an external field $v_{\rm ext}$ in terms of its wave function $\varphi_\sigma(\mathbf{r})$ is:

$$\sum_\sigma \int d^3\mathbf{r}\, \varphi^*_\sigma(\mathbf{r})\Big(-\nabla^2 + v_{\rm ext}(\mathbf{r})\Big)\varphi_\sigma(\mathbf{r})$$

And the expectation value for the energy of a two particle interaction in terms of a single-particle wave function $\varphi_\sigma(\mathbf{r})$ is:

$$\frac{1}{2}\sum_{\sigma\sigma'} \int d^3\mathbf{r}\, d^3\mathbf{r}'\, \varphi^*_\sigma(\mathbf{r})\varphi^*_{\sigma'}(\mathbf{r}')\, \frac{e^2}{|\mathbf{r}-\mathbf{r}'|}\, \varphi_{\sigma'}(\mathbf{r}')\varphi_\sigma(\mathbf{r})$$

Hence, if we replace in the expectation values *single*-particle wave functions by *many*-particle field operators, i.e. $\varphi^*_\sigma(\mathbf{r}) \to \Phi^\dagger_\sigma(\mathbf{r})$ and $\varphi_\sigma(\mathbf{r}) \to \Phi_\sigma(\mathbf{r})$, we arrive at the second-quantized Hamiltonian (5.1). This formal similarity is the reason why

the field operator formalism is called second quantization. Single-particle expectation values appear to have become operators for physical quantities, while one-particle wave functions appear to have become field operators. This similarity is *only* an appearance, we don't have a quantized quantum mechanics, only another mathematical language for the same old quantum mechanics.

The field operators in (5.1) may be expanded in terms of a set of single-particle wave functions $\varphi_i(\mathbf{r})$ independent of spin:

$$\Phi^\dagger_\sigma(\mathbf{r}) = \sum_i \varphi^*_i(\mathbf{r}) c^\dagger_{i\sigma} \quad , \quad \Phi_\sigma(\mathbf{r}) = \sum_i \varphi_i(\mathbf{r}) c_{i\sigma} \tag{5.2}$$

While $\Phi^\dagger_\sigma(\mathbf{r})$ [$\Phi_\sigma(\mathbf{r})$] creates [annihilates] a particle with spin σ at position $\mathbf{r}$, the operator $c^\dagger_{i\sigma}$ [$c_{i\sigma}$] creates [annihilates] an electron in a state of spin σ whose wave function is $\varphi_i(\mathbf{r})$. Even though the $\varphi_i(\mathbf{r})$'s are independent of spin, the expansion (5.2) is exact since the $\varphi_i(\mathbf{r})$'s span the one-particle Hilbert space, i.e. they form a complete set. Our approximation of using a "minimal" basis set consists of using only a few orbitals $\varphi_i(\mathbf{r})$ (still independent of spin). Inserting the expansion (5.2) into (5.1) yields:

$$\begin{aligned} H &= \sum_{ij\sigma} \underbrace{\int d^3\mathbf{r}\, \varphi^*_i(\mathbf{r}) \Big(-\nabla^2 + v_{\text{ext}}(\mathbf{r}) \Big) \varphi_j(\mathbf{r})}_{(H_0)_{ij}} c^\dagger_{i\sigma} c_{j\sigma} \quad + \\ &+ \frac{1}{2} \sum_{ijk\ell} \sum_{\sigma\sigma'} \underbrace{\int d^3\mathbf{r}\, d^3\mathbf{r}'\, \varphi^*_i(\mathbf{r}) \varphi^*_j(\mathbf{r}') \frac{e^2}{|\mathbf{r}-\mathbf{r}'|} \varphi_k(\mathbf{r}') \varphi_\ell(\mathbf{r})}_{W_{ij,k\ell}} c^\dagger_{i\sigma} c^\dagger_{j\sigma'} c_{k\sigma'} c_{\ell\sigma} \end{aligned} \tag{5.3}$$

In order to simplify expressions that involve indices i and σ, like the one above, we may introduce the abbreviated notation 1 to mean $i_1\sigma_1$ and 2 to mean $i_2\sigma_2$, etc. . But i and σ do not always come in pairs in (5.3). We can nevertheless use this new notation by using the Kronecker delta, i.e.

$$H = \sum_{12} \underbrace{\delta_{\sigma_1\sigma_2} (H_0)_{i_1 i_2}}_{(H_0)_{12}} c^\dagger_1 c_2 + \frac{1}{2} \sum_{1234} \underbrace{\delta_{\sigma_1\sigma_4} \delta_{\sigma_2\sigma_3} W_{i_1 i_2, i_3 i_4}}_{W_{12,34}} c^\dagger_1 c^\dagger_2 c_3 c_4 \quad . \tag{5.4}$$

For convenience, we may write the matrix elements as:[4]

$$(H_0)_{12} = \langle 1|H_0|2\rangle = \delta_{\sigma_1\sigma_2} (H_0)_{i_1 i_2} \qquad \text{and} \tag{5.5}$$

$$W_{12,34} = \langle 1|\langle 2|W|3\rangle|4\rangle = \delta_{\sigma_1\sigma_4} \delta_{\sigma_2\sigma_3} W_{i_1 i_2, i_3 i_4} \tag{5.6}$$

As can be seen from (2.2), the many-particle operator H_0 is a sum of single-particle operators which act on a *single* particle. This is the reason why H_0 is called a single-particle operator: While the Coulomb interaction W involves two particles, H_0 only involves the interaction of *one* particle with the external field.

[4]Note that (to be correct) we would have to write $(H_0)_{12} = \langle 1|h_0|2\rangle$, where h_0 is the *single-particle* operator in (5.3) and not the many-particle operator $H_0 = \sum h_0$ (summed over all particles). Usually when we mean h_0, we write H_0 instead.

We want to consider (5.5) more generally for any effective single-particle Hamiltonian H_{eff}. This Hamiltonian may depend on spin because, even though the external field arising from the nuclei is independent of spin, we may wish to consider the situation where the electrons move in an effective spin dependent field, as for example in spin-polarized DFT. Hence, we rewrite (5.5) as:[5]

$$(H_{\text{eff}})_{12} = \delta_{\sigma_1\sigma_2}(H_{\text{eff}})^{\sigma_1}_{i_1 i_2} \quad \text{where} \quad (H_{\text{eff}})^{\sigma}_{ij} = \int d^3\mathbf{r}\, \varphi_i^*(\mathbf{r})\Big(-\nabla^2 + v^\sigma(\mathbf{r})\Big)\varphi_j(\mathbf{r}) \tag{5.7}$$

Where $v^\sigma(\mathbf{r})$ is some spin-dependent effective potential like $v^\sigma_S(\mathbf{r})$ in Eq. (2.44).

Let us now focus on the orbitals $\varphi_i(\mathbf{r})$ in which the field operators (5.2) are expanded. We consider these orbitals to be either Bloch or Wannier orbitals constructed from a single-particle Hamiltonian H' independent of spin. The Hamiltonian H' is not necessarily H_{eff} itself. However, we demand that the underlying crystal structure and lattice constant in H_{eff} and H' agree, such that both H_{eff} and H' commute with the same translation operator $T_{\mathbf{R}}$. For later reference, we distinguish between two cases:

A. Case A shall be the case in which $H' = H_{\text{eff}}$, i.e. the basis functions stem from H_{eff} itself.

   For example, we may expand the field operators in terms of Bloch eigenstates $\psi_{n\mathbf{k}}$ of the single-particle operator $H_0 = -\nabla^2 + v_{\text{ext}}(\mathbf{r})$ itself:

$$\Phi^\dagger_\sigma(\mathbf{r}) = \sum_{n\mathbf{k}} \psi^*_{n\mathbf{k}}(\mathbf{r}) c^\dagger_{n\mathbf{k}\sigma} \quad , \quad \Phi_\sigma(\mathbf{r}) = \sum_{n\mathbf{k}} \psi_{n\mathbf{k}}(\mathbf{r}) c_{n\mathbf{k}\sigma} \tag{5.8}$$

   This is called a "Bloch eigenbasis". Inserting (3.7) into (5.3) yields

$$\langle \psi_{n\mathbf{k}} | H_0 | \psi_{m\mathbf{k}'} \rangle = \delta_{nm}\delta_{\mathbf{k}\mathbf{k}'} E_n(\mathbf{k}) \quad . \tag{5.9}$$

   Hence, in a Bloch eigenbasis representation, the matrix H_0 becomes diagonal.

   On the other hand, we can expand the field operators in terms of Wannier functions. In this case, we write the letter a for the creation and annihilation operator:

$$\Phi^\dagger_\sigma(\mathbf{r}) = \sum_{\mathbf{R}n} w^*_{\mathbf{R}n}(\mathbf{r}) a^\dagger_{\mathbf{R}n\sigma} \quad , \quad \Phi_\sigma(\mathbf{r}) = \sum_{\mathbf{R}n} w_{\mathbf{R}n}(\mathbf{r}) a_{\mathbf{R}n\sigma} \tag{5.10}$$

   This is a "Wannier basis", in which the matrix H_0 will not be diagonal, since Wannier states are not eigenfunctions of H_0.

B. Case B shall be the general case in which the basis functions do not *necessarily* stem from H_{eff} itself. Hence, case B includes case A.

   The Bloch basis is not a Bloch *eigenbasis* anymore but since we demand that both H_{eff} and H' commute with the same translation operators $T_{\mathbf{R}}$, the matrix $(H_{\text{eff}})_{12}$ will still be diagonal in $\mathbf{k}$ but not necessarily in the band index n:

$$\langle \psi_{n\mathbf{k}} | H_{\text{eff}} | \psi_{m\mathbf{k}'} \rangle = \delta_{\mathbf{k}\mathbf{k}'} \langle \psi_{n\mathbf{k}} | H_{\text{eff}} | \psi_{m\mathbf{k}'} \rangle \tag{5.11}$$

   Where we used Bloch's theorem (3.4) as well as $[H_{\text{eff}}, T_{\mathbf{R}}] = [H', T_{\mathbf{R}}] = 0$.

[5] Note carefully that our minimal basis φ_i is always independent of spin, and $(H_{\text{eff}})_{12}$ is always diagonal in spin. However, the two spin sub blocks are in general unequal, i.e. $(H_{\text{eff}})^{\uparrow}_{ij} \neq (H_{\text{eff}})^{\downarrow}_{ij}$.

5.2 Single-Particle Hamiltonian

We now turn to the evaluation of matrix elements of a single-particle effective Hamiltonian H_{eff} (which for convenience we will call just H) in Wannier representation, i.e. considering matrix elements of H with Wannier functions $|\mathbf{R}n\rangle$. Since the $H(\mathbf{r}) = H(\mathbf{r}+\mathbf{R})$, H_{12} only depends on the difference of the sites $\mathbf{R}_1$ and $\mathbf{R}_2$:

$$H^{\sigma}_{\mathbf{R}_1 n_1, \mathbf{R}_2 n_2} = H^{\sigma}_{(\mathbf{R}_1 - \mathbf{R}_2) n_1, \mathbf{0} n_2} \equiv H^{\sigma}_{(\mathbf{R}_1 - \mathbf{R}_2) n_1, n_2} \tag{5.12}$$

Hence, this property allows us to write our hopping matrix element in a different form with fewer indices. Nevertheless, there is still redundancy in $H^{\sigma}_{\mathbf{R}nm}$ (or $H_{\mathbf{R}nm}$) since H is Hermitian:

$$H^{\sigma}_{\mathbf{R}nm} = H^{\sigma *}_{-\mathbf{R}mn} \tag{5.13}$$

We can use this relation for numerical tests and, in particular, for reducing computing time and memory storage.

When the Wannier functions have been constructed from H itself, i.e. case A, using a gauge transformation of the first kind only (isolated treatment), the $H_{\mathbf{R}nm}$'s are equivalent to the Fourier components of the band structure[6]

$$H_{\mathbf{R}nm} = \langle \mathbf{R}n | H | \mathbf{0}m \rangle = \delta_{nm} \frac{\Omega}{(2\pi)^3} \int\limits_{\text{BZ}} d^3\mathbf{k}\, e^{i\mathbf{k}\mathbf{R}} E_n(\mathbf{k}) \ . \tag{5.14}$$

Where we used (4.1) and $H|\psi_{n\mathbf{k}}\rangle = E_n(\mathbf{k})|\psi_{n\mathbf{k}}\rangle$. Put in other words: If we treat all bands isolated, the $H_{\mathbf{R}nm}$ can be directly calculated from the band structure, but only if we calculate the matrix elements of the same Hamiltonian H from which we have constructed the Wannier functions.

However, we are interested in obtaining matrix elements from maximally localized (generalized) Wannier functions constructed by gauge transformations of the second kind which leads to generalized Bloch states that are no longer eigenstates of H with eigenvalue $E_n(\mathbf{k})$. Moreover, we wish to evaluate matrix elements for the case B. Hence, Eq. (5.14) is not particularly helpful. For these reasons, we have developed a method which enables us to evaluate $H_{\mathbf{R}nm}$ in a more rigorous way, i.e. using their original definition as a matrix element

$$H^{\sigma}_{\mathbf{R}nm} = \int d^3\mathbf{r}\, w^*_{\mathbf{R}n}(\mathbf{r}) \Big(-\nabla^2 + v^{\sigma}(\mathbf{r}) \Big) w_{\mathbf{0}m}(\mathbf{r}) \tag{5.15}$$

without being restricted to the conditions mentioned above anymore. We will start with our basic formalism for LMTO-ASA wave functions which will prove its usefulness in the evaluation of Coulomb matrix elements, too. Evaluating (5.15), we will neglect the spin index because we will be able to calculate the matrix elements for any external field.

[6] We note that from (3.42), it follows that $H_{\mathbf{R}nn} = H_{\alpha\mathbf{R}nn}$ for the rotations α in the point group of the crystal, see [30] Eq. (5.1.39). Also, $H_{\mathbf{R}nn}$ is gauge invariant since the band structure is completely unaffected by gauge transformations. These special properties do not hold for the general case below, however.

5.2.1 Basic Formalism

The basic formalism we are about to develop takes advantage of two facts:

i.) The Wannier functions are decomposed into contributions arising from every muffin-tin sphere (4.6). Furthermore, inside each atomic sphere, we have an expansion in terms of spherical harmonics (C.24). This is the "ASA aspect" we take advantage of.

ii.) The radial part of the wave function is a linear combination of $\phi_{\nu\ell}(r)$ and $\dot{\phi}_{\nu\ell}(r)$, see (4.30). This is the "LMTO aspect" we take advantage of.

Hence, this formalism can also be used to evaluate matrix elements of Bloch functions; their delocalized nature complicates things in the case of Coulomb interaction matrix elements, however. The formalism is designed to speed up the numerical evaluation of matrix elements, which will become particular important when we use the formalism to evaluate interaction matrix elements. But now, we consider the matrix elements:

$$H_{\mathbf{R}nm} = \langle \mathbf{R}n|H|\mathbf{0}m\rangle = \int d^3\mathbf{r}\; w^*_{\mathbf{R}n}(\mathbf{r}) H w_{\mathbf{0}m}(\mathbf{r}) \quad , \qquad H = -\nabla^2 + v(\mathbf{r}) \tag{5.16}$$

Since H commutes with the translation operator, we may use (4.6) and (4.4) to find

$$H_{\mathbf{R}nm} = \sum_i \int d^3\mathbf{r}\; w^*_n(\mathbf{R}_i - \mathbf{R};\mathbf{r}) H w_m(\mathbf{R}_i;\mathbf{r}) \;\; , \tag{5.17}$$

where the integral is taken over a single sphere only. In order to calculate Eq. (5.17), we must evaluate integrals of the form

$$I = \int d^3\mathbf{r}\; f^*_1(\mathbf{r}) f_2(\mathbf{r}) \qquad \text{where} \quad f_i(\mathbf{r}) = \sum_L R_{iL}(r) Y_L(\hat{\mathbf{r}}) \;\; , \quad i = \{1,2\} \;\; . \tag{5.18}$$

That is, the functions $f_i(\mathbf{r})$ are given by a spherical harmonics expansion. From the above and the ortho-normality of the spherical harmonics, it follows that:

$$I = \sum_L \int dr\; r^2\; R^*_{1L}(r)\; R_{2L}(r) \tag{5.19}$$

Having completed the ASA aspect, we now turn to the LMTO aspect.

Since the expansion inside each atomic sphere is given by Eq. (4.30), the radial functions $R(r)_{1L}$ in (5.19) will always be given in terms of $\phi_{\nu\ell}(r)$ and $\dot{\phi}_{\nu\ell}(r)$. Let us (for convenience) drop the index ν and define

$$\phi_{\ell;0}(r) \equiv \phi_\ell(r) = \phi_{\nu\ell}(r) \quad , \qquad \phi_{\ell;1}(r) \equiv \dot{\phi}_\ell(r) = \dot{\phi}_{\nu\ell}(r) \quad . \tag{5.20}$$

Now, the functions $R(r)_{2L}$ are generally not given in these terms, since we have to consider the Hamiltonian acting on the second Wannier function in Eq. (5.17). However, as will be shown later, H can be considered acting onto the functions (5.20). Therefore, we write:

$$\chi_{\ell;p}(r) = H\phi_{\ell;p}(r) \qquad\qquad p = \{0,1\} \tag{5.21}$$

The explicit expression for $\chi_{\ell;p}(r)$ is given by (5.31) below, for now we assume that $\chi_{\ell;p}(r)$ is known. If we introduce

$$A_{iL;0} = A_{iL} \ , \quad A_{iL;1} = B_{iL} \tag{5.22}$$

and use (4.30), we see that:

$$R_{1L}(r) = \sum_p A_{1L;p}\, \phi_{\ell;p}(r) \qquad \text{and} \qquad R_{2L}(r) = \sum_p A_{2L;p}\, \chi_{\ell;p}(r) \tag{5.23}$$

We will use this form to calculate the integral (5.19) very efficiently. It is clear that any integral can be reduced to a linear combination of "basic" integrals. Those basic integrals consist of the (very limited) combinations of the $\phi(r)$'s and $\chi(r)$'s. Inserting (5.23) into (5.19) yields:

$$I = \sum_{Lp_1p_2} A^*_{1L;p_1} A_{2L;p_2} \int dr\, r^2\, \phi_{\ell;p_1}(r)\, \chi_{\ell;p_2}(r) = \sum_{Lp_1p_2} a_{L;p_1p_2} b_{\ell;p_1p_2} \tag{5.24}$$

where

$$a_{L;p_1p_2} \equiv A_{1L;p_1} A^*_{2L;p_2} \qquad \text{and} \qquad b_{\ell;p_1p_2} \equiv \int dr\, r^2\, \phi_{\ell;p_1}(r)\, \chi_{\ell;p_2}(r) \tag{5.25}$$

The time consuming task to evaluate integrals is now *limited* to evaluating only four basic integrals $b_{\ell;p_1p_2}$ for each ℓ.[7] Note that $\phi_{\ell;p}(r)$ and thus the basic integrals are real.

Having also completed the LMTO aspect, we mention that:

i.) In the singe-particle operator case, things are easy and labeling the basic integrals and coefficients in such a manner seems unnecessary. However, one may regard this case as a small exercise since in the two-particle operator case, i.e. Coulomb interaction, things will become more complicated and labeling the corresponding expressions helps to keep track of things.

ii.) Looking at the LMTO-method again, we realize that when we choose $H = \mathbf{1}$, i.e. a non-physical Hamiltonian in (5.21), so that $\chi_{\ell;p}(r) = \phi_{\ell;p}(r)$, we find

$$b_{\ell;00} = 1 \ , \quad b_{\ell;01} = b_{\ell;10} = 0 \ , \quad b_{\ell;11} = \langle \dot{\phi}^2_{\nu\ell} \rangle \ . \tag{5.26}$$

Note that $\langle \dot{\phi}^2_{\nu\ell} \rangle$ arises from the LMTO-treatment of the Hamiltonian which is used to constructed the Wannier functions (which is of course *not* $\mathbf{1}$). These relations are useful to check the numerical evaluation of $b_{\ell;p_1p_2}$.

[7] E.g. using orbitals up to *d*, only 12 integrals $b_{\ell;p_1p_2}$ need to be evaluated, no matter how many times they will be required later in (5.17) and (5.24).

Hamiltonian acting on radial basis functions:

Again, we distinguish between our two cases (introduced on page 67):

A. The effect of H on the second Wannier function can be carried out easily because we are working in a linear basis. Since in the LMTO method $(H - E_{\nu\ell})\phi_\ell(r) = 0$ and $(H - E_{\nu\ell})\dot{\phi}_\ell(r) = \phi_\ell(r)$,[8] we find simple expressions for (5.21):

$$\chi_{\ell;0}(r) = E_{\nu\ell}\phi_{\ell;0}(r) \ , \quad \chi_{\ell;1}(r) = \phi_{\ell;0}(r) + E_{\nu\ell}\phi_{\ell;1}(r) \tag{5.27}$$

From which it is easy to show that

$$b_{\ell;00} = E_{\nu\ell} \ , \quad b_{\ell;01} = 1 \ , \quad b_{\ell;10} = 0 \ , \quad b_{\ell;11} = E_{\nu\ell}\langle\dot{\phi}^2_{\nu\ell}\rangle \ . \tag{5.28}$$

For some applications, this is all we are interested in. We have used these expressions in Refs. [28, 47], however, there we have used a slightly different formalism, i.e. the effect of H was taken into account by acting onto the $A_{2L;p}$ coefficients.[9] The quantities $E_{\nu\ell}$ and $\langle\dot{\phi}^2_{\nu\ell}\rangle$ are so-called potential parameters which follow directly from the LMTO calculation; hence, this special case may serve as a numerical test case for the general treatment which follows.

B. This is the general case in which the basis Wannier functions, and hence $\phi_{\ell;p}(r)$, do not necessarily stem from $H = -\nabla^2 + v(\mathbf{r})$ itself (but from H'). Thus, we have to consider the operator H acting on any wave function. Within the ASA, $v(\mathbf{r})$ is spherical symmetric inside every sphere. Moreover, the Laplacian ∇^2 takes a simple form in spherical coordinates.[10] Hence, the Hamiltonian H inside the atomic sphere (i.e. $r < S$) is:

$$H = -\nabla^2 + v(r) = -\frac{1}{r}\frac{\partial^2}{\partial r^2}\, r + \frac{\mathbf{L}^2}{r^2} + v(r) \tag{5.29}$$

This Hamiltonian is acting on the expansion (5.18). Thus:[11]

$$H\sum_L R_L(r)Y_L(\hat{\mathbf{r}}) = \sum_L \underbrace{\left(-\frac{1}{r}\frac{\partial^2}{\partial r^2}\, r + \frac{\ell(\ell+1)}{r^2} + v(r)\right) R_L(r)}_{H\,R_L(r)}\, Y_L(\hat{\mathbf{r}}) \tag{5.30}$$

Note that this function is already present as a spherical harmonics expansion, again. Accordingly, the effect of H can be carried out on $R_L(r)$, and since $R_L(r)$ is a linear combination of $\phi_\ell(r)$ and $\dot{\phi}_\ell(r)$, the effect of H may be carried out on the radial basis functions $\phi_{\ell;p}(r)$ directly:

$$\chi_{\ell;p}(r) = H\phi_{\ell;p}(r) = \left(-\frac{1}{r}\frac{\partial^2}{\partial r^2}\, r + \frac{\ell(\ell+1)}{r^2} + v(r)\right)\phi_{\ell;p}(r) \tag{5.31}$$

This is the desired expression we generally use for calculating $\chi_{\ell;p}(r)$.

[8] See Eq. (3.11)-(3.12) in Ref. [31].
[9] See Eq. (3.31) in Ref. [47].
[10] See e.g. Eq. (6-37) in [51] or Eq. (16.30) in [52].
[11] Note that: $\mathbf{L}^2 Y_\ell^m(\Omega) = \ell(\ell+1)Y_\ell^m(\Omega)$

5.2.2 Band Structure

We will now discuss how the band structure can be obtained from the matrix elements of an effective Hamiltonian $H_{\mathbf{R}nm}$ for the general case B (which includes case A). To this end, we return to the Bloch representation. Since H is still diagonal in $\mathbf{k}$, i.e. (5.11), we may define a matrix $H^{\mathbf{k}}_{nm}$ for each $\mathbf{k}$-point:

$$H^{\mathbf{k}}_{nm} \equiv \langle \psi_{n\mathbf{k}} | H | \psi_{m\mathbf{k}} \rangle = \sum_{\mathbf{R}} e^{-i\mathbf{k}\mathbf{R}} H_{\mathbf{R}nm} \tag{5.32}$$

Where we used (4.2) but not (4.11), hence generalized Bloch and Wannier functions appear in (5.32). Thus, we need to diagonalize (the Hermitian) matrix $H^{\mathbf{k}}_{nm}$ to obtain the energy eigenvalues for this $\mathbf{k}$-point. By means of the unitary matrix in Eq. (4.11), we find:

$$E_n(\mathbf{k}) = \left(U^{\mathbf{k}} H^{\mathbf{k}} U^{\mathbf{k}\dagger} \right)_{nn} \tag{5.33}$$

Remarks:

i.) We can evaluate $H^{\mathbf{k}}_{nm}$, and hence $E_n(\mathbf{k})$ for any given $\mathbf{k}$-point, without being restricted to the $\mathbf{k}$-points on the cubic mesh in the Marzari-Vanderbilt method. Hence, we may actually calculate the band structure along high symmetry lines (inside the IBZ) obtained from $H_{\mathbf{R}nm}$. This way, we are in a position to re-calculate the original band structure for case A (and make a comparison).

ii.) When our Wannier functions are fairly well localized, we expect that $H_{\mathbf{R}nm}$ decays for large enough $|\mathbf{R}|$. Hence, we hope to be able to truncate the $\mathbf{R}$-sum in (5.32) after a few shells (see appendix C.6). We will show some examples concerning this point in the following.

iii.) Consider case A and an isolated treatment for the construction of the Wannier functions, i.e. a gauge transformation of the first kind only. Accordingly, the Bloch states in (5.32) are eigenstates of H (and not generalized Bloch states) and it follows that $H^{\mathbf{k}}_{nm} = \delta_{nm} E_n(\mathbf{k})$.

5.2.3 Examples

In the following examples, we calculate the band structure from hopping matrix elements $H_{\mathbf{R}nm}$ in Wannier representation. Since (in case A) the original band structure can be re-obtained from $H_{\mathbf{R}nm}$, we are in a position to check the correctness of the numerical calculations and, moreover, gain some experience about the approximation of truncating the $\mathbf{R}$-sum in (5.32). Furthermore, we will show that the choice of the minimal basis set is crucial. That is, in case B the band structure of H is poorly reproduced when H' is extremely different from H.

Example 1

We wish to start by looking at the easiest case, i.e. for case A when the Wannier functions arise from an isolated treatment of the bands. Here, the matrix elements $H_{\mathbf{R}nm}$ are simply the Fourier components of the band structure (5.14). Returning to Bloch representation, i.e. inserting (5.14) into (5.32), gives[12]

$$H^{\mathbf{k}}_{nm} = \sum_{\mathbf{R}} e^{-i\mathbf{k}\mathbf{R}} \underbrace{\frac{\delta_{nm}}{N} \sum_{\mathbf{k}'} e^{i\mathbf{k}'\mathbf{R}} E_n(\mathbf{k}')}_{H_{\mathbf{R}nm}} = \delta_{nm} E_n(\mathbf{k}) \ , \tag{5.34}$$

which is already diagonal. This is also obvious from (5.9), but we wish to follow the general procedure. Inserting (5.34) into (5.33) yields:

$$E_n(\mathbf{k}) = \left(U^{\mathbf{k}} H^{\mathbf{k}} U^{\mathbf{k}\dagger}\right)_{nn} = H^{\mathbf{k}}_{nn} = E_n(\mathbf{k}) \tag{5.35}$$

The band structure equals the band structure – not very illuminating. However, there is more we can look at. That is, we first *evaluate* $H_{\mathbf{R}nm}$ from Eq. (5.14) and then use Eq. (5.32), truncated to a certain number of shells in the $\mathbf{R}$-sum, to re-evaluate the band structure in order to see the effect of this truncation. Or, put in other words, to see how quickly the Fourier components decay.

We have used the discretized form of (5.14) to evaluate the Fourier components of the Hartree band structure of copper (Fig. 3.10), i.e.

$$H_{\mathbf{R}nn} = \frac{1}{N} \sum_{\mathbf{k}} e^{i\mathbf{k}\mathbf{R}} E_n(\mathbf{k}) \ , \tag{5.36}$$

where we used a cubic $\mathbf{k}$-mesh with $\Delta k = 0.1\ (2\pi/a)$ which equals using $20^3/2 = 4000$ points in Brillouin zone (for FCC). The re-calculated band structure is shown in Fig. 5.1 where 5 shells, i.e. 79 sites (see appendix C.6), have been included in the $\mathbf{R}$-sum in (5.32). The overall band structure is reproduced fairly well, although at points along the symmetry lines where band crossings occur, the disagreement is serious. Even if we truncate the $\mathbf{R}$-sum after 30 shells, i.e. 1061 sites, the mismatch at these points remains significant (Fig. 5.2), despite the fact that such a large number of sites have been included. One would hope to achieve a better agreement of the two curves. The reason for this discrepancy is obvious: Consider Fig. 4.1 in which the 2nd band is highlighted. Since we chose the band index such that $E_n(\mathbf{k}) \leq E_{n+1}(\mathbf{k})$, all connected bands become very "unnatural" in their form, in particular band crossings produce sharp kinks in the bands. In the treatment above, each of these bands is Fourier transformed and these kinks, as is well known, have a slowly decaying Fourier spectrum. Thus, truncating the $\mathbf{R}$-sum in (5.32) leads to errors.

Furthermore, the isolated treatment is not desired since the resulting localized Wannier functions are only poorly localized, i.e. they are not maximally localized Wannier functions in their original sense, see section 4.3. For this reason, we prefer the composite treatment.

[12] Note that $\sum_{\mathbf{R}} e^{-i(\mathbf{k}-\mathbf{k}')\mathbf{R}} = N\delta_{\mathbf{k}\mathbf{k}'}$ and that we used the discretized version of (5.14).

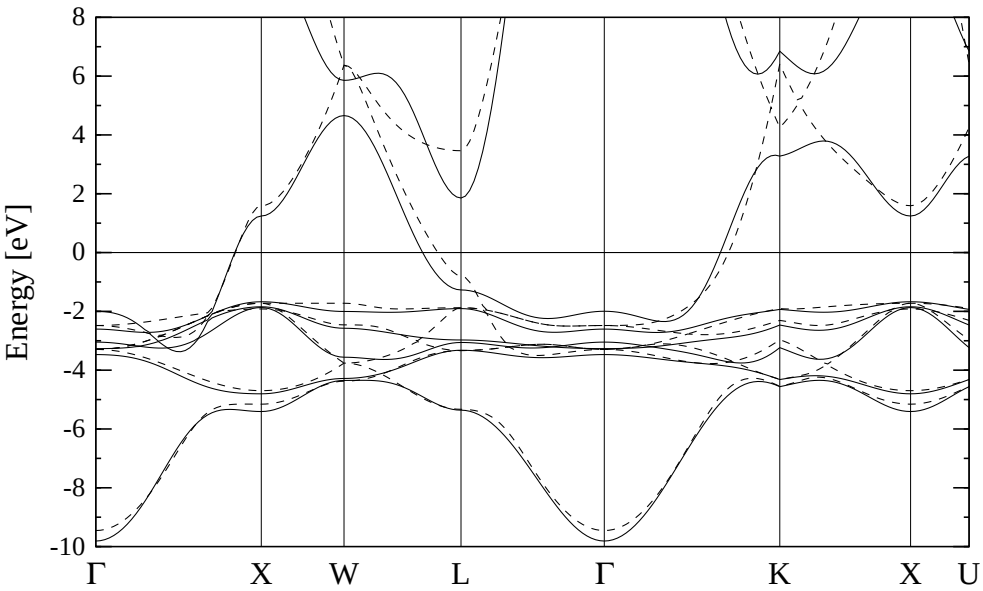

Figure 5.1: Hartree band structure of copper (dashed) and $\sum_{\mathbf{R}} e^{-i\mathbf{k}\mathbf{R}} H_{\mathbf{R}nn}$ where the sum is truncated after 5 shells (solid), with energy relative to the Fermi energy.

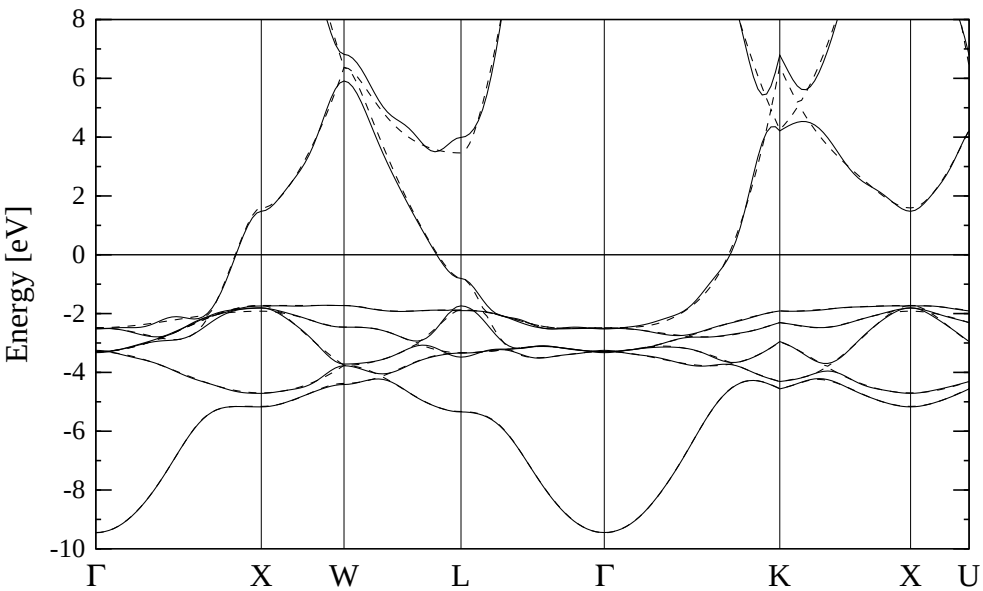

Figure 5.2: Same as Fig. 5.1, except now the sum is truncated after 30 shells. Note that the mismatch of the two curves is still significant at points along the symmetry lines where band crossings occur.

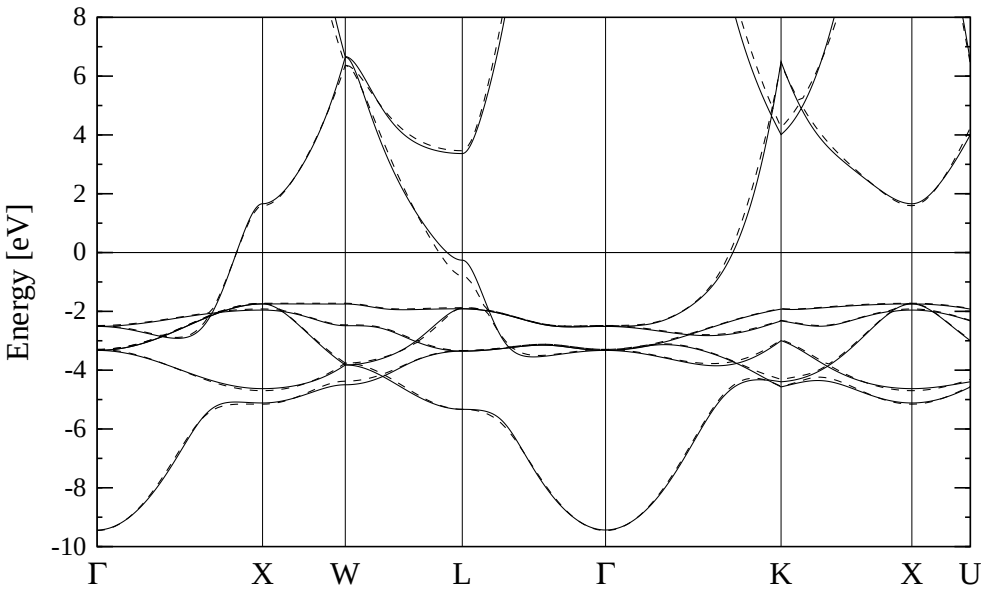

Figure 5.3: Hartree band structure of copper (dashed) and energy eigenvalues of $\sum_{\mathbf{R}} e^{-i\mathbf{k}\mathbf{R}} H_{\mathbf{R}nm}$ where the sum is truncated after 5 shells (solid). Again with energy relative to the Fermi energy.

Example 2

Example 1 has clearly shown that an isolated treatment of the bands leads to slowly decaying matrix elements $H_{\mathbf{R}nn}$. We now take a look at the case where the Wannier functions arise from a composite treatment of Bloch eigenfunctions of H. Except this detail, the current example equals the preceeding. Since the basis orbitals are generalized Wannier functions, $H_{\mathbf{R}nm}$ is no longer diagonal, and the $H_{\mathbf{R}nm}$'s need to be evaluated as matrix elements as described above. We can, however, since we are still considering case A, use Eq. (5.28) avoiding the explicit evaluation of (5.21) and the integration in (5.25).

Figure 5.3 shows the eigenvalues of 5.32 where only 5 shells (79 sites) have been included in the $\mathbf{R}$-sum. The agreement (for this truncation) is much better than in the preceeding example. Especially at band crossings an accurate reproduction is achieved. From Tab. 4.1, we see that the Wannier functions are very well localized. Accordingly, the matrix elements $H_{\mathbf{R}nm} = \langle \mathbf{R}n|H|\mathbf{0}m\rangle$ decay with larger $\mathbf{R}$.

In this connection, we note that Tab. 4.1 shows the averaged *densities* and not averaged wavefunctions themselves. Also note that, unlike the Fourier components of the band structure, the $H_{\mathbf{R}nm}$ (we are dealing with now) are gauge-dependent.

To summerize, we note that the use of such a small number of shells in the $\mathbf{R}$-sum was only made possible by using rapidly decaying Wannier functions which, in turn, lead to rapidly decaying matrix elements $\langle \mathbf{R}n|H|\mathbf{0}m\rangle$.

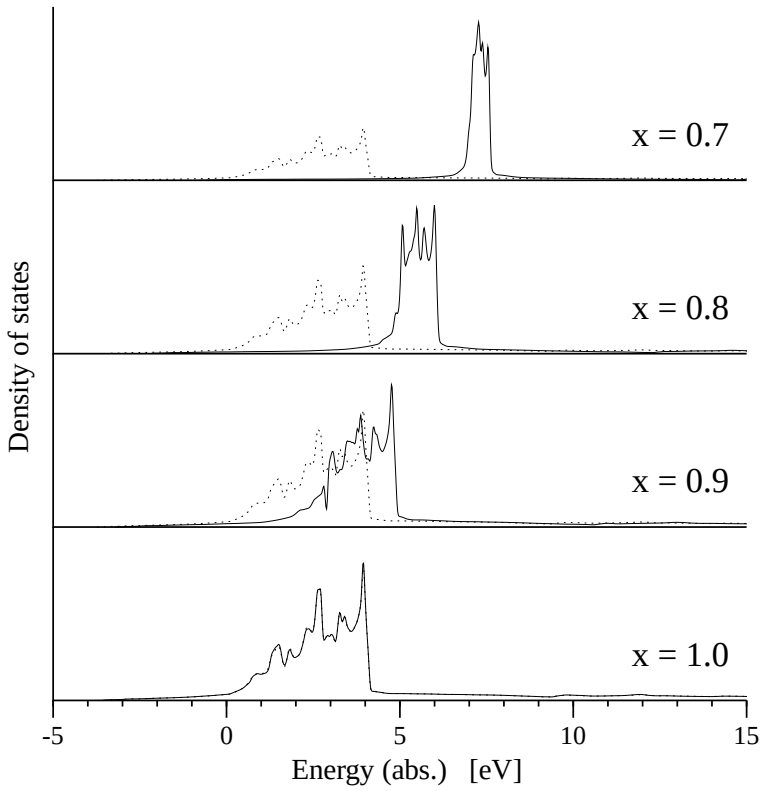

Figure 5.4: Hartree density of states (dashed) and density of states obtained from energy eigenvalues of (5.32) where the sum is truncated after 9 shells (solid) for some x.

Example 3

We now take a look at the general case B where the Wannier functions are obtained from H' which is not necessarily equal to the Hamiltonian H whose matrix elements are evaluated. The Hamiltonian H will be the same as in the preceeding examples 1 and 2. We choose H' to be dependent on an extra variable x which controls the disagreement of $H'(x)$ with H, i.e.:

$$H'(x) = -\nabla^2 + (1-x)\, v_0 + x\, v_{\mathrm{H}} \tag{5.37}$$

Where v_0 and v_{H} are given by (3.48) and (3.47), such that $H'(1) = H$, i.e. the Hartree Hamiltonian, and $H'(0) = H_0$ is the effective Hamiltonian for the situation when the Coulomb repulsion among the valence electrons is artificially switched off (see section 3.5). For some x, we have: (i) obtained the Wannier functions (which depend of x). (ii) calculated the matrix elements for H. (iii) re-calculated the band structure via (5.32). (iv) calculated the density of states using the tetrahedron method. Clearly for $x = 1$, the re-obtained DOS is in very good agreement with the DOS obtained from the band structure directly (Fig. 5.4). This is just the example 2 (expressed in terms of the DOS).

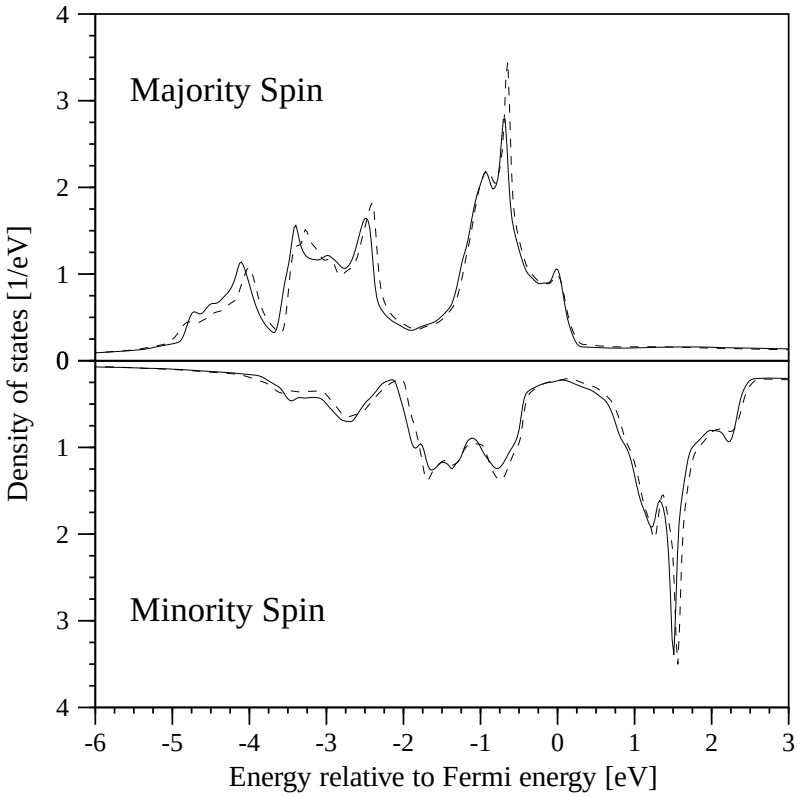

Figure 5.5: Density of states for spin-polarized iron from LSDA (dashed) and the DOS obtained from the matrix elements $\langle \mathbf{R}n|H^{\sigma}_{\mathrm{LSDA}}|\mathbf{0}m\rangle$ (solid). Again, the sum in (5.32 was truncated after 9 shells.

For x further away from 1, the disagreement between the curves becomes more and more significant, since the generalized Wannier functions span the one-particle space of $H'(x)$, limited to a few orbitals. So, when x is away from 1, the space spanned by these orbitals is not appropriate for expanding H.

Consider the situation for $x = 0$ (not shown in figure): The $3d$-like Wannier functions are very core-like, as Fig. 3.7 suggests. Hence, being extremely localized, they don't allow hopping matrix elements $\langle \mathbf{R}n|H|\mathbf{0}m\rangle$ with next neighbor $\mathbf{R}$'s (for $3d$-orbitals) to be large. Accordingly, the $3d$-bands turn out to become too narrow for decreasing x.

Example 4

While the preceeding examples have been designed to illustrate the various cases and to check the numerical correctness of our calculations, the example we will now look at is of more practical use.

We consider the spin-polarized DFT calculation for BCC iron, whose density of states is shown in Fig. 7.2. A result of this LSDA calculation is the potential $v^{\sigma}_{S}(\mathbf{r})$ which defines

the spin-dependent effective Hamiltonian $H^{\sigma}_{\mathrm{LSDA}}$. Our minimal basis of Wannier functions is considered independent of spin, however. Hence, we have (in addition) performed a self-consistent Hartree calculation for iron which is *not* spin-polarized, since v^{σ}_{xc} is the only spin-dependent term in (2.42), see page 23. Through the Hartree Hamiltonian H', we obtain a basis set of (spin-independent) Wannier functions. The spectra of H' and $H^{\sigma}_{\mathrm{LSDA}}$ are not too different[13], hence we may expand $H^{\sigma}_{\mathrm{LSDA}}$ in terms of these Wannier functions and obtain the spin-polarized DOS.

Figure 5.5 shows a comparison of the DOS from LSDA and the DOS re-calculated from the matrix elements $\langle \mathbf{R}n|H^{\sigma}_{\mathrm{LSDA}}|\mathbf{0}m\rangle$ for both spin directions. The agreement of the two curves is very good, which means that an expansion in terms of spin-independent orbitals for a magnetic material is possible. This is desirable, since it reduces the number of orbitals by a factor of two. Moreover, if we had to include all the spin-dependent orbitals, the number of Coulomb matrix elements, which is already large, would increase by a factor of $2^4 = 16$.

We should mention that iron was deliberately chosen for this example, since iron has the largest magnetic moment. The expansion works even better for cobalt and nickel.

5.3 Coulomb Interaction

Our methods developed to evaluate the Coulomb interaction term in Wannier representation will be described next. The Coulomb matrix elements are given by:

$$W_{12,34} = \int d^3\mathbf{r}\, d^3\mathbf{r}' \;\; w_1^*(\mathbf{r})\, w_2^*(\mathbf{r}') \;\; \frac{e^2}{|\mathbf{r}-\mathbf{r}'|} \;\; w_3(\mathbf{r}')\, w_4(\mathbf{r}) \tag{5.38}$$

Here, we use the abbreviated notation 1 to mean $\mathbf{R}_1 n_1$ and 2 to mean for $\mathbf{R}_2 n_2$, etc. Let us first take a brief look at general properties of the matrix elements which are useful for minimizing computing time and memory storage. From (5.38) and (4.4), it follows that

$$W_{12,34} = W_{(\mathbf{R}_1-\mathbf{R}_4 n_1)(\mathbf{R}_2-\mathbf{R}_4 n_2),(\mathbf{R}_3-\mathbf{R}_4 n_3)(\mathbf{0} n_4)} \;\; . \tag{5.39}$$

That is, we may always translate the lattice site indices in a way that $\mathbf{R}_4 \to \mathbf{0}$. Hence, we can define:

$$W_{12,34} \equiv W^{\mathbf{R}_1-\mathbf{R}_4;\mathbf{R}_2-\mathbf{R}_4;\mathbf{R}_3-\mathbf{R}_4}_{n_1 n_2, n_3 n_4} \tag{5.40}$$

Moreover, since $\mathbf{r}$ and $\mathbf{r}'$ in (5.38) can be interchanged, we have $W_{12,34} = W_{21,43}$ and since W is Hermitian, we have $W_{12,34} = W^*_{43,21}$. It follows that:

$$W^{\mathbf{R}_1;\mathbf{R}_2;\mathbf{R}_3}_{n_1 n_2, n_3 n_4} = W^{\mathbf{R}_2-\mathbf{R}_3;\mathbf{R}_1-\mathbf{R}_3;-\mathbf{R}_3}_{n_2 n_1, n_4 n_3} = \tag{5.41}$$

$$\left(W^{-\mathbf{R}_1;\mathbf{R}_3-\mathbf{R}_1;\mathbf{R}_2-\mathbf{R}_1}_{n_4 n_3, n_2 n_1}\right)^* = \left(W^{\mathbf{R}_3-\mathbf{R}_2;-\mathbf{R}_2;\mathbf{R}_1-\mathbf{R}_2}_{n_3 n_4, n_1 n_2}\right)^*$$

[13] We have not plotted the DOS of H', but we note that all bands are in the same energy regions (within some eV), unlike the huge discrepancy in example 3.

We will use these relations in chapter 6. Now, we explore the fact the Wannier functions are given by (4.6). The spatial integrals in (5.38) are extended over all space. Inserting (4.6) into (5.38) and using translations (4.4) yields:

$$W_{12,34} = \sum_{\mathbf{R}\mathbf{R}'} W(12,34;\mathbf{R},\mathbf{R}') \tag{5.42}$$

The sum is over all lattice sites and the expression $W(12,34;\mathbf{R},\mathbf{R}')$ is defined by

$$W(12,34;\mathbf{R},\mathbf{R}') \equiv \int d^3\mathbf{r}\, d^3\mathbf{r}' \;\; w^*_{n_1}(\mathbf{R}_A;\mathbf{r})\, w^*_{n_2}(\mathbf{R}_B;\mathbf{r}') \;\times \tag{5.43}$$

$$\times \frac{e^2}{|\mathbf{r}-\mathbf{r}'+\mathbf{R}-\mathbf{R}'|} \;\; w_{n_3}(\mathbf{R}_C;\mathbf{r}')\, w_{n_4}(\mathbf{R}_D;\mathbf{r}) \quad ,$$

and the integrals are now only over the muffin-tin sphere at the origin. Here, we introduced the definitions:

$$\mathbf{R}_A \equiv \mathbf{R}-\mathbf{R}_1 \;\; , \quad \mathbf{R}_B \equiv \mathbf{R}'-\mathbf{R}_2 \;\; , \quad \mathbf{R}_C \equiv \mathbf{R}'-\mathbf{R}_3 \;\; , \quad \mathbf{R}_D \equiv \mathbf{R}-\mathbf{R}_4 \tag{5.44}$$

When evaluating $W(12,34;\mathbf{R},\mathbf{R}')$, we distinguish whether the sites $\mathbf{R}$ and $\mathbf{R}'$ are:

- Equal: $\mathbf{R} = \mathbf{R}'$
- Unequal: $\mathbf{R} \neq \mathbf{R}'$

Since the numerical evaluation of Coulomb integrals is very time consuming, we truncate the spacial extent of our Wannier functions. In terms of Eq. (5.43), this has the consequence that whenever one of the $\mathbf{R}_{A\ldots D}$ is beyond a certain number of shells, the contribution $W(12,34;\mathbf{R},\mathbf{R}')$ (to the total integral) is set to zero.[14] Further, this truncation has the consequence that the $\mathbf{R}\mathbf{R}'$-sum in (5.42) may be truncated too. In the following, we propose two methods to evaluate $W(12,34;\mathbf{R},\mathbf{R}')$. The first method, i.e. the spherical expansion method, is computationally very efficient and accurate, however, we have only applied this method to the case $\mathbf{R} = \mathbf{R}'$. Extending this method to the case in which $\mathbf{R} \neq \mathbf{R}'$ seems difficult, but possible by using the expressions in Ref. [53]. The second method is based on Fourier transforming the Coulomb interaction e^2/r and using the "fast Fourier transformation" (FFT). This method is not restricted to the case $\mathbf{R} = \mathbf{R}'$, but it is computationally more time consuming and not quite as accurate as the first method. As we will discuss in section 6.3.2, only contributions (5.43) for $\mathbf{R} = \mathbf{R}'$ will be required for our Hartree-Fock approach, however. Before turning to these methods, we wish to show how $W(12,34;\mathbf{R},\mathbf{R}')$ can be approximated for the case $\mathbf{R} \neq \mathbf{R}'$.

If we assume that the Wannier functions have a high charge density near the center of each atomic site, the contributions in (5.43) arising from small $|\mathbf{r}|$ and $|\mathbf{r}'|$ will be largest. Hence, we may approximately write

$$|\mathbf{r}-\mathbf{r}'+\mathbf{R}-\mathbf{R}'| \approx |\mathbf{R}-\mathbf{R}'| \qquad \text{where} \quad \mathbf{R}-\mathbf{R}' \neq \mathbf{0} \;\; . \tag{5.45}$$

[14] Remember that our Wannier functions $\mathbf{0}n$ are always constructed in a way that their contribution at the site $\mathbf{0}$ is largest.

In the limit $|\mathbf{R}-\mathbf{R}'| \to \infty$, this approximation will be correct, since $|\mathbf{r}|$ and $|\mathbf{r}'|$ are restricted to the Wigner-Seitz sphere. Inserting (5.45) into (5.43) gives

$$\frac{e^2}{|\mathbf{R}-\mathbf{R}'|} \int d^3\mathbf{r}\, w^*_{n_1}(\mathbf{R}_A;\mathbf{r})\, w_{n_4}(\mathbf{R}_D;\mathbf{r}) \int d^3\mathbf{r}'\, w^*_{n_2}(\mathbf{R}_B;\mathbf{r}')\, w_{n_3}(\mathbf{R}_C;\mathbf{r}') \quad (5.46)$$

as an approximation for $W(12,34;\mathbf{R},\mathbf{R}')$. Evaluating (5.46) is easy, since the two integrals can be calculated independently using Eqs. (5.24) and (5.26).

5.3.1 Spherical Expansion Method

As mentioned above, we will consider

$$I = W(12,34;\mathbf{R},\mathbf{R}) = \int d^3\mathbf{r}\, d^3\mathbf{r}'\;\; w^*_{n_1}(\mathbf{R}_A;\mathbf{r})\, w^*_{n_2}(\mathbf{R}_B;\mathbf{r}')\;\times \quad (5.47)$$

$$\times\, \frac{e^2}{|\mathbf{r}-\mathbf{r}'|}\;\; w_{n_3}(\mathbf{R}_C;\mathbf{r}')\, w_{n_4}(\mathbf{R}_D;\mathbf{r}) \quad ,$$

where the integrals are taken over the central site. Inserting the expansion (5.18) for the Wannier functions and making use of the well-known expansion[15]

$$\frac{1}{|\mathbf{r}-\mathbf{r}'|} = \sum_{k=0}^{\infty} \frac{4\pi}{2k+1}\, \frac{r_<^k}{r_>^{k+1}} \sum_{m=-k}^{k} Y^*_K(\hat{\mathbf{r}}')\, Y_K(\hat{\mathbf{r}}) \;\; , \qquad K=\{k,m\} \quad (5.48)$$

where $r_>$ ($r_<$) is the length of the greater (smaller) of the two vectors $\mathbf{r}$ and $\mathbf{r}'$, we find (using the abbreviation $L_{1\ldots4}$ to mean L_1, L_2, L_3, L_4):

$$I = \sum_{k,L_{1\ldots4}} e^2 \int dr\, r^2\, R^*_{1L_1}(r)\, R_{4L_4}(r) \int dr'\, r'^2\, R^*_{2L_2}(r')\, R_{3L_3}(r')\;\times \quad (5.49)$$

$$\times\;\; \frac{r_<^k}{r_>^{k+1}}\;\; \frac{4\pi}{2\ell+1} \sum_{m=-k}^{k} C_{L_4L_1K}\, C_{L_2L_3K}$$

Where the integrals are taken from 0 to the Wigner-Seitz radius S. The coefficients $C_{LL'L''}$ are called Gaunt coefficients, see appendix B, which are real and vanish unless the vector addition rules are satisfied. If we define[16]

$$C^k_{L_{1\ldots4}} \equiv \frac{4\pi}{2k+1} \sum_{m=-k}^{k} C_{L_4L_1K}\, C_{L_2L_3K} \quad (5.50)$$

$$I^k_{L_{1\ldots4}} \equiv e^2 \int dr\, r^2\, R^*_{1L_1}(r)\, R_{4L_4}(r) \int dr'\, r'^2\, R^*_{2L_2}(r')\, R_{3L_3}(r')\, \frac{r_<^k}{r_>^{k+1}} \;\; , \quad (5.51)$$

the integral takes the form:

$$I = \sum_{k,L_{1\ldots4}} C^k_{L_{1\ldots4}}\, I^k_{L_{1\ldots4}} \quad (5.52)$$

[15] See for example Eq. (3.70) in Ref. [52].

[16] Note that this definition differs by the factor of $4\pi/(2k+1)$ from the definition we used in Refs. [47, 28].

LMTO's	$s\,p$	$s\,p\,d$	$s\,p\,d\,f$
$k_{\max}$	2	4	6
$C^k_{L_{1\ldots4}}$	768	32,805	458,752
non-vanishing	47	806	6,778
diff. abs. values	7	64	414

Table 5.1: Here, $k_{\max}$ is the k-cutoff in (5.53). Next, the total number of coefficients $C^k_{L_{1\ldots4}}$ is given, which is easy to obtain, e.g. $7{\cdot}16^4$ = 458,752 . Hereafter, the number of non-vanishing $C^k_{L_{1\ldots4}}$ is shown. The last row shows the number of different *absolute* values which occur within the non-vanishing $C^k_{L_{1\ldots4}}$.

The task is now to determine $C^k_{L_{1\ldots4}}$ and $I^k_{L_{1\ldots4}}$. We start by looking at the easy part, i.e. the constants $C^k_{L_{1\ldots4}}$. Using Eq. (B.7), we can write (5.50) as

$$C^k_{L_{1\ldots4}} = \delta_{m_1-m_4,m_3-m_2}\; c^k(L_1,L_4)\; c^k(L_3,L_2) \;\; . \tag{5.53}$$

The coefficients $c^k(\ell'm',\ell''m'')$ are tabulated in Ref. [54], and in order to be non-vanishing, k must satisfy the conditions:[17]

$$|\ell'-\ell''| \le k \le \ell'+\ell'' \quad \text{and} \quad k+\ell'+\ell''=2g \qquad (g \text{ integral}) \tag{5.54}$$

Thus, in the practical case in which the expansion of the wave functions is truncated after e.g. f-orbitals, the seemingly infinite series occurring in (5.48), and thus the k-sums following, are limited. Furthermore, a large number of the remaining $C^k_{L_{1\ldots4}}$ vanish (Tab. 5.1). Since many of the coefficients $C^k_{L_{1\ldots4}}$ vanish, one should numerically only evaluate the integrals $I^k_{L_{1\ldots4}}$ for the indices k, L_1, L_2, L_3, L_4 for which $C^k_{L_{1\ldots4}}$ are non-vanishing.

We now consider the remaining term $I^k_{L_{1\ldots4}}$. To do this, we will use the formalism developed in section 5.2. In complete analogy to Eqs. (5.24), (5.25), we now find

$$I^k_{L_{1\ldots4}} = \sum_{p_{1\ldots4}} a_{L_{1\ldots4}p_{1\ldots4}}\; b^k_{\ell_{1\ldots4}p_{1\ldots4}} \;, \tag{5.55}$$

where

$$a_{L_{1\ldots4}p_{1\ldots4}} = A^*_{1L_1;p_1} A^*_{2L_2;p_2} A_{3L_3;p_3} A_{4L_4;p_4} \tag{5.56}$$

$$b^k_{\ell_{1\ldots4}p_{1\ldots4}} = e^2 \int dr\, r^2\, \phi_{\ell_1;p_1}(r)\, \phi_{\ell_4;p_4}(r) \int dr'\, r'^2\, \phi_{\ell_2;p_2}(r')\, \phi_{\ell_3;p_3}(r')\, \frac{r^k_<}{r^{k+1}_>} \;\; . \tag{5.57}$$

It should be noted that these basic integrals are symmetric with respect to some of their indices. If we introduce the joined index $n_1 = \{\ell_1, p_1\}$, etc. then:

$$\begin{aligned} b^k_{n_1n_2n_3n_4} &= b^k_{n_4n_2n_3n_1} = b^k_{n_1n_3n_2n_4} = b^k_{n_4n_3n_2n_1} = \\ &= b^k_{n_2n_1n_4n_3} = b^k_{n_2n_4n_1n_3} = b^k_{n_3n_1n_4n_2} = b^k_{n_3n_4n_1n_2} \end{aligned} \tag{5.58}$$

[17] See Eq. (10) on p. 176 in [54].

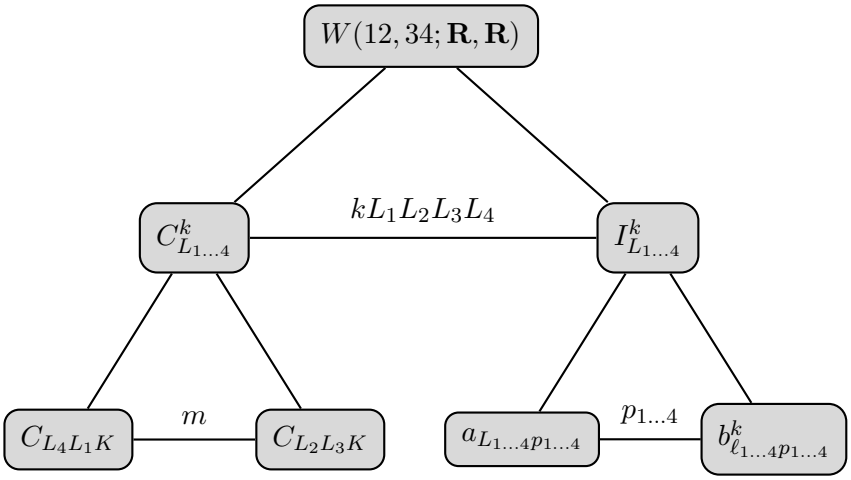

Figure 5.6: Decomposition of integral (5.47). On top of each of the horizontal lines, the indices over which a summation is performed are shown.

Also, we should mention that the (rather cumbersome) special cases appearing in the last term in (5.57), i.e. $r' < r$ or $r' > r$, may be avoided by splitting the r' integral into two integrals. We find a form which is more convenient for numerical evaluation:

$$\begin{aligned} \frac{b^k_{n_{1\ldots4}}}{e^2} &= \int_0^S dr\, r^{1-k}\, \phi_{n_1}(r)\, \phi_{n_4}(r) \int_0^r dr'\, r'^{k+2}\, \phi_{n_2}(r')\, \phi_{n_3}(r') \;+ \\ &+ \int_0^S dr\, r^{k+2}\, \phi_{n_1}(r)\, \phi_{n_4}(r) \int_r^S dr'\, r'^{1-k}\, \phi_{n_2}(r')\, \phi_{n_3}(r') \end{aligned} \tag{5.59}$$

Finally, we can take a look at Fig. 5.6 which shows the steps involved in decomposing the integral (5.47). Remember that the integral (5.47) is not the complete Coulomb integral (5.38), it is only a contribution to the complete integral in Eq. (5.38). If we would consider *atomic* wave functions, it would be the complete Coulomb integral, however. For atomic wave functions, many of the expressions become very simple, since a (non-relativistic) atomic wave function is not an expansion in terms of spherical harmonics, but rather a *single* radial function multiplied by a spherical harmonic. We used this method for evaluating the Coulomb matrix elements for the hydrogen atom wave functions, see appendix C.2.

5.3.2 FFT Method

The method we have just described is very accurate and computationally efficient, but it is restricted to the case $\mathbf{R} = \mathbf{R}'$. Furthermore, it uses the spherical expansion of the linearized wave functions, and may seem a little sophisticated[18]. Sometimes, however, Coulomb ma-

[18]Hence, implementation may seem hard, with all the Gaunt coefficients, summations, integrations, etc. .

trix elements may not be required to such an accuracy, and if only a few matrix elements are needed, the following method, which evaluates the matrix elements in a rigorous way, is recommended. Moreover, it is always good to be able to calculate the same quantities with different methods, allowing to compare results, e.g. for debugging.

To calculate $W(12,34;\mathbf{R},\mathbf{R}')$ for any lattice sites $\mathbf{R}$ and $\mathbf{R}'$, we make use of the Fourier transformation[19]

$$\int d^3\mathbf{q}\,\frac{e^{i\mathbf{q}\mathbf{r}}}{q^2} = \frac{2\pi^2}{|\mathbf{r}|} \tag{5.60}$$

and find for Eq. (5.43):

$$W(12,34;\mathbf{R},\mathbf{R}') = \frac{e^2}{2\pi^2}\int d^3\mathbf{q}\,\frac{1}{q^2}\,e^{i\mathbf{q}(\mathbf{R}-\mathbf{R}')}\,f_1(\mathbf{q})\,f_2(-\mathbf{q}) \tag{5.61}$$

where

$$f_1(\mathbf{q}) = \int d^3\mathbf{r}\,e^{i\mathbf{q}\mathbf{r}}\,w^*_{n_1}(\mathbf{R}_A;\mathbf{r})\,w_{n_4}(\mathbf{R}_D;\mathbf{r}) \tag{5.62}$$

$$f_2(\mathbf{q}) = \int d^3\mathbf{r}\,e^{i\mathbf{q}\mathbf{r}}\,w^*_{n_2}(\mathbf{R}_B;\mathbf{r})\,w_{n_3}(\mathbf{R}_C;\mathbf{r}) \tag{5.63}$$

These functions are just the Fourier transforms of a product of some Wannier functions in a muffin-tin sphere. These can be calculated very efficiently by evaluating the Wannier functions on a cubic mesh in $\mathbf{r}$-space with some Δx (the distance between the mesh points) and then applying a standard FFT algorithm. To do this, we have used the routine `fourn` in Ref. [48]. For details on how to apply the FFT to continuous functions, Ref. [55] is very useful. The result of this Fourier transformation is $f_{1,2}(\mathbf{q})$ on a cubic mesh in $\mathbf{q}$-space with some Δq. We perform the remaining $\mathbf{q}$-integral in the following way. Let us call the integrand in (5.61) without the q^{-2} term

$$F(\mathbf{q}) = e^{i\mathbf{q}(\mathbf{R}-\mathbf{R}')}\,f_1(\mathbf{q})\,f_2(-\mathbf{q})\ . \tag{5.64}$$

Since $F(\mathbf{q})$ is a smooth function at $\mathbf{q}=\mathbf{0}$, a divergence arises in the complete integrand from q^{-2}. In order to treat this divergence, we split the integral by subtracting and adding $F(\mathbf{0})$:

$$\int d^3\mathbf{q}\,\frac{F(\mathbf{q})}{q^2} = \int d^3\mathbf{q}\,\frac{F(\mathbf{q})-F(\mathbf{0})}{q^2} + F(\mathbf{0})\int d^3\mathbf{q}\,\frac{1}{q^2} \tag{5.65}$$

The first non-vanishing term of a polynomial expansion of the numerator $F(\mathbf{q})-F(\mathbf{0})$ is of order q^2 (see section 5.3.3). Hence, the polynomial expansion of the integrand starts with a constant and the divergence is avoided.

[19] It is straightforward to do the integral using spherical coordinates and using

$$\int_0^\infty dx\,\frac{\sin x}{x} = \frac{\pi}{2}\ .$$

All integrals are over a cube with length $2p = N\Delta q$. The first integral in (5.65) is evaluated by transforming the integral into a sum over little cubes with volume $(\Delta q)^3$. At $\mathbf{q} = \mathbf{0}$, the value of the integrand is calculated via the second derivative of $F(\mathbf{q})$ at $\mathbf{q} = \mathbf{0}$ numerically.

The remaining integral in (5.65) is simply a constant given by:

$$\int_{-p}^{+p} dq_x \int_{-p}^{+p} dq_y \int_{-p}^{+p} dq_z \, \frac{1}{q^2} = p \int_{-1}^{+1} dq_x \int_{-1}^{+1} dq_y \int_{-1}^{+1} dq_z \, \frac{1}{q^2} = p \cdot C \tag{5.66}$$

Where a change in the variables was made, and $C = 15.34825$, which we have evaluated in the appendix C.4.

The cubic grid in real space we use in (5.62) (and in (5.63)) has $N^3 = 128^3$ points with spacing $\Delta x = 0.1a_0$. In applying the FFT to continuous Fourier transformations, the spacing of the $\mathbf{q}$-mesh is determined by N and Δx, i.e. $\Delta q = 2\pi/(N\Delta x) \approx 0.49/a_0$. Using the FFT, one has to be very careful about the choice of these values, since the FFT is a discrete Fourier transformation. In particular, it is important to make sure that the results of a FFT calculation do not depend on the values N and Δx (see section 5.3.4).

Note that each integral in (5.62), (5.63) could be calculated from the spherical-harmonic expansions (using the expressions in appendix C.5). However, a large number of such integrals, for all the $\mathbf{q}$-points, would be required and the method would become (computationally) extremely expensive. An FFT algorithm generates *all* the $\mathbf{q}$ values needed with a single calculation and is much more efficient. However, because of finite mesh sizes and compromises between real and $\mathbf{q}$-space integrals, it is not as accurate as the spherical expansion method, when the latter is applicable.

Yukawa Potential

Finally, it should be mentioned that this method can easily be extended to a Yukawa potential (which is a screened Coulomb potential), i.e. instead of (5.60) we use[20]

$$\frac{e^{-\alpha r}}{|\mathbf{r}|} = \frac{1}{2\pi^2} \int d^3\mathbf{q} \, \frac{e^{i\mathbf{q}\mathbf{r}}}{q^2 + \alpha^2} \quad . \tag{5.67}$$

Note that Eq. (5.65) is not required anymore, because the divergence in the integrand has disappeared. Nevertheless, when (5.65) is evaluated as a sum over small cubes, a large contribution arises from the cube around $\mathbf{q} = \mathbf{0}$ when α is small. Therefore, this contribution is treated separately to achieve higher precision: We assume $F(\mathbf{q})$ to be constant within this cube (of size $(\Delta q)^3$) and evaluate its contribution to the total integral as:

$$F(\mathbf{0})\, 4\pi \int_0^{q_0} dq \, \frac{q^2}{q^2 + \alpha^2} = F(\mathbf{0})\, 4\pi \, \left(q_0 - \alpha \arctan \frac{q_0}{\alpha} \right) \quad , \quad q_0 = \Delta q \left(\frac{3}{4\pi} \right)^{\frac{1}{3}} \tag{5.68}$$

That is, we approximate the cube by a sphere of equal volume (with radius q_0) and treat the remaining integral analytically. All other cubes are treated regularly.

[20] Again, the integral may straightforwardly be carried out in spherical coordinates. See also Ref. [44].

5.3.3 Analytical Test Case

We wish to illustrate both methods for a simple artificial wave function, which allows the evaluation of all integrals analytically. Moreover, this test case serves as a reference for checking the numerical correctness of the methods, especially the accuracy of the FFT method. We choose the wave function to be constant within a radius of a_0 (the Bohr radius) and zero elsewhere. Since we use atomic Rydberg units (in which $a_0 = 1$), we have

$$\psi(\mathbf{r}) = \begin{cases} \sqrt{\frac{3}{4\pi}} & r \leq 1 \\ 0 & r > 1 \end{cases} \qquad \text{with density } n(\mathbf{r}) = |\psi(\mathbf{r})|^2 = \begin{cases} \frac{3}{4\pi} & r \leq 1 \\ 0 & r > 1 \end{cases} \quad , \tag{5.69}$$

which is normalized to unity. Using both methods, we will evaluate the Coulomb energy

$$U = \int d^3\mathbf{r}\, d^3\mathbf{r}' \; \frac{e^2\, n(\mathbf{r})\, n(\mathbf{r}')}{|\mathbf{r} - \mathbf{r}'|} = W(\psi\psi, \psi\psi; \mathbf{0}, \mathbf{0}) \quad . \tag{5.70}$$

Spherical expansion method:

The spherical harmonics expansion of the wave function, i.e. $\psi(\mathbf{r}) = \sum_L R_L(r) Y_L(\hat{\mathbf{r}})$, is (trivially)

$$R_L(r) = \delta_{\ell,0} \cdot \begin{cases} \sqrt{3} & r \leq 1 \\ 0 & r > 1 \end{cases} \qquad \text{, since } Y_0^0(\vartheta, \varphi) = \frac{1}{\sqrt{4\pi}} \quad . \tag{5.71}$$

That is an "s-wave" function. Hence, the k-cutoff in (5.53) equals zero due to $k \leq \ell' + \ell'' = 0$. Accordingly, the multiple sum (5.52) reduces to $U = C^0_{0000}\, I^0_{0000}$. From (5.50) and the definition of the Gaunt coefficients, it is easy to see that $C^0_{0000} = 1$. We only need to evaluate I^0_{0000}, where we can split the integral as in Eq. (5.59):

$$U = I^0_{0000} = 9e^2 \left[\int_0^1 dr\, r \int_0^r dr'\, r'^2 + \int_0^1 dr\, r^2 \int_r^1 dr'\, r' \right] = 18 \left[\frac{1}{15} + \frac{1}{15} \right] \tag{5.72}$$

Hence, our final result is $U = 2.4\ \mathrm{Ryd}$.

FFT method:

First, we need to evaluate the Fourier transform (5.62), which is straightforwardly done in spherical coordinates

$$f(\mathbf{q}) = \int d^3\mathbf{r}\, e^{-i\mathbf{q}\mathbf{r}}\, n(\mathbf{r}) = \frac{3}{4\pi} \int_{r \leq 1} d^3\mathbf{r}\, e^{-i\mathbf{q}\mathbf{r}} = \frac{3(\sin q - q\cos q)}{q^3} \equiv f(q) \ , \tag{5.73}$$

which is a smooth function everywhere. Note that $f(-\mathbf{q}) = f(\mathbf{q})$. In the limit for small q, we find $f(\mathbf{q}) \approx 1 - q^2/10$, by expanding sin and cos. Thus $f(\mathbf{0}) = 1$, as is also evident from normalization. Now, for small q, the function $F(\mathbf{q}) = f^2(\mathbf{q})$ is approximately $1 - q^2/5$.

Accordingly, the first non-vanishing term of the polynomial expansion of the numerator $F(\mathbf{q}) - F(\mathbf{0})$ in (5.65) is $-q^2/5$. Hence, the polynomial expansion of the corresponding integrand in (5.65) starts with a constant and divergence at $\mathbf{q} = \mathbf{0}$ is avoided. However, doing the calculation analytically, we are not worried about this divergence, since another q^2-term arises if we perform the integration of $F(\mathbf{q})/q^2$ in spherical coordinates. That is,[21]

$$U = \frac{1}{\pi^2} \int d^3\mathbf{q}\, \frac{F(\mathbf{q})}{q^2} = \frac{4}{\pi} \int_0^\infty dq\, f^2(q) = \frac{4}{\pi}\, \frac{3^2\pi}{15} = 2.4\,\mathrm{Ryd}\ , \tag{5.74}$$

which equals our previous result. Performing this calculation numerically (using FFT), we obtain a result of $U = 2.38$ Ryd.[22] In addition, we are in a position to numerically obtain $f(\mathbf{q})$ by Fourier transforming our test wave function (on the $\mathbf{r}$-mesh), as we would within the FFT method, and compare the result with the analytical expression in Eq. (5.73). This comparison was made as well, and the agreement is also very good.[23]

5.3.4 Numerical Comparisons and Results

Choice of N and Δx in FFT Method

Firstly, note that when applying the FFT (which is a discrete Fourier transformation) onto continuous Fourier transformations, Δx and Δq are not independent of each other, but $N = 2\pi\Delta x\Delta q$. Moreover, within the FFT, N is always a power of two.

As mentioned above, it is important to make sure that the results of the FFT method do not depend on the values N and Δx. In order to find a good choice for these values, which determine the spacing of the $\mathbf{q}$-mesh $\Delta q = 2\pi/(N\Delta x)$, we picked out a typical Wannier function and applied the FFT method for various values of N and Δx.

We have chosen the 2nd Wannier function from the Hartree calculation of copper in the central site, whose localization properties are shown in Tab. 4.1. For this Wannier function, we evaluate the term (5.61) with $\mathbf{R} = \mathbf{R}' = \mathbf{0}$, which is by far the most dominant contribution to the total Coulomb energy in Eq. (5.42), since this Wannier function is very localized, as can be seen from Tab. 4.1. First, we have calculated the interaction energy using the spherical expansion method, yielding 27.60 eV, which serves as a reference. The energies obtained from FFT method are shown in Fig. 5.7.

When Δx is chosen too small, the $(N\Delta x)^3$ cube in real space does not cover the complete Wigner-Seitz sphere (just a small fraction), and the evaluated energy turns out smaller than the correct value. On the other hand, when Δx is chosen too big, the $(N\Delta q)^3$ cube in $\mathbf{q}$-space becomes too small and our final $\mathbf{q}$-summation misses points. This is the explanation

[21] Here, we used:

$$\int_0^\infty dx\, \frac{(\sin x - x\cos x)^2}{x^6} = \frac{\pi}{15}$$

[22] For a choice of $N = 128$ and $\Delta x = 0.1$, see below.

[23] If we had bad agreement, our numerically result of $U = 2.38$ Ryd would probably not be in such good agreement with the analytically result (5.74) either.

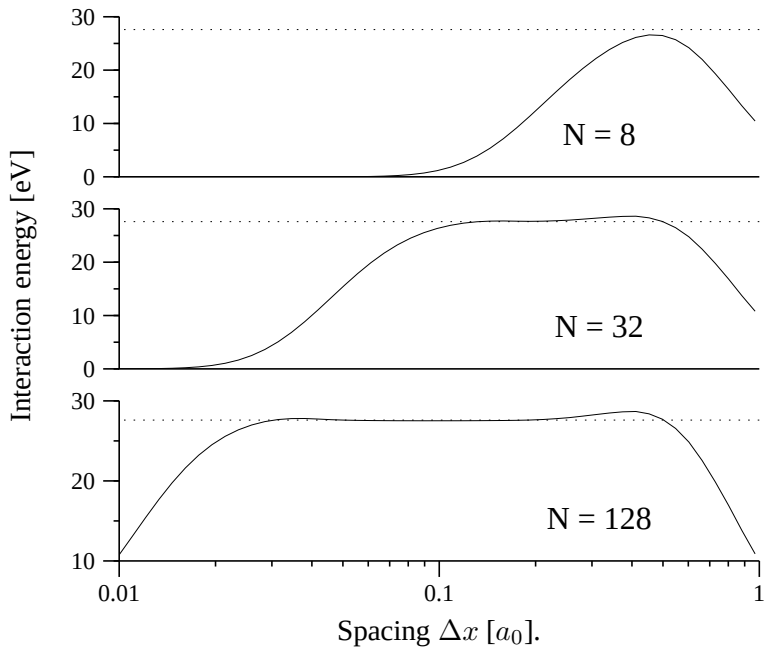

Figure 5.7: FFT method applied to a $3d$-like Wannier function of copper using various choices of N and Δx (solid); The reference value is 27.60 eV (dashed).

for the behavior of the curves in Fig. 5.7 for all N. When N itself is too small, points are neglected both in **r**-space and in **q**-space. Hence, the method does not work when N is too small.

For large N, e.g. 128, we have the freedom to choose Δx, and as can be seen very clearly from Fig. 5.7, the evaluated energy is not affected by this choice. Moreover, the energy is almost in perfect agreement with our result from the spherical expansion method. For our further calculations, we therefore choose $N = 128$ and $\Delta x = 0.1a_0$, i.e. in the middle of the flat plateau. Since the plateau is approximately one decade wide, we expect this choice to be secure for other Wannier functions too.

Computational Remark: Since Δx and Δq are not independent of each other, one always has to compromise, unless N is chosen very large. However, this may not be possible since there are N^3 points for which complex values need to be stored: 128^3 double precision complex numbers require 32 MB of memory; and for 256^3 points we already need 256 MB. In addition, the computing time of the FFT increases with $N^3 \log_2 N$, which is of course much better than without using FFT, where computing time would increase by N^6.

Comparison of Both Methods

$m =$	0	1	2	3	4	5	6	7	8
$n = 0$	23.91	22.81	24.18	23.85	22.95	14.42	14.00	14.06	13.66
	23.85	22.75	24.11	23.79	22.88	14.39	13.97	14.03	13.63
$n = 1$	22.81	25.38	24.92	24.62	23.36	14.48	14.16	13.73	14.53
	22.75	25.31	24.85	24.55	23.29	14.45	14.12	13.69	14.49
$n = 2$	24.18	24.92	27.60	25.28	24.25	15.08	14.98	14.12	14.46
	24.11	24.85	27.51	25.20	24.18	15.04	14.94	14.09	14.42
$n = 3$	23.85	24.62	25.28	27.57	25.01	14.64	14.82	14.64	14.36
	23.79	24.55	25.20	27.49	24.94	14.60	14.78	14.60	14.32
$n = 4$	22.95	23.36	24.25	25.01	25.19	14.33	14.03	14.21	14.26
	22.88	23.29	24.18	24.94	25.11	14.30	14.00	14.18	14.23
$n = 5$	14.42	14.48	15.08	14.64	14.33	14.01	10.04	9.52	9.91
	14.39	14.45	15.04	14.60	14.30	13.99	10.04	9.52	9.91
$n = 6$	14.00	14.16	14.98	14.82	14.03	10.04	13.90	9.59	9.60
	13.97	14.12	14.94	14.78	14.00	10.04	13.88	9.59	9.60
$n = 7$	14.06	13.73	14.12	14.64	14.21	9.52	9.59	13.70	9.48
	14.03	13.69	14.09	14.60	14.18	9.52	9.59	13.69	9.49
$n = 8$	13.66	14.53	14.46	14.36	14.26	9.91	9.60	9.48	13.77
	13.63	14.49	14.42	14.32	14.23	9.91	9.60	9.49	13.75

Table 5.2: Direct inter-band terms U_{nm} obtained from the spherical expansion method (upper line) and U_{nm} obtained from FFT method (below). Note that (from Eq. (5.41)) $U_{nm} = U_{mn}$ and the $U_{nm} = U^*_{nm}$, i.e. U_{nm} is real. All energies are in electron Volts.

In the preceeding section, it has already been shown that very good agreement of the two methods is achieved. Again, we consider (5.43) with $\mathbf{R} = \mathbf{R}' = \mathbf{0}$ for the Wannier function from the Hartree calculation of copper in the central site; but now we will look at all the direct inter-band terms, explicitly:[24]

$$U_{nm} = W(\mathbf{0}n\mathbf{0}m, \mathbf{0}m\mathbf{0}n; \mathbf{0}, \mathbf{0}) \tag{5.75}$$

The contribution of this energy to the total Coulomb energy strongly depends on the localization of the Wannier functions. However, since all the Wannier functions under consideration are well localized, the U_{nm} may serve as a first estimate of direct inter-band Coulomb matrix elements with maximally localized Wannier functions from a Hartree calculation. These are shown in Tab. 5.2. Again, the energies are in excellent agreement for the two methods.

[24] Above, we were only looking at U_{22}.

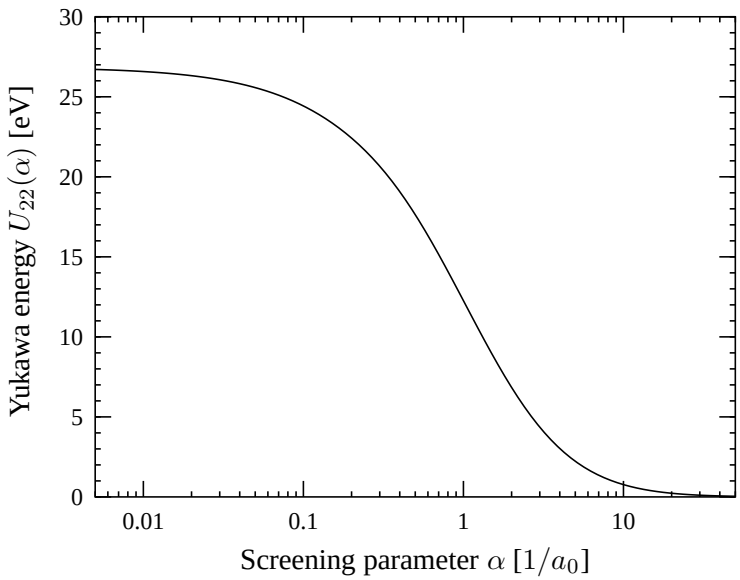

Figure 5.8: Screening of Coulomb interaction U_{22} using the FFT method.

Yukawa Potential

As an example of the effect of screening, we have, for the U_{22} Coulomb matrix element, included screening by using the Yukawa potential and applying the FFT method using Eqs. (5.67) and (5.68). The result of this calculation is shown in Fig. 5.8. Since the Wannier function w_2 is extremely well localized, the curve may be regarded as the total Yukawa interaction energy. Clearly, for $\alpha \to 0$, the Yukawa matrix element approaches the value of the Coulomb matrix element.[25] For $\alpha \to \infty$, we find the Yukawa energy approaching zero, which is evident from the RHS of Eq. (5.67). Note that we have used a logarithmic axis α to plot $U_{22}(\alpha)$, which makes these two features, i.e. the limits $\alpha \to 0$ and $\alpha \to \infty$, more visible to the eye. The overall shape of the curve is not very surprising: With increasing screening, the matrix element becomes smaller. Some screened Coulomb matrix elements for lithium have also been calculated in Ref. [56] using the FFT method.

5.3.5 Coulomb d-matrix

In our work, we are using a minimal basis of orthogonal localized Wannier functions for expanding the field operators (5.2). These Wannier functions then appear in the matrix elements Eq. (5.3). However, often other basis sets are being used. One could start from a set of (overlapping) "quasi atomic" orbitals, i.e. a radial wave function times a spherical harmonic, at each lattice site $\mathbf{R}$. As a consequence, our basis would be characterized by $L = \{\ell, m\}$ and $\mathbf{R}$ which has certainly many advantages, but this characterization implies that the basis is non-orthogonal, since the crystal lattice has no continuous rotation

[25] We actually obtain a slightly different value, since the divergence is treated differently using (5.68) and not using (5.65). The later treatment is numerically more precise, however. Note that, from (5.67), we see that for $\alpha = 0$ (no screening) the Yukawa potential *is* the Coulomb potential.

symmetry. However, the formalism of second quantization demands an orthogonal basis, which may be obtained from the non-orthogonal basis via the so-called Löwdin transformation [57]. Here, the transformed basis functions are linear combinations of different quasi atomic orbitals from different sites.[26] These Löwdin orbitals are orthogonal, but no longer characterized by $L = \{\ell, m\}$ and less localized than the quasi atomic orbitals, they have more similarity with localized Wannier orbitals.

Nevertheless, despite these complications, if we use atomic orbitals, the basis is characterized by $L = \{\ell, m\}$ which allows us to completely isolate the (on-site) Coulomb interaction among (pure) $3d$-states. We write our (quasi) atomic d-wave function as:

$$\psi_m(\mathbf{r}) = R_{\ell=2}(r) Y^m_{\ell=2}(\vartheta, \varphi) \qquad m = \{-2, -1, 0, +1, +2\} \tag{5.76}$$

Hence, if we use Eqs. (5.49) to (5.52) and set $\ell_1 = \ldots = \ell_4 = 2$, we obtain:[27]

$$W_{m_{1\ldots4}} = \sum_{k=0,2,4} C^k_{m_{1\ldots4}} F^k \tag{5.77}$$

This is the Coulomb d-matrix which contains interaction matrix elements between the various d-orbitals. The coefficients F^k are the so-called Slater integrals [59] (sometimes also called "Racca coefficients") defined by:

$$F^k \equiv e^2 \int dr\, r^2 \int dr'\, r'^2\, |R_{\ell=2}(r)|^2\, \frac{r^k_<}{r^{k+1}_>}\, |R_{\ell=2}(r')|^2 \tag{5.78}$$

Note that only the three integrals F^0, F^2 and F^4 are required to determine all the Coulomb d-matrix elements. We may exploit properties of the Coulomb d-matrix in terms of F^k by examining the coefficients $C^k_{m_{1\ldots4}}$ which are defined by Eq. (5.53). From (5.54), we realize that the coefficients $C^k_{m_{1\ldots4}}$ vanish unless $k = \{0, 2, 4\}$ which justifies the restriction of the k-sum in (5.77) to these values. In the appendix C.7, we explicitly give the coefficients $C^k_{m_{1\ldots4}}$. Table C.2 enables us to determine averaged Coulomb interactions (5.77) in terms of Slater integrals F^k. An averaged direct Coulomb interaction U and an averaged exchange Coulomb interaction J may be defined as:[28]

$$U \equiv \frac{1}{25} \sum_{mm'} W_{mm'm'm} = F^0 \tag{5.79}$$

$$J \equiv \frac{1}{20} \sum_{m \neq m'} W_{mm'mm'} = \frac{2}{35} \left(F^2 + \frac{10}{9} \cdot F^4 \right) \tag{5.80}$$

Often [11, 18, 60], one assumes $F^4/F^2 = 0.625$ which corresponds to the atomic ratio. Thus, U and J determine the three Slater integrals and are usually treated as semiempirical parameters. For example, one chooses U and J in such a way that the spin magnetic

[26] See also the linear combinations of atomic orbitals (LCAO) method [58].

[27] Again, $m_{1\ldots4}$ is to mean $m_1 m_2 m_3 m_4$, etc.

[28] Sometimes [18], a basis using cubic harmonics (which are linear combinations of spherical harmonics) is preferred. Consequently, the Coulomb matrix elements are different and the following expressions change slightly.

moment (or other physical quantities that are available from experimental studies) are predicted correctly by some many-particle calculation. In addition to U and J, we can define an averaged intra-orbital Hubbard-U as:

$$U_{\text{diag}} \equiv \frac{1}{5} \sum_m W_{mmmm} = F^0 + \frac{2}{35} \left(F^2 + \frac{5}{9} \cdot F^4 \right) \tag{5.81}$$

However, we are in a position to evaluate the Slater integrals numerically. The radial wave functions appearing in (5.78) may be estimated by our radial functions $\phi_d(r)$ arising within the LMTO method for the d-orbitals, which corresponds to choosing a wave function in the center of the occupied part of the d-band (at the energy $E_{\nu d}$). Thus, the ($3d$) Slater integrals are given via Eq. (5.57) as:

$$F^k = b^k_{22220000} = e^2 \int dr\, r^2\, \phi^2_{\nu d}(r) \int dr'\, r'^2\, \phi^2_{\nu d}(r')\, \frac{r^k_<}{r^{k+1}_>} \tag{5.82}$$

In this sense, we could refer to our basic integrals $b^k_{\ell_{1\ldots4} p_{1\ldots4}}$ as "extended Slater integrals". Although we do not use the quasi atomic basis for our calculations, the Slater integrals provide a very useful estimate for the size of Coulomb matrix elements via Eqs. (5.79), (5.80) and (5.81). In particular, no Wannier functions are needed for their determination. In fact, not even Bloch states enter (5.82). For any (self-consistent) one-particle Hamiltonian, used for constructing a basis, we can easily evaluate F^k by: (i) Solving the radial Schrödinger equation (3.10) for an energy E in the energy range we are interested in, i.e. usually a few eV below the Fermi level, and $\ell = 2$. (ii) Evaluating (5.78) with the obtained radial d-wave function.

Chapter 6

Hartree-Fock Approximation

Using the techniques of the preceeding chapters, we are in a position to write down the full "second-quantized" Hamiltonian (5.3) in Wannier representation with matrix elements calculated from first principles. The full complexity of the many-body problem is included in this Hamiltonian and because it is far too complicated to be treated in its full generality, we apply the Hartree-Fock approximation which corresponds to treating the Coulomb interaction to first order perturbation theory in U.

6.1 Preliminaries

We have already dealt with the Hartree approximation in chapter 2, which we can regard as a special case of the local density approximation in which the (local) exchange-correlation potential is omitted. As is well-known, in the Hartree approximation, the (many-particle) wave function is just a simple product of one-particle wave functions which is not properly antisymmetrized. In the Hartree-Fock approximation, the trial function is a Slater determinant, accounting for the antisymmetry of the many-fermion wave function. Rayleigh-Ritz minimization of the energy $\langle H \rangle$ in terms of the trial function yields the well-known Hartree-Fock equations, see e.g. Ref. [51], which are Schrödinger equations, however, unlike the Hartree or Kohn-Sham equation, with a non-local exchange term. Therefore, it is difficult to solve the Hartree-Fock equations. In the formalism of second quantization, this non-locality is not a problem, as we shall see.

Because the Hartree-Fock approximation lies in taking just a *single* Slater determinant for the wave function of the interacting system, although this wave function is a linear combination of all possible N-particle Slater determinants that can be constructed from a complete one-particle basis, the Hartree-Fock total energy $\langle H \rangle$ must be a strict upper bound to the true total energy.

Let us write our Hamiltonian (5.3) as

$$H = \sum_{12\sigma} (H_0)_{12}\, a^\dagger_{1\sigma} a_{2\sigma} + \frac{1}{2} \sum_{1234} \sum_{\sigma\sigma'} W_{12,34}\, a^\dagger_{1\sigma} a^\dagger_{2\sigma'} a_{3\sigma'} a_{4\sigma} \quad . \tag{6.1}$$

Here and throughout this chapter, we use the abbreviated notation 1 to mean $\mathbf{R}_1 n_1$ and 2 to mean $\mathbf{R}_2 n_2$, etc. , and $a^\dagger_{1\sigma}$ creates an electron in a Wannier state of spin σ and wave function $\langle \mathbf{r}|\mathbf{R}_1 n_1\rangle$, etc. It turns out, see Ref. [44], that the Hartree-Fock approximation consists in replacing the product of four particle annihilation and creation operators by:

$$\langle a^\dagger_{2\sigma'} a_{3\sigma'}\rangle a^\dagger_{1\sigma} a_{4\sigma} + \langle a^\dagger_{1\sigma} a_{4\sigma}\rangle a^\dagger_{2\sigma'} a_{3\sigma'} - \langle a^\dagger_{1\sigma} a_{3\sigma'}\rangle a^\dagger_{2\sigma'} a_{4\sigma} - \langle a^\dagger_{2\sigma'} a_{4\sigma}\rangle a^\dagger_{1\sigma} a_{3\sigma'} \quad (6.2)$$

Where the expectation values denote $\langle\Phi_0|\ldots|\Phi_0\rangle$, and $|\Phi_0\rangle$ is the ground state of the interacting system.[1] Inserting the Hartree-Fock approximation (6.2) into (6.1) yields an effective non-interacting Hamiltonian. After renumbering the indices and using $W_{12,34} = W_{21,43}$, we find:

$$H_{\text{eff}} = \sum_{12\sigma} \underbrace{\left[(H_0)_{12} + \Sigma^{\text{HF}}_{12,\sigma}\right]}_{X^\sigma_{12}} a^\dagger_{1\sigma} a_{2\sigma} = \sum_{12\sigma} X^\sigma_{12}\, a^\dagger_{1\sigma} a_{2\sigma} \quad (6.3)$$

where Σ^{HF} is the Hartree-Fock contribution to the self-energy:

$$\Sigma^{\text{HF}}_{12,\sigma} = \sum_{34\sigma'} \Big[W_{13,42} - \delta_{\sigma\sigma'} W_{31,42}\Big] \langle a^\dagger_{3\sigma'} a_{4\sigma'}\rangle = \Sigma^{\text{Hart}}_{12} + \Sigma^{\text{Fock}}_{12,\sigma} \quad (6.4)$$

Note that the effective hopping matrix elements X^σ_{12} in (6.3) depend on the term $\langle a^\dagger_3 a_4\rangle$, i.e. the expectation value of an annihilation and a creation operator within the ground state of H_{eff}, hence, Eq. (6.3) defines a self-consistency problem which can be solved by iteration. The Hartree-Fock self-energy consists of two terms the Hartree (or direct) and the Fock (or exchange) term. The Hartree term

$$\Sigma^{\text{Hart}}_{12} = \sum_{34} W_{13,42} \sum_{\sigma'} \langle a^\dagger_{3\sigma'} a_{4\sigma'}\rangle \quad (6.5)$$

is independent of spin.[2] Hence, just as within a spin-polarized Hartree (DFT-LSDA) calculation (Sec. 2.5), no spin magnetic moment can develop. The Fock term

$$\Sigma^{\text{Fock}}_{12,\sigma} = -\sum_{34} W_{31,42} \langle a^\dagger_{3\sigma} a_{4\sigma}\rangle \quad (6.6)$$

is responsible for the spin-dependency of the Hartree-Fock self-energy. It accounts for Pauli's exclusion principle, i.e. the fact that electrons with same spin tend to stay apart, as well as for the self-interactions included in the Hartree term, see section 6.3.3.

6.2 Computational Techniques

Equation (6.3) defines the problem we wish to solve. However, a few tools need to be developed to solve this problem.

[1] See Ref. [44].

[2] Unless self-interactions are not included, see section 6.3.3.

6.2.1 Occupation Matrix

The occupation matrix, or density matrix, for the (effective many-particle) ground state $|\Phi_0\rangle$ of H_{eff} is defined by:

$$A_{12}^{\sigma} \equiv \langle a_{1\sigma}^{\dagger} a_{2\sigma} \rangle = \langle \Phi_0 | a_{1\sigma}^{\dagger} a_{2\sigma} | \Phi_0 \rangle \tag{6.7}$$

Let us suppose the effective matrix elements X_{12}^{σ} are known. The ground state $|\Phi_0\rangle$ is (most easily) given by the (antisymmetrized) product of the one-particle states $|\psi_{n\mathbf{k}\sigma}\rangle$ whose eigenenergies are below the Fermi energy. Using X_{12}^{σ} in Eq. (5.32) for each spin direction, we obtain the band structure via Eq. (5.33). By applying the tetrahedron method, we are in a position to obtain the Fermi level E_F using (3.40) and the procedure described in section 3.4. Using the operators $c_{n\mathbf{k}\sigma}^{\dagger}$ and $c_{n\mathbf{k}\sigma}$ introduced in Eq. (5.8), the expectation value in the ground state is expressed as

$$\langle c_{n\mathbf{k}\sigma}^{\dagger} c_{n'\mathbf{k}'\sigma'} \rangle = \delta_{nn'} \delta_{\mathbf{k}\mathbf{k}'} \delta_{\sigma\sigma'} \Theta(E_F - E_n^{\sigma}(\mathbf{k})) \ , \tag{6.8}$$

where Θ is the step function defined in Eq. (B.9). This expectation value vanishes unless the state created and the state annihilated are equal and the eigenenergy $E_n^{\sigma}(\mathbf{k})$ of this state is below the Fermi energy E_F, since if we remove a state $|\psi_{n'\mathbf{k}'\sigma'}\rangle$ from the ground state, we can only come back to the ground state by adding the same state $|\psi_{n\mathbf{k}\sigma}\rangle$ (when this state is occupied, i.e. its eigenenergy is below the Fermi level). The relation between our Bloch and Wannier states is given by (4.1) with the Bloch states transformed by unitary matrices $U_{mn}^{\mathbf{k}}$ which are obtained upon diagonalization of (5.32), i.e. the unitary matrices appearing in (5.33). It follows that the relation between our Bloch and Wannier creation and annihilation operators are:

$$a_{\mathbf{R}n\sigma}^{\dagger} = \frac{1}{N} \sum_{\mathbf{k}m} e^{-i\mathbf{k}\mathbf{R}} U_{mn}^{\mathbf{k}} c_{m\mathbf{k}\sigma}^{\dagger} \ , \quad a_{\mathbf{R}n\sigma} = \frac{1}{N} \sum_{\mathbf{k}m} e^{i\mathbf{k}\mathbf{R}} U_{mn}^{\mathbf{k}*} c_{m\mathbf{k}\sigma} \tag{6.9}$$

Inserting (6.9) into Eq. (6.7) and using (6.8) yields:

$$A_{12}^{\sigma} = \frac{1}{N} \sum_{\mathbf{k}} e^{-i\mathbf{k}(\mathbf{R}_1 - \mathbf{R}_2)} \sum_m U_{mn_1}^{\mathbf{k}} U_{mn_2}^{\mathbf{k}*} \Theta(E_F - E_m^{\sigma}(\mathbf{k})) \tag{6.10}$$

As one would anticipate, the expectation values only depend on the difference of $\mathbf{R}_1$ and $\mathbf{R}_2$. Therefore, we cast A_{12}^{σ} into a form like (5.12) and define

$$A_{\mathbf{R}n_1n_2}^{\sigma} \equiv \frac{1}{N} \sum_{\mathbf{k}} e^{-i\mathbf{k}\mathbf{R}} \sum_m U_{mn_1}^{\mathbf{k}} U_{mn_2}^{\mathbf{k}*} \Theta(E_F - E_m^{\sigma}(\mathbf{k})) \ , \tag{6.11}$$

such that

$$A_{12}^{\sigma} = A_{(\mathbf{R}_1 - \mathbf{R}_2)n_1n_2}^{\sigma} \ . \tag{6.12}$$

The occupation matrix is closely related to the charge density. The spin density *operator* is given by:

$$\hat{n}^{\sigma}(\mathbf{r}) = \Phi_{\sigma}^{\dagger}(\mathbf{r}) \Phi_{\sigma}(\mathbf{r}) \tag{6.13}$$

We can think of this operator as examining the spin density by trying to remove a particle at position $\mathbf{r}$ with spin σ and putting it back. Hence, $\langle\Phi_0|\hat{n}^\sigma(\mathbf{r})|\Phi_0\rangle$ is the ground state spin density. Using (5.10) and taking the expectation value of (6.13) yields the spin density for the ground state in terms of Wannier functions:[3]

$$n^\sigma(\mathbf{r}) = \langle\Phi_0|\hat{n}^\sigma(\mathbf{r})|\Phi_0\rangle = \sum_{12} w_1^*(\mathbf{r})\, w_2(\mathbf{r})\, \langle a_{1\sigma}^\dagger a_{2\sigma}\rangle \tag{6.14}$$

Note that the Wannier functions are independent of spin. Let us examine the (spin) density inside the central muffin-tin. Using Eqs. (4.4) and (4.6), we find:[4]

$$n^\sigma(\mathbf{r}) = \sum_{12} w_{n_1}^*(\mathbf{R}-\mathbf{R}_1;\mathbf{r})\, w_{n_2}(\mathbf{R}-\mathbf{R}_2;\mathbf{r})\, A^\sigma_{(\mathbf{R}_1-\mathbf{R}_2)n_1n_2} \quad \forall\, \mathbf{R} \tag{6.15}$$

Since the lattice sums include all sites, we have added a vector $\mathbf{R}$ to $\mathbf{R}_1$ and $\mathbf{R}_2$ making $n^\sigma(\mathbf{r})$ the density inside any muffin-tin.[5] This should also turn out this way, since $n^\sigma(\mathbf{r}) = n^\sigma(\mathbf{r}+\mathbf{R})$. Equation (6.15) turns out to be very useful for numerical tests, allowing us to check the correctness of the occupation matrix by evaluating the RHS using the Wannier functions and evaluating the LHS using the moment expansion of the density (see section 3.3.4).

6.2.2 Self-energy

Being able to evaluate the occupation matrix, we now focus on the Hartree-Fock contribution to the self-energy (6.4):

$$\Sigma^{\mathrm{HF}}_{12,\sigma} = \sum_{34\sigma'} \Big[W_{13,42} - \delta_{\sigma\sigma'} W_{31,42}\Big] A^{\sigma'}_{34} \tag{6.16}$$

Using Eqs. (5.40) and (6.12) yields:

$$\Sigma^{\mathrm{HF}}_{12,\sigma} = \sum_{34\sigma'} \Big[W^{\mathbf{R}_1-\mathbf{R}_2;\mathbf{R}_3-\mathbf{R}_2;\mathbf{R}_4-\mathbf{R}_2}_{n_1n_3,n_4n_2} - \delta_{\sigma\sigma'} W^{\mathbf{R}_3-\mathbf{R}_2;\mathbf{R}_1-\mathbf{R}_2;\mathbf{R}_4-\mathbf{R}_2}_{n_3n_1,n_4n_2}\Big] A^{\sigma'}_{(\mathbf{R}_3-\mathbf{R}_4)n_3n_4}$$

At this point it is not obvious that X_{12} only depends on the difference of the sites $\mathbf{R}_1$ and $\mathbf{R}_2$. The multiple sum involves a sum $\mathbf{R}_3$ and a sum $\mathbf{R}_4$ over all sites. We can replace $\mathbf{R}_3 \to \mathbf{R}_3+\mathbf{R}_2$ and $\mathbf{R}_4 \to \mathbf{R}_4+\mathbf{R}_2$ since these sums include all sites anyway. After these substitutions, one finds:

$$\Sigma^{\mathrm{HF}}_{12,\sigma} = \sum_{34\sigma'} \Big[W^{\mathbf{R}_1-\mathbf{R}_2;\mathbf{R}_3;\mathbf{R}_4}_{n_1n_3,n_4n_2} - \delta_{\sigma\sigma'} W^{\mathbf{R}_3;\mathbf{R}_1-\mathbf{R}_2;\mathbf{R}_4}_{n_3n_1,n_4n_2}\Big] A^{\sigma'}_{(\mathbf{R}_3-\mathbf{R}_4)n_3n_4}$$

As desired, only terms $\mathbf{R}_1-\mathbf{R}_2$ appear. Hence, the Hartree-Fock self-energy can be written in the form (5.12). To summerize these results, we write:

$$\Sigma^{\mathrm{HF}}_{\mathbf{R}n_1n_2,\sigma} = \sum_{34\sigma'} \Big[W^{\mathbf{R};\mathbf{R}_3;\mathbf{R}_4}_{n_1n_3,n_4n_2} - \delta_{\sigma\sigma'} W^{\mathbf{R}_3;\mathbf{R};\mathbf{R}_4}_{n_3n_1,n_4n_2}\Big] A^{\sigma'}_{(\mathbf{R}_3-\mathbf{R}_4)n_3n_4} \tag{6.17}$$

[3] Note that Φ_0 denotes the many-particle ground state while $\Phi_\sigma^\dagger(\mathbf{r})$ and $\Phi_\sigma(\mathbf{r})$ are field operators.
[4] Since $w_{\mathbf{R}n}(\mathbf{r}) = w_n(-\mathbf{R};\mathbf{r})$ if $|\mathbf{r}| < S$.
[5] Leaving the term $A^\sigma_{(\mathbf{R}_1-\mathbf{R}_2)n_1n_2}$ unaffected.

6.2.3 Self Consistency

As mentioned above, Eq. (6.3) defines a self-consistency problem which we solve by iteration. In essence, the self-consistency cycle equals the one introduced in section 2.2, now in the language of second quantization. The self-consistency cycle is organized as follows:

1. Make an initial guess for X^σ_{12}, e.g. $X^\sigma_{12} = (H_0)_{12}$.
2. Evaluate the occupation matrix A^σ_{12} .
3. Recalculate $\widetilde{X}^\sigma_{12} = (H_0)_{12} + \Sigma^{\mathrm{HF}}_{12,\sigma}$ using Eq. (6.17).
4. Compare the new $\widetilde{X}^\sigma_{12}$ with the old X^σ_{12}. If some criterion for convergence is satisfied, exit the cycle.
5. Set X^σ_{12} to $\alpha\widetilde{X}^\sigma_{12} + (1-\alpha)X^\sigma_{12}$ and go back to step 2.

6.2.4 Total Energy

Although not necessary for evaluating the effective Hamiltonian (6.3), the total energy is an important quantity which we can calculate. Assuming the effective Hamiltonian (6.3) has been evaluated, i.e. the effective hopping matrix elements X^σ_{12} have been determined, we are now in a position to calculate the total energy of the valence electrons which is given by the expectation value of the Hamiltonian (6.1):

$$\langle H\rangle = \sum_{12}(H_0)_{12}\sum_\sigma\langle a^\dagger_{1\sigma}a_{2\sigma}\rangle + \frac{1}{2}\sum_{1234}W_{12,34}\sum_{\sigma\sigma'}\langle a^\dagger_{1\sigma}a^\dagger_{2\sigma'}a_{3\sigma'}a_{4\sigma}\rangle \tag{6.18}$$

From Wick's theorem[6], which can be applied since the Hartree-Fock ground state is a Slater determinant, it follows that the second expectation value is given by:

$$\langle a^\dagger_{1\sigma}a^\dagger_{2\sigma'}a_{3\sigma'}a_{4\sigma}\rangle = \langle a^\dagger_{1\sigma}a_{4\sigma}\rangle\langle a^\dagger_{2\sigma'}a_{3\sigma'}\rangle - \langle a^\dagger_{1\sigma}a_{3\sigma'}\rangle\langle a^\dagger_{2\sigma'}a_{4\sigma}\rangle \tag{6.19}$$

Inserting (6.19) into (6.18) yields (after renumbering some of the quantum numbers):

$$\langle H\rangle = \sum_{12\sigma}\left[(H_0)_{12} + \tfrac{1}{2}\Sigma^{\mathrm{Hart}}_{12} + \tfrac{1}{2}\Sigma^{\mathrm{Fock}}_{12,\sigma}\right]A^\sigma_{12} \tag{6.20}$$

The first energy term, i.e. $\sum_{12\sigma}(H_0)_{12}A^\sigma_{12}$, is the sum of non-interacting one-particle energies. The second energy term is the *direct energy*, it represents the direct average interaction among electrons. The last energy term is the *exchange energy*. This is a correction to the direct energy due to antisymmetry (i.e. *exchange* symmetry) of the many-fermion wave function. The negative sign appearing in Eq. (6.6) is responsible for this correction lowering the total energy. Physically, this can be understood as follows.[7] The short-range part of the Coulomb potential in the direct energy over-counts the interaction energy, since the electrons with same spin tend to stay apart. This over-counting is subtracted by the exchange energy.

[6] See e.g. Ref. [44].
[7] See also [51].

Note that the factors $\frac{1}{2}$ in the direct and exchange energy do not appear in

$$\langle H_{\text{eff}} \rangle = \sum_{12\sigma} \left[(H_0)_{12} + \Sigma^{\text{HF}}_{12,\sigma} \right] A^{\sigma}_{12} = \sum_{12\sigma} X^{\sigma}_{12} A^{\sigma}_{12} \ . \tag{6.21}$$

Here, we would mistakenly double count the interaction energies.

A form for computational evaluation of the total energy per atom is:

$$\langle H \rangle = \sum_{\mathbf{R}nm\sigma} \left[(H_0)_{\mathbf{R}nm} + \tfrac{1}{2} \Sigma^{\text{HF}}_{\mathbf{R}nm,\sigma} \right] A^{\sigma}_{\mathbf{R}nm} \tag{6.22}$$

6.3 Hartree Calculation

We have now developed all the tools to perform a many-particle calculation within the formalism of second quantization using first principle matrix elements. We choose this calculation to be as simple as possible, since we don't know what kind of surprises may be waiting for us.

We are in a position to compare the results of a "first-quantized" Hartree calculation, i.e. within LDA omitting the exchange-correlation potential, to a "second-quantized" Hartree calculation. Using (6.5), our problem is to find the solution of

$$H_{\text{eff}} = \sum_{12} X_{12} \sum_{\sigma} a^{\dagger}_{1\sigma} a_{2\sigma} \qquad \text{where} \qquad X_{12} = (H_0)_{12} + \Sigma^{\text{Hart}}_{12} \ . \tag{6.23}$$

Usually, one would have to solve this equation self-consistently, as described above, however, since we can evaluate the Hartree Hamiltonian H_{Hart} from LDA, the ground state is already known.[8] Thus, the occupation matrix, $\Sigma^{\text{Hart}}_{12}$, and hence the matrix X_{12}, can be evaluated. The resulting X_{12} may then be compared to the matrix elements $(H_{\text{Hart}})_{12}$. The main purpose for this calculation is to gain some experience needed for the Hartree-Fock calculation.

6.3.1 Basis

The question arises which basis we should use for this approach, see also appendix C.8. As mentioned earlier, any basis is equally good, *as long as* it is complete, however, since we use a minimal basis[9], the choice of the one particle basis is important. Since the result from this calculation is the Hartree Hamiltonian, one should use the Hartree basis. By Hartree basis we mean a minimal basis of Wannier functions constructed from H_{Hart}. On the other hand, one might argue that the matrix elements $(H_0)_{12}$ enter the effective hopping matrix elements X_{12} too, and that the Hartree basis is not very good for describing the non-interacting Hamiltonian H_0.[10] This suggests the use of H_0 as the starting point to construct

[8] In fact, calculating H_{Hart} in first quantization (DFT-LDA omitting XC) actually involves a self-consistent calculation too.

[9] Consisting only of Wannier orbitals with $(4)s$, $(4)p$ and $(3)d$ character.

[10] See e.g. Fig. 7.3.

the basis set. However, $(H_0)_{12}$ is only *one* term in X_{12} and the Hartree basis is designed to describe the full Hartree Hamiltonian, i.e. H_0 *plus* the Hartree self-energy Σ^{Hart}. Thus, it is not surprising that the Hartree basis cannot describe the band structure of H_0 itself. Accordingly, we use the Hartree basis for this approach.

6.3.2 Analogy: First and Second Quantization

Just as a check, let us calculate the Hartree self-energy (6.5) and see if these matrix elements are equal to the matrix elements of the potential caused by the classical Hartree interaction, i.e. the Hartree term in (2.15). Using Eqs. (5.38) and (6.5) gives

$$\Sigma_{12}^{\mathrm{Hart}} = \int d^3\mathbf{r}\; w_1^*(\mathbf{r})\; w_2(\mathbf{r}) \int d^3\mathbf{r}'\; \frac{e^2}{|\mathbf{r}-\mathbf{r}'|} \sum_{\sigma'} \underbrace{\sum_{34} w_3^*(\mathbf{r}')\; w_4(\mathbf{r}')\; \langle a_3^\dagger a_4 \rangle}_{n^{\sigma'}(\mathbf{r}')} \quad , \tag{6.24}$$

where we used (6.14). Since the total charge density $n(\mathbf{r})$ is just the sum of the spin-up and the spin-down density, see Eq. (2.40), we find

$$\Sigma_{12}^{\mathrm{Hart}} = \int d^3\mathbf{r}\; w_1^*(\mathbf{r})\; w_2(\mathbf{r}) \int d^3\mathbf{r}'\; \frac{e^2 n(\mathbf{r}')}{|\mathbf{r}-\mathbf{r}'|} = \Big\langle 1 \Big| \int d^3\mathbf{r}'\; \frac{e^2 n(\mathbf{r}')}{|\mathbf{r}-\mathbf{r}'|} \Big| 2 \Big\rangle \quad , \tag{6.25}$$

as we wished to proof. This little calculation was kept general, the ASA form of the Wannier function (4.6) was not taken into account. We will now look at this calculation again (using (4.6)), and, as we shall shortly see, the evaluation of our Coulomb matrix elements (5.42) needs to be modified in order for our (second quantization) Hartree calculation to be consistent with the first quantization Hartree calculation.

Using Eqs. (5.42), (5.43) and (6.15), we can write $\Sigma_{12}^{\mathrm{Hart}}$ as:

$$\sum_{\mathbf{R}} \int d^3\mathbf{r}\; w_{n_1}^*(\mathbf{R}-\mathbf{R}_1;\mathbf{r})\; w_{n_2}(\mathbf{R}-\mathbf{R}_2;\mathbf{r}) \sum_{\mathbf{R}'} \int d^3\mathbf{r}'\; \frac{e^2\; n(\mathbf{r}')}{|\mathbf{r}-\mathbf{r}'+\mathbf{R}-\mathbf{R}'|} \tag{6.26}$$

But from (5.17), the matrix elements of the Hartree term are given by:

$$\sum_{\mathbf{R}} \int d^3\mathbf{r}\; w_{n_1}^*(\mathbf{R}-\mathbf{R}_1;\mathbf{r})\; w_{n_2}(\mathbf{R}-\mathbf{R}_2;\mathbf{r}) \int d^3\mathbf{r}'\; \frac{e^2\; n(\mathbf{r}')}{|\mathbf{r}-\mathbf{r}'|} \tag{6.27}$$

Now in order that (6.26) equals (6.27), i.e.

$$\sum_{34} \Big\langle 1 \Big| \Big\langle 3 \Big| \frac{e^2}{|\mathbf{r}-\mathbf{r}'|} \Big| 4 \Big\rangle \Big| 2 \Big\rangle \sum_{\sigma'} A_{34}^{\sigma'} = \Big\langle 1 \Big| \int d^3\mathbf{r}'\; \frac{e^2 n(\mathbf{r}')}{|\mathbf{r}-\mathbf{r}'|} \Big| 2 \Big\rangle \quad , \tag{6.28}$$

we have to restrict the $\mathbf{R}'$-sum in (6.26) to $\mathbf{R}$, such that the denominator reduces to $|\mathbf{r}-\mathbf{r}'|$ as in (6.27). This corresponds to modifying Eq. (5.42) to

$$W_{12,34} = \sum_{\mathbf{R}} W(12,34;\mathbf{R},\mathbf{R}) \quad . \tag{6.29}$$

However, Eq. (5.42) is not wrong, it follows from the ASA form of the Wannier functions. So how is it possible that we need to modify our old atomic sphere expansion of the Coulomb interaction in order to achieve the desired agreement (6.28)? To answer this question, we need to understand why it is sufficient to restrict the evaluation of the Hartree term in (6.27) to a single muffin-tin sphere which is done in our Hartree and DFT calculations. Since there are as many electrons as protons in one atom of the solid, the total charge inside the unit cell equals zero. Hence, electrons do (approximately) not feel a Coulomb force from the neighbor atoms.[11] Accordingly, the potential from the nuclear point charge and the electronic charge density can be restricted to a single muffin-tin. If we were to include the potential from neighboring valence electrons,[12] we would also have to include the potential from neighboring ion charge densities. This seems, however, to be a difficult task, since the atomic spheres are overlapping. Thus, we neglect terms $\mathbf{R} \neq \mathbf{R}'$ in Eq. (5.42) altogether in order to be consistent with our previous calculations.

6.3.3 Self-interaction

In density functional theory, one always assumes that all the electrons move in the same effective potential constructed from the total charge density. However, in the real world, an electron does not interact with itself. Therefore, to be correct, we would have to construct the potential for an electron from all the *other* states, i.e. excluding the charge density from the state of the electron we consider. Consequently, a different one-particle potential for all the electrons would be required, and DFT would become much more complicated. One may also argue that, since we usually have many electrons in the system, the effect of this extra electron is small.

As mentioned earlier, the Fock term accounts for the self-interactions included in the Hartree term, as can be understood as follows. From Pauli's exclusion principle it follows that $a^\dagger_{1\sigma} a^\dagger_{2\sigma'}$ and $a_{3\sigma'} a_{4\sigma}$ are zero[13] when $1\sigma = 2\sigma'$ or $3\sigma' = 4\sigma$ respectively, since two fermions cannot be created (annihilated) in the same one-particle state. For this condition, the interaction term in (6.1) should vanish. By means of (6.2), we realize that this is (indeed) the case, since if $1\sigma = 2\sigma'$, the first and third term and the second and last term cancel; and if $3\sigma' = 4\sigma$, the first and last term and the second and third term cancel.

In the Hartree approximation, this cancellation does not occur. By explicitly inserting the term[14] $(1 - \delta_{13}\delta_{\sigma\sigma'}) \cdot (1 - \delta_{24}\delta_{\sigma\sigma'})$ in Eq. (6.5), self-interactions are not included anymore. The first thing we realize is that this has the consequence that the Hartree self-energy (6.5) becomes spin-dependent.[15] Nevertheless, since we include self-interactions in DFT-LDA, we also include them in the second quantized version of the Hartree equations, i.e. we do not explicitly insert the above term.

[11] Nevertheless, hopping enters the total energy of the solid, which assumes its minimum for the ground state, allowing for crystal binding.

[12] As we would by using (6.26).

[13] The zero operator, to be more correct.

[14] The indices have changed a little, since we did some renumbering of the indices when going from (6.1) and (6.2) to (6.3).

[15] Since we cannot write the σ'-sum right in front of the occupation matrix.

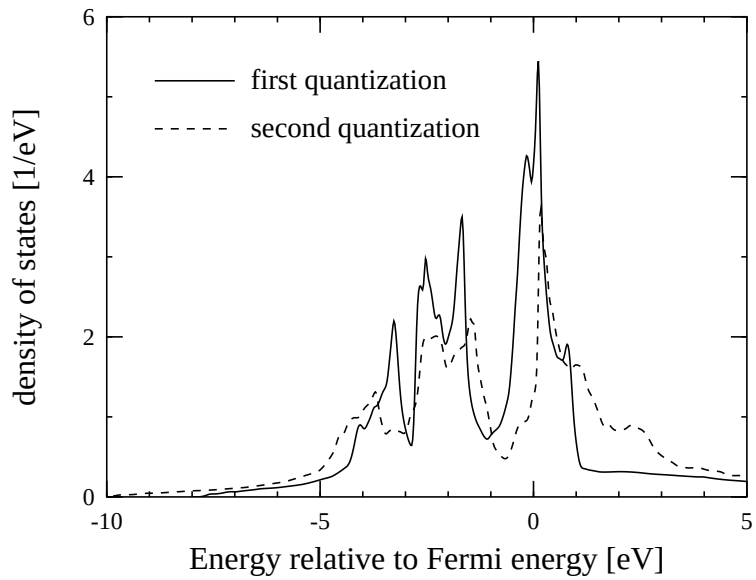

Figure 6.1: Total (both spin) density of states from Hartree calculation.

6.3.4 Example Iron

Let us compare the Hartree band structures obtained from a first quantization and a second quantization calculation. Taking (6.29) into account, there is no difference between the two, i.e. Eq. (6.28) holds (when self-interactions are included). Numerically, however, we can only take a finite number of Coulomb matrix elements appearing in the LHS of Eq. (6.28) into account; while on the RHS of (6.28), the electronic density appears explicitly, avoiding this problem. Hence, following the procedure outlined below Eq. (6.23), we can estimate the error involved by only using nearest-neighbor Coulomb matrix elements. By using a minimal basis, we have already restricted ourselves to nine band indices, but we still have to deal with site indices. Using (5.40), only three site indices are appearing in (6.17). Nevertheless, if we only consider nearest-neighbor site indices, the number of Coulomb matrix elements appearing in (6.17) is $9^3 \cdot 9^4 = 4,782,969$ for BCC and even $13^3 \cdot 9^4 = 14,414,517$ for FCC. By a glance at the table in appendix C.6, it becomes obvious that we have to restrict the site indices somehow. We restrict ourselves to nearest-neighbor Coulomb matrix elements. By next neighbor matrix elements, we mean a matrix element in which the four site indices are (pairwise) maximally a next neighbor distance apart.[16] Since (5.40), we can consider $\mathbf{R}_4 = \mathbf{0}$. In the case of FCC there are $421 \cdot 9^4 = 2,762,181$ such matrix elements. Using symmetry (5.41), we still need to evaluate $691,335$ matrix elements. Each of those is evaluated by including second nearest-neighbor sites in (6.29).

Having the above in mind, it is not surprising that we do not achieve complete agreement in Fig. 6.1 where a comparison of the first and second quantized Hartree calculation for iron is plotted.[17]

[16] It also follows that the resulting $X_{\mathbf{R}nm}$ are only evaluated up to nearest-neighbor $\mathbf{R}$.

[17] The DOS from the first quantized calculation, i.e. DFT without XC, is also shown in Fig. 7.1.

6.4 Hartree-Fock Calculation

Having discussed the Hartree calculation in such detail, there is not a whole lot more to say about the Hartree-Fock calculation. The only difference is the exchange term in Eq. (6.17).

As described in section C.8, we use the Hartree basis for the Hartree-Fock calculation.

Since (6.4) consists of two terms, one may be tempted to start from a (first quantization) Hartree calculation and treat the Fock term "on top", such that the effective hopping matrix elements take the form

$$X^{\sigma}_{12} = (H_0)_{12} + \left\langle 1 \middle| \int d^3\mathbf{r}' \, \frac{e^2 n(\mathbf{r}')}{|\mathbf{r}-\mathbf{r}'|} \middle| 2 \right\rangle + \Sigma^{\text{Fock}}_{12,\sigma} = (H_{\text{Hart}})_{12} + \Sigma^{\text{Fock}}_{12,\sigma} \ , \qquad (6.30)$$

where we used (6.28). However, the Hartree self-energy depends on the effective ground state of H_{eff} and this is not taken into account by (6.30), since $(H_{\text{Hart}})_{12}$ is evaluated for the ground state of the Hartree but not the effective Hartree-Fock Hamiltonian H_{eff}. In other words, using (6.30), we would not consider that the occupation matrix, and hence the Hartree self-energy in (6.4), depends on the Hartree-Fock ground state H_{eff}. Thus, we do not use (6.30), but rather (6.4), in connection with (6.3) within the self-consistency cycle as described in Sec. 6.2.3.

Example (cont.)

We will now continue our example from Sec. 6.3.4, and look at the Hartree-Fock calculation for iron.

In the Hartree calculation, we had to include self-interactions, i.e. not explicitly insert $(1-\delta_{13}\delta_{\sigma\sigma'}) \cdot (1-\delta_{24}\delta_{\sigma\sigma'})$ in the Hartree self-energy, in order to be consistent with DFT. Now, however, the Fock self-energy cancels the self-interactions included in the Hartree term. This suggests to use the self-energy

$$\Sigma^{\text{HF}}_{12,\sigma} = \sum_{34} W_{13,42} \sum_{\sigma'} A^{\sigma'}_{34} - \sum_{34} (1-\delta_{13}\delta_{\sigma\sigma'})(1-\delta_{24}\delta_{\sigma\sigma'}) W_{31,42} A^{\sigma}_{34} \ , \qquad (6.31)$$

that is, not to allow the Fock self-energy to cancel the Hartree self-interactions by deliberately excluding the cancellation. The upper plot in Fig. (6.2) shows the band structure, found self-consistently by using (6.31), instead of the correct Hartree-Fock term (6.4). But the spin moment was found to be 0.82 μ_B/atom which is much smaller than the experimental value of 2.22 μ_B/atom. Using the correct Hartree-Fock term (6.4), we find the band structure shown in the lower plot. Here, the spin moment is 2.90 μ_B/atom which is too large, but this is reasonable since Hartree-Fock overestimates spin moments (see discussion, Sec. 7.2). Now, however, the lack of self-interactions causes the d-bands to be too low in energy. We believe that one should use the correct Hartree-Fock self-energy, in particular since the total energy is lower. After all, Hartree-Fock is just first order perturbation theory in U, and the band structure can not be regarded as the final answer.

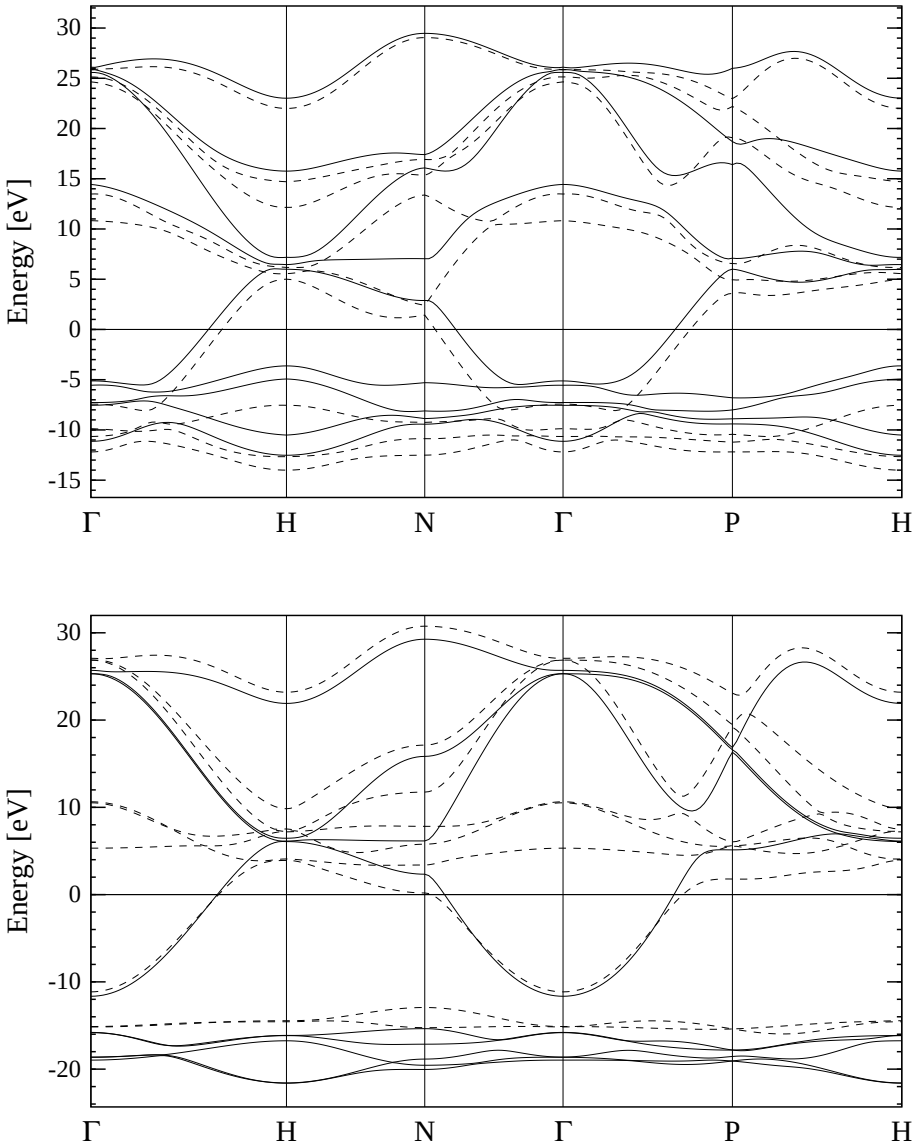

Figure 6.2: Spin-polarized Hartree-Fock band structure relative to Fermi energy [Majority spin (solid), minority spin (dashed)]. In the upper plot Eq. (6.31) was used and the spin moment was found to be $0.82\ \mu_B$/atom and total energy $\langle H \rangle = -45.4$ Ryd/atom, while in the lower plot we used (6.4) and found $2.90\ \mu_B$/atom and -49.4 Ryd/atom.

Chapter 7

Results

In this chapter, we present results for the $3d$ transition metals Fe, Co, Ni and Cu, which follow from applying the methods and techniques described in the preceeding chapters. A few of the following results have already appeared in some of the illustrations and examples. We wish, however, to present the collected results for these metals in a standardized form. This chapter is organized as follows: After some general remarks about the actual calculations and the standardized form, we give the explicit data for the $3d$ transition metals. To discuss the results, we perform some additional calculations for these systems and examine the trends in several of the calculated quantities with respect to the atomic number.

7.1 Calculations

To begin with, for each metal, a self-consistent Hartree, an LDA and an LSDA calculation (chapter 2) at experimental equilibrium volume was performed. The one-electron band problem was solved using the LMTO method (chapter 3). From the Hartree calculation (which we perform using spd-orbitals), we obtain maximally localized Wannier functions using the Marzari-Vanderbilt method (Sec. 4.2). Here, we use the composite treatment of the energy bands (Sec. 4.3). From these maximally localized Wannier functions, serving as a minimal basis for our many-particle problem, the Wannier function projected DOS was evaluated in order to estimate their localization with respect to energy. Having established our basis set, we have determined various matrix elements, as described in chapter 5:

i.) The matrix elements for the Hartree Hamiltonian itself which allows re-evaluation of the Hartree band structure. This is an important numerical test. For all four metals, excellent agreement was achieved, as shown for copper in Fig. 5.3.

ii.) The matrix elements for the LSDA Hamiltonian, in order to see whether the (spin-independent) basis is coping with spin-polarized Hamiltonians with non-vanishing magnetic moment arising from exchange and correlation. For all four metals, good agreement was achieved, as already shown for iron in Fig. 5.5.

iii.) The matrix elements for the Hamiltonian which contains only the core potential, as given in Eq. (3.48).

iv.) The Coulomb matrix elements using the spherical expansion method (Sec. 5.3.1), proceeding as described in Sec. 6.3.4.

Using the matrix elements evaluated in points iii.) and iv.), we perform a Hartree-Fock calculation (chapter 6). Four pages have been devoted to each metal.

Page 1: The first four parameters are input parameters for the calculation, but all other parameters, except, of course, experimental spin magnetic moment, are computational results. Shown is the

1.) atomic number Z.
2.) number of valence electrons.
3.) assumed crystal lattice (either FCC or BCC).
4.) assumed experimental equilibrium volume (from Ref. [31]).
5.) total energy (of the valence electrons per atom in Rydbergs) resulting from the self-consistent Hartree calculation (chapter 2).
6.) LDA total energy.
7.) LSDA total energy.
8.) Hartree-Fock total energy, i.e. Eq. (6.22).
9.) Slater integral F^0 (see Eq. (5.82)), in electron Volts, where the radial wave function was obtained from the Hartree calculation.
10.) averaged direct Coulomb interaction U, defined by the middle term in Eq. (5.79).
11.) estimate for the Hubbard-U from constrained LDA, as already shown in Tab. 2.2 in Sec. 2.4.
12.) experimental spin magnetic moment, in units μ_B/atom, from Ref. [46].
13.) LSDA magnetic moment obtained from Eq. (2.45).
14.) magnetic moment obtained from Hartree-Fock (see chapter 6).

Also on the first page is a figure showing the density of states (both spins), relative to the Fermi energy, in units 1/eV, from the Hartree calculation (chapter 2).

Page 2: The upper table on the second page contains some properties of the maximally localized Wannier functions which have been calculated from the Hartree calculation using the method by Marzari and Vanderbilt (Sec. 4.2). Each row shows a property for the nine Wannier functions. The properties are discussed and illustrated in Sec. (4.3). Shown is (in the rows) the

1.) total portion of the nth Wannier function in its "home" sphere, i.e. Eq. (4.32) with $\mathbf{R} = \mathbf{0}$.
2.) total s-character of the nth Wannier function. By total we mean the total spatial extent of the function from all MT spheres, as in the last column of Tab. 4.1.
3.) total p-character.

4.) total d-character.

5.) central energy E_n associated with the nth Wannier function (according to Eq. (4.45)) relative to the Fermi energy.

6.) measure of the energetic width of the nth Wannier function in terms of energy given by Eq. (4.46).

7.) portion of the density of states of the nth Wannier function at the Fermi level, i.e. $N_j(E_F)/N(E_F)$ (in percent), see also Eq. (4.36).

8.) projected NOS at the Fermi level $n_n(E_F)$. The values account for both spins, such that $0 \leq n_j(E_F) \leq 2$.

The two lower tables show (on-site) direct and exchange Coulomb matrix elements for the Wannier functions mentioned above. By means of Eq. (5.40), these are defined as:

$$U_{nm} = W^{\mathbf{000}}_{nm,mn} \quad \text{and} \quad J_{nm} = W^{\mathbf{000}}_{nm,nm}$$

Note that from (5.41) it follows that $U_{nm} = U_{mn}$, $J_{nm} = J_{mn}$ and $U_{nm} = U^*_{nm}$, $J_{nm} = J^*_{nm}$. That is, the matrices U and J are symmetric and their elements are real. Generally, however, Coulomb matrix elements are complex. The matrix elements were evaluated using the spherical expansion method (Sec. 5.3.1), proceeding as described in Sec. 6.3.4. Hence, not only the contribution of the "home" sphere, but also next neighbor portions of the Wanner functions are taken into account by equation (6.29).[1]

Page 3: The upper figure shows the density of states for spin-polarized DFT, i.e. for the LSDA calculation. While Figs. 7.2, 7.7 and 7.12 show the DOS for the majority and minority spin, Fig. 7.17 shows the total DOS, since the LSDA yields the same energy bands for both spin directions for copper.

The lower figure on the 3rd page shows two graphs. In the lower graph, the density of states of the non-interacting (one-particle) Hamiltonian $H_0 = -\nabla + v_0(\mathbf{r})$, where $v_0(\mathbf{r})$ is the "core potential" (3.48), is shown. Since hybridization among the ℓ-characters of the (unoccupied) bands is almost negligible, the three bands shown are almost pure and we have labeled them by their ℓ-character. The d-bands are extremely narrow. Hence, the DOS has a sharp peak, up to a few thousand states per eV, indicated by the vertical line.
Above, we have plotted the DOS obtained by the matrix elements of H_0 within the Hartree basis ($x = 1$), see Sec. 5.2.3 example 3, for 9 shells included in the $\mathbf{R}$-sum in (5.32). In this sense, the lower graph shows the DOS in the eigenbasis.

Page 4: On the last page, we give our Hartree-Fock results (chapter 6).

The upper figure shows the band structure for majority and minority spin, obtained from the effective hopping matrix elements $X^{\uparrow}_{12}$ and $X^{\downarrow}_{12}$, within the Hartree basis.

Below, the spin-resolved density of states is shown.

[1] This explains why direct matrix elements for copper (Tab. 7.8) are slightly larger than the values shown in table 5.2.

7.1.1 Iron

Atomic Number		26
Valence electrons		8
Lattice		BCC
Wigner-Seitz radius [a_0]		2.662
(Valence) Total energy:	Hartree	-43.128
[Ryd/atom]	LDA	-44.867
	LSDA	-44.894
	Hartree-Fock	-49.373
Coulomb energy U^{3d}:	Slater F^0	21.62
[eV]	Matrix elements	21.09
	Constrained LDA	11.7
Magnetic moment:	Experimental	2.22
[μ_B/atom]	LSDA	2.18
	Hartree-Fock	2.90

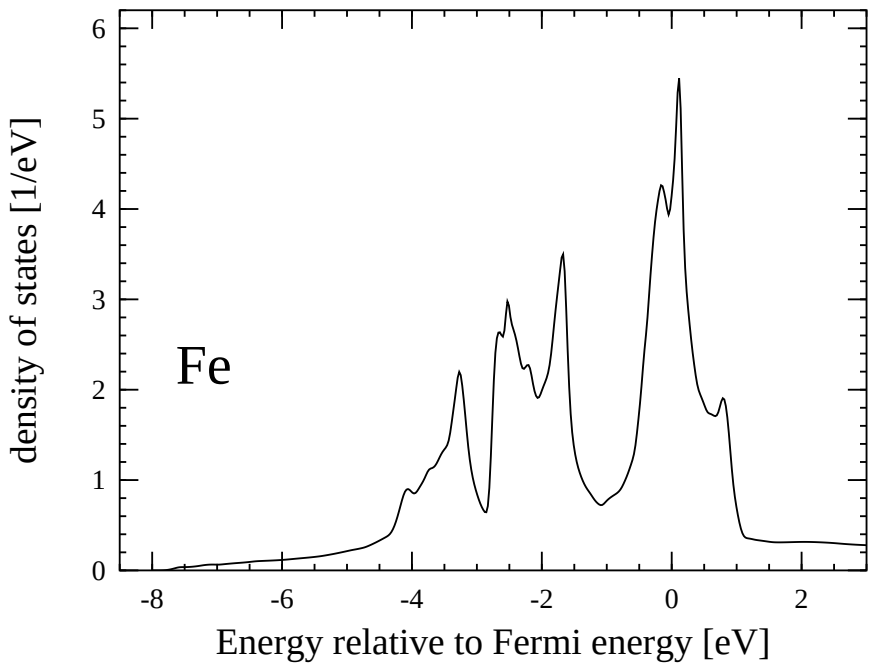

Figure 7.1: Total (both spins) density of states obtained from the “first quantization” Hartree calculation.

n	0	1	2	3	4	5	6	7	8
$\sum_\ell C_\ell^{\mathbf{0}n}$	.9761	.9765	.9596	.9800	.9773	.8754	.8731	.8763	.8776
$\sum_{\mathbf{R}} C_{\ell=0}^{\mathbf{R}n}$	.0019	.0018	.0081	.0019	.0017	.2224	.2381	.2265	.2168
$\sum_{\mathbf{R}} C_{\ell=1}^{\mathbf{R}n}$	.0955	.0726	.1797	.0611	.0728	.5480	.5509	.5347	.5417
$\sum_{\mathbf{R}} C_{\ell=2}^{\mathbf{R}n}$	.9026	.9256	.8121	.9370	.9255	.2295	.2110	.2388	.2415
E_n [eV]	-1.39	-1.79	0.49	-2.08	-1.81	10.05	10.27	9.75	9.93
σ_n [eV]	7.25	6.68	9.49	6.14	6.63	12.77	12.76	12.73	12.83
% DOS	10.2	10.0	10.8	10.5	10.1	12.0	12.2	12.3	11.9
$n_n(E_F)$	1.73	1.74	1.54	1.77	1.74	0.62	0.60	0.63	0.64

Table 7.1: Some properties of the nine maximally localized Wannier functions.

U_{nm}	0	1	2	3	4	5	6	7	8
0	22.42	20.90	20.10	20.96	20.86	14.16	13.32	13.96	13.50
1	20.90	23.04	19.95	21.55	21.53	14.07	13.54	13.58	14.15
2	20.10	19.95	20.77	20.05	19.83	12.95	13.46	13.37	13.22
3	20.96	21.55	20.05	23.27	21.67	13.46	14.05	13.98	13.98
4	20.86	21.53	19.83	21.67	22.99	13.71	13.28	14.25	14.12
5	14.16	14.07	12.95	13.46	13.71	13.67	9.45	9.58	9.64
6	13.32	13.54	13.46	14.05	13.28	9.45	13.52	9.27	9.50
7	13.96	13.58	13.37	13.98	14.25	9.58	9.27	13.75	9.65
8	13.50	14.15	13.22	13.98	14.12	9.64	9.50	9.65	13.81

J_{nm}	0	1	2	3	4	5	6	7	8
0	22.42	0.84	0.61	0.75	0.99	0.86	0.73	0.81	0.42
1	0.84	23.04	0.77	0.88	0.84	0.70	0.51	0.48	0.86
2	0.61	0.77	20.77	0.88	0.70	0.96	0.93	0.92	0.60
3	0.75	0.88	0.88	23.27	0.82	0.33	0.78	0.64	0.69
4	0.99	0.84	0.70	0.82	22.99	0.52	0.46	0.75	0.83
5	0.86	0.70	0.96	0.33	0.52	13.67	0.58	0.56	0.57
6	0.73	0.51	0.93	0.78	0.46	0.58	13.52	0.45	0.56
7	0.81	0.48	0.92	0.64	0.75	0.56	0.45	13.75	0.55
8	0.42	0.86	0.60	0.69	0.83	0.57	0.56	0.55	13.81

Table 7.2: Direct and exchange Coulomb matrix elements for Wannier functions. All energies are eV's.

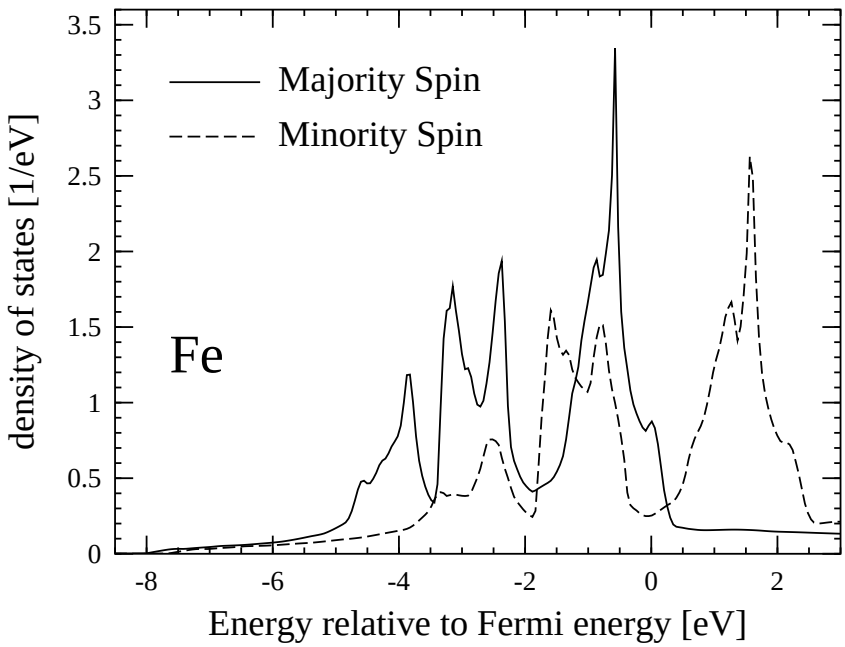

Figure 7.2: Density of states (per spin) from LSDA.

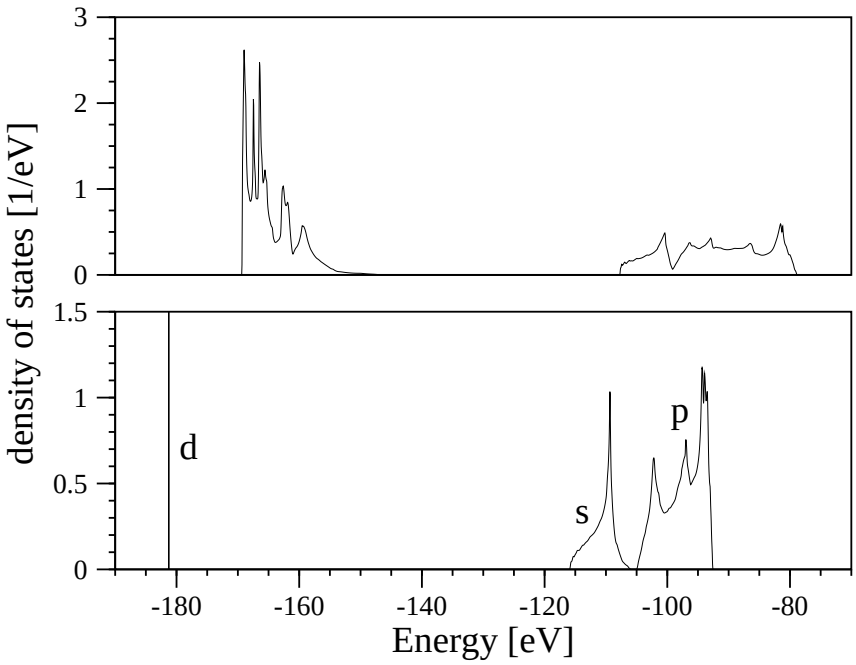

Figure 7.3: Total (both spin) density of states for the non-interacting Hamiltonian H_0 in (i) eigenbasis (lower graph). (ii) “Hartree” basis (upper graph).

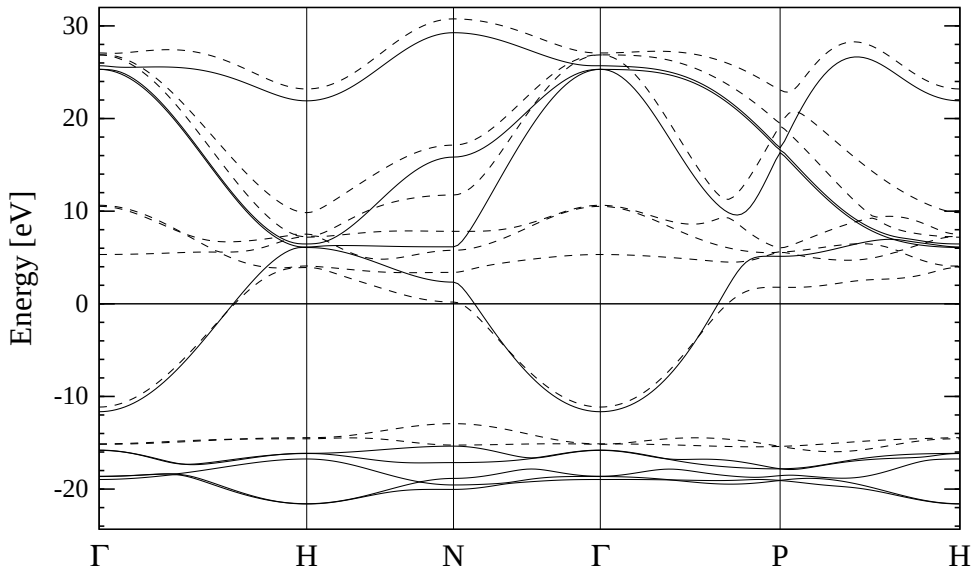

Figure 7.4: Spin-polarized Hartree-Fock band structure relative to Fermi energy. [Majority spin (solid), minority spin (dashed)]

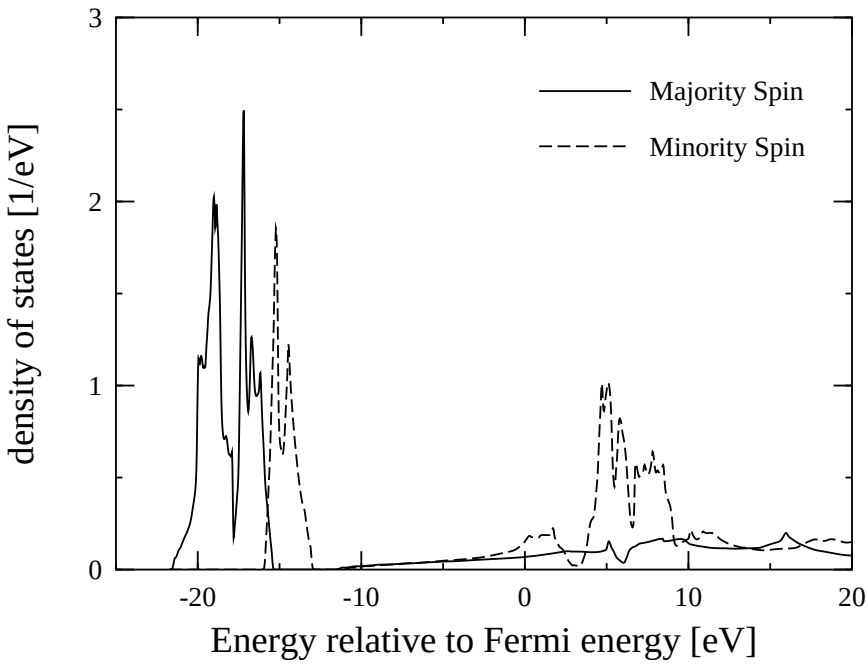

Figure 7.5: Density of states (per spin) for Hartree-Fock band structure.

7.1.2 Cobalt

Atomic Number		27
Valence electrons		9
Lattice		FCC
Wigner-Seitz radius [a_0]		2.621
(Valence) Total energy:	Hartree	-58.798
[Ryd/atom]	LDA	-60.965
	LSDA	-60.975
	Hartree-Fock	-66.354
Coulomb energy U^{3d}:	Slater F^0	23.18
[eV]	Matrix elements	22.59
	Constrained LDA	12.2
Magnetic moment:	Experimental	1.72
[μ_B/atom]	LSDA	1.58
	Hartree-Fock	1.90

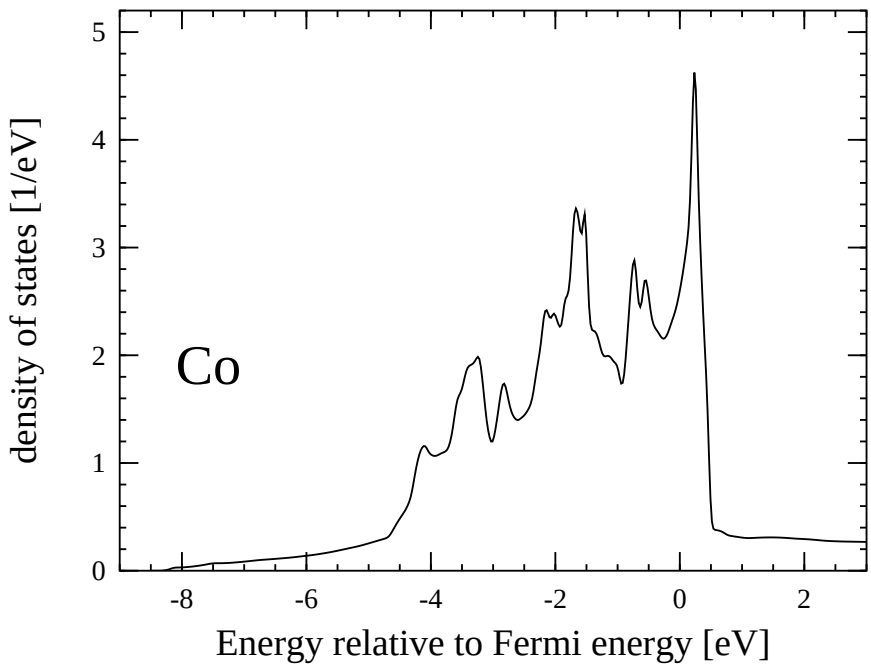

Figure 7.6: Total (both spins) density of states obtained from the “first quantization” Hartree calculation.

n	0	1	2	3	4	5	6	7	8
$\sum_\ell C_\ell^{\mathbf{0}n}$	.9806	.9598	.9810	.9893	.9835	.8722	.8802	.8713	.8832
$\sum_{\mathbf{R}} C_{\ell=0}^{\mathbf{R}n}$	.0053	.0120	.0018	.0008	.0031	.2442	.1836	.2699	.1892
$\sum_{\mathbf{R}} C_{\ell=1}^{\mathbf{R}n}$	.0696	.1973	.0643	.0153	.0400	.5782	.5808	.5609	.5551
$\sum_{\mathbf{R}} C_{\ell=2}^{\mathbf{R}n}$	.9250	.7907	.9338	.9839	.9568	.1776	.2357	.1691	.2557
E_n [eV]	-1.72	1.04	-1.84	-2.89	-2.32	10.81	10.50	10.96	9.99
σ_n [eV]	6.45	9.68	6.23	3.84	5.26	12.22	12.34	12.15	12.38
% DOS	9.6	10.5	9.7	9.4	10.0	13.3	12.5	12.6	12.5
$n_n(E_F)$	1.77	1.50	1.77	1.88	1.80	0.54	0.59	0.52	0.64

Table 7.3: Some properties of the nine maximally localized Wannier functions.

U_{nm}	0	1	2	3	4	5	6	7	8
0	23.96	20.79	22.88	22.90	22.78	13.85	14.15	13.71	14.36
1	20.79	21.32	20.99	21.32	21.07	13.19	13.63	12.81	13.49
2	22.88	20.99	24.41	23.00	22.55	13.41	14.49	13.62	14.75
3	22.90	21.32	23.00	25.64	24.01	13.74	14.66	14.08	14.77
4	22.78	21.07	22.55	24.01	24.89	13.92	14.15	13.85	14.77
5	13.85	13.19	13.41	13.74	13.92	13.30	9.72	8.90	9.85
6	14.15	13.63	14.49	14.66	14.15	9.72	13.88	9.47	10.20
7	13.71	12.81	13.62	14.08	13.85	8.90	9.47	13.33	9.62
8	14.36	13.49	14.75	14.77	14.77	9.85	10.20	9.62	14.16

J_{nm}	0	1	2	3	4	5	6	7	8
0	23.96	0.93	0.67	1.04	0.98	0.86	0.53	0.69	0.59
1	0.93	21.32	0.66	0.79	0.84	0.82	0.89	0.67	1.09
2	0.67	0.66	24.41	1.02	1.11	0.43	0.87	0.59	0.66
3	1.04	0.79	1.02	25.64	0.66	0.44	0.53	0.67	0.47
4	0.98	0.84	1.11	0.66	24.89	0.60	0.49	0.67	0.58
5	0.86	0.82	0.43	0.44	0.60	13.30	0.72	0.56	0.72
6	0.53	0.89	0.87	0.53	0.49	0.72	13.88	0.61	0.69
7	0.69	0.67	0.59	0.67	0.67	0.56	0.61	13.33	0.61
8	0.59	1.09	0.66	0.47	0.58	0.72	0.69	0.61	14.16

Table 7.4: Direct and exchange Coulomb matrix elements for Wannier functions. All energies are eV's.

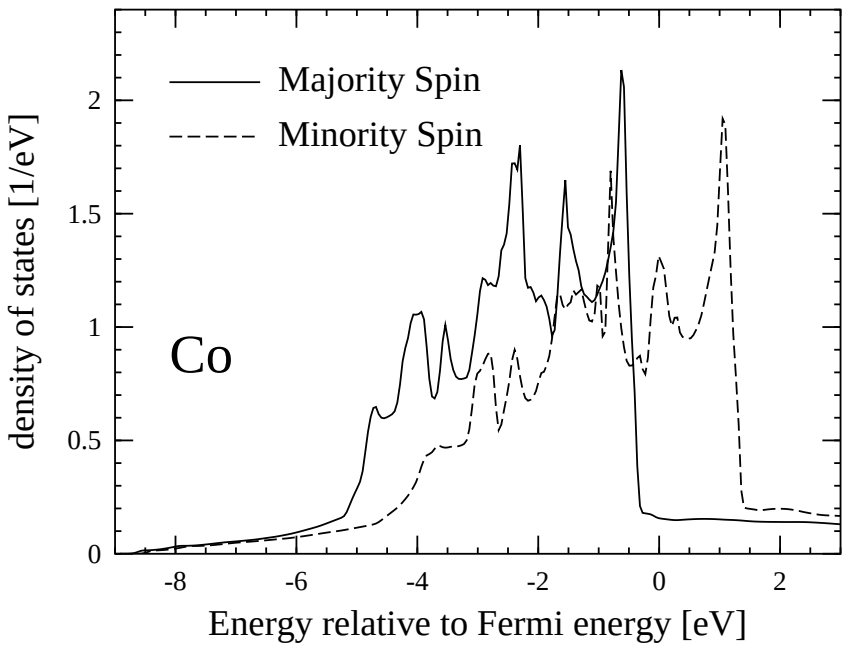

Figure 7.7: Density of states (per spin) from LSDA.

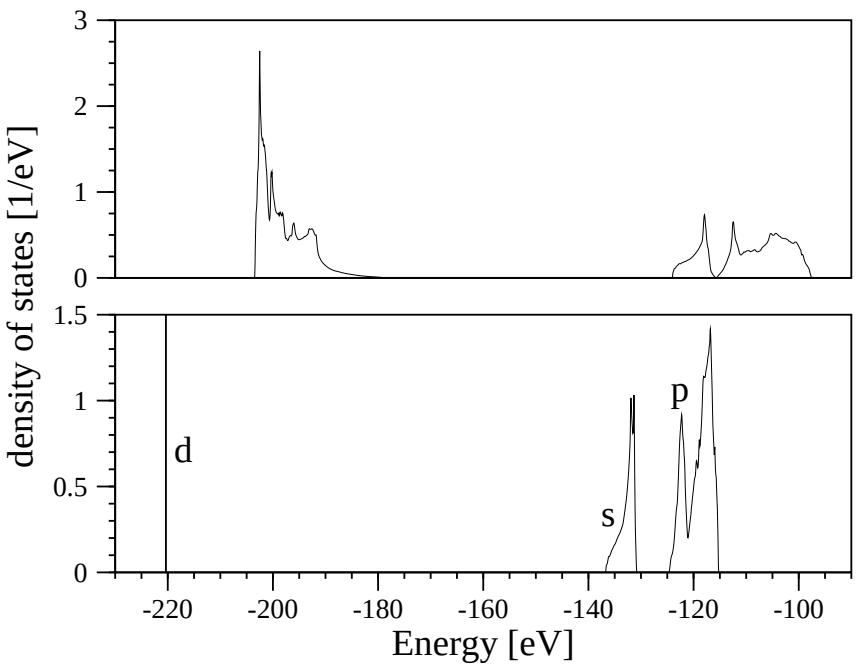

Figure 7.8: Total (both spin) density of states for the non-interacting Hamiltonian H_0 in (i) eigenbasis (lower graph). (ii) “Hartree” basis (upper graph).

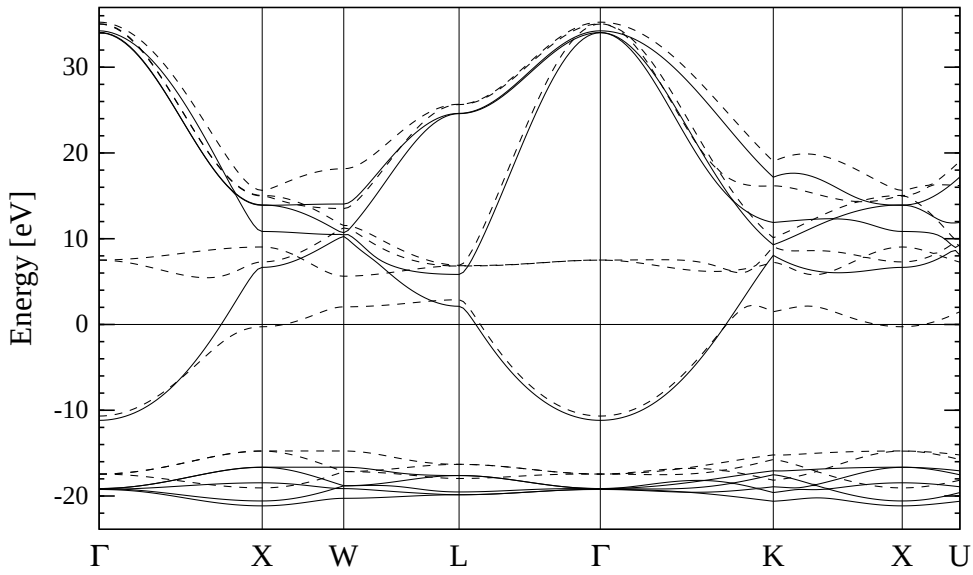

Figure 7.9: Spin-polarized Hartree-Fock band structure relative to Fermi energy. [Majority spin (solid), minority spin (dashed)]

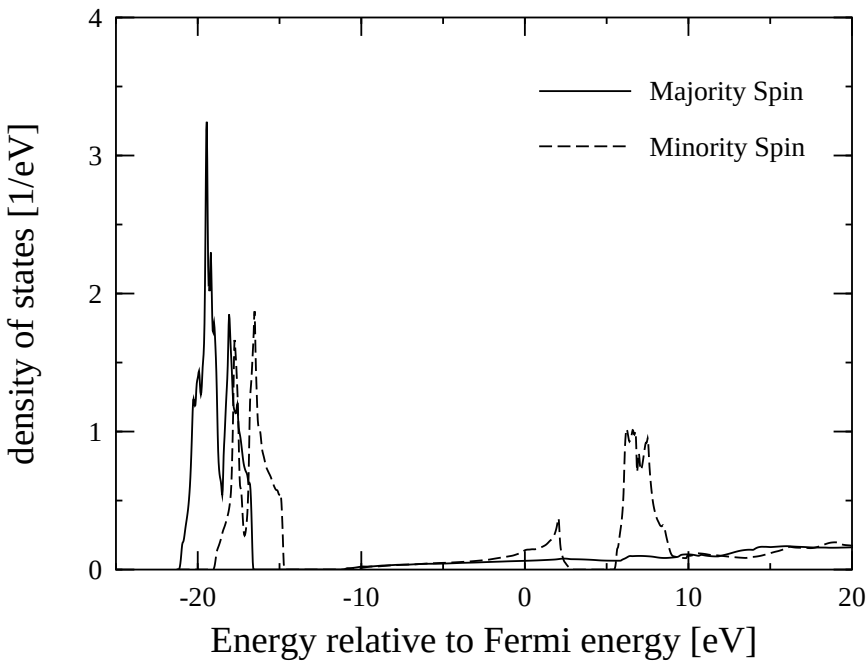

Figure 7.10: Density of states (per spin) for Hartree-Fock band structure.

7.1.3 Nickel

Atomic Number		28
Valence electrons		10
Lattice		FCC
Wigner-Seitz radius [a_0]		2.602
(Valence) Total energy:	Hartree	-77.698
[Ryd/atom]	LDA	-80.360
	LSDA	-80.363
	Hartree-Fock	-86.926
Coulomb energy U^{3d}:	Slater F^0	24.69
[eV]	Matrix elements	22.61
	Constrained LDA	12.5
Magnetic moment:	Experimental	0.62
[μ_B/atom]	LSDA	0.58
	Hartree-Fock	0.76

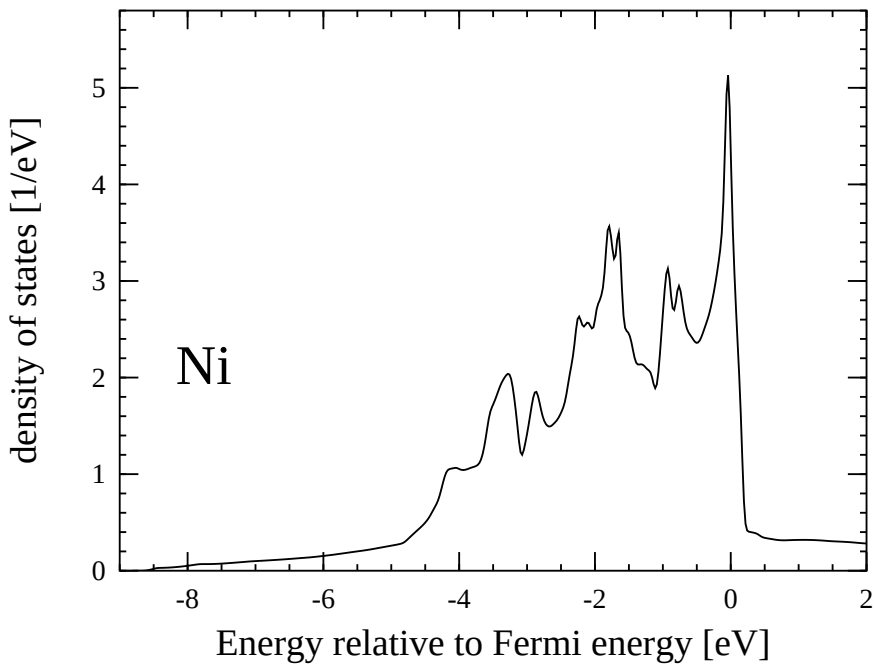

Figure 7.11: Total (both spins) density of states obtained from the “first quantization” Hartree calculation.

n	0	1	2	3	4	5	6	7	8
$\sum_\ell C_\ell^{\mathbf{0}n}$	.9865	.9593	.9732	.9828	.9684	.8888	.8862	.8827	.8787
$\sum_{\mathbf{R}} C_{\ell=0}^{\mathbf{R}n}$	.0011	.0305	.0019	.0013	.0096	.1843	.2124	.2392	.2312
$\sum_{\mathbf{R}} C_{\ell=1}^{\mathbf{R}n}$	.0363	.1867	.1208	.0637	.1430	.5242	.5188	.5160	.5504
$\sum_{\mathbf{R}} C_{\ell=2}^{\mathbf{R}n}$	.9626	.7827	.8773	.9350	.8473	.2915	.2688	.2448	.2184
E_n [eV]	-2.28	1.07	-0.51	-1.72	0.03	9.27	9.42	9.58	10.22
σ_n [eV]	4.90	9.43	7.84	6.07	8.45	12.25	12.22	12.17	12.15
% DOS	9.5	10.7	10.0	9.5	10.3	12.7	12.3	12.5	12.5
$n_n(E_F)$	1.83	1.50	1.66	1.79	1.60	0.70	0.67	0.64	0.59

Table 7.5: Some properties of the nine maximally localized Wannier functions.

U_{nm}	0	1	2	3	4	5	6	7	8
0	26.16	21.87	23.67	23.70	22.64	15.58	15.59	14.87	14.45
1	21.87	22.07	21.05	21.57	20.73	13.92	14.68	14.19	13.03
2	23.67	21.05	23.99	22.38	21.64	15.00	14.59	14.34	14.54
3	23.70	21.57	22.38	25.46	22.91	15.77	15.08	14.83	14.45
4	22.64	20.73	21.64	22.91	23.17	14.38	14.07	14.74	14.38
5	15.58	13.92	15.00	15.77	14.38	14.72	10.95	10.63	10.34
6	15.59	14.68	14.59	15.08	14.07	10.95	14.51	9.83	10.20
7	14.87	14.19	14.34	14.83	14.74	10.63	9.83	14.35	9.75
8	14.45	13.03	14.54	14.45	14.38	10.34	10.20	9.75	14.06

J_{nm}	0	1	2	3	4	5	6	7	8
0	26.16	0.90	0.68	1.08	0.91	0.56	0.78	0.50	0.56
1	0.90	22.07	0.85	0.75	0.97	0.68	1.33	1.13	0.28
2	0.68	0.85	23.99	0.93	1.02	0.87	0.84	0.55	0.85
3	1.08	0.75	0.93	25.46	0.66	0.76	0.55	0.77	0.68
4	0.91	0.97	1.02	0.66	23.17	0.73	0.37	1.04	1.21
5	0.56	0.68	0.87	0.76	0.73	14.72	0.85	0.74	0.63
6	0.78	1.33	0.84	0.55	0.37	0.85	14.51	0.37	0.64
7	0.50	1.13	0.55	0.77	1.04	0.74	0.37	14.35	0.47
8	0.56	0.28	0.85	0.68	1.21	0.63	0.64	0.47	14.06

Table 7.6: Direct and exchange Coulomb matrix elements for Wannier functions. All energies are eV's.

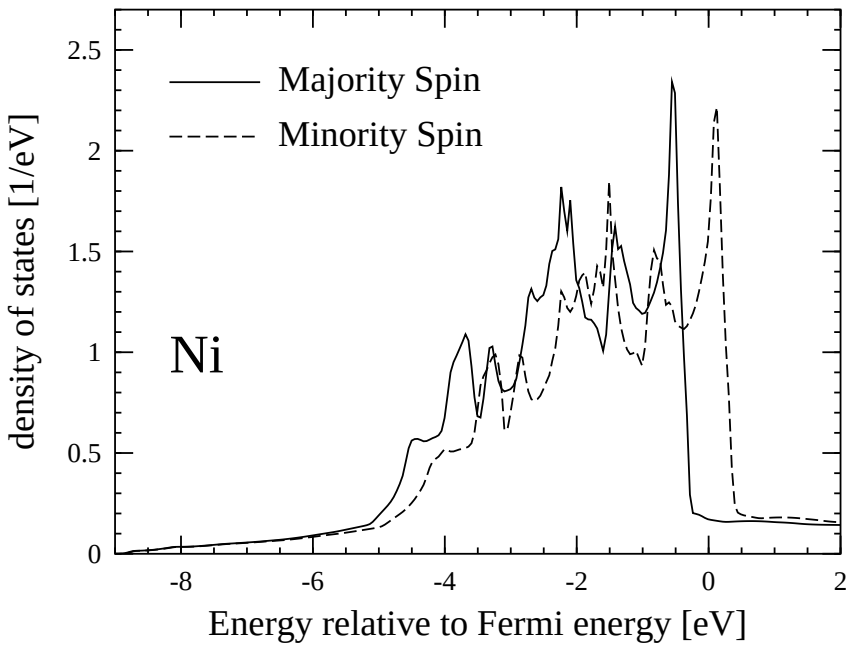

Figure 7.12: Density of states (per spin) from LSDA.

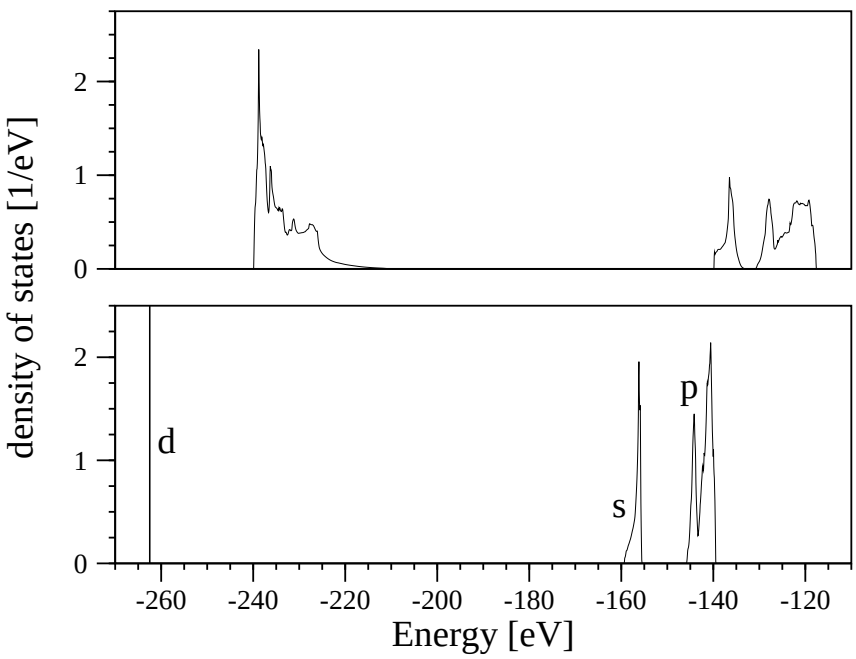

Figure 7.13: Total (both spin) density of states for the non-interacting Hamiltonian H_0 in (i) eigenbasis (lower graph). (ii) “Hartree” basis (upper graph).

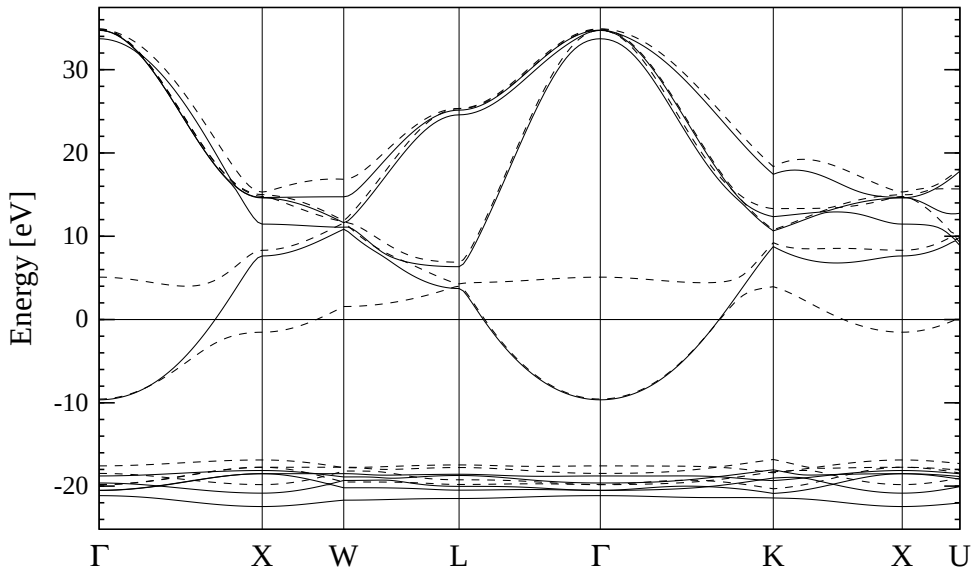

Figure 7.14: Spin-polarized Hartree-Fock band structure relative to Fermi energy. [Majority spin (solid), minority spin (dashed)]

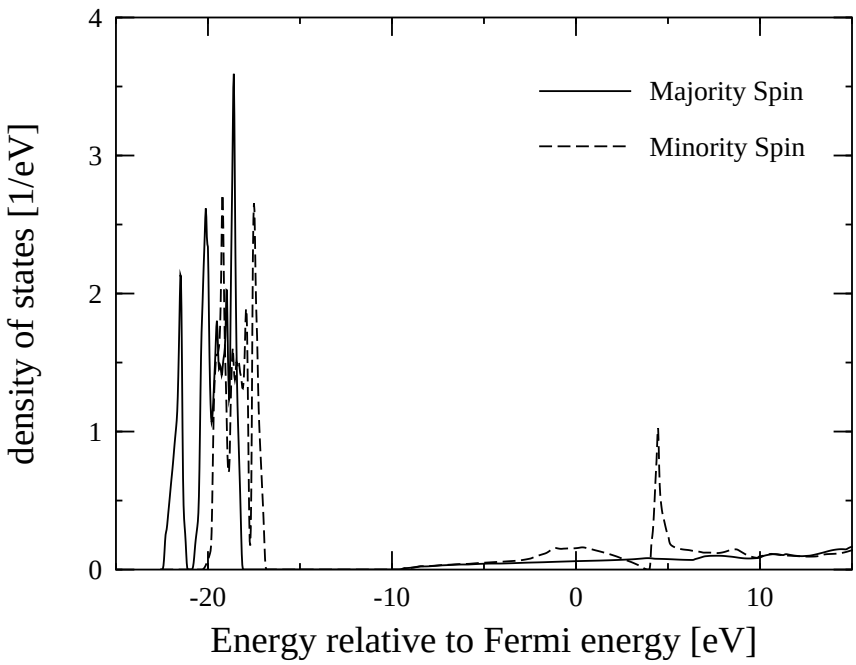

Figure 7.15: Density of states (per spin) for Hartree-Fock band structure.

7.1.4 Copper

Atomic Number		29
Valence electrons		11
Lattice		FCC
Wigner-Seitz radius [a_0]		2.669
(Valence) Total energy:	Hartree	-100.099
[Ryd/atom]	LDA	-103.316
	LSDA	-103.316
	Hartree-Fock	-111.231
Coulomb energy U^{3d}:	Slater F^0	26.27
[eV]	Matrix elements	24.48
	Constrained LDA	17.6
Magnetic moment:	Experimental	0
[μ_B/atom]	LSDA	0
	Hartree-Fock	0

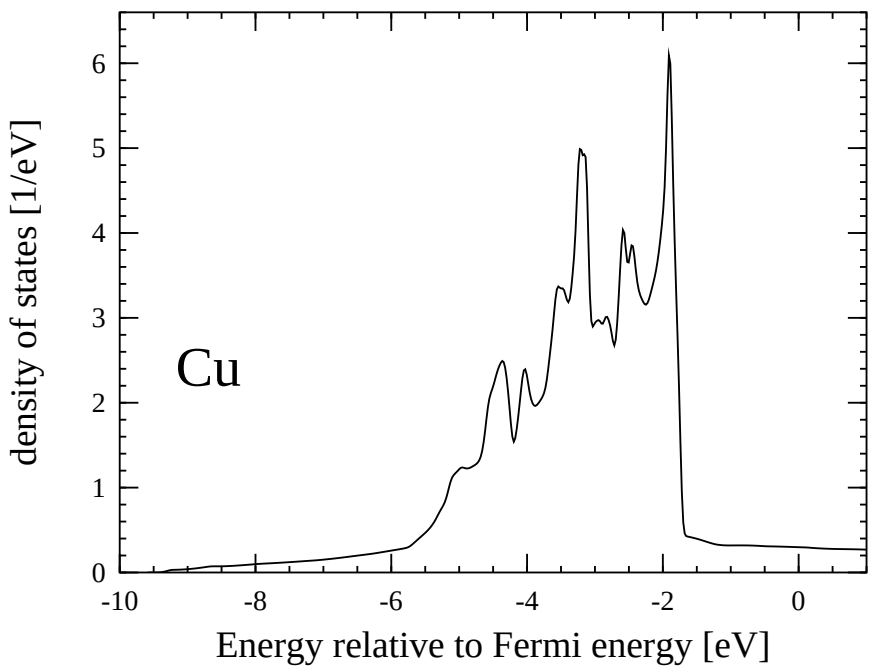

Figure 7.16: Total (both spins) density of states obtained from the “first quantization” Hartree calculation.

n	0	1	2	3	4	5	6	7	8
$\sum_\ell C_\ell^{\mathbf{0}n}$	.9725	.9782	.9896	.9897	.9775	.8857	.8837	.8807	.8821
$\sum_{\mathbf{R}} C_{\ell=0}^{\mathbf{R}n}$	.0040	.0024	.0009	.0008	.0035	.2137	.2203	.2463	.2293
$\sum_{\mathbf{R}} C_{\ell=1}^{\mathbf{R}n}$	.1416	.0988	.0257	.0266	.1023	.5633	.5713	.5694	.5746
$\sum_{\mathbf{R}} C_{\ell=2}^{\mathbf{R}n}$	.8544	.8988	.9735	.9726	.8942	.2230	.2084	.1843	.1960
E_n [eV]	0.01	-0.82	-2.26	-2.24	-0.73	9.59	9.80	9.96	9.93
σ_n [eV]	7.64	6.60	3.87	3.91	6.71	11.05	11.02	10.96	10.99
% DOS	9.3	9.6	8.6	8.6	9.2	14.0	13.5	13.7	13.6
$n_n(E_F)$	1.64	1.71	1.87	1.87	1.70	0.59	0.56	0.53	0.54

Table 7.7: Some properties of the nine maximally localized Wannier functions.

U_{nm}	0	1	2	3	4	5	6	7	8
0	23.92	22.81	24.18	23.85	22.95	14.42	14.01	14.06	13.66
1	22.81	25.38	24.92	24.62	23.36	14.48	14.16	13.73	14.53
2	24.18	24.92	27.60	25.28	24.25	15.08	14.98	14.12	14.46
3	23.85	24.62	25.28	27.57	25.01	14.64	14.82	14.64	14.36
4	22.95	23.36	24.25	25.01	25.19	14.34	14.04	14.21	14.26
5	14.42	14.48	15.08	14.64	14.34	14.05	10.05	9.52	9.92
6	14.01	14.16	14.98	14.82	14.04	10.05	13.94	9.59	9.61
7	14.06	13.73	14.12	14.64	14.21	9.52	9.59	13.74	9.49
8	13.66	14.53	14.46	14.36	14.26	9.92	9.61	9.49	13.81

J_{nm}	0	1	2	3	4	5	6	7	8
0	23.92	0.95	0.80	1.03	0.97	1.00	0.60	1.05	0.89
1	0.95	25.38	0.81	0.92	1.07	0.93	0.78	0.46	0.79
2	0.80	0.81	27.60	1.17	1.04	0.61	0.65	0.35	0.52
3	1.03	0.92	1.17	27.57	0.67	0.49	0.57	0.70	0.40
4	0.97	1.07	1.04	0.67	25.19	0.51	0.85	0.89	0.82
5	1.00	0.93	0.61	0.49	0.51	14.05	0.72	0.53	0.69
6	0.60	0.78	0.65	0.57	0.85	0.72	13.94	0.60	0.57
7	1.05	0.46	0.35	0.70	0.89	0.53	0.60	13.74	0.59
8	0.89	0.79	0.52	0.40	0.82	0.69	0.57	0.59	13.81

Table 7.8: Direct and exchange Coulomb matrix elements for Wannier functions. All energies are eV's.

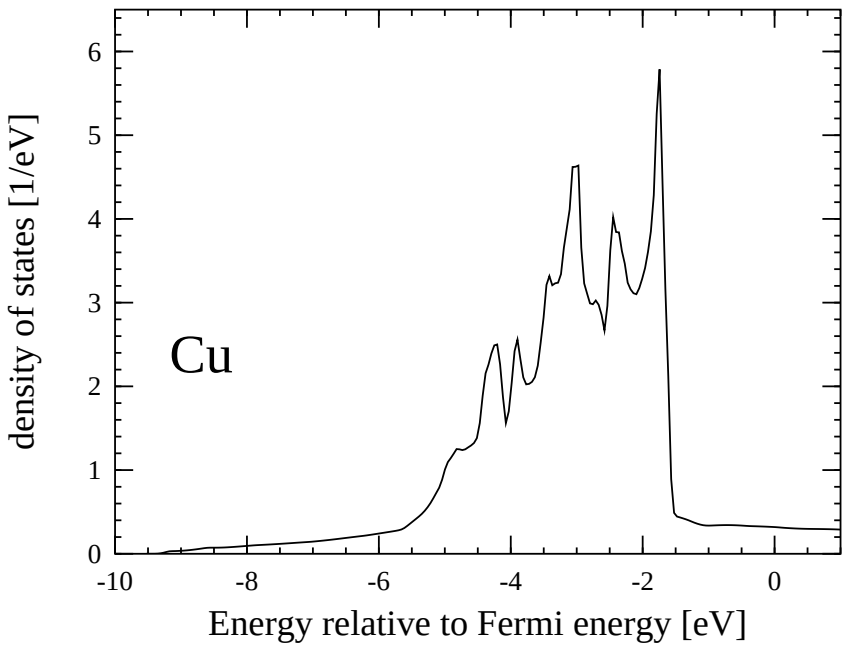

Figure 7.17: Total (both spins) density of states from LSDA.

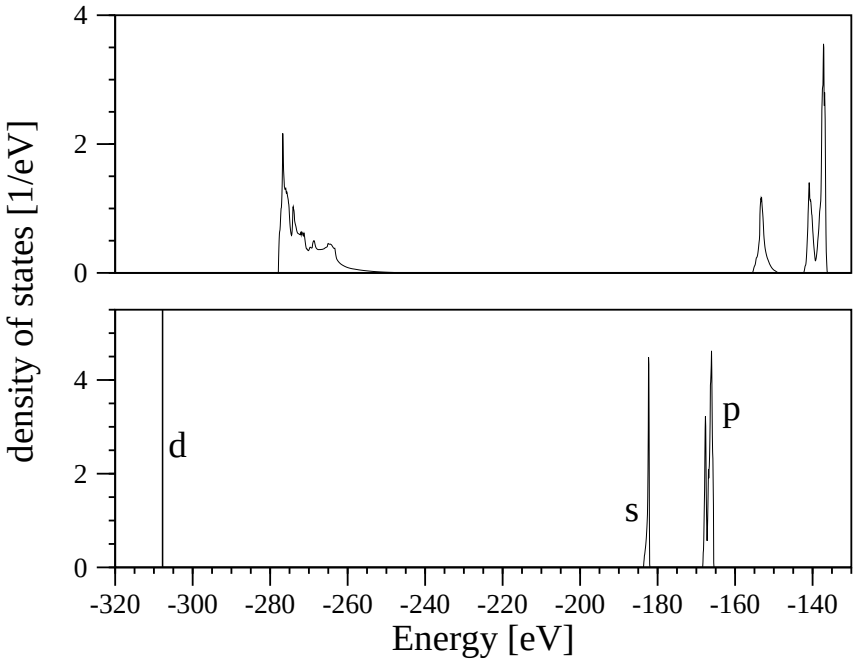

Figure 7.18: Total (both spin) density of states for the non-interacting Hamiltonian H_0 in (i) eigenbasis (lower graph). (ii) “Hartree” basis (upper graph).

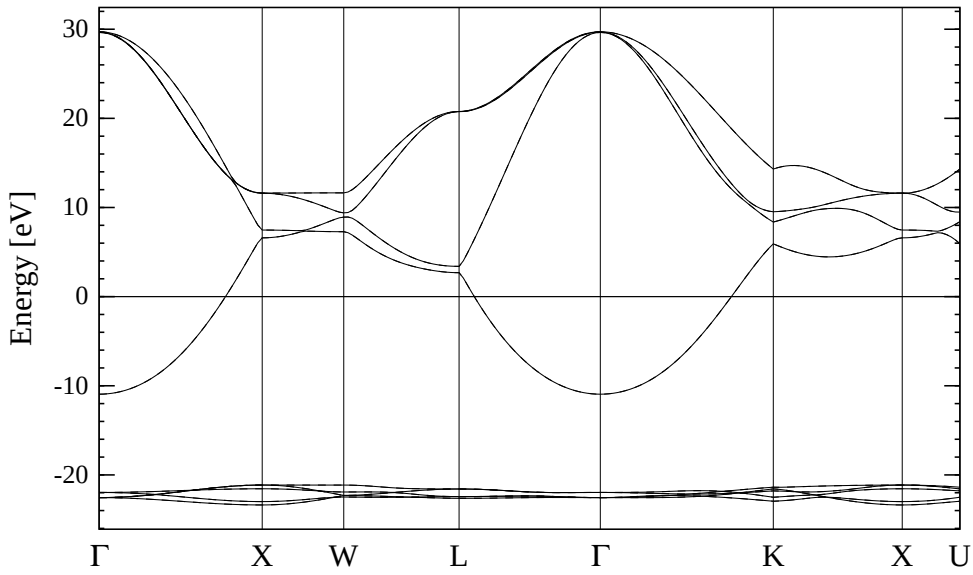

Figure 7.19: Spin-polarized Hartree-Fock band structure relative to Fermi energy. [Majority spin (solid), minority spin (dashed)]

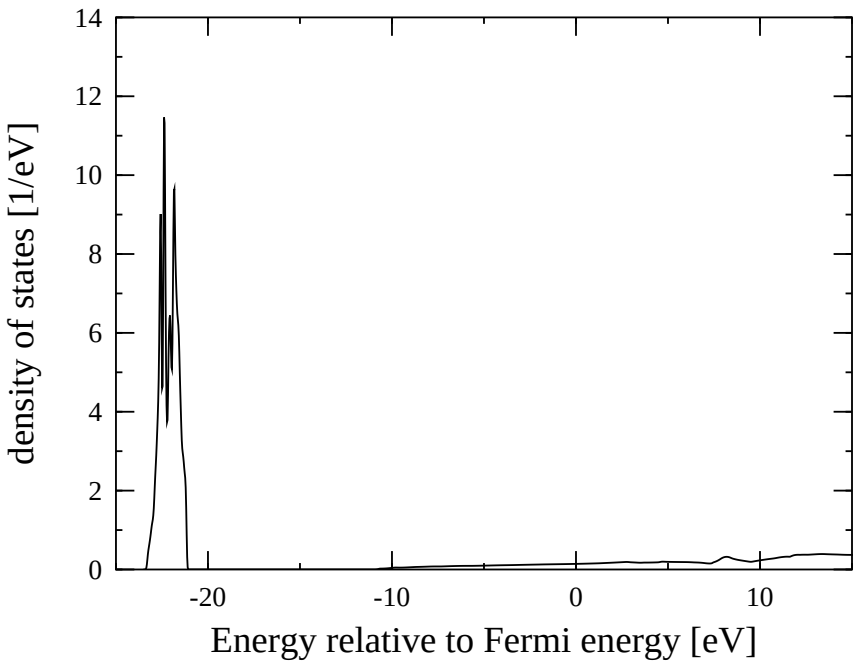

Figure 7.20: Total (both spins) density of states for Hartree-Fock band structure.

7.2 Discussion

For all metals, Wannier functions 0 through 4 are most localized, with at least 95% of their density in the home sphere, as can be seen from the upper table (1. row) on the second page of each metal in the preceeding section. These Wannier functions also have the largest d-character (4. row), greater than 78%, and we refer to them as a d-like Wannier function. Most of these d-like Wannier functions have their associated energy (5. row) below the Fermi level, and the associated width (6. row) is relatively small (compared to the other Wannier functions), as a consequence of their large d-character. Accordingly, the projected occupation $n_n(E_F)$ is also largest for the d-like Wannier functions.

Slater Integrals

Since for all four metals, the Wannier functions 0 through 4 have the largest d-character ($> 78\%$), we can calculate an averaged direct Coulomb d-interaction from the matrix elements that are shown in the lower table on the second page of each metal in the preceeding section. The results are given in Tab. 7.9, together with Slater integrals, obtained from the radial d-wave functions, see section 5.3.5. Compared to the estimates obtained from Slater integrals, the corresponding averaged energies obtained from the Coulomb matrix elements are slightly smaller, since the Wannier functions are (i) not pure in their d-character. (ii) not restricted to their home sphere. Nevertheless, the Slater integrals offer a good estimate of the size of Coulomb matrix elements, and are easy to obtain.

Metal	$U = F^0$	F^2	F^4	J	U_{diag}	F^4/F^2	$U - U_{sp}$
Fe	21.621	9.611	5.914	0.925	22.358	0.615	
	21.092			0.810	22.501		10.534
Co	23.175	10.312	6.346	0.992	23.966	0.615	
	22.592			0.871	24.046		11.955
Ni	24.692	11.000	6.773	1.059	25.535	0.616	
	22.608			0.876	24.171		11.294
Cu	26.272	11.724	7.225	1.129	27.171	0.616	
	24.485			0.943	25.930		13.741

Table 7.9: For each metal, the first line shows the three Slater integrals and quantities calculated therefrom, i.e. the last term in Eqs. (5.80) and (5.81). The second line shows the corresponding values evaluated from the Coulomb matrix elements in the preceeding sections, that is the middle term in Eqs. (5.80) and (5.81). All energies in eV's.

The Slater integrals F^2 and F^4 for Fe, Co and Ni are also given in Ref. [61], but for *ions*, e.g. Fe^{2+}, Co^{3+}. Since the lack of Coulomb repulsion localizes the orbitals, the integrals are (a few eV) larger compared to ours. Considering this effect, the Slater integrals are in good agreement with ours.

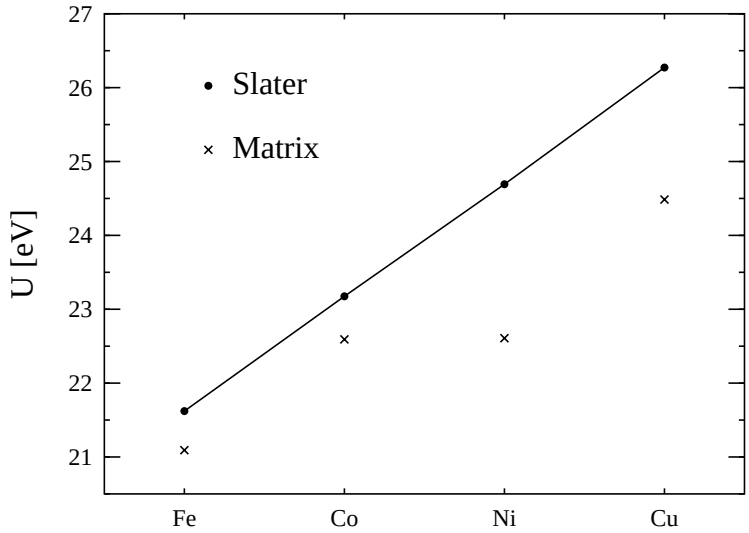

Figure 7.21: The averaged direct Coulomb interaction U (see Eq. (5.79)) as a function of the atomic number Z evaluated as: (i) The Slater integral F^0. (ii) The averaged Coulomb matrix with Wannier functions.

We also give the ratio F^4/F^2, which is often set to 0.625, e.g. in Ref. [62], in order to determine the complete Coulomb d-matrix from U and J, see section 5.3.5.[2]

Also in Tab. 7.9, we have calculated $U - U_{sp}$. Here, U_{sp} is the average of the 4×4 sub block of direct sp Coulomb matrix elements, i.e. the block with matrix elements of the Wannier functions 5 through 8 which have rather large s- and p-character. Why this is an interesting quantity to know will be explained below, where we discuss our results with respect to many-particle model Hamiltonians.

In Fig. 7.21, we have plotted the data of the first column of Tab. 7.9. It is interesting to note that the Slater integral F^0 as a function of the atomic number is found to be on a straight line, i.e. $F^0(Z) = 1.55\ \mathrm{eV} \cdot Z - 18.60\ \mathrm{eV}$. Qualitatively, this behavior can be explained, since for increasing Z, the valence electrons are drawn closer to the nuclei, causing a higher localization (within the atomic sphere). Accordingly, more localized wave functions lead to larger Coulomb matrix elements.

Magnetic Moments

As mentioned above, we have performed LSDA calculations for the metals Fe, Co, Ni and Cu. Before turning to the ferromagnetic metals, we would like to point out the situation for Cu. Although Cu has no magnetic moment, we may still perform such a calculation since the LSDA formalism is only an extension to the LDA. During the self-consistency cycle, we are able to track the size of the magnetic moment. Starting from a state for which the

[2] In some references [18, 60], the ratio "F^2/F^4" is set to 0.625. We wonder whether these are probably printing errors or the word "ratio" is understood in a different sense.

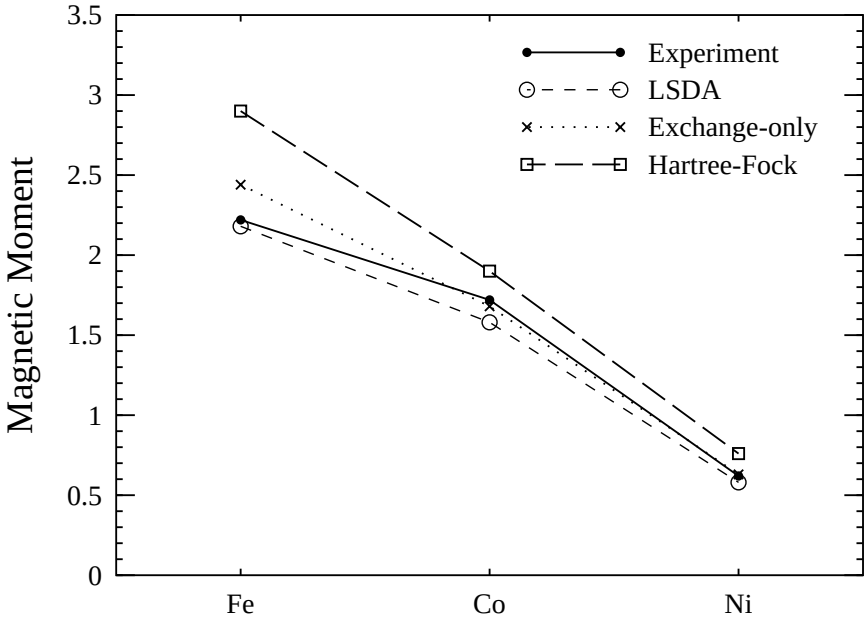

	Experiment	LSDA	Exchange-only	Hartree-Fock
Fe	2.22	2.18	2.44	2.90
Co	1.72	1.58	1.68	1.90
Ni	0.62	0.58	0.63	0.76

Figure 7.22: Magnetic moments for $3d$ ferromagnets from experiment [46] and different theories, in units of μ_B/atom.

spin symmetry is broken, we find the magnetic moment to converge to zero again. This behavior is different for the materials mentioned above, for which the LSDA converges to a spin-polarized solution when starting from a state with broken symmetry. The spin-up and spin-down DOS are equal, and Fig. 7.17 shows the total density of states that is found upon self-consistency.

For the $3d$ transition ferromagnets, a comparison of the magnetic moment obtained from LSDA is made in Fig. 7.22. As can be seen, the predicted magnetic moment agrees with experiment very well. The qualitative behavior of the magnetic moment, as we move from Fe to Ni, which means that the number of d electrons is increased from 8 to 10, can be explained by the Friedel Model and the Stoner theory [63].

In addition, we have performed "exchange-only" LSDA calculations in which the exchange-correlation potential (2.43) is replaced by an exchange-only potential. This exchange-only potential is obtained by omitting the correlation terms in the Barth-Hedin potential (C.18),[3] and is a local (density) approximation of the non-local Hartree-Fock potential. Using the

[3]The correlation terms are the terms with subscript c appearing in (C.16).

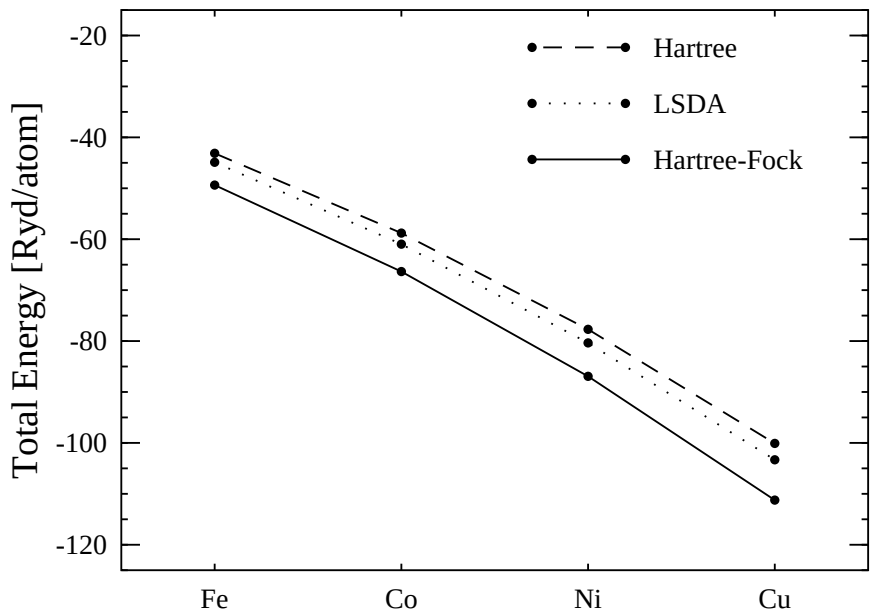

Figure 7.23: Total energies of valence electrons from different approximations for the $3d$ transition metals Fe thru Cu.

(local) exchange-only potential, we obtain an approximation for the Hartree-Fock solution since correlations are neglected. Put in other words, we obtain a solution which is closer to Hartree-Fock than (X+C) LSDA, but still an approximation, since the Hartree-Fock potential is non-local. The bands we have obtained look similar to the LSDA bands, thus, we have not plotted them. The magnetic moments were found to be larger than in LSDA, see Fig. 7.22. This indicates that Hartree-Fock overestimates magnetic moments, and (indeed) our Hartree-Fock magnetic moments are even larger than the magnetic moments from the exchange-only calculations.

Total Energies

In order to discuss the (absolute) total energies from different approximations, we have collected the results (Sec. 7.1) in Fig. 7.23. Firstly, the total energy of the valence electrons is a decreasing function of Z, since without considering interaction, more low lying d-states[4] are being occupied, lowering the total energy. On the other hand, more electrons are causing Coulomb repulsion which increases the total energy, however, this is a smaller effect. The Hartree-Fock trial function is a Slater determinant, whereas in Hartree and LSDA, the trial function is just a simple product of one-particle wave functions. Thus, the Hartree-Fock total energy comes closest to the true total energy and provides a strict upper bound. Accordingly, since the LSDA energies are higher than Hartree-Fock total energies (Fig. 7.23), the difference between the two is a lower bound for the error in the LSDA energy, which we find increasing with Z (4.48, 5.38, 6.56, 7.91 Ryd for Fe, Co, Ni, Cu respectively). These

[4] See Figs. 7.3, 7.8, 7.13 and 7.18.

Ref.	Fe		Co		Ni		Cu	
	U	J	U	J	U	J	U	J
[9]	1.2	0.73	2.4	0.50	3.7	0.27		
[12]	1.63	1.09			2.45	1.70	4.08	
[18]					2.47	0.5		
[60]	2.3	0.9	3	0.9	4	0.9	4	0.9
here	21.1	0.81	22.6	0.87	22.6	0.88	24.5	0.94

Table 7.10: Averaged direct and exchange Coulomb matrix elements used in several references. However, direct comparison of the values is difficult, since different models and approximations were being used. Energies in eV.

errors appear very large; even for the corresponding atoms, see Ref. [49], the errors are quite large (2.21, 2.33, 2.40, 2.46 Ryd).

The difference of the Hartree to the Hartree-Fock total energy (6.24, 7.56, 9.23, 11.13 Ryd) is also increasing with Z, since the exchange energy, which is missing in Hartree, becomes smaller with higher electronic density.

Within the local density approximation, the LSDA total energy is (not surprisingly) better than Hartree total energy, since exchange-correlation effects are (locally) accounted for.

Finally, we note that the difference between the LDA and LSDA total energy, i.e. the energy of spin polarization, is very small for the ferromagnets and zero for Cu (27, 10, 3, 0 mRyd), lowering the energy of the spin-polarized solution of the Kohn-Sham equations. Of course, these are relative differences in the total energy. The accuracy of our absolute total energy greatly exceeds the energy gained by spin polarization (of the ferromagnets).

Size of Coulomb Matrix Elements

We now wish to discuss the size of our Coulomb matrix elements. The Coulomb matrix elements we have determined from first principle Wannier functions are extremely large compared to the U's commonly used in model Hamiltonians. In Tab. 7.10, we give U's and J's found in the literature, as well as our own results. How can this huge discrepancy be explained? To answer this question, it is important to look at the models that are being used.

In this work, we have started from hopping matrix elements of the completely non-interacting Hamiltonian H_0 in Eqs. (6.1) and (6.3). When looking at the DOS of H_0,[5] it is not surprising that large U's are needed to pull the $3d$-bands back into the region of the $4s$ and $4p$-bands of the LDA or Hartree band structure. While our procedure is very elementary, usually more sophisticated procedures are used. One starts from an LDA calculation and some model calculation with screened Coulomb matrix elements is added on top, since the LDA band structure is already reasonable and looks like a good starting point. Despite the success of some of these procedures, some points can be questioned. (i) Starting from LDA, it is not

[5] In Figs. 7.3, 7.8,7.13 and 7.18.

clear which correlations are already included in the LDA treatment. (ii) The Coulomb interaction is usually restricted to $3d$-orbitals. Thus, these corrections to LDA are not systematic. Often, as mentioned in the introduction, U and J are just semiempirical fitting parameters which are adjusted in a way that experimental quantities, e.g. the magnetic moment, are correctly reproduced by the model.

Most model calculations assume very localized, pure (in ℓ-character) Wannier functions. In particular, they often assume that LDA or some one-electron-like treatment is adequate for non-d electron states, and that the only explicit correlations that need to be included are related to on-site Coulomb U's for the d (or f) states. These types of assumptions raise some difficulties for us to connect our treatment to the model Hamiltonians, since the orthogonalization of localizing our Wannier functions requires mixed ℓ-character of the resulting orbitals.

There are factors which suggest smaller U's for model Hamiltonian calculation. Starting from our large U's, these factors include:

i.) Since we calculate U's for all of the orbitals, we are implicitly including correlation effects for spd-states. But, as mentioned above, in model Hamiltonian calculation, the Coulomb interaction is usually restricted to d-orbitals. Consider Eq. (6.5) with only diagonal (on-site) matrix elements $W_{nn,nn}$ of equal size. The effect of such a term is just an overall shift of the bands. Therefore, if we restrict the interaction to d-orbitals, it seems reasonable to subtract the sp-interaction from the d-interaction, since only the difference between the two accounts for correlation effects. Thus, we have also calculated $U - U_{sp}$ in Tab. 7.9 which is about half the size of U. However, things are more complicated since the Coulomb matrix is not diagonal. Nevertheless, this is a step towards smaller U's.

ii.) Because we have the freedom of choosing the basis set, we can regard this set as consisting of less localized one-particle states which has the consequence that the U's are smaller. In this sense, the Slater integral F^0 is an upper bound for U. The lower bound is zero, since if we consider completely delocalized Wannier functions[6] as our basis set, the U's become zero for an infinite number of mesh points in Eq. (4.3). On the other hand, the model Hamiltonians we are dealing with, e.g. the multi-band Hubbard Hamiltonian, always assume localized basis sets.

As an example of this, we have calculated a less localized Wannier state (by doing fewer steps in the Marzari-Vanderbilt minimization procedure). In this case, the highest d-character state, which is almost pure d-like, has only 58% of its charge density in the center muffin-tin, and 95% within the first 3 shells. Now, we only find U about 13 eV for this less localized d-state.

However, with such less localized Wannier states, the tight-binding assumption for the one-particle matrix elements would no longer hold, i.e. one cannot restrict them to a few neighbor shells, and also the Hubbard assumption that only on-site Coulomb matrix elements are non-vanishing would no longer hold.

[6] One can actually construct these by choosing a negative step size in Eq. (4.23). Of course, this is not the purpose of the Marzari-Vanderbilt method.

iii.) Since we are working with bare unscreened Coulomb matrix elements, we would have to apply a many-body approximation which includes screening effects, i.e. go far beyond Hartree-Fock, for example use the RPA[7]. However, in Refs. [9, 18], for instance, second order perturbation theory (which does not include screening) was used, requiring to use screened Coulomb matrix elements.[8] One may also think of the non-d states having some screening contribution to the effective U's. The screened interaction for Ni is given Ref. [64] as 2.2 eV, while the unscreened interaction is given as approximately 27 eV, which is in good agreement with the Slater integral $F^0 = 24.7$ eV.

These problems highlight the fact that there is no ab-initio method of deriving the model multi-band Hubbard Hamiltonian. We have determined all the matrix elements of the full second-quantized Hamiltonian (6.1) from first principles. Nevertheless, solving this Hamiltonian (in its full generality) seems impossible. One has to keep in mind that the Hubbard Hamiltonian is just a *model* Hamiltonian, i.e. a simplified version of the full Hamiltonian (6.1), which allows to study physical effects without going through all the complications the full Hamiltonian involves. However, reasonable estimates for the parameters involved are necessary to apply the results to real materials.

Off-site Coulomb Matrix Elements

In the preceeding discussion, we have only talked about on-site Coulomb matrix elements. A central assumption of the Hubbard model is that the electrons only interact when being at the same lattice site. That is, all off-site Coulomb matrix elements are omitted. Consider direct matrix elements $W_{12,21}$ for $\mathbf{R}_1 \neq \mathbf{R}_2$ with localized Wannier functions. Within the ASA, the contributions from all atomic spheres are taken into account by Eq. (5.42). From Eqs. (5.43) and (5.44), we see that a large contribution arises if $\mathbf{R}_{A\ldots D} = \mathbf{0}$. Hence, $\mathbf{R} \neq \mathbf{R}'$ in Eq. (5.43) (since $\mathbf{R}_1 \neq \mathbf{R}_2$) and the contribution is approximately given by (5.46). Without knowing the Wannier functions, we may estimate the size of the intra-band off-site Coulomb matrix element as $W_{12,21} \approx e^2/|\mathbf{R}_1 - \mathbf{R}_2|$ when we assume the Wannier functions to be very localized. For nearest-neighbor matrix elements, we find about 6 eV for our metals.[9] This seems very large and how can these terms be omitted in the Hubbard model altogther? Following the discussion in section 6.3.2, one has to use (6.29) (instead of (5.42)) and terms with $\mathbf{R} \neq \mathbf{R}'$ are omitted in (6.29).[10] Consequently, since the potential from the nuclear point charge and the electronic charge density can be restricted to a single muffin-tin, the Coulomb matrix elements may, to some approximation, be restricted to on-site elements.

[7] Random-phase approximation which is a summation of all bubble diagrams. This seems to be difficult to apply to multi-band systems, however.

[8] And, as shown on page 89, these are smaller than bare ones.

[9] Using Eqs. (A.3) and (A.6).

[10] The impact of using (6.29) (instead of (5.42)) on the size of on-site Coulomb matrix elements is small when the Wannier functions are well localized, since for this situation $W(12, 34; \mathbf{0}, \mathbf{0})$ is (by far) the largest contribution in (5.42) and (6.29).

Chapter 8

Conclusions & Outlook

8.1 Conclusions

We have shown in this work that ab-initio band structure methods, namely the LMTO method [31, 32] within the ASA, can be used for a first-principles calculation of well localized Wannier functions [29]. This was achieved by using a method proposed by Marzari and Vanderbilt [33]. The resulting maximally localized Wannier functions for the $3d$ transition metals Fe, Co, Ni and Cu have at least 87% of their charge density within the home MT sphere. In order to construct the (generalized) Wannier functions, rotations among the Bloch bands at each $\mathbf{k}$-point are necessary which mix their ℓ-characters even more. Hence, the resulting Wannier functions are not pure with respect to their ℓ-character; for well localized d-like Wannier functions, we have found a d-character greater than 78%.

These Wannier functions serve as a minimal basis, i.e. a one-particle basis for the valence band states containing only $4s$, $4p$ and $3d$-orbitals, in which the many-particle Hamiltonian is expanded. From these localized Wannier functions, constructed from Hartree band states, the on-site and inter-site one-particle matrix elements of the many-particle Hamiltonian were calculated. A good localization of the Wannier functions is needed to keep tight-binding (hopping) matrix elements restricted to a small number of near neighbors. We have proposed two methods to evaluate Coulomb matrix elements from Wannier functions. The Coulomb matrix elements within the localized Wannier states are similarly most important between on-site and nearest-neighbor Wannier functions.

The result is thus an electronic multi-band Hamiltonian in second quantization with first-principles one- and two-particle matrix elements. The Hamiltonian is of the form of an extended multi-band Hubbard model but without adjustable parameters, i.e. the parameters are directly calculated for the given materials. The only approximations still involved are the ones inherent to the ab-initio band structure method used [e.g., the muffin-tin assumption, the ASA approximation, the choice of linearized orbitals in the LMTO and the "frozen-core" approximation] and the truncation in the number of bands (states) per site. In this multi-band Hamiltonian, the hopping matrix elements are obtained for completely non-interacting valence electrons moving in the effective core potential. Hence, in contrast to other approaches which use LDA as the starting point, we start from a well defined situation

where the problem of double counting interactions (already included in the effective LDA band structure) is avoided.

This resulting multi-band Hamiltonian was studied within the Hartree-Fock approximation for the $3d$ transition metals Fe, Co, Ni and Cu. For the ferromagnets, the resulting magnetic moments of this treatment were found to be about 20 to 30 % larger than within LSDA which is due to the fact that Hartree-Fock tends to overestimate exchange effects. This is also indicated by a local exchange-only calculation, where the magnetic moments were found to be about ten percent larger than within LSDA. The resulting Hartree-Fock total energy is lower than in LSDA, providing an error estimate for the absolute LSDA energy. The (Hartree-Fock) band structure shows the $3d$-bands below the $4s$ and $4p$-bands. Responsible for this behavior is the Fock self-energy term which subtracts the self-interactions included in the Hartree self-energy term.

For the metals mentioned above, we find on-site direct Coulomb matrix elements ("Hubbard-U's") on the magnitude of 21 to 25 eV for $3d$ Wannier states. This is the magnitude discussed already earlier [6] and similar to those for atomic $3d$-states, as well as the magnitude of the ($3d$) Slater integral F^0. These U-values are much larger than commonly expected or used in models. We have discussed reasons why it may be justified to use smaller U's in model Hamiltonian studies, e.g. dielectric screening, highlighting the fact that reasonable estimates for model parameters are necessary to apply the results to real materials.

8.2 Outlook

Our current approach can, of course, be further extended in many directions. We would like to suggest some possibilities:

i.) One can study the first-principle Hamiltonian within many-body methods or approximations which go beyond Hartree-Fock. For example, second order perturbation theory in U [9, 18], random-phase approximation (RPA) which is a summation of all bubble diagrams, a multi-band version of the DMFT as in Refs. [10, 13, 15, 17].

ii.) Another promising extension would be to perform Hartree-Fock calculations on the first quantized level, i.e. solve the Hartree-Fock equations which involves solving the Schrödinger equation for a non-local potential. This way, one could exploit analogies between effective single-particle properties from first and second quantization calculations in order to further bridge the gap between first-principles calculations for real materials and model Hamiltonian calculations.

iii.) We have (as usual) only considered the valence electrons in a frozen-core potential, which contains exchange-correlation from the core electrons in the local approximation. One may try to consider the many-particle effects of all electrons, i.e. not use the frozen-core approximation. However, since the number of electrons is quite large in the $3d$ transition metals, one would probably have to start by looking at easier systems, e.g lithium. In any case, this approach would require applying the LMTO method several times (for each principal quantum number), since the LMTO can only cope with one type of ℓ-orbitals at a time, e.g. $2s$ but not $2s$ and $1s$ simultaneously.

iv.) Using the FFT method (Sec. 5.3.2), we can evaluate screened Coulomb matrix elements for the Yukawa potential which arises from the Thomas-Fermi approximation. One can also try to consider screening by a Lindhard theory, generalized to real band structures and matrix elements between Bloch functions instead of free electron (plane-wave) matrix elements, and calculate Coulomb matrix elements using the resulting dielectric function.

v.) Also, the method could be applied to really correlated systems, e.g. heavy fermion systems (like UPt_3), superconductors, semiconductors, quantum dots, etc. However, such systems have more than one atom per unit cell and consist of different atoms which leads to additional complications.

Ultimately, the goal is to establish a reliable method suitable to describing electronic properties of solids. This new method should treat electron-electron interactions by using a many-particle method (on the second quantized level) and not depend upon LDA such as the (other) current approaches in this area.

Appendix A

Conventions

Units Throughout, we use atomic Rydberg units where $\hbar = 2m = e^2/2 = 1$. At some points however, for clarity, we will write quantities like $\hbar$, the mass of the electron m or the charge of the electron e explicitly. Note that

$$a_0 = \hbar^2/me^2 \approx 0.529 \text{ Å} \qquad \text{and} \qquad \text{Ryd} = e^2/2a_0 \approx 13.6 \text{ eV} \quad . \tag{A.1}$$

Here is a useful conversion table for atomic Rydberg and MKSA units:

Quantity	Symbol	Rydberg	MKSA
Length	ℓ	1	5.2917725 $\cdot 10^{-11}$ m
Energy	E	1	2.1798741 $\cdot 10^{-18}$ J
Charge	q	1	1.1329105 $\cdot 10^{-19}$ C
Charge density	n	1	7.6452571 $\cdot 10^{11}$ C/m^3
some constants:			
Planck's quantum	$\hbar$	1	1.05457266 $\cdot 10^{-34}$ J·s
(Abs.) charge of electron	e	$\sqrt{2}$	1.60217733 $\cdot 10^{-19}$ C
Bohr radius, $\hbar^2/me^2$	a_0	1	5.29177249 $\cdot 10^{-11}$ m
Energy 1 electron Volt	eV	$\approx$ 1/13.6	1.60217733 $\cdot 10^{-19}$ J
Rydberg energy, $e^2/2a_0$	Ryd	1	2.1798741 $\cdot 10^{-18}$ J
Hartree energy, e^2/a_0		2	4.3597482 $\cdot 10^{-18}$ J
Speed of light	c	$\approx$ 274	2.99792458 $\cdot 10^{8}$ m/s
Bohr magneton	μ_B	$\sqrt{2}$	9.2740154 $\cdot 10^{-24}$ J/T
Mass of electron	m_e	1/2	9.1093897 $\cdot 10^{-31}$ kg

Vectors Vectors in $\mathbb{R}^3$ are represented by bold letters. We have:

$$\mathbf{r} = (r_x, r_y, r_z) \ , \quad r = |\mathbf{r}| = \sqrt{\mathbf{r}\cdot\mathbf{r}} \ , \quad \hat{\mathbf{r}} \equiv \Omega \equiv \{\vartheta, \varphi\}$$

$$r_x = r\sin\vartheta\cos\varphi \ , \quad r_y = r\sin\vartheta\sin\varphi \ , \quad r_z = r\cos\vartheta$$

Angular momentum quantum numbers We use the common short hand notation $L = \{\ell, m\}$. For explicit calculations, this notation can be regarded as $L = \ell^2 + \ell + m$:

L	0	1	2	3	4	5	6	7	8	9	...
ℓ	0	1	1	1	2	2	2	2	2	3	...
m	0	−1	0	+1	−2	−1	0	+1	+2	−3	...

FCC Lattice (face-centered cubic) Set of tranlation vectors:

$$\mathbf{a}_1 = \frac{a}{2}(\mathbf{e}_y + \mathbf{e}_z)\ , \ \ \mathbf{a}_2 = \frac{a}{2}(\mathbf{e}_z + \mathbf{e}_x)\ , \ \ \mathbf{a}_3 = \frac{a}{2}(\mathbf{e}_x + \mathbf{e}_y) \tag{A.2}$$

Relations between the real space lattice constant a, the volume of the primitive cell Ω, the Wigner-Seitz radius S and the nearest-neighbor distance R^0:

$$\Omega = \frac{a^3}{4} = \frac{4\pi}{3}\, S^3\ , \quad a = \left(\frac{16\pi}{3}\right)^{\frac{1}{3}} S\ , \quad R^0 = \frac{1}{\sqrt{2}}\, a = \left(\frac{32\pi^2}{9}\right)^{\frac{1}{6}} S \tag{A.3}$$

Reciprocal lattice points $\mathbf{k}$ with high symmetry in FCC structure: (in units $2\pi/a$)

	Γ	X	W	L	K	U
k_x	0	1	1	.5	.75	1
k_y	0	0	.5	.5	.75	.25
k_z	0	0	0	.5	0	.25

The irreducible wedge of the Brillouin zone (IBZ) is spanned by these six $\mathbf{k}$-points. Consequently, the IBZ may be expressed in terms three tetrahedra. These tetrahedra are given by the four corner $\mathbf{k}$-points. The IBZ can, for example, be expressed as the three tetrahedra:

$$\Gamma\ \mathrm{X}\ \mathrm{L}\ \mathrm{K}\quad ,\quad \mathrm{X}\ \mathrm{W}\ \mathrm{L}\ \mathrm{K}\quad ,\quad \mathrm{X}\ \mathrm{W}\ \mathrm{U}\ \mathrm{L} \tag{A.4}$$

BCC Lattice (body-centered cubic)

$$\mathbf{a}_1 = \frac{a}{2}(\mathbf{e}_y + \mathbf{e}_z - \mathbf{e}_x)\ , \ \ \mathbf{a}_2 = \frac{a}{2}(\mathbf{e}_z + \mathbf{e}_x - \mathbf{e}_y)\ , \ \ \mathbf{a}_3 = \frac{a}{2}(\mathbf{e}_x + \mathbf{e}_y - \mathbf{e}_z) \tag{A.5}$$

$$\Omega = \frac{a^3}{2} = \frac{4\pi}{3}\, S^3\ , \quad a = \left(\frac{8\pi}{3}\right)^{\frac{1}{3}} S\ , \quad R^0 = \frac{\sqrt{3}}{2}\, a = \left(3\pi^2\right)^{\frac{1}{6}} S \tag{A.6}$$

$[2\pi/a]$	Γ	H	N	P
k_x	0	1	.5	.5
k_y	0	0	.5	.5
k_z	0	0	0	.5

The IBZ is simply a *single* tetrahedron:

$$\Gamma\ \mathrm{H}\ \mathrm{N}\ \mathrm{P} \tag{A.7}$$

Appendix B

Mathematical definitions

Spherical harmonics

Legendre polynomials:

$$P_\ell(x) = \frac{1}{2^\ell\,\ell!}\,\frac{d^\ell}{dx^\ell}(x^2-1)^\ell$$

Associated Legendre function:[1]

$$P_\ell^m(x) = (-1)^m(1-x^2)^{\frac{m}{2}}\,\frac{d^m}{dx^m}P_\ell(x) \qquad m \geq 0$$

A definition that accounts for positive and negative m is:

$$P_\ell^m(x) = \frac{(-1)^m}{2^\ell\,\ell!}\,(1-x^2)^{\frac{m}{2}}\,\frac{d^{\ell+m}}{dx^{\ell+m}}(x^2-1)^\ell$$

Spherical harmonics: (see Ref. [52])

$$Y_L(\hat{\mathbf{r}}) \equiv Y_\ell^m(\vartheta,\varphi) \equiv \langle\vartheta\varphi|\ell m\rangle = \sqrt{\frac{2\ell+1}{4\pi}\,\frac{(\ell-m)!}{(\ell+m)!}}\,P_\ell^m(\cos\vartheta)\,e^{im\varphi} \tag{B.1}$$

Orthogonality:

$$\langle L|L'\rangle = \sum_\Omega \langle L|\Omega\rangle\langle\Omega|L'\rangle = \int_{4\pi} d^2\Omega\,Y_L^*(\Omega)\,Y_{L'}(\Omega) = \delta_{LL'} \tag{B.2}$$

Completeness:

$$\langle\Omega|\Omega'\rangle = \sum_L \langle\Omega|L\rangle\langle L|\Omega'\rangle = \sum_L Y_L(\Omega)\,Y_L^*(\Omega') = \delta^2(\Omega-\Omega') \tag{B.3}$$

[1] Phase convertion according to Condon-Shortley, as in Refs. [54, 52].

Spherical Bessel function

The spherical Bessel function is defined by (see also [52] Eq. 16.10 and [65] Eq. 10.1.25):

$$j_\ell(x) = (-x)^\ell \left(\frac{1}{x}\frac{d}{dx}\right)^\ell \left(\frac{\sin x}{x}\right) \tag{B.4}$$

Gaunt coefficients

Definition (see Eq. (6) page 175 in Ref. [54]):

$$c^k(L,L') \equiv \sqrt{\frac{2}{2k+1}} \int_{-1}^{+1} dx\, \Theta_k^{m-m'}(x)\, \Theta_\ell^m(x)\, \Theta_{\ell'}^{m'}(x) \tag{B.5}$$

where $\quad \Theta_\ell^m(x) \equiv \sqrt{\frac{2\ell+1}{2}\,\frac{(\ell-m)!}{(\ell+m)!}}\, P_\ell^m(x)$

The Gaunt coefficients are real and obey the symmetry relation:

$$c^k(L,L') = (-1)^{m-m'} c^k(L',L) \tag{B.6}$$

It follows that:

$$C_{LL'L''} \equiv \int d^2\Omega\, Y_L(\Omega)\, Y_{L'}^*(\Omega)\, Y_{L''}(\Omega) = \delta_{m'',m'-m} \sqrt{\frac{2\ell''+1}{4\pi}}\, c^{\ell''}(L',L) \tag{B.7}$$

Moments

The qth order moment of a density function $f(x)$ about x_0 is defined as: (see Ref. [50])

$$M_q = \int dx\, f(x)\, (x-x_0)^q \tag{B.8}$$

The moment about the origin is the moment about $x_0 = 0$.

Remark: In our case, the density function $f(x)$ is the density of states.

Step function

$$\Theta(x) \equiv \begin{cases} 0 & x<0 \\ 1/2 & x=0 \\ 1 & x>0 \end{cases} \qquad \text{so that} \quad \int_{-\infty}^{y} dx\, \delta(x) = \Theta(y) \tag{B.9}$$

Appendix C

Miscellaneous

C.1 Symmetry and Brillouin Zone Integration

We denote $\alpha\mathbf{k}$ as the rotation α in the point group of the crystal applied to the vector $\mathbf{k}$. To replace the integral in (3.39) by an integral over the IBZ, it is required that (3.42) and

$$\langle\psi_{\alpha\mathbf{k}}|P|\psi_{\alpha\mathbf{k}}\rangle = \langle\psi_{\mathbf{k}}|P|\psi_{\mathbf{k}}\rangle \qquad \forall\ \alpha \tag{C.1}$$

hold, where for simplicity, we have dropped the band index n. From[1]

$$\{\alpha|\mathbf{t}\}\psi_{\mathbf{k}}(\mathbf{r}) = \exp[i\phi(\alpha,\mathbf{k})]\psi_{\alpha\mathbf{k}}(\mathbf{r}) \tag{C.2}$$

it follows that

$$\alpha|\psi_{\mathbf{k}}\rangle = \exp[i\phi(\alpha,\mathbf{k})]|\psi_{\alpha\mathbf{k}}\rangle \quad \text{and} \quad \langle\psi_{\mathbf{k}}|\alpha^{\dagger} = \exp[-i\phi(\alpha,\mathbf{k})]\langle\psi_{\alpha\mathbf{k}}| \ . \tag{C.3}$$

Here, $\alpha^{\dagger}$ is defined by $\alpha^{\dagger}\alpha = 1$, i.e. the inverse operation to α, and $\phi(\alpha,\mathbf{k})$ is an arbitrary real function. Hence, we can write (C.1) as:

$$\langle\psi_{\mathbf{k}}|\alpha^{\dagger}P\alpha|\psi_{\mathbf{k}}\rangle = \langle\psi_{\mathbf{k}}|P|\psi_{\mathbf{k}}\rangle \quad \rightarrow \quad \alpha^{\dagger}P\alpha = P \quad \rightarrow \quad [P,\alpha] = 0 \tag{C.4}$$

Accordingly, we have to require that the projection operator P commutes with all the rotations α in the point group of the crystal.

Proof that P_ℓ and α commute

The projection operator P_ℓ onto the ℓ-component is defined by:

$$P_\ell \equiv \sum_m |\ell m\rangle\langle\ell m| \tag{C.5}$$

A rotation α of the point group is in general an improper rotation, but may always be decomposed as $\alpha = \Pi\beta$, where Π is the parity operator defined by $\Pi\psi(\mathbf{r}) = \psi(-\mathbf{r})$ and β is

[1] See Eq. (3.6.5) in Ref. [30]

a proper rotation. We realize that, if $\mathbf{L}$ is the angular momentum operator of a system, these rotations β can be expressed as[2]

$$\beta = e^{-i\mathbf{L}\cdot\vec{\beta}} \quad . \tag{C.6}$$

Acting on any state $|\psi\rangle$, it rotates $|\psi\rangle$ in the positive sense about the axis $\vec{\beta}$ by angle $|\vec{\beta}|$. Next, we realize that:

$$\mathbf{L}^2|\ell m\rangle = \ell(\ell+1)|\ell m\rangle \qquad \text{and} \qquad \mathbf{L}_z|\ell m\rangle = m|\ell m\rangle \tag{C.7}$$

Since β and $\mathbf{L}^2$ commute, the state $\beta|\ell m\rangle$ is again an eigenstate of $\mathbf{L}^2$:

$$\mathbf{L}^2\beta|\ell m\rangle = \beta\mathbf{L}^2|\ell m\rangle = \ell(\ell+1)\beta|\ell m\rangle \tag{C.8}$$

The operators β and $\mathbf{L}_z$ do not commute, we can nevertheless expand the state $\beta|\ell m\rangle$ in terms of $|\ell' m'\rangle$. Since, from (C.8), we already know that its eigenvalue is $\ell(\ell+1)$, we can expand $\beta|\ell m\rangle$ in terms of just $|\ell m'\rangle$. Moreover, from parity operation onto spherical harmonics (B.1), i.e.[3]

$$\langle\vartheta\varphi|\Pi|\ell m\rangle = \langle\pi-\vartheta,\varphi+\pi|\ell m\rangle = (-1)^\ell\langle\vartheta\varphi|\ell m\rangle \quad , \tag{C.9}$$

we see that $|\ell m\rangle$ is an eigenstate of Π. Therefore it is possible to expand $\alpha|\ell m\rangle$ in terms of $|\ell m'\rangle$ and write:

$$\alpha|\ell m\rangle = \sum_{m'}|\ell m'\rangle\langle\ell m'|\alpha|\ell m\rangle \qquad \text{and} \qquad \langle\ell m|\alpha = \sum_{m'}\langle\ell m|\alpha|\ell m'\rangle\langle\ell m'|$$

Now it is easy to see that P_ℓ and α commute:

$$P_\ell\alpha = \sum_m|\ell m\rangle\langle\ell m|\alpha = \sum_{mm'}|\ell m\rangle\langle\ell m|\alpha|\ell m'\rangle\langle\ell m'|$$

$$\alpha P_\ell = \sum_m\alpha|\ell m\rangle\langle\ell m| = \sum_{mm'}|\ell m'\rangle\langle\ell m'|\alpha|\ell m\rangle\langle\ell m|$$

As we wished to prove.

C.2 Coulomb Matrix Elements for the Hydrogen Atom

We consider the well-known hydrogen atom whose wave functions are explicitly known.[4] The one-particle energies are simply given by the Lyman formula $E_n = -E_{\mathrm{Ryd}}/n^2$ which only depends on the principal quantum number n. A hydrogen state depends on the three quantum numbers n,ℓ,m. It is helpful to reduce the number of indices at each Coulomb matrix element from 12 to 4 by introducing $i=\{n,\ell,m\}$:

$$\psi_i(\mathbf{r}) \equiv \psi_{n\ell m}(\mathbf{r}) = R_{n\ell}(r)Y_\ell^m(\hat{\mathbf{r}}) \tag{C.10}$$

We simply label the states by:

[2] See e.g. Eq. (17-1) Ref. [51].
[3] See e.g. Eq. (6-64) Ref. [51].
[4] See Eq. (6.43) and (6.60)-(6.65) Ref. [66], or Eq. (7-19) and (7-20) Ref. [51].

i	0	1	2	3	4	5	6	7	8	9	10	11	12	13
$n\ell$	1s	2s	2p	2p	2p	3s	3p	3p	3p	3d	3d	3d	3d	3d
m	0	0	-1	0	+1	0	-1	0	+1	-2	-1	0	+1	+2

We have calculated all Coulomb matrix elements for the wave functions up to principal quantum number 3, using the method in section 5.3.1. Thus, we are considering 1+4+9=14 states and 14^4=38,416 matrix elements. Explicitly, we calculated:

$$W_{i_1 i_2 i_3 i_4} = \int d^3\mathbf{r}\, d^3\mathbf{r}'\, \psi^*_{i_1}(\mathbf{r})\psi^*_{i_2}(\mathbf{r}')\, \frac{e^2}{|\mathbf{r}-\mathbf{r}'|}\, \psi_{i_3}(\mathbf{r}')\psi_{i_4}(\mathbf{r}) \tag{C.11}$$

Since $\mathbf{r}$ and $\mathbf{r}'$ may be interchanged and since the interaction is an hermitian operator, we have the trivial symmetry among the indices

$$W_{i_1 i_2 i_3 i_4} = W_{i_2 i_1 i_4 i_3} = W^*_{i_4 i_3 i_2 i_1} = W^*_{i_3 i_4 i_1 i_2} \ , \tag{C.12}$$

which reduces the number of matrix elements that have to be evaluated from 38,416 to 9,751. Additional symmetry arises from properties of the spherical harmonics which causes all matrix elements to be real and many to vanish. From the 9,751 matrix elements, 1,062 do not vanish. And from the initial 38,416 matrix elements, 3,800 do not vanish. And from these 3,800 elements, only 274 differ in their absolute value.

Since, we don't want to list all these 274 numbers, we choose to restrict ourselves to the five states up to $n = 2$. From the 5^4=625 matrix elements, only 16 different absolute values occur from 107 non-vanishing matrix elements. These are given in the table below together with their sign and indices.

$\lvert W_{i_1 i_2 i_3 i_4}\rvert$ [Ryd]	$\lvert W_{i_1 i_2 i_3 i_4}\rvert$ [eV]	sign and $i_1 i_2 i_3 i_4$
1.250000	17.00712	$+0000$
0.485597	6.60688	$+0220$, $+0330$, $+0440$
0.419753	5.71103	$+0110$
0.391406	5.32535	$+3333$
0.370312	5.03836	$+2222$, $+2442$, $+4444$
0.349219	4.75136	$+2332$, $+3443$
0.324219	4.41122	$+1221$, $+1331$, $+1441$
0.300781	4.09234	$+1111$
0.178710	2.43148	$+0001$
0.058594	0.79721	-1124, $+1133$, $+1212$, $+1313$, $+1414$
0.043896	0.59723	$+0011$, $+0101$
0.042188	0.57399	$+2424$
0.034141	0.46451	-0024, $+0033$, $+0202$, $+0303$, $+0404$
0.025745	0.35028	$+0124$, -0133, $+0142$, -0212, -0313, -0414
0.021094	0.28700	$+2323$, -2433, $+3434$
0.017163	0.23352	$+0111$, $+0221$, $+0331$, $+0441$

By means of (C.12) and the table, all 625 matrix elements can be obtained. Here is an example:

$$W_{2p,2p,1s,2s} = W_{3301} = W_{0133} = -0.35028 \text{ eV}$$

Moreover, we should note that when the charge of the nucleus is Z, the one-particle energies are $E_n = -E_{\mathrm{Ryd}} Z^2/n^2$ and the Coulomb matrix elements are the ones for hydrogen multiplied by Z.

The energies (2.36) and (2.37) may be compared to the corresponding values obtained from hydrogen-atom-like wave functions (for $Z = 3$). Using the table above we find:[5]

$$U_{00} = 51.02 \text{ eV} \quad , \quad U_{11} = 12.28 \text{ eV} \quad , \quad U_{01} = 17.13 \text{ eV} \tag{C.13}$$

$$\varepsilon_0 = -122.45 \text{ eV} \quad , \quad \varepsilon_1 = -30.61 \text{ eV} \tag{C.14}$$

C.3 Exchange-Correlation Potential and Energy

Barth and Hedin [36] have proposed useful estimates for the exchange-correlation energy $\varepsilon_{\mathrm{xc}}(n^\uparrow, n^\downarrow)$ and the exchange-correlation potential $v^\sigma_{\mathrm{xc}}(n^\uparrow, n^\downarrow)$ for the spin-polarized case, which is a generalization of the spinless case proposed earlier by Hedin and Lundqvist [67]. The estimates are local, i.e. the $\varepsilon_{\mathrm{xc}}$ and v^σ_{xc} only depend on the densities $n^\uparrow$ and $n^\downarrow$ at $\mathbf{r}$. The total density (at $\mathbf{r}$) is $n = n^\uparrow + n^\downarrow$. Remembering that we use atomic Rydberg units, the electron gas parameter r_s is given by:

$$\frac{4\pi}{3}\, r_s^3\, a_0^3 = \frac{1}{n} \quad \leftrightarrow \quad r_s = \left(\frac{3}{4\pi} \cdot \frac{1}{n}\right)^{1/3} \tag{C.15}$$

Using the definitions

$$\begin{aligned}
&x = \frac{n^\uparrow}{n} \qquad a = 2^{-1/3} \qquad f(x) = \frac{x^{4/3} + (1-x)^{4/3} - a}{1-a} \\
&\gamma = \frac{4\,a}{3\,(1-a)} \approx 5.1298 \qquad \alpha_0 = \left(\frac{4}{9\pi}\right)^{1/3} \qquad \varepsilon_{\mathrm{x}}^0 = \frac{3}{2\pi\,\alpha_0} \approx 0.9163 \\
&c^P = 0.0504 \qquad c^F = 0.0254 \qquad r^P = 30 \qquad r^F = 75 \\
&\varepsilon_{\mathrm{x}}^P(r_s) = -\frac{\varepsilon_{\mathrm{x}}^0}{r_s} \qquad \varepsilon_{\mathrm{c}}^P(r_s) = -c^P\, F\left(\frac{r_s}{r^P}\right) \qquad \varepsilon_{\mathrm{c}}^F(r_s) = -c^F\, F\left(\frac{r_s}{r^F}\right) \\
&\text{where } F(z) = (1+z^3)\ln\left(1+\frac{1}{z}\right) + \frac{z}{2} - z^2 - \frac{1}{3} \\
&\mu_{\mathrm{x}}^P(r_s) = \frac{4}{3}\,\varepsilon_{\mathrm{x}}^P \qquad \mu_{\mathrm{c}}^P(r_s) = -c^P\,\ln\left(1+\frac{r^P}{r_s}\right) \qquad \nu_{\mathrm{c}}(r_s) = \gamma\,(\varepsilon_{\mathrm{c}}^F - \varepsilon_{\mathrm{c}}^P) \\
&A(r_s) = \mu_{\mathrm{x}}^P(r_s) + \nu_{\mathrm{c}}(r_s) \qquad B(r_s) = \mu_{\mathrm{c}}^P(r_s) - \nu_{\mathrm{c}}(r_s) \quad ,
\end{aligned} \tag{C.16}$$

the exchange-correlation energy and potential are given by (see Fig. C.1):

$$\varepsilon_{\mathrm{xc}}(n^\uparrow, n^\downarrow) = \varepsilon_{\mathrm{x}}^P(r_s) + \varepsilon_{\mathrm{c}}^P(r_s) + \gamma^{-1} f(x)\,\left[\mu_{\mathrm{x}}^P(r_s) + \nu_{\mathrm{c}}(r_s)\right] \tag{C.17}$$

$$v^\sigma_{\mathrm{xc}}(n^\uparrow, n^\downarrow) = (2n^\sigma/n)^{1/3} A(r_s) + B(r_s) \tag{C.18}$$

[5] Note that: $U_{ij} = Z \cdot W_{ijji}$

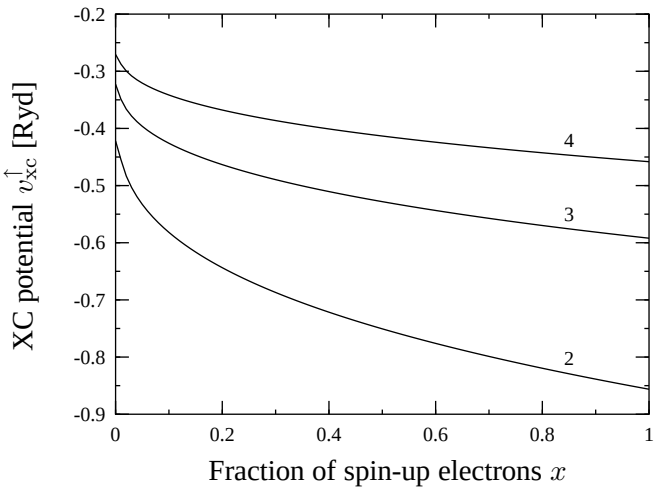

Figure C.1: The result (C.18) as a function of the spin-up electrons x for various electronic densities. The r_s values are indicated next to the curves.

Note that when $n^{\uparrow} = n^{\downarrow} = n/2$, i.e. the spinless case, we find $x = \frac{1}{2}$ and $f(\frac{1}{2}) = 0$. Hence, the above expressions reduce to (see Fig. C.2):

$$\varepsilon_{\rm xc}(n) = \varepsilon_{\rm x}^{P}(r_s) + \varepsilon_{\rm c}^{P}(r_s) \tag{C.19}$$

$$v_{\rm xc}(n) = \mu_{\rm x}^{P}(r_s) + \mu_{\rm c}^{P}(r_s) \tag{C.20}$$

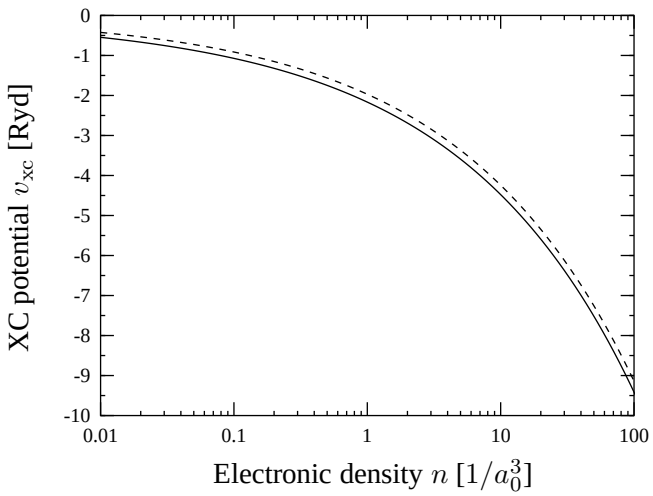

Figure C.2: The function Eq. (C.20) for the spinless case (solid) and (for comparison) the exchange potential from a uniform electron gas in Hartree-Fock approximation (dashed), see Eq. (1.1) in Ref. [36].

C.4 Evaluation of $\int_{-1}^{+1} dx \int_{-1}^{+1} dy \int_{-1}^{+1} dz \, \frac{1}{r^2}$

We wish to evaluate the integral

$$C \equiv \int_{-1}^{+1} dx \int_{-1}^{+1} dy \int_{-1}^{+1} dz \, \frac{1}{r^2} \quad . \tag{C.21}$$

To this end, we divide the volume V of the $2 \times 2 \times 2$ box into two parts: (i) The volume V_1 of a sphere with radius 1. (ii) The remaining volume V_2. Now, we evaluate C for the two volumes separately:

$$C = \int_{V_1} d^3\mathbf{r} \frac{1}{r^2} + \int_{V_2} d^3\mathbf{r} \frac{1}{r^2} = C_1 + C_2 \qquad \text{trivially } \; C_1 = 4\pi \tag{C.22}$$

The second integral is solved by numerical Monte Carlo integration, see Ref. [48], with a number of sample points N on the order of 10^{14}. By separating the volume, higher accuracy is achieved since the error estimate (Eq. (7.6.1) in [48]) depends on the variance of $1/r^2$ in the volume. Obviously, the variance is smaller for V_2 than for V. As a final result we find[6]

$$C = 15.34825 \quad . \tag{C.23}$$

C.5 Spherical Harmonics Expansion

Any function $A(\mathbf{r})$ within a (muffin-tin) sphere may be expanded in terms of spherical harmonics:

$$A(\mathbf{r}) = \sum_L A_L(r) Y_L(\hat{\mathbf{r}}) \tag{C.24}$$

If two functions $A(\mathbf{r})$ and $B(\mathbf{r})$ are given via their coefficients $A_L(r)$ and $B_L(r)$, then the corresponding coefficients $F_L(r)$ of the function $F(\mathbf{r}) = A(\mathbf{r})B(\mathbf{r})$ are given by

$$F_L(r) = \sum_{L_1, L_2} A_{L_1}(r) B_{L_2}(r) C_{L_1 L L_2} \quad , \tag{C.25}$$

as can easily be seen from the definition of the Gaunt coefficients $C_{LL'L''}$ in appendix B. We may use (C.25) to multiply a function with a plane wave $e^{\mathbf{k}}(\mathbf{r}) \equiv e^{-i\mathbf{kr}}$ whose coefficients are given by (see Eq. (16.127) in Ref. [52])

$$e_L^{\mathbf{k}}(r) = 4\pi j_\ell(kr) \left[i^\ell Y_L(\hat{\mathbf{k}}) \right]^* \quad , \tag{C.26}$$

where j_ℓ is the spherical Bessel function (B.4).

[6] With an error estimate which is small enough for allowing the statement: The result is “absolutely correct” to the digits given.

C.6 Lattice Properties

The FCC and the BCC Bravais lattice is defined by the set of translation vectors (A.2) and (A.5) respectively. From these definitions, one can calculate the number of next neighbors. All these next neighbors belong to the 1st shell, the second next neighbors belong to the 2nd shell, etc. The table shows some properties of the FCC and BCC lattice.

FCC

n	$d/S \approx$	#	Σ
0	0	1	1
1	1.8094	12	13
2	2.5589	6	19
3	3.1340	24	43
4	3.6188	12	55
5	4.0459	24	79
6	4.4321	8	87
7	4.7872	48	135
8	5.1178	6	141
9	5.4282	36	177
10	5.7218	24	201
11	6.0011	24	225
12	6.2679	24	249
13	6.5239	72	321
14	7.0078	48	369
15	7.2376	12	381
16	7.4603	48	429
17	7.6766	30	459
18	7.8870	72	531
19	8.0919	24	555
20	8.2917	48	603
21	8.4868	24	627
22	8.6776	48	675
23	8.8642	8	683
24	9.0470	84	767
25	9.2262	24	791
26	9.4019	96	887
27	9.5744	48	935
28	9.7439	24	959
29	10.0743	96	1055
30	10.2355	6	1061
31	10.3942	96	1157

BCC

n	$d/S \approx$	#	Σ
0	0	1	1
1	1.7589	8	9
2	2.0310	6	15
3	2.8722	12	27
4	3.3680	24	51
5	3.5178	8	59
6	4.0620	6	65
7	4.4264	24	89
8	4.5414	24	113
9	4.9749	24	137
10	5.2766	32	169
11	5.7445	12	181
12	6.0077	48	229
13	6.0929	30	259
14	6.4225	24	283
15	6.6590	24	307
16	6.7360	24	331
17	7.0355	8	339
18	7.2521	48	387
19	7.3228	24	411
20	7.5992	48	459
21	7.8001	72	531
22	8.1239	6	537
23	8.3122	24	561
24	8.3740	48	609
25	8.6167	36	645
26	8.7944	56	701
27	8.8528	24	725
28	9.0828	24	749
29	9.2516	72	821
30	9.3071	48	869
31	9.5262	24	893

The columns in the table show: (i) The number n of the shell. (ii) The distance d of the sites belonging to that shell to the "center" site **0**, divided by the Wigner-Seitz radius S. (iii) The number of sites # in the nth shell. (iv) The number of sites Σ up to (including) shell n.

C.7 Coefficients $C^k_{m_1 m_2 m_3 m_4}$

The coefficients $C^k_{m_{1\ldots4}}$ are defined by Eq. (5.53) for $\ell_1 = \ell_2 = \ell_3 = \ell_4 = 2$ and form a subset of the coefficients $C^k_{L_{1\ldots4}}$. The Gaunt coefficients $c^k(L, L')$, see Eq. (B.5), are tabulated in Ref. [54]. From (5.54), it follows that the coefficients $C^k_{m_{1\ldots4}}$ vanish unless $k = \{0, 2, 4\}$. Next, from Eq. (B.6), we see that

$$C^k_{m_1 m_2 m_3 m_4} = C^k_{m_2 m_1 m_4 m_3} = C^k_{m_4 m_3 m_2 m_1} = C^k_{m_3 m_4 m_1 m_2} \quad . \tag{C.27}$$

The explicit values of the coefficients $C^k_{m_{1\ldots4}}$ follow. For $k = 0$ we simply have:

$$C^0_{m_{1\ldots4}} = \delta_{m_1 m_4} \delta_{m_2 m_3} \tag{C.28}$$

Next, for $k = 2$, one finds:

$$C^2_{mm'm'm} = \frac{1}{49} \begin{pmatrix} 4 & -2 & -4 & -2 & 4 \\ -2 & 1 & 2 & 1 & -2 \\ -4 & 2 & 4 & 2 & -4 \\ -2 & 1 & 2 & 1 & -2 \\ 4 & -2 & -4 & -2 & 4 \end{pmatrix} \tag{C.29}$$

$$C^2_{mm'mm'} = \frac{1}{49} \begin{pmatrix} 4 & 6 & 4 & 0 & 0 \\ 6 & 1 & 1 & 6 & 0 \\ 4 & 1 & 4 & 1 & 4 \\ 0 & 6 & 1 & 1 & 6 \\ 0 & 0 & 4 & 6 & 4 \end{pmatrix} \tag{C.30}$$

For $k = 4$, one finds:

$$C^4_{mm'm'm} = \frac{1}{441} \begin{pmatrix} 1 & -4 & 6 & -4 & 1 \\ -4 & 16 & -24 & 16 & -4 \\ 6 & -24 & 36 & -24 & 6 \\ -4 & 16 & -24 & 16 & -4 \\ 1 & -4 & 6 & -4 & 1 \end{pmatrix} \tag{C.31}$$

$$C^4_{mm'mm'} = \frac{1}{441} \begin{pmatrix} 1 & 5 & 15 & 35 & 70 \\ 5 & 16 & 30 & 40 & 35 \\ 15 & 30 & 36 & 30 & 15 \\ 35 & 40 & 30 & 16 & 5 \\ 70 & 35 & 15 & 5 & 1 \end{pmatrix} \tag{C.32}$$

The remaining $C^k_{m_{1\ldots4}}$ (which are not given by Eqs. (C.28) to (C.32) above) can be determined by Tab. C.1 in connection with Eq. (C.27).

From the above, we can evaluate various m-sums for fixed k which are shown in Tab. C.2.

$C^k_{m_{1\ldots4}}$	k	$\{m_1, m_2, m_3, m_4\}$
$-\sqrt{36}/49$	2	$\{-2,+2,+1,-1\}$
$-\ \ 6$	2	$\{-2,+1,0,-1\}$, $\{-1,+2,+1,0\}$
$-\ \ 1$	2	$\{-1,+1,0,0\}$
$+\ \ 6$	2	$\{-2,0,-1,-1\}$, $\{0,+2,+1,+1\}$
$+\ 16$	2	$\{-2,+2,0,0\}$
$+\ 24$	2	$\{-2,+1,-1,0\}$, $\{-1,+2,0,+1\}$
$-\sqrt{1225}/441$	4	$\{-2,+2,-1,+1\}$
$-\ 900$	4	$\{-1,+1,0,0\}$
$-\ 600$	4	$\{-2,+1,-1,0\}$, $\{-1,+2,0,+1\}$
$-\ 150$	4	$\{-2,0,-1,-1\}$, $\{0,+2,+1,+1\}$
$-\ \ 25$	4	$\{-2,+2,+1,-1\}$
$+\ 150$	4	$\{-2,+1,0,-1\}$, $\{-1,+2,+1,0\}$
$+\ 225$	4	$\{-2,+2,0,0\}$

Table C.1: Non-vanishing $C^k_{m_{1\ldots4}}$ which are not of the form $C^k_{mm'm'm}$ or $C^k_{mm'mm'}$. They can all be written in a form $C^k_{m_{1\ldots4}} = \pm\sqrt{x}/D_k$, where x and D_k are integers.

	$\sum_{mm'} C^k_{mm'm'm}$	$\sum_{m\neq m'} C^k_{mm'mm'}$	$\sum_{m} C^k_{mmmm}$
$k=0$	25	0	5
$k=2$	0	$8/7$	$2/7$
$k=4$	0	$80/63$	$10/63$

Table C.2: Various m-sums over coefficients $C^k_{m_{1\ldots4}}$ for fixed k.

C.8 Variation of One-Particle Basis

For a second-quantized Hartree calculation, the Hartree basis is the right choice, as explained in section 6.3.1. However, this was not obvious to us when we started working on this problem, and it is not clear whether this is the best choice for a Hartree-Fock calculation. Therefore, we introduced a basis which depends on a parameter x through the Hamiltonian:

$$H'(x) = -\nabla^2 + (1-x)\, v_0 + x\, v_{\mathrm{H}} = H_0 + x \cdot \text{“Hartree term”}$$

This (auxiliary) Hamiltonian is used to construct the basis, as in section 5.2.3 example 3. In essence, x controls the localization of the basis within the MT sphere. For small x, the Wannier functions become more localized.[7] As mentioned before, $H'(x=0) = H_0$ is the Hamiltonian in which the interaction among the valence electrons is artificially switched off. Thus, it is very illuminating to look at the positions of the energy eigenvalues of H' as a function of x, which can be seen for copper in Fig. C.3. As can clearly be seen, the Hartree interaction term has a huge impact on the band structure. It is also interesting to take a look at the Slater integrals (5.78) as a function of x (Fig. C.4). Here, we have also plotted the averaged exchange interaction J as given by Eq. (5.80). It is not surprising that these are monotonic decreasing functions, since for larger x, the radial wave functions become less localized and thus the Slater integrals decrease.

Now, for a Hartree-Fock calculation, is not clear which basis (which will still be limited) is best. Therefore, we have minimized the total effective energy (6.20), i.e. performed calculations for different x and regard the Hartree-Fock total energy as a function of x in order to determine its minimal value. These calculations have shown that $E(x)$ assumes it minimum at $x = 1$ too[8] (or least very close to $x = 1$) such that the Hartree basis is a good choice. It is important to realize that when the Hartree-Fock total energy is evaluated as a function of x, not only the basis depends on x, but also the term $\Sigma^{\mathrm{HF}}_{12,\sigma}$ depends on x via the occupation matrix A^{σ}_{12} and the Coulomb matrix $W_{12,34}$.

[7] We should note that the localization of wave function can be expressed in terms of the so-called “inverse participation number”, see Ref. [68].

[8] Similar as the solid curve in Fig. 2.1.

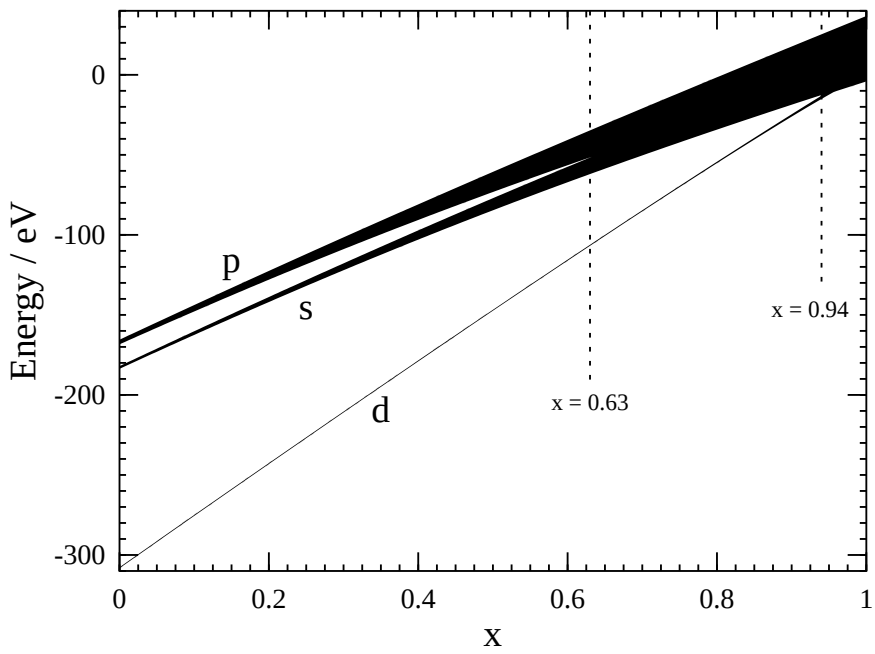

Figure C.3: Position of bands as a function of x for Cu (see text).

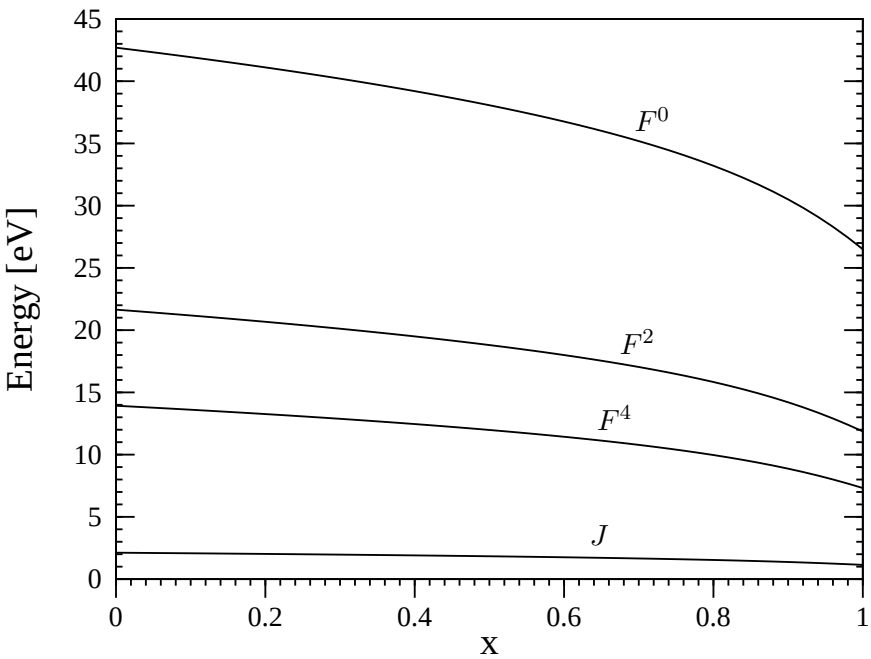

Figure C.4: Slater integrals F^0, F^2, F^4 and $J = (F^2 + 10/9F^4)/17.5$ as a function of x for Cu.

Index

Bibliography

[1] P. Hohenberg and W. Kohn, Phys. Rev. **136**, B 864 (1964).

[2] W. Kohn and L.J. Sham, Phys. Rev. **140**, A1133 (1965).

[3] J. Rose, J. Smith, F. Guinea and J. Ferrante, Phys. Rev. B **29**, 2963 (1984).

[4] M. Cardona and L. Ley (Eds.), *Photoemission in Solids* (Springer-Verlag, Berlin, 1978).

[5] D.E. Eastman, F.J. Himpsel and J.A. Knapp, Phys. Rev. Lett. **44**, 95 (1980).

[6] J. Hubbard, Proc. Roy. Soc. **A276**, 238 (1963).

[7] V.I. Anisimov, J. Zaanen and O.K. Andersen, Phys. Rev. B **44**, 943 (1991).

[8] M.M. Steiner, R.C. Albers, D.J. Scalapino and L.J. Sham, Phys. Rev. B **43**, 1637 (1991).

[9] M.M. Steiner, R.C. Albers and L.J. Sham, Phys. Rev. B **45**, 13272 (1992); Phys. Rev. Lett. **72**, 2923 (1994).

[10] V.I. Anisimov, A.I. Poteryaev, M.A. Korotin, A.O. Anokhin and G. Kotliar, J. Phys. Cond. Matter **9**, 7359 (1997).

[11] A.I. Lichtenstein and M.I. Katsnelson, Phys. Rev. B **57**, 6884 (1998).

[12] V. Drchal, V. Janis and J. Kudrnovsky, Phys. Rev. B **60**, 15664 (1999).

[13] M.I. Katsnelson and A.I. Lichtenstein, J. Phys. Cond. Matter **11**, 1037 (1999).

[14] A. Liebsch and A.I.Lichtenstein, Phys. Rev. Lett. **84**, 1591 (2000).

[15] M.B. Zölfl, T. Pruschke, J. Keller, A.I. Poteryaev, I.A. Nekrasov and V.I. Anisimov, Phys. Rev. B **61**, 12810 (2000).

[16] T. Wegner, M. Potthoff and W. Nolting, Phys. Rev. B **61**, 1386 (2000).

[17] I.A. Nekrasov, K. Held, N. Blümer, A.I. Poteryaev, V.I. Anisimov and D. Vollhardt, Eur. Phys. J. B **18**, 55 (2000).

[18] T. Wegner, *Zur Theorie von Korrelations- und Temperatureffekten in Spektroskopien: Die ferromagnetischen 3d-Übergangsmetalle* Doc. diss. at the Humboldt-University of Berlin, Germany (2000).

[19] N.E. Bickers and D.J. Scalapino, Ann. Phys. **193**, 206 (1989).

[20] For a review see: A. George, G. Kotliar, W. Krauth and M.J. Rozenberg, Rev. Mod. Phys. **68**, 13 (1996).

[21] W. Metzner and D.Vollhardt, Phys. Rev. Lett. **62**, 324 (1989).

[22] P.H. Dederichs, S. Blügel, R. Zeller and H. Akai, Phys. Rev. Lett. **53** 2512 (1984).

[23] Mark S. Hybertsen, M. Schlüter and Niels E. Christensen, Phys. Rev. **B39**, 9028 (1988).

[24] A.K. McMahan, R.M. Martin and S. Satpathy, Phys. Rev. B **38**, 6650 (1988).

[25] O. Gunnarsson, O.K. Andersen, O. Jepsen and J. Zaanen, Phys. Rev. B **39**, 1708 (1989).

[26] A.K. McMahan, J.F. Annett and R.M. Martin, Phys. Rev. B **42**, 6268 (1990).

[27] M. Alouani, R.C. Albers and J.M. Wills, Synthetic Metals **55-57**, 3358 (1993).

[28] I. Schnell, G. Czycholl and R.C. Albers, Phys. Rev. B **65**, 075103 (2002).

[29] G. H. Wannier, Phys. Rev. **52**, 191 (1937).

[30] J. Callaway, *Quantum Theory of the Solid State* (Academic Press, San Diego, 1974).

[31] H.L. Skriver, *The LMTO Method* (Springer-Verlag, Berlin, 1984).

[32] O.K. Andersen, Phys. Rev. B **12**, 3060 (1975).

[33] N. Marzari and D. Vanderbilt, Phys. Rev. B **56**, 12847 (1997).

[34] A. Svane and O.K. Andersen, Phys. Rev. B **34**, 5512 (1986).

[35] R.M. Dreizler and E.K.U. Gross, *Density Functional Theory* (Springer, New York, 1990).

[36] U. von Barth and L. Hedin, J. Phys. C **5**, 1629-1642 (1972).

[37] E. Esposito, A.E. Carlson, D.D. Ling, H. Ehrenreich and C.D. Gelat, Phil. Mag. A **41**, 251 (1980).

[38] J.F. Janak, Phys. Rev. B **18**, 7165 (1978)

[39] O.K. Andersen: "Electronic Structure of Metals", *Troisième Cycle de la Physique en Suisse Romande* Geneve 1978 (unpublished).

[40] P. Söderling, *Theoretical Studies of Elastic, Thermal, and Structural Properties of Metals* Doc. diss. at Uppsala University, Sweden (1994).

[41] David J. Singh: *Planewaves, Pseudopotentials and the LAPW Method* (Kluwer Academinc Publishers, Boston/Dordrecht/London, 1994).

[42] P. Blaha, K. Schwarz and J. Luitz, WIEN97 Package, Vienna University of Technology (1998).

[43] O. Jepsen and O.K. Andersen, Solid State Commun. **9**, 1763 (1971); G. Lehmen and M. Taut, Phys. Status Solidi (b) **54**, 469 (1972).

[44] G. Czycholl, *Theoretische Festkörperphysik* (Vieweg, Braunschweig/Wiesbaden, Germany, 2000).

[45] N.W. Ashcroft and N.D. Mermin, *Solid State Physics* (Saunders, Philadelphia, 1976).

[46] U. Mizutani, *Electron Theory of Metals* (Cambridge University Press, Cambridge, England, 2001).

[47] I. Schnell, *Behandlung von Korrelationseffekten in ab-initio Bandstrukturrechnungen* Diploma thesis, University of Bremen, Germany (1999).

[48] W.H. Press, S.A. Teukolsky, W.T. Vetterling and B.P. Flannery, *Numerical Recipes in C* (Cambridge University Press, Cambridge, England, 1992).

[49] V.L. Moruzzi, J.F. Janak and A.R. Williams, *Calculated Electronic Properties of Metals* (Pergamon, New York, 1978).

[50] M.R. Spiegel, *Probability and Statistics* (McGraw-Hill Book Company, New York, 1975).

[51] G. Baym, *Lectures on Quantum Mechanics* (Addison-Wesley, New York, 1969).

[52] J.D. Jackson, *Classical Electrodynamics* (John Wiley, New York, 1975).

[53] M. Springborg and O.K. Andersen, J. Chem. Phys. **87** (12), 7125 (1987).

[54] E.U. Condon and G.H. Shortley, *The Theory of Atomic Spectra* (Cambridge University Press, Cambridge, England, 1953).

[55] E. Oran Brigham, *The Fast Fourier Transform* (Prentice-Hall, Englewood Cliffs, 1974).

[56] O. Peschel, *Vergleich von ab-initio- mit Modellrechnungen zur elektronischen Bandstruktur von Metallen* Diploma thesis, University of Bremen, Germany (2002).

[57] P.O. Löwdin, J. Chem. Phys. **18**, 365 (1950).

[58] H. Eschrig, *Optimized LCAO Method* (Springer, New York, 1989).

[59] J.C. Slater, Phys. Rev. **34**, 1293 (1929).

[60] A.I. Lichtenstein and M.I. Katsnelson, *Magnetism of Correlated Systems: Beyond LDA* (2001) which appears in the book: K. Baberschke, M. Donath and W. Nolting (Eds.) *Band-Ferromagnetism* (Springer-Verlag, Berlin, 2001).

[61] F.M.F. de Groot, J.C. Fuggle, B.T. Thole and G.A. Sawatzky, Phys. Rev. B **42**, 5459 (1990).

[62] V.I. Anisimov, I.V. Solovyev, M.A. Korotion, M.T. Czyzyk and G.A. Sawatzky, Phys. Rev. B **48**, 16929 (1993).

[63] W.A. Harrison, *Electronic Structure and the Properties of Solids* (W.H. Freeman and Company, San Francisco, 1980); E.C. Stoner, Proc. Roy. Soc. A **165**, 372 (1938).

[64] M. Springer and F. Aryasetiawan, Phys. Rev. B **57**, 4364 (1998).

[65] M. Abramowitz and I.A. Stegun, *Handbook of Mathematical Functions* (Dover Publications, New York, 1964).

[66] W. Nolting, *Theoretische Physik 5, Teil 2* (Zimmermann-Neufang, Ulmen, 1993).

[67] L. Hedin and B.I. Lundqvist, J. Phys. C **4**, 2064-2083 (1971).

[68] B. Kramer and A. MacKinnon, *Localisation – Theory and Experiment*, Preprint 1993.